Instituut voor
Kern- en Stralingsfysica
Departement natuurkunde en sterrenkunde
Faculteit Wetenschappen

KATHOLIEKE UNIVERSITEIT
LEUVEN

Electromagnetically induced transparency for single gamma photons

Promotor:
Prof. Dr. J. Odeurs

Proefschrift ingediend tot
het behalen van de graad van
doctor in de wetenschappen
door

Stijn Gheysen

2006

De auteur is aspirant van het Fonds voor Wetenschappelijk Onderzoek - Vlaanderen

Dank aan allen die hun licht hebben laten schijnen op dit werk.
Jullie veelkleurig spectrum leeft voort in deze woorden en symbolen.

"And the disciples had not seen Jesus because of the great light in which he was, or which was about him; for their eyes were darkened because of the great light in which he was. But they saw only the light, which shot forth many light-rays. And the light-rays were not like one another, but the light was of divers kind, and it was of divers type, from below upwards, one [ray] more excellent than the other, ..., in one great immeasurable glory of light; it stretched from under the earth right up to heaven."

Pistis Sophia[1]

[1] gnostic manuscript, 250-300 AD, translated by G. S. R. Mead, 1921

Contents

Introduction

The quest for nuclear EIT

According to the title, this thesis should deal with electromagnetically induced transparency (or: EIT) in the domain of gamma photons and nuclei. But maybe the title should have started with *"The (long and painful) quest for ..."*, making it, however, too long and less appealing. With this introductory section, we just want to warn the reader that we have not found the holy grail. However, the quest itself has been gratifying.
The holy grail in this work is embodied by the realization of EIT in the nuclear realm. EIT is a well-known phenomenon in quantum optics, where it is commonly observed in a three-level Λ-scheme as a transparency window in the absorption spectrum of resonant radiation. More details about this 'optical' EIT and a blueprint for implementation in nuclear schemes are discussed in chapter 2.
From a chronological point of view, the quest starts with a series of Mössbauer experiments on a $FeCO_3$ single crystal, presented in chapter 1. The ^{57}Fe nuclei in this crystal experience a hyperfine level crossing at $T \approx 31\,\mathrm{K}$ in the first excited state, which makes it a potential candidate for the investigation of nuclear three-level systems. This was recognized already more than ten years ago, when our group performed Mössbauer experiments on a $FeCO_3$ powder [1]. At the level crossing, a reduced absorption was observed that could not be explained at that time. Now, a first analysis of the Mössbauer spectra for a single crystal is again showing an important misfit, in the form of less absorption at the level crossing than expected.
These experimental results seem to long for an interpretation in terms of EIT. To that purpose we develop two models that take into account a mixing interaction between the crossing levels and that treat the resonant scattering of gamma radiation in a semiclassical way. These models, which are designated as

the Blume-Kistner and the Maxwell-Schrödinger model, are discussed in chapter 3 along with their application to the analysis of the experimental data.
Because in this thesis we emphasize the single-photon nature of the nuclear scattering process, in chapter 4 we take it one step further and consider a fully quantum mechanical approach to the resonant scattering in an ensemble of Λ-type nuclei. This model is nowadays referred to as the 'coherent path model' and is based on the work of Heitler, Harris and Hoy. The results obtained are compared with the semiclassical solutions, yielding some interesting fundamental questions concerning the nature of nuclear (multiple) scattering.
Transparency is not the sole feature of EIT. It is also accompanied by a slow group velocity of the transmitted radiation, which has led to some famous slow light experiments. The last chapter is devoted to a discussion of the timing properties of the transmitted gamma radiation, including an estimate of its group velocity.
But first, as a prelude, we want to sketch the background in which the second part of the title (*"... single (gamma) photons"*) should be envisioned.

The photon

> All the fifty years of conscious brooding have brought me no closer to the answer to the question, "What are light quanta?" Of course today every rascal thinks he knows the answer, but he is deluding himself.
>
> Albert Einstein [2]

The photon concept is deeply interwoven with the history of quantum mechanics and the interpretation of the particle-wave duality. Arthur Zajonc formulates this even more boldly, stating that the history of light is entwined with that of the 'mind' [3].
Light and light phenomena have always had an important role in man's understanding of the world to which he is born. From its mythical and religious perceptions to the empirical observations, the concept of light indeed reflects the human state of mind. We should, therefore, not be surprised to witness the revival of the idea of light consisting of light particles, photons, in our present, materialistic world view, although this was certainly not intended by its two main protagonists, Planck and Einstein.
Because light can only be observed *indirectly*, *i.e.* in its interaction with matter, it also adopts some properties of these massive particles. The quantization of light and the picture of a photon as a localized particle should hence be understood as emerging properties from the detection mechanism, not necessarily inherent to light itself, although many physicists seem to have assigned to them

an ontological status.
It is one of the major breakthroughs of quantum mechanics that has taught us the importance of the measurement itself. The fact that we, as an observer, determine a priori the set of possible final states onto which the state of the measured system is projected, has deep repercussions regarding the interpretation of so-called hard, empirical evidence. It reminds us the words of Einstein, who warned us that "the human mind has first to construct forms independently before we can find them in things."

According to the modern quantum theory of light [4,5], the notion of a photon appears as the single-mode excitation of the electromagnetic field, bearing more resemblance with concepts as phonons, plasmons or polaritons than with electrons or protons. Although this theory has achieved remarkable agreement with experiments, it has to deal with severe formal problems such as the renormalization procedure [6].
Another very promising theory capable of addressing the fundaments of light is formulated in (linear) stochastic electrodynamics or (L)SED [7]. The central premise of SED is that the quantum behavior of otherwise classical particles is a result of its interaction with the vacuum field [8]. This zero-point field, or empty photon mode of the electromagnetic field, now plays a major role in the development of the usual quantum formalism, reducing its postulates to predictions of a more general, underlying theory. This vacuum field ensues from the classical Maxwell equations in a natural way, *i.e.* as a solution of the source-free equations, instead of the usual gauged null solution. Nequaquam vacuum[2] ...
Hence, SED re-enthrones the classical Maxwell equations, along with their wave description of light. Although they share some common ideas, SED can not be treated on the same footing as ordinary semiclassical theories, which only *combine* the quantum description of matter with the classical equations of radiation.
Nevertheless, in this work we rely on both quantum and semiclassical theories as they have proven to provide a very useful mathematical formalism. From the conceptual or interpretational level, however, we should keep an open mind, unconstrained from traditional thinking, and realize that quantum theory might not have the final word.

[2](can be translated as "there is no empty space") inscription found on the tomb of Christian Rosenkreutz, in *Fama Fraternitatis* (1614),

Single photons

In the last five years research on single photons has become immensely popular. It is not only the interest in the fundamental properties of single photon states, but especially the promising features with respect to quantum state engineering [9,10] that drives this research effort. It is shown that most quantum computing schemes that work by means of linear optics as well as schemes for quantum cryptography, see *e.g.* [11,12], require sources of single photons.
A variety of single photon sources has already been investigated. For an overview and comparison of the state-of-the-art techniques we refer to [13]. Also, the open-access journal *New Journal of Physics* has devoted an entire issue on single photon research [14]. The different single-photon sources can still address only a part of the ideal source implementation, *i.e.* the creation of exactly one photon, at precisely the time required and with a convenient spatio-temporal shape. It can also be desirable to produce trains of single photons at high repetition rates.
In this work a very simple source of single photons is considered, *i.e.* radioactive nuclei embedded in a solid material. Some single-photon characteristics of this radioactive source are discussed in section 2.2 and 4.2.3. It is clear that this source of single photons does not provide photons 'on demand' and also their spatio-temporal shape is restricted to the decay mode of the emitting nucleus. But, perhaps these (initial) features can be modified, or even controlled, by allowing the photons to interact with a nuclear medium that is able to reshape or fine tune them depending on the envisioned application.
The study of these nuclear systems contributes to the single-photon research in a very original way, by exploiting the advantage of an easily achievable single-photon source and truly single-photon events.

Photon wave function

First of all, although it is a very interesting field of study, this work is *not* about the philosophical interpretations of fundamental quantum concepts. With the following discussion we only hope to put things in the right perspective.
With the term 'wave function' we do not necessarily mean a function that satisfies the quantum mechanical 'wave' equations, rather we are referring to a complex vector function of space and time coordinates $\mathbf{r}$ and t that describes the quantum state of a single photon.
For massive particles, the coordinate representation of the wave function, $\phi(\mathbf{r},t)$ is defined as the projection of the state vector $|\psi\rangle$ on the eigenstates $|\mathbf{r}\rangle$ of the position operator $\hat{\mathbf{r}}$

$$\phi(\mathbf{r},t) = \langle \mathbf{r}|\psi\rangle. \tag{1}$$

In the quantum description of photons, however, this approach does not work due to the lack of a well-defined position operator $\hat{\mathbf{r}}$, which arises from the difficulties with the localizability of the photon. According to Bialynicki-Birula [15], this can be circumvented by using *any* function of $\mathbf{r}$ that adequately describes photon states. He states that "all that really should matter is that the wave function be precisely defined and that its interpretation be not extended beyond the limits of its applicability". Also, "it should be pointed out that in relativistic quantum theory, even for particles with nonvanishing rest mass, the position operator and the localization associated with it do not live up to our nonrelativistic expectations", *i.e.* they also experience some degree of nonlocalizibility, similar to photons.
A useful approach to the photon wave function in our case, which is the emission and detection of single gamma photons, is found in the work of Glauber [16] and Scully and Zubairy [17]. It boils down to the following quote:

> What is a photon and where is it? A photon is what a photodetector detects and a photon *is* where the photodetector detects it.
>
> Roy J. Glauber

In resonant fluorescence experiments involving nuclei and gamma photons, the latter are commonly detected by means of a proportional counter. The detection principle is based on the ionization of (gas) atoms, which produces a detectable current. In this process the ionizing photon is destroyed. Therefore, the probability that a photon ionizes a detector atom at position $\mathbf{r}$ and between times t and $t + dt$ is proportional to $w(\mathbf{r}, t)dt$ [17] with

$$w(\mathbf{r}, t) = |\langle \psi_f | E^{(+)}(\mathbf{r}, t) | \psi_i \rangle|^2, \tag{2}$$

where $|\psi_i\rangle$ and $|\psi_f\rangle$ are the initial and final state of the photon field. The photon is annihilated by the positive frequency part of the electric field operator

$$\mathbf{E}^{(+)}(\mathbf{r}, t) = \sum_{\mathbf{k},\lambda} \mathcal{E}_{\mathbf{k}} \epsilon_{\mathbf{k}}^{\lambda} a_{\mathbf{k},\lambda} e^{i(\mathbf{k}.\mathbf{r} - \omega_k t)}, \tag{3}$$

where $\mathcal{E}_{\mathbf{k}} = (\hbar\omega_k / 2\epsilon_0 V)^{1/2}$, $\epsilon_{\mathbf{k}}^{\lambda}$ a unit polarization vector, belonging to polarization state λ, and $a_{\mathbf{k},\lambda}$ the annihilation operator of a photon with wave vector $\mathbf{k}$ and polarization λ.
If $|\psi_i\rangle$ corresponds to a *single* photon state, designated by $|\psi_\gamma\rangle$, then $|\psi_f\rangle$ can only coincide with the vacuum state $|0\rangle$. Hence, the function

$$\psi(\mathbf{r}, t) = \langle 0 | \mathbf{E}^{(+)}(\mathbf{r}, t) | \psi_\gamma \rangle \tag{4}$$

can be interpreted as a *single photon wave function.*
It must be emphasized that in this approach the space and time dependent

wave function only emerges from the photon interaction with a detector atom. This model is very suitable for our purpose, especially in the case of the coherent path model of chapter 4, but should not be taken any further.

Remark 1: If $|\psi_f\rangle$ is unknown and a statistical average is taken over $|\psi_i\rangle$, then the probability $w(\mathbf{r},t)$ can be recast as

$$w(\mathbf{r},t) = \langle E^{(-)}(\mathbf{r},t)E^{(+)}(\mathbf{r},t)\rangle, \tag{5}$$

which equals the average light intensity at point $\mathbf{r}$ and time t and is also closely related to the first-order coherence function

$$G^{(1)}(\mathbf{r}_1,\mathbf{r}_2;t_1,t_2) = \langle E^{(-)}(\mathbf{r}_1,t_1)E^{(+)}(\mathbf{r}_2,t_2)\rangle. \tag{6}$$

Remark 2: The appearance of only the positive frequency part of the electric field in the expression of the photon wave function bears a deeper meaning. Plane wave solutions of the Maxwell wave equations in free space can have a positive or a negative frequency part

$$e^{-i\omega t+\mathbf{kr}} \qquad \text{or} \qquad e^{+i\omega t-\mathbf{kr}}, \tag{7}$$

respectively. According to relativistic quantum mechanics [18], solutions with positive frequency correspond to particles, while the negative frequency solutions correspond to antiparticles. But photons have no antiparticles, or, formulated in another way, they are considered identical. Therefore, the negative frequency part contains no additional information and can be discarded as redundant. Using only the positive frequency part, it is possible to construct a Schrödinger-type of wave equation, which is similar to the Dirac equations for the neutrino, see *e.g.* [15,17,19] leading to the assertion that it can be identified with the true photon wave function.

Chapter 1

$FeCO_3$ Mössbauer experiments

In this chapter we first give a detailed description of the $FeCO_3$ or mineral siderite crystal, from the low energy crystallographic to the high energy nuclear structure. In a second part we describe the experimental setup and present the Mössbauer spectra that have been obtained under different experimental conditions.

1.1 Siderite crystal

Ferrous carbonate or $FeCO_3$, naturally occurring as the mineral *siderite*, chemically belongs to the carbonate group and structurally to the calcite ($CaCO_3$) subgroup (hexagonal space group $R\bar{3}c$). The basic anionic CO_3^{2-} complex of carbonates consists of an equilateral triangle of oxygen atoms in coordination bonds with the central carbon atom. The threefold symmetry of the triangular carbonate groups explains the trigonal symmetry that many members of this class possess.

Cations with small ionic radius (Ni, Mg, Zn, Co, Fe, Mn and Ca) are generally incorporated into carbonates having a rhombohedral unit cell. Its structure can be visualized as a cubic lattice which has been contracted along a

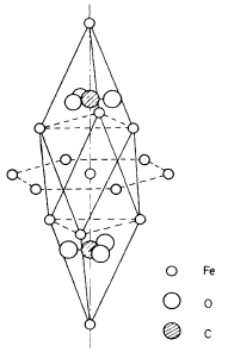

Figure 1.1: Illustration of the crystal structure of $FeCO_3$ [20]. The vertical axis is the trigonal and optical axis of the crystal. The central Fe^{2+} ion has 6 nearest neighbors, three in the plane above and three in the plane below. The six next-nearest neighbors lie in the plane containing the central ion.

body diagonal, as illustrated in Fig. 1.1. The diagonal of deformation becomes the prominent axis of symmetry.
A rhombohedron consists of 6 equal rhombi or quadrilateral, 'diamond'-shaped planes. Hence, it is completely parameterized by an opening angle α and side a. Descriptions of rhombohedral carbonates are usually given in terms of a triple hexagonal cell. Fig. 1.2 shows the relationship between the steep, true rhombohedral unit cell ($a = 5.83\,\text{Å}$, $\alpha = 47°45'$), the morphologic (or cleavage) cell (axial ratios $a : c = 1 : 0.819$) and the hexagonal unit cell ($a = 4.72\,\text{Å}$, $c = 15.45\,\text{Å}$) [22].
All crystals in the calcite group show a perfect rhombohedral cleavage to which, historically, the indices $\{10\bar{1}1\}$ have been assigned. These are the crystal faces of the morphologic cell in Fig. 1.2. Also the axial ratios are still expressed in this morphologic unit cell axis system. From these ratios one can derive the angle of the $c-axis$ (or 'axis of highest symmetry' or 'optical axis') with respect to the $\{hk\bar{i}l\}$ cleavage plane according to [21]

$$\beta = \frac{\pi}{2} - \arctan\left(\frac{c(h+k)}{l\cos\phi}\right) \tag{1.1}$$

Substituting the values for the case of $FeCO_3$, the angle of the c-axis with the $\{10\bar{1}1\}$ is calculated[1] to be $\beta = 46°36'$. This angle will come into play when considering the orientation of the crystal with respect to non-scalar external

[1] In the hexagonal system, the negative end of the a_3 axis is taken as $\phi = 0°$. According to this definition $\phi = 30°$ for $\{h0\bar{h}l\}$ planes.

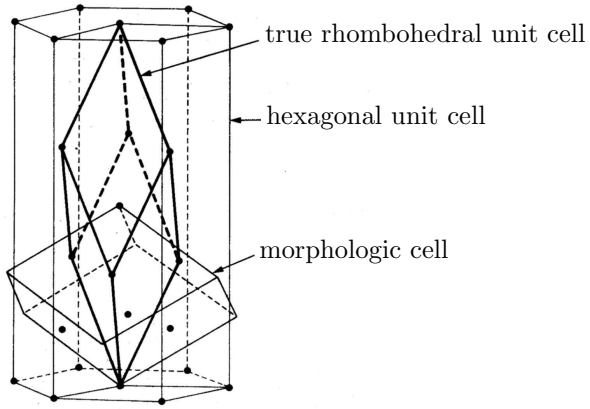

Figure 1.2: Relation of the steep, true unit cell to the cleavage rhombohedron (morphologic cell). The hexagonal cell is also shown. [21]

fields, see the discussion of the experimental geometry in section 1.2.

Natural siderite is usually impure, with impurities quoted up to 17%, see table 1.1, mainly Mg and Mn, possibly Ca and Zn. All of them are chemically equivalent with Fe. Because the Mg and Mn ions have similar ionic radii (0.072 nm and 0.083 nm respectively, compared with 0.078 nm of the Fe ion [30]), they are expected to be found on substitutional sites. Complete series of $Fe_xMg_{1-x}CO_3$ and $Fe_xMn_{1-x}CO_3$ are possible [21]. $MgCO_3$ or *magnesite* and $MnCO_3$ or *rhodochrosite* are also commonly found in nature; once the Fe exceeds 50% of the metal content, it is called *siderite*. A Ca ion has a larger radius (0.100 nm [30]) and will not easily substitute for Fe. It is well documented, however, that calcite can appear as a coexisting carbonate species, in the siderite crystal structure [21].

The chemical composition of our siderite crystal has been obtained through an atomic absorption spectroscopy study [31]. Expressed in atomic proportions, the total cation content of the sample is 84.2% Fe, 8.1% Ca, 6.4% Mn with small traces ($< 1\%$) of Na, Al, Mg, K and Sr.

1.1.1 Electronic structure

Before discussing any nuclear properties, we take a brief and heuristic look into the electronic structure of $FeCO_3$, as summarized in Fig. 1.3. As they give rise to the electric field gradient (efg), an antiferromagnetic hyperfine field and relaxation effects, knowledge of these electronic levels is of paramount impor-

Table 1.1: Overview of 'recent' hyperfine studies of $FeCO_3$. The composition of the samples is recalculated to atomic proportions for ease of comparison. B (B_{sat}) is the (saturated) magnetic hyperfine field, Δ is the quadrupole splitting, IS is the isomer shift and f the recoilless fraction. These parameters are considered in more detail further in this chapter. RT stands for 'room temperature' ($\approx 293\,K$).

purity	Néel temperature	hyperfine fields	ref.
powder (Bokal USSR deposit)	$\sim 35\,K$	-	[23]
$Fe_{0.83}Mn_{0.05}R^2{}_{0.12}$ (Roxbury, US)	$\sim 38\,K$	-	[24]
powder (Kokai-do, Korea)	-	$B_{4.2K} = 17(1.5)\,T$ $\Delta_{RT} = 1.87(1)\,mm/s$ $\Delta_{77K} = 2.1(1)\,mm/s$ IS=1.38(2) mm/s	[25]
$Fe_{0.79}Mg_{\sim 0.1}R_{\sim 0.1}$	-	-	[26]
$Fe_{\sim 0.95}Mn_{\sim 0.045}$	38.4(2) K	$B_{sat} = 18.4(2)\,T$ $\Delta_{<38K} = 2.06(3)\,mm/s$ IS=1.36(3) mm/s	[27]
- (artificially grown)	38.3(3) K	$B_{sat} = 18.4(3)\,T$ $\Delta_{4.2K} = 2.02(3)\,mm/s$	[28]
$Fe_{0.95}Mn_{0.045}Mg_{0.005}$ (Ivigtut, Greenland)	39.3(5) K	$\Delta_{RT} = 1.770(4)\,mm/s$ IS_{RT}=1.002(4) mm/s	[29]

tance for further analysis and discussion of the Mössbauer spectra.
Applying Hund's rules to the [Ar]$3d^6$ ground state electron configuration of the Fe^{2+} free ion yields a ^5D ground state. In a crystal lattice, the Fe^{2+} ions are subjected to electric fields originating from the ligands, giving rise to a so-called 'crystal field' [32, 33]. The crystal field in $FeCO_3$ is predominantly cubic, splitting the ^5D ground state into an orbital doublet ^5E and a triplet $^5T_2$, separated by $\sim 1.25\,\text{eV}$ [20,34]. The next largest perturbation is a trigonal distortion of the crystal field, which splits the $^5T_2$ state into an orbital singlet $^5A_1$ and a lower lying ^5E doublet state (split by $\sim 200\,\text{meV}$). A detailed theoretical study of the ^5D ground state splitting [35] shows that the ^5E excited state should be taken into account to obtain more accurate level splittings and level admixtures. In our low temperature case however, we can easily neglect the influence of the ^5E excited state, as was also done in [20, 28, 34, 36]. Then, the $^5T_2$ state can be shown to be equivalent to a ^5P state with the eigenstates of $\hat{L}_z$ and $\hat{S}_z$ ($|m_l, m_s\rangle$) as basis functions. The spin-orbit coupling splits the ^5E ground state further into 5 equally spaced doublets (split by $\sim 13\,\text{meV}$). The lowest doublet has the $|1, -2\rangle$ and $|-1, 2\rangle$ basis functions, while the basis functions of the first excited doublet are linear combinations of $|1, -1\rangle$ and $|-1, 1\rangle$. The presence of an exchange interaction[3] however, lifts this two-fold degeneracy (in a molecular field approximation), which results in a splitting of the order of 6 meV [36].
In summary, the first 4 lowest-lying states of the Fe^{2+} ion in $FeCO_3$ can be roughly approximated by the following $|m_l, m_s\rangle$ states (in order of increasing energy): $|-1, 2\rangle$, $|1, -2\rangle$, $|-1, 1\rangle$ and $|1, -1\rangle$.

1.1.2 Electric field gradient

The efg appears as a second order correction term in the description of the electrostatic field generated by the electron cloud at the position of the nucleus. It gives rise to the quadrupole hyperfine interaction, which is treated in section 1.1.4. The efg can be expressed as (the expectation value of) a traceless tensor operator of rank 2 [37][4]:

$$\hat{V}_{ij}(\mathbf{r}) = -\frac{eN}{4\pi\epsilon_0}\frac{x_i x_j - r^3\delta_{ij}}{r^5} \tag{1.2}$$

with eN the electronic charge of the unit cell and $x_{i/j}$ the Cartesian coordinates of the valence electron. In general, one chooses a principal axis system (or PAS)

[3] Within the same hexagonal (0001) layer the iron spins interact ferromagnetically, interlayer interactions are antiferromagnetic [24].

[4] In [37] the efg is defined in cgs-units and already evaluated in electron space.

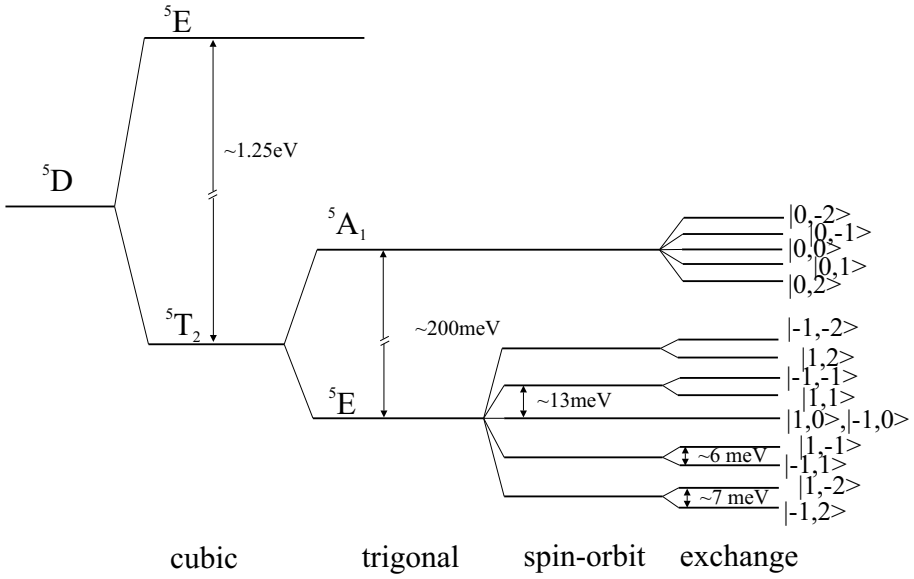

Figure 1.3: Electronic levels of Fe^{2+} for successive inclusion of cubic, trigonal, spin-orbit and exchange interactions, taking into account the approximations discussed in the body text.

such that the efg expressions are reduced to only 2 parameters, *i.e.* V_{zz} and η (together with the 3 Euler angles of the PAS this makes the 5 free parameters associated with a rank 2 traceless operator). η is the asymmetry parameter, which is a measure of the deviation of axial symmetry:

$$\eta = \frac{V_{xx} - V_{yy}}{V_{zz}}. \tag{1.3}$$

The PAS is defined such that $|V_{zz}| \geq |V_{xx}| \geq |V_{yy}|$ and thus $0 \leq \eta \leq 1$. In order to find the efg, this tensor operator should be evaluated in electron space $V_{ij} = \langle\psi_e|\hat{V}_{ij}|\psi_e\rangle$. Using the low-lying electron levels obtained in the previous section, we find[5] that $V_{zz} = (eN/4\pi\epsilon_0)(2/5)\langle r^{-3}\rangle$ and $V_{xx} = V_{yy} =$

[5] Assuming that the electron wave functions be separable into a product of a radial function and a spherical harmonic: $\psi_e(\mathbf{r}) = (U(r)/r)Y^L_{m_L}(\theta,\phi)$, then $\langle r^{-3}\rangle = \int_0^\infty U(r)r^{-3}dr$ [38]. Values for $\langle r^{-3}\rangle$ can be calculated by Hartree-Fock or Density Functional Theory methods, or can be found by comparison with experimental data. Expressions for $Y^L_{m_L}$ are found in [39].

$(-eN/4\pi\epsilon_0)(1/5)\langle r^{-3}\rangle$, which means that $\eta = 0$. This could already be expected from symmetry considerations as the trigonal axis in $FeCO_3$ implies an axially symmetric efg along this axis. An estimate of the value of V_{zz} is calculated by combining the experimental value of the quadrupole splitting $\Delta \approx 1.80\,\mathrm{mm/s}$ (see section 1.3 for a definition of Δ and the experimental results) with the nuclear quadrupole moment of $Q = 0.16\,\mathrm{b}$ obtained in [40]. We find that $V_{zz} = 10.82 \times 10^{21}\mathrm{V/m^2}$.
It can be further shown that all sublevels of the ${}^5E$ ground state produce the same efg.

This line of reasoning of course only applies for a perfect $FeCO_3$ crystal, without impurities. The 6.4% Mn content on substitutional lattice sites, however, can disturb the axial efg at the Fe site. Ab initio calculations [41] show that a Mn impurity can have a small, but non-negligible influence on the efg. In order to estimate this effect, one Fe is replaced with Mn in different *cubic* lattices, and then V_{zz} is calculated. Three different cases are considered. First, in an $AuCu_3$ fcc lattice, with Fe instead of Cu, the non-Fe ion leads to the presence of an axially symmetric efg at the Fe positions (labelled by 'XFe_3'). Second, if one stacks two Fe bcc lattices on top of each other and replace the middle layer of Fe with another ion, then this impurity induces two different axial efg's at two distinguishable Fe positions, *i.e.* Fe in the center of the cube ('X-Fe-c') and Fe located at the border faces ('X-Fe-b'). In Fig. 1.4 these values are plotted for different impurities (elements of the fourth period). It is seen that the change of V_{zz} upon addition of Mn is of the order of $1 \times 10^{21}\,\mathrm{V/m^2}$, which is about 10% of the V_{zz} value in $FeCO_3$.
A Mn content of 6.4% means that, in the mean, one out of sixteen Fe ions is replaced by a Mn ion. If the Gaussian spread on this distribution would be small[6], then there is a 75% chance of having one Mn in the twelve nearest and next-nearest neighbors of Fe in the $FeCO_3$ crystal lattice, as shown in Fig. 1.1. The chance of having two or more Mn is much smaller. If one of the six nearest neighbors of Fe is replaced by Mn, the axial symmetry is broken. The magnitude of the altered efg is the same for all six sites, but the orientation differs. The same arguments hold for the next-nearest neighbors.
These observations will play an important role when analyzing and discussing the experimental results.

[6]The probability distribution of the ratio of Mn over Fe is most likely Gaussian, but we ignore the line width of this distribution.

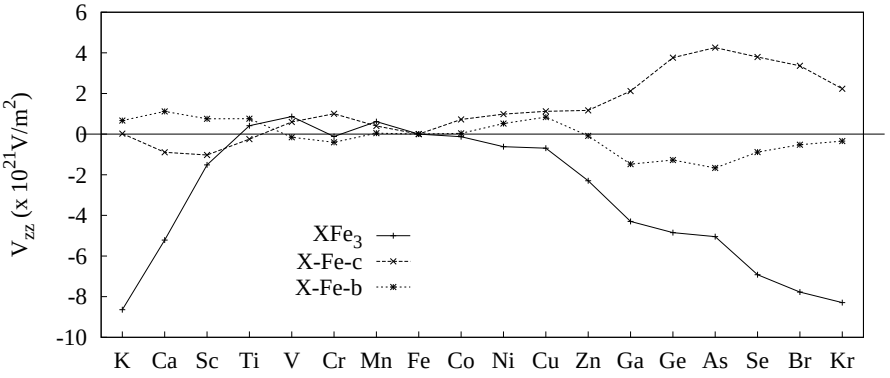

Figure 1.4: Ab initio calculated values of the V_{zz} component of the efg for the three different cases discussed in the body text.

1.1.3 Magnetic hyperfine field

The magnetic hyperfine field **B** has three main contributions, *i.e.* an orbital ($\mathbf{B}_{orb}$), a spin dipolar ($\mathbf{B}_{dip}$) and a Fermi contact contribution ($\mathbf{B}_F$). The expression of the magnetic hyperfine field operator (in cgs-units) is given by [42]:

$$\hat{\mathbf{B}} = \hat{\mathbf{B}}_{orb} + \hat{\mathbf{B}}_{dip} + \hat{\mathbf{B}}_F, \tag{1.4}$$

$$= -\frac{2\mu_B}{\hbar}\frac{\hat{\mathbf{L}}}{r^3} - \frac{2\mu_B}{\hbar}\left(\frac{3(\hat{\mathbf{S}}.\mathbf{r})\mathbf{r}}{r^5} - \frac{\hat{\mathbf{S}}}{r^3}\right) - 2\mu_B\frac{8}{3}\pi\,\hat{\mathbf{S}}\hat{\delta}(\mathbf{r}), \tag{1.5}$$

with $\hat{\mathbf{L}}$ and $\hat{\mathbf{S}}$ the orbital momentum and spin operator, μ_B the Bohr magneton and $\hat{\delta}(\mathbf{r})$ the Dirac delta function operator. Previous studies have shown that the Fe^{2+} magnetic moments point along the c-axis [23]. If we choose the c-axis as quantization axis, then the magnetic field description is limited to its z-component. Evaluated in the $|-1,2\rangle$ electron ground state we find $B = (\mu_B)(18/5)\langle r^{-3}\rangle + B_F$, with $B_F = -(32\pi\mu_B/3)|\psi_e(0)|^2$. The magnetic field generated by the $|1,-2\rangle$ first excited state, however, is equal in magnitude but opposite in sign[7].

It is known that $FeCO_3$ is paramagnetic at high temperatures, but shows an antiferromagnetic behavior below the Néel temperature of $T_N \approx 38\,\mathrm{K}$ (see Table 1.1 for experimental values of T_N). At low temperatures, spins of the neighbor-

[7]The Fermi contact field also changes sign as the $|m_s = -2\rangle$ valence state polarizes the spin of the s orbitals in the same but opposite way as does the $|m_s = 2\rangle$ state.

ing Fe ions order in an antiparallel way while the next-nearest neighbors order in a parallel way. This means that, perpendicular to the c-axis, ferromagnetic sheets are antiferromagnetically aligned with one another (see also Fig. 1.1). Furthermore, the magnetic hyperfine field displays a particular temperature dependence, which can be seen in Fig. 1.7. This is explained by fluctuations between the two low-lying electronic states, which respectively give $+B$ and $-B$ and the same efg [28]. In the antiferromagnetic state the energetically lowest state is more likely to be occupied than the higher state. If P_1 and P_2 are the occupation numbers of the low and high state respectively ($P_1 + P_2 = 1$), the net magnetic hyperfine field B_{net} at the nucleus is given by [28]

$$B_{net} = P_1 B + P_2(-B). \tag{1.6}$$

The relaxation rates W_{12} (W_{21}) from the low state to the high state (and vice versa) may be determined by the relationship $W_{12}/W_{21} = P_2/P_1$. Above T_N, there is no net magnetic field, so $P_1 = P_2$ and the relaxation rates are equal. For decreasing temperature, as $P_1 > P_2$, there is an increasing magnetic field. An intuitive explanation is that the relaxation rate W_{12} decreases and, therefore, the nucleus starts to 'feel' the magnetic field during a precession period (given by its Larmor frequency). The temperature dependence of these relaxations and the effect on the magnetic hyperfine field will be discussed later, while analyzing the experimental data.

1.1.4 Hyperfine interaction

At the smallest scale of the energy spectrum, the interaction of both the nuclear electric quadrupole moment Q with the efg and the nuclear magnetic dipole moment μ with the magnetic field generated by the electron cloud has to be considered. The combination of these two interactions is referred to as the *hyperfine interaction*, which is of the scale of μeV. A general expression of the hyperfine Hamiltonian is given by

$$\hat{H} = -\frac{\mu}{\hbar}\hat{\mathbf{I}}.\hat{\mathbf{B}}_{hf} - \sum_q \sqrt{\frac{4\pi}{5}} \frac{eQ}{I(2I-1)\hbar^2} \hat{I}^2 Y_q^2(\theta_I, \phi_I) \hat{V}_q^2 \tag{1.7}$$

with I ($\hat{\mathbf{I}}$) the nuclear spin (operator) and $\hat{V}_q^2(\theta_I, \phi_I)$ the efg tensor operator expressed in spherical tensor form with (θ_I, ϕ_I) the spherical coordinates of the nuclear spin.

In the case of a pure $FeCO_3$ crystal, the efg is axially symmetric along the trigonal c-axis. Because the magnetic moments point along the c-axis, they generate a collinear magnetic hyperfine field. It is argued, however, that, in a natural, impure $FeCO_3$ crystal, this simple picture can be disturbed, leading

to a (small) deviation of axial symmetry. Therefore, we are retaining the non-axial components in expression (1.7).
The Hamiltonian can be further simplified by choosing the PAS of the efg as our reference axis system. The principle axis system of the magnetic hyperfine field operator $\hat{\mathbf{B}}_{hf}$ can be specified in the efg PAS by the Euler angles (α, β, γ). In general, transformation of a spherical tensor T^n of rank n from an $A1$ to an $A2$ coordinate system is given by [43]

$$T^n_q(A2) = \sum_{q'=-n}^{n} D^n_{q'q}(\alpha, \beta, \gamma) T^n_{q'}(A1) \tag{1.8}$$

with the Wigner rotation matrix elements

$$D^n_{q'q}(\alpha, \beta, \gamma) = e^{-i\alpha q'} d^n_{q'q}(\beta) e^{-i\gamma q}, \tag{1.9}$$

and $d^n_{q'q}(\beta)$ the d functions[8]. Applying Eq. (1.8) to $\hat{\mathbf{B}}$, we find the three field components[9] $\hat{B}^1_0 = \cos\beta\,\hat{B}$ and $\hat{B}^1_{\pm 1} = e^{\pm i\alpha}\sin\beta\,\hat{B}/\sqrt{2}$ with $\hat{B}$ the magnetic field operator in its own PAS (having only a $\hat{B}_z$ component). The hyperfine Hamiltonian is now written as:

$$\begin{aligned} \hat{H} &= -\frac{\mu\hat{B}}{I\hbar}\left[\cos\beta\,\hat{I}_z + \frac{1}{2}\sin\beta\left(\hat{I}_+ e^{i\alpha} + \hat{I}_- e^{-i\alpha}\right)\right] \\ &\quad + \frac{eQ\hat{V}_{zz}}{4I(2I-1)\hbar^2}\left[\left(3\hat{I}_z^2 - \hat{I}^2\right) + \frac{\eta}{2}\left(\hat{I}_+^2 + \hat{I}_-^2\right)\right], \end{aligned} \tag{1.10}$$

with $\hat{I}_\pm$ the nuclear spin raising/lowering operators. The first part of each interaction term is axially symmetric, while β and η parameterize the deviation of axial symmetry[10]. An obvious choice of nuclear basis is the set of $|I, m_I\rangle$ states, which are eigenfunctions of the $\hat{I}^2$ and $\hat{I}_z$ operators. In the case of axial symmetry, these states are also eigenfunctions of $\hat{H}$.
If $\beta \neq 0$ and/or $\eta \neq 0$, the non-axially symmetrical part of the magnetic dipole term will mix $|m_I\rangle$, $|m'_I\rangle$ states with $|m_I - m'_I| = 1$, whereas the quadrupole term will mix states with $|m_I - m'_I| = 2$. Therefore, from hereon, we will speak of this non-axially symmetrical part of the hyperfine Hamiltonian as the *mixing interaction*. In the most general case, no analytical solution for the

[8] Expressions for the d-functions are found in many textbooks. Those most relevant in this work are listed in appendix B.

[9] The γ-dependence can be completely removed by applying a suitable unitary transformation.

[10] If $\eta = 0$, then $\alpha = 0$ because of axial symmetry.

eigenvalues and eigenvectors of this Hamiltonian is possible and we have to rely on numerical simulations[11].

Collinear magnetic field ($\beta = 0$)

Luckily, the most important case in our study can be solved analytically. This is the case of the ^{57}Fe Mössbauer nuclear scheme, involving the $I_g = 1/2$ and $I_e = 3/2$ nuclear states (and as long as $\beta = 0$).
The ground state hyperfine levels are the eigenvectors of the $I_g = 1/2$ hyperfine Hamiltonian. The $|m_I = -1/2\rangle$ and $|m_I = 1/2\rangle$ states are easily identified as such, having energies

$$E_{m_I} = \hbar\omega_{L,g} m_I + \hbar\omega_Q \left(3m_I^2 - I(I+1)\right) \tag{1.11}$$

where we have introduced the Larmor frequency $\omega_{L,g} = -\frac{\mu_g B}{I\hbar}$ of the ground state and the quadrupole frequency $\omega_Q = \frac{eQV_{zz}}{4I(2I-1)\hbar}$. The electronic operators $\hat{B}$ and $\hat{V}_{zz}$ are evaluated in electron space, of course, yielding $B = \langle\psi_e|\hat{B}|\psi_e\rangle$ and $V_{zz} = \langle\psi_e|\hat{V}_{zz}|\psi_e\rangle$. Note that only the magnetic field splits the $|m_I = \pm 1/2\rangle$ states (by $\hbar\omega_L$).
The solution to the first excited nuclear level is less straightforward. The matrix representation of the $I = 3/2$ Hamiltonian in the $|I = 3/2, m_I = 3/2, -1/2, -3/2, 1/2\rangle$ basis states (mind the order!) is

$$H = \hbar \begin{pmatrix} \frac{3}{2}\omega_{L,e} + 3\omega_Q & \sqrt{3}\eta\omega_Q & 0 & 0 \\ \sqrt{3}\eta\omega_Q & -\frac{1}{2}\omega_{L,e} - 3\omega_Q & 0 & 0 \\ 0 & 0 & -\frac{3}{2}\omega_{L,e} + 3\omega_Q & \sqrt{3}\eta\omega_Q \\ 0 & 0 & \sqrt{3}\eta\omega_Q & \frac{1}{2}\omega_{L,e} - 3\omega_Q \end{pmatrix}. \tag{1.12}$$

This particular block matrix form is chosen to highlight that only states belonging to the same class are mixed, *i.e.* states that are related by $|m_I - m'_I| = 2$. The calculation of the eigenvalues and eigenvectors of these 2×2 Hamiltonians

[11] More exactly: polynomial equations higher than fourth degree are incapable of algebraic solutions in terms of a finite number of rational operations and root extractions (Abel's impossibility theorem) [44].

yields:

$$\left|\pm\frac{\widetilde{3}}{2}\right\rangle = \frac{1}{\sqrt{3\eta^2+R_{\pm3/2}^2}}\left(\sqrt{3}\eta\left|\pm\frac{3}{2}\right\rangle + R_{\pm3/2}\left|\mp\frac{1}{2}\right\rangle\right) \quad (1.13)$$

$$\text{with} \quad E_{\pm\frac{\widetilde{3}}{2}} = \hbar\omega_Q\left(R_{\pm3/2}+w_{\mp1/2}\right) \quad (1.14)$$

$$\left|\pm\frac{\widetilde{1}}{2}\right\rangle = \frac{1}{\sqrt{3\eta^2+R_{\pm1/2}^2}}\left(\sqrt{3}\eta\left|\mp\frac{3}{2}\right\rangle + R_{\pm1/2}\left|\pm\frac{1}{2}\right\rangle\right) \quad (1.15)$$

$$\text{with} \quad E_{\pm\frac{\widetilde{1}}{2}} = \hbar\omega_Q\left(R_{\pm1/2}+w_{\pm1/2}\right) \quad (1.16)$$

where we have introduced the following parameters:

$$R_{\pm3/2} = \frac{w_{\mp1/2}-w_{\pm3/2}}{2} + \sqrt{\left(\frac{w_{\pm3/2}-w_{\mp1/2}}{2}\right)^2+3\eta^2} \quad (1.17)$$

$$R_{\pm1/2} = \frac{w_{\pm1/2}-w_{\mp3/2}}{2} - \sqrt{\left(\frac{w_{\mp3/2}-w_{\pm1/2}}{2}\right)^2+3\eta^2} \quad (1.18)$$

$$w_{\pm3/2} = \frac{\pm\frac{3}{2}\omega_{L,e}+3\omega_Q}{\omega_Q} \quad (1.19)$$

$$w_{\pm1/2} = \frac{\pm\frac{1}{2}\omega_{L,e}-3\omega_Q}{\omega_Q} \quad (1.20)$$

In the case of a small deviation of axial symmetry such that $\eta \ll \left(w_{\pm3/2}-w_{\mp1/2}\right)/(2\sqrt{3})$ we find that

$$E_{\pm\frac{\widetilde{3}}{2}} \approx \hbar\omega_Q\left(w_{\pm3/2}+\frac{3\eta^2}{w_{\pm3/2}-w_{\mp1/2}}\right)+\mathcal{O}(\eta^4). \quad (1.21)$$

Similar expressions can be obtained for $E_{\pm\frac{\widetilde{1}}{2}}$ and the corresponding eigenvectors. This means that the non-axial perturbation is limited to an η^2 influence on the original levels. For example, in the case of $\eta = 5\%$ and $w_{\pm3/2}-w_{\mp1/2} \geq 1/4$ the effect of the perturbation on the energy is smaller than $(1/w_{\pm3/2})\%$. These conditions will be valid in most cases.
However, a special case exists where this line of reasoning is not applicable. Let us consider the condition when $\omega_L = 3\omega_Q$. Then, $w_{-3/2} = w_{1/2}$ or the $|-3/2\rangle$ and $|1/2\rangle$ unperturbed levels are accidentally degenerate. They experience a so-called *level crossing*. It is straightforward to find that a small non-axial perturbation changes their energies in first order: $E_{-\frac{\widetilde{3}}{2}} = \hbar\omega_Q\left(w_{-3/2}+\sqrt{3}\eta\right)$ and $E_{+\frac{\widetilde{1}}{2}} = \hbar\omega_Q\left(w_{+1/2}-\sqrt{3}\eta\right)$. Moreover, the perturbation mixes the crossing

levels completely and independently of the value of η:

$$\left|-\widetilde{\frac{3}{2}}\right\rangle = \frac{1}{\sqrt{2}}\left(\left|-\frac{3}{2}\right\rangle + \left|\frac{1}{2}\right\rangle\right), \tag{1.22}$$

$$\left|\widetilde{\frac{1}{2}}\right\rangle = \frac{1}{\sqrt{2}}\left(\left|-\frac{3}{2}\right\rangle - \left|\frac{1}{2}\right\rangle\right). \tag{1.23}$$

The $|3/2\rangle$ and $|-1/2\rangle$ levels, however, have a large energy difference ($6\omega_Q$) and thus are not affected by the non-axial perturbation.

Remark In this section we have deduced the eigenvalues and eigenstates of the full hyperfine Hamiltonian, *including* a non-axial component of the efg. Working in the basis of these eigenstates implicitly takes into account the mixing interaction. In section 3.2 and chapter 4, however, the mixing interaction is treated on a same footing as the gamma-nucleus interaction, in the basis of eigenstates of the axial hyperfine Hamiltonian.

Noncollinear magnetic field ($\beta \neq 0$)

The deviation of the magnetic field vector from the c-axis can have its origin in crystal imperfections or in the specific geometry of an externally applied magnetic field.
It makes little sense to deal with this problem in a general way other than with numerical methods. We can, however, find a good analytical approximation in the following special case. If two levels are (nearly) degenerate and β is small, then the influence of the perpendicular part of the magnetic field can be approximated by applying perturbation theory [45] in this two-level system.
Let us consider the two cases that are most relevant to this thesis. If there is only an (axially symmetric) efg present, *e.g.* above T_N of an antiferromagnetic material, then all $\pm m$ levels are degenerate. According to the Hamiltonian in Eq. (1.10), the $|\pm 1/2\rangle$ levels of both the ground and excited state of ^{57}Fe are affected in first order, while the $|\pm 3/2\rangle$ levels only in third order. For small β the latter can be neglected. From a first order perturbation calculation, we learn that the $|\pm 1/2\rangle$ levels are fully mixed

$$\left|\widetilde{\frac{1}{2}}\right\rangle = \frac{1}{\sqrt{2}}\left(e^{i\alpha}\left|\frac{1}{2}\right\rangle + \left|-\frac{1}{2}\right\rangle\right), \tag{1.24}$$

$$\left|-\widetilde{\frac{1}{2}}\right\rangle = \frac{1}{\sqrt{2}}\left(e^{i\alpha}\left|\frac{1}{2}\right\rangle - \left|-\frac{1}{2}\right\rangle\right), \tag{1.25}$$

with an energy difference $E_{\tilde{\frac{1}{2}}} - E_{-\tilde{\frac{1}{2}}} = |2W_{\frac{1}{2},-\frac{1}{2}}|$ with

$$W_{\frac{1}{2},-\frac{1}{2}} = \frac{\hbar\omega_{L,g}}{2}\sin\beta \qquad \text{for the ground state and} \tag{1.26}$$

$$W_{\frac{1}{2},-\frac{1}{2}} = \frac{\hbar\omega_{L,e}}{2}\sin\beta \qquad \text{for the excited state.} \tag{1.27}$$

If there is a combination of an efg and a magnetic hyperfine field, *e.g.* below T_N, then it is possible that some states are accidentally degenerate. This is the case for the $|-3/2\rangle$ and $|1/2\rangle$ levels in the excited state of ^{57}Fe, when $\omega_L = 3\omega_Q$. Then, it can be shown by a second order perturbation calculation that the crossing levels are fully mixed (as expressed in Eq. (1.22) and Eq. (1.23), but the first states have now an additional factor $\exp 2i\alpha$) and $E_{-\tilde{\frac{3}{2}}} - E_{\tilde{\frac{1}{2}}} = |2W_{-\frac{3}{2},\frac{1}{2}}|$ with

$$W_{-\frac{3}{2},\frac{1}{2}} = \frac{\sqrt{3}\hbar\omega_L}{2}\sin^2\beta. \tag{1.28}$$

So, a small non-axial component of the magnetic field only has a $\sin^2\beta$ effect on the energy of the crossing levels.
In section 3.1.2 simulations show that in order to have an observable ($|-3/2\rangle$,$|1/2\rangle$) level splitting, *i.e.* of the order of the inverse life time of the excited states, a strong magnetic field ($\perp$ c-axis) should be applied. In that case, however, not only the crossing levels are mixed, but all levels show an appreciable degree of admixture.

1.2 Mössbauer spectroscopy

Mössbauer spectroscopy is a very successful technique applied by a worldwide and interdisciplinary group of researchers who are interested in harvesting environmental information at the nuclear level. At the heart of the technique lies the so-called Mössbauer effect, named after its discoverer Rudolf L. Mössbauer [46]. The Mössbauer effect is an elastic process of (gamma) photon emission and absorption without observable recoil of the nucleus/nuclei involved. The probability for a recoil-free emission and absorption is given by the Debye-Waller [47] or Lamb-Mössbauer factor [48]:

$$f = \exp\left[-\frac{E_R}{kT_D}\left(\frac{3}{2} + \frac{\pi^2T^2}{T_D^2}\right)\right] \qquad (T \ll T_D), \tag{1.29}$$

with k the Boltzmann constant. This expression quantifies the knowledge that the recoil-free fraction: (a) decreases with increasing gamma energy E_γ ($E_R = E_\gamma^2/(2mc^2)$), (b) increases with increasingly rigid interatomic bonds

(through the Debye temperature T_D) and (c) increases with decreasing temperature T. Although the standard mathematical framework describing the Mössbauer effect gives satisfactory results, it can be argued that its semi-empirical ways are not completely convincing[12] and that more fundamental research is needed, with emphasis on its relation to the zero-point oscillations [49, 50].
There has been some controversy in deducing the Lamb-Mössbauer factor in $FeCO_3$. Goldanski et al. [51] first reported a highly anisotropic f, which was explained as the Goldanski-Karyagin effect. This has later been refuted by the work of Housley et al. [26, 52], which correctly included the polarization dependence of the absorption lines. The most recent values of the Lamb-Mössbauer factor in $FeCO_3$ are $f_{\mathbf{k}\|c} = 0.72(2)$ and $f_{\mathbf{k}\perp c} = 0.75(2)$ (at 300 K) [29], which confirm the lack of spatial anisotropy.

Experimental setup

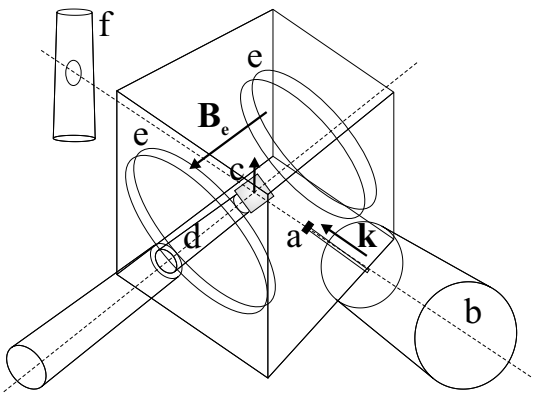

Figure 1.5: The Mössbauer experimental setup consists of: (a) radioactive source (small black disk on top of rod), (b) transducer, (c) crystal (shaded area), (d) cold finger, (e) external magnet (here represented by Helmholtz coils) and (f) detector. For more details, see body text.

In Fig. 1.5 the experimental setup is sketched. A conventional Mössbauer setup always includes a radioactive source (a) (here: ^{57}Co in Rh matrix) that is mounted on a transducer (b). The linear vibrations, which vary in this case between -7 mm/s and $+7$ mm/s, Doppler shift the energy of the emitted gamma radiation. This allows for a resonant scan of the hyperfine energy structure of

[12] For example, the Mössbauer effect occurs without thermal Doppler broadening, whereas the non-elastic scattering exhibits the expected thermal broadening.

the sample under investigation (c).
As shown in Fig. 1.5, our setup additionally features a cold finger (d) and external magnet (e). The sample is mounted on top of the cold finger, which is temperature controlled by a helium flow cryostat. The temperature was stabilized to 0.1 K and calibrated at the boiling point of liquid nitrogen. In principle, the cold finger allows operating temperatures down to 4.2 K. Both transducer and cold finger are firmly attached to the cryostat that houses a 4.4 T superconducting magnet. Finally, a Kr gas proportional counter (f) detects the transmitted radiation.
The signal processing setup has a standard configuration. The amplified signal from the proportional counter is retained if it passes through a single channel analyzer, set at 14.4 keV. The output signal of the single channel analyzer is then stored in a 'Mössbauer data system' where it is combined with the signal of the clock, which drives the transducer. In this way the number of gamma counts (or gamma intensity I) is recorded as a function of the transducer velocity v.

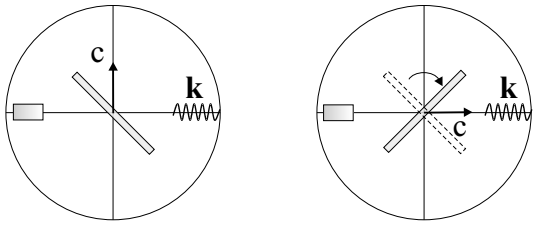

a) perpendicular geometry b) parallel geometry

Figure 1.6: Two geometries are studied: the incident radiation **k** is perpendicular (a) and **k** is parallel to the c-axis (b) (the shaded box on the left represents the detector).

As we are dealing with a *single* crystal with a preferential direction (c-axis), we can define the direction of the incident source radiation **k** and the direction of the external magnetic field $\mathbf{B}_e$ with respect to this c-axis. As shown in Fig. 1.5, the external magnetic field is always perpendicular to the plane spanned by (**k**,c-axis). The angle (θ) between the incident radiation and the c-axis can be varied by a rotation around the cold finger axis, as shown in Fig. 1.6. Two geometries are studied, *i.e.* the 'parallel geometry' ($\theta = 0$) and the 'perpendicular geometry' ($\theta = \pi/2$). Note that because the angle of the c-axis to the crystal surface (cleavage plane) is $\approx 45°$ (see section 1.1), the effective thickness of the crystal is the same in both geometries.
In all but the last experiment, no external magnetic field is applied.

1.3 Mössbauer spectra

Two $FeCO_3$ crystals have been studied: one has a physical thickness of $d = 168\,\mu$m, the other has $d = 64\,\mu$m. A dimensionless effective optical thickness can be defined as

$$T_e = \sigma_0 f \chi \rho \frac{d}{\sin(\beta + \theta)}, \tag{1.30}$$

with σ_0 the maximal resonant absorption cross-section, f the recoil-free fraction, χ the isotopic enrichment or natural isotopic abundance of ^{57}Fe and ρ the concentration of Fe in the crystal. Because the radiation is incident at an angle $\pi - (\beta + \theta)$ (with β given by Eq. (1.1)) with respect to the crystal surface, the distance travelled through the crystal is larger than for normal incidence. According to its definition, T_e is the number of resonant scattering events that take place during the propagation of the gamma radiation through the crystal. The value of T_e for the $d = 168\,\mu$m $FeCO_3$ crystal, taking into account the geometry of the setup, the measured impurity percentages and the general parameters of ^{57}Fe as summarized in Appendix A, is calculated to $T_e = 7.9 \approx 8$, while the thinner crystal has a value of $T_e = 3$. In the remainder of this thesis we distinguish both crystals by their effective thickness value.

1.3.1 A first analysis

The presentation of the measured Mössbauer (velocity) spectra in the next section already includes a first, crude analysis. The data are fitted with the Recoil program [53], using the 'Lorentzian absorption profile' procedure. This fitting procedure simply tries to find a best fit $f(v)$ by fitting each absorption line i with a Lorentzian profile $L_i(v)$:

$$f(v) = BG - \sum_i L_i(v) \tag{1.31}$$

with

$$L_i(v) = \frac{A_i}{\pi} \frac{\Gamma_i}{(v - v_i)^2 + \Gamma_i^2} \tag{1.32}$$

where BG is the spectral background, A_i is the area, v_i the resonance velocity and Γ_i the half width of the absorption line.
The number of free parameters can be considerably reduced by taking into account two physics 'rules'. First, according to parity invariance, the (m_g, m_e) and $(-m_g, -m_e)$ transitions are equal in all of their properties. Here, this means that they have the same A and Γ. Second, the positions of the absorption lines v_i are not random, but are related through the underlying hyperfine interaction physics (see section 1.1.4).

Above 38 K, $FeCO_3$ is paramagnetic, so the nuclei only experience an efg. If we assume, for now, that the efg is axially symmetric ($\eta = 0$), then, according to Eq. (1.10), the $I_e = 3/2$ excited state of ^{57}Fe is split in two two-fold degenerate levels $|m_e = \pm 3/2\rangle$ and $|m_e = \pm 1/2\rangle$, while the $I_g = 1/2$ ground state is unaffected. In order to have a resonant absorption, the v-modulated energy of the source photon $E(v) = E_\gamma(1 + v/c)$ should match the energy difference of an excited level $|m_e\rangle$ and ground level $|m_g\rangle$ of the absorber. Then, the resonance velocity is given by:

$$v_{m_e,m_g} = IS + \frac{c}{E_\gamma}\left[\hbar\omega_Q\left(3m_e^2 - 15/4\right)\right], \tag{1.33}$$

with IS the isomer shift[13] (already expressed in units of velocity). The efg splitting Δ of the excited state in terms of the transducer velocity is defined by

$$\Delta = \frac{c}{E_\gamma} 6\hbar\omega_Q. \tag{1.34}$$

Below 38 K, $FeCO_3$ becomes antiferromagnetic (see section 1.1.3) and all $|m\rangle$ are affected. For now, we assume that the magnetic hyperfine field is collinear with the efg (as should be the case in *pure* $FeCO_3$). If we define the parameters

$$\beta_g = \frac{c}{E_\gamma}\hbar\omega_{L,g} \qquad \text{and} \qquad \beta_e = -\frac{c}{E_\gamma}\hbar\omega_{L,e}, \tag{1.35}$$

then the resonance velocity of a (m_e, m_g) transition is given by

$$v_{m_e,m_g} = IS + \frac{\Delta}{6}\left(3m_e^2 - 15/4\right) + \beta_e m_e + \beta_g m_g. \tag{1.36}$$

According to their definition and using the values in Appendix A, it can be seen that β_e and β_g are related by $\beta_g = 1.7516\,\beta_e$. The choice of the parameters Δ, β_g and β_e becomes clear when we draw the expected hyperfine level scheme in Fig. 1.7 as a function of temperature (and hence, as a function of magnetic hyperfine field). The shaded rectangle shows the level crossing, which occurs at $\beta_e = \Delta/2$ or $T \approx 31$ K.

Because we are dealing with single crystals, the orientation of the radiation wave vector with respect to the crystal axes should be taken into account. If $(0, \theta, \phi)$ are the Euler angles that describe the orientation of $\mathbf{k}$ in the crystal axis system (*e.g.* the PAS of the efg), then the components in a multipole expansion of the electromagnetic field transform according to Eq. (1.8). The electromagnetic interaction of the ^{57}Fe nucleus with gamma radiation has mainly

[13] The isomer shift arises from the difference in the electronic environment of the source and absorber nuclei, which can alter the nuclear energies.

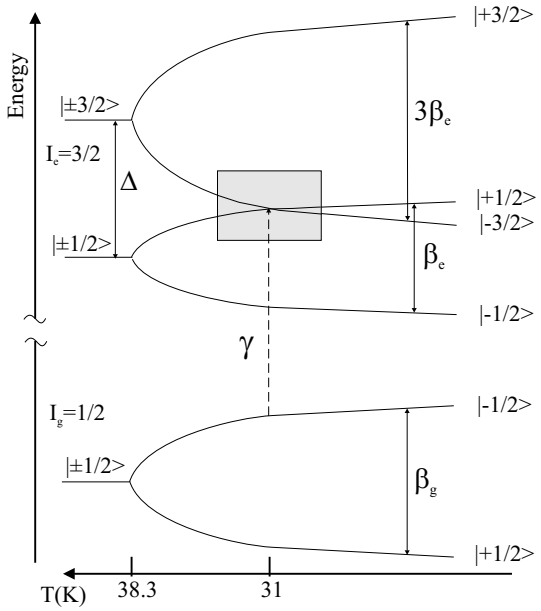

Figure 1.7: The hyperfine levels of ^{57}Fe as a function of temperature. The parameters Δ, β_g and β_e are defined in the body text. γ represents the gamma transition.

a magnetic dipole (M1) character. Therefore, the interaction Hamiltonian $\mathcal{H}^\sigma$, for a particular polarization σ, can be written as

$$\mathcal{H}^\sigma_{M1} = \sum_{\Delta m=-1}^{1} D^1_{\Delta m,\sigma}(-\phi,-\theta,0)\mathcal{H}(\Delta m), \tag{1.37}$$

where $\mathcal{H}(\Delta m)$ designates the electromagnetic interaction that induces a Δm transition. A more general derivation is presented in section 3.1. Explicit expressions for interaction with $\sigma = \pm 1$ polarized radiation are given by

$$\begin{aligned}\mathcal{H}^+_{M1} &= \cos^2\frac{\theta}{2}e^{i\phi}\,\mathcal{H}^+(\Delta m=+1) + \frac{1}{\sqrt{2}}\sin\theta\,\mathcal{H}^+(\Delta m=0)\\ &\quad + \sin^2\frac{\theta}{2}e^{-i\phi}\,\mathcal{H}^+(\Delta m=-1) \qquad (1.38)\\ \mathcal{H}^-_{M1} &= \sin^2\frac{\theta}{2}e^{i\phi}\,\mathcal{H}^-(\Delta m=+1) - \frac{1}{\sqrt{2}}\sin\theta\,\mathcal{H}^-(\Delta m=0)\\ &\quad + \cos^2\frac{\theta}{2}e^{-i\phi}\,\mathcal{H}^-(\Delta m=-1) \qquad (1.39)\end{aligned}$$

This means that in the parallel geometry ($\theta = 0$) each polarization can induce only one transition according to $\Delta m = \sigma$, whereas if $\theta \neq 0$ each polarization induces three Δm transitions. So in general, there are six possible gamma transitions (m_e, m_g) between the $I_e = 3/2^-$ and $I_g = 1/2^-$ states. According to the parity invariance, these six lines can be grouped in three doublets. These doublets, their splittings Δv_i and center shifts CS_i are identified as (see also Fig. 1.12):

doublet 1: $(3/2, 1/2) - (-3/2, -1/2)$ with $\Delta v_1 = 3\beta_e + \beta_g,\ CS_1 = IS + \Delta/2$
doublet 2: $(1/2, 1/2) - (-1/2, -1/2)$ with $\Delta v_2 = \beta_e + \beta_g,\ CS_2 = IS - \Delta/2$
doublet 3: $(1/2, -1/2) - (-1/2, 1/2)$ with $\Delta v_3 = \beta_g - \beta_e,\ CS_3 = IS - \Delta/2$

Because β_e and β_g are related to each other, all Δv_i's are fixed as soon as one doublet is fitted[14]. One is led to assume that the center shifts CS_i of the doublets are also fixed if IS and Δ are obtained from a room temperature spectrum. However, it is known that (the measured) IS and Δ are both temperature dependent. The center of gravity of the absorption lines gains a shift in addition to the isomer shift, which is positive for decreasing crystal temperature. This is explained by a difference in the second order Doppler shift between source and absorber [54, 55]. A detailed theory of the temperature dependence of the efg, however, is not yet found, but most data can be described by a $T^{3/2}$ dependence [56], giving a larger efg for decreasing temperature. Because of this temperature dependence, the values of IS and Δ can only be fixed over a relatively small temperature interval. They are considered temperature independent over the range of our low temperature spectra, which was $\Delta T \approx 20\,\mathrm{K}$.
In summary, taking into account the above arguments, the fit function $f(v)$ now reads as the sum of three Lorentzian doublets:

$$f(v) = BG - \sum_{i=1}^{3} \frac{A_i}{2\pi} \left(\frac{\Gamma_i}{(v - (CS_i - \Delta v_i))^2 + \Gamma_i^2} + \frac{\Gamma_i}{(v - (CS_i + \Delta v_i))^2 + \Gamma_i^2} \right). \tag{1.40}$$

The application of 'basic' physics knowledge has reduced the number of fit parameters[15] from 19 to 10: the background BG, the area A_i and half width Γ_i of each doublet, the isomer shift IS, the quadrupole splitting Δ and the magnetic hyperfine splitting β_g (or β_e).

[14] There is of course another way of taking advantage of this knowledge: all doublets can be fitted simultaneously *with* the above constraints on their splittings. However, this way of fitting is not accounted for in the Recoil program.

[15] This is in the case of a nonparallel geometry. In the parallel geometry the number of fit parameters is reduced from 13 to 8.

1.3.2 T_e=8, no external magnetic field

In this section we present the measured Mössbauer spectra of the $T_e = 8$ crystal without the application of an external magnetic field. In the next section we treat the case with external field. Fig. 1.8 shows the Mössbauer spectra for both geometries at room temperature (RT). The results are summarized in Table 1.2. We have used the common notation where π designates the $(\pm 3/2, \pm 1/2)$ high energy transition and σ the $(\pm 1/2, \pm 1/2)$ low energy transition. All values are given in units of mm/s, but can easily be transformed to eV units by multiplication with E_γ/c.
It should be noticed that the errors (1 standard deviation) presented in Table 1.2, and estimated by the Recoil program, are too small. This is obvious from the fact that the IS and Δ for both geometries should coincide.

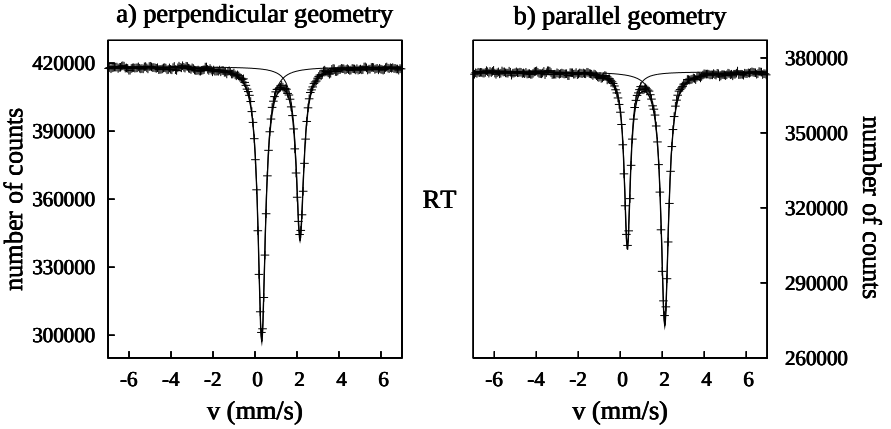

Figure 1.8: Mössbauer spectra of $FeCO_3$ (T_e=8) at RT and for both perpendicular and parallel geometry. The solid line gives the best Lorentzian fit.

The same RT Mössbauer experiment on $FeCO_3$ has been reported in [26, 29, 51]. These papers were mainly concerned with the asymmetry in the areas of the π and σ lines, their change with geometry and the (an)isotropy of f, see also section 1.2. A detailed calculation in [52] shows that the area ratio A_π/A_σ depends on the geometry (angle θ) and the effective thickness T_e of the single crystal. In Fig. 1.9 these theoretical curves for A_π/A_σ, in the case of a perfect single crystal, are drawn together with the experimentally deduced values. It is seen that there is a considerable mismatch between theory and experiment, except for the results of [29]. This implies that (1) the errors on the experimental values are not well estimated and/or (2) both the $FeCO_3$ sample in [26] and our sample are no perfect crystals. In [26] the authors designate the

Table 1.2: Best fit values of the $FeCO_3$ (T_e = 8) Mössbauer spectra at room temperature to the fit model described in section 1.3.1.

θ	IS (mm/s)	Δ (mm/s)	Γ_π (mm/s)	Γ_σ (mm/s)	A_π/A_σ
$\pi/2$	1.233(1)	1.825(2)	0.216(1)	0.213(1)	0.634(2)
0	1.228(1)	1.783(2)	0.220(1)	0.175(1)	1.783(6)

microscopic inhomogeneities (about 10% Mg cation content) as the culprit that causes distributions of isomer shifts and efg magnitudes, nonzero efg asymmetry parameters and a deviation of the principal axis of the efg from the optical axis. For the moment, we acknowledge the fact that we are dealing with an imperfect crystal, as was also clear from the chemical analysis, but we postpone an in-depth discussion to section 3.1.4.

Another interesting result of these RT spectra is that this experiment, as well as previous ones, shows the particular feature that the line widths Γ_π and Γ_σ in both geometries are more or less equal, except for $\Gamma_\sigma^{\|}$. This cannot be understood from straightforward physics principles, like relaxation broadening (which would affect the $\pi(\sigma)$ lines for both geometries analogously) or plain thickness broadening (which would primarily broaden the line with highest intensity). This issue is addressed again in section 3.1.4 when we apply a thickness and polarization dependent model to the data.

Figs. 1.10 and 1.11 show the Mössbauer spectra for temperatures below T_N. In Fig. 1.12 a close-up of the spectrum at $T = 31\,\mathrm{K}$ is shown, where the absorbtion lines are related to the transitions in the ^{57}Fe hyperfine structure. The values of the parameters deduced from the fits are graphically presented in Fig. 1.13. The center shifts are not displayed because they were held fixed for all (low temperature) spectra at $CS_1 = 2.34\,\mathrm{mm/s}$ and $CS_2 = CS_3 = 0.31\,\mathrm{mm/s}$. In the perpendicular geometry, we first fit the splitting of doublet 2 because its absorption lines are best resolved. Then, Δv_1 and Δv_3 are calculated according to the model outlined in section 1.3.1. Due to the absence of the second doublet in the parallel geometry, the splitting of the first doublet is taken as a reference. Both are shown in the upper left part of Fig. 1.13. In the same figure, the reduced χ^2 of each spectrum is given as a measure of the goodness-of-fit[16]. These χ^2-values give us an idea of how good the model can describe the experimental data. Clearly, for $T = 29/31\,\mathrm{K}$ the dis-

[16]In section 3.1.3 a more detailed overview of the χ^2 theory is presented.

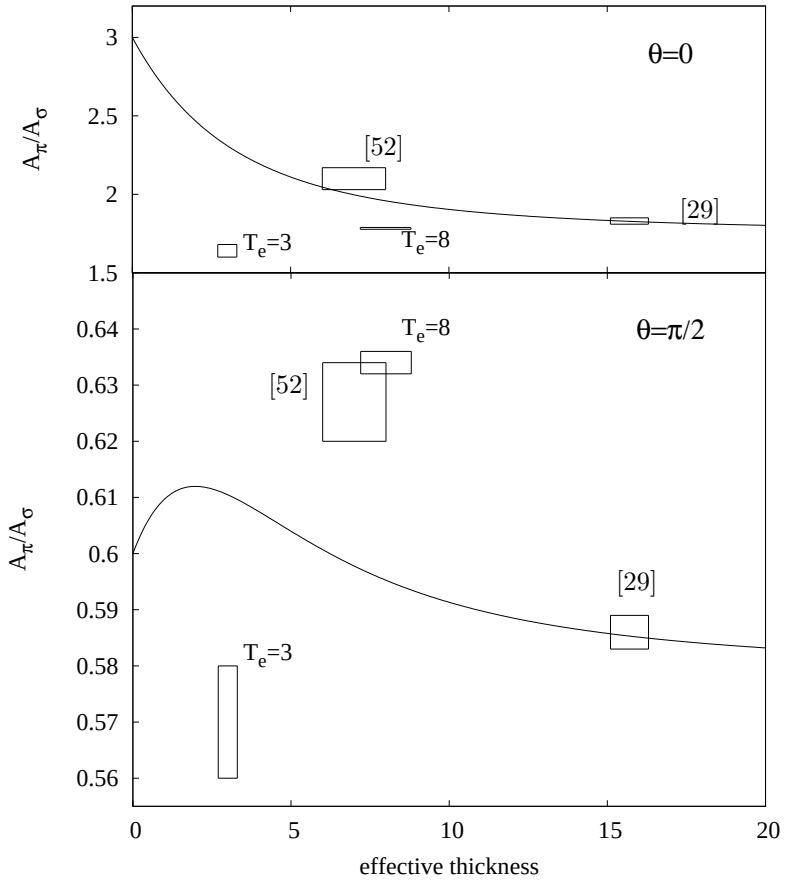

Figure 1.9: Comparison of theoretical area ratios versus effective thickness [52] with the experimentally deduced values, drawn with boxes as $1\,\sigma$ error limits, from several experiments. The upper graph shows the area ratio in the parallel geometry, whereas the lower graph corresponds to the perpendicular geometry.

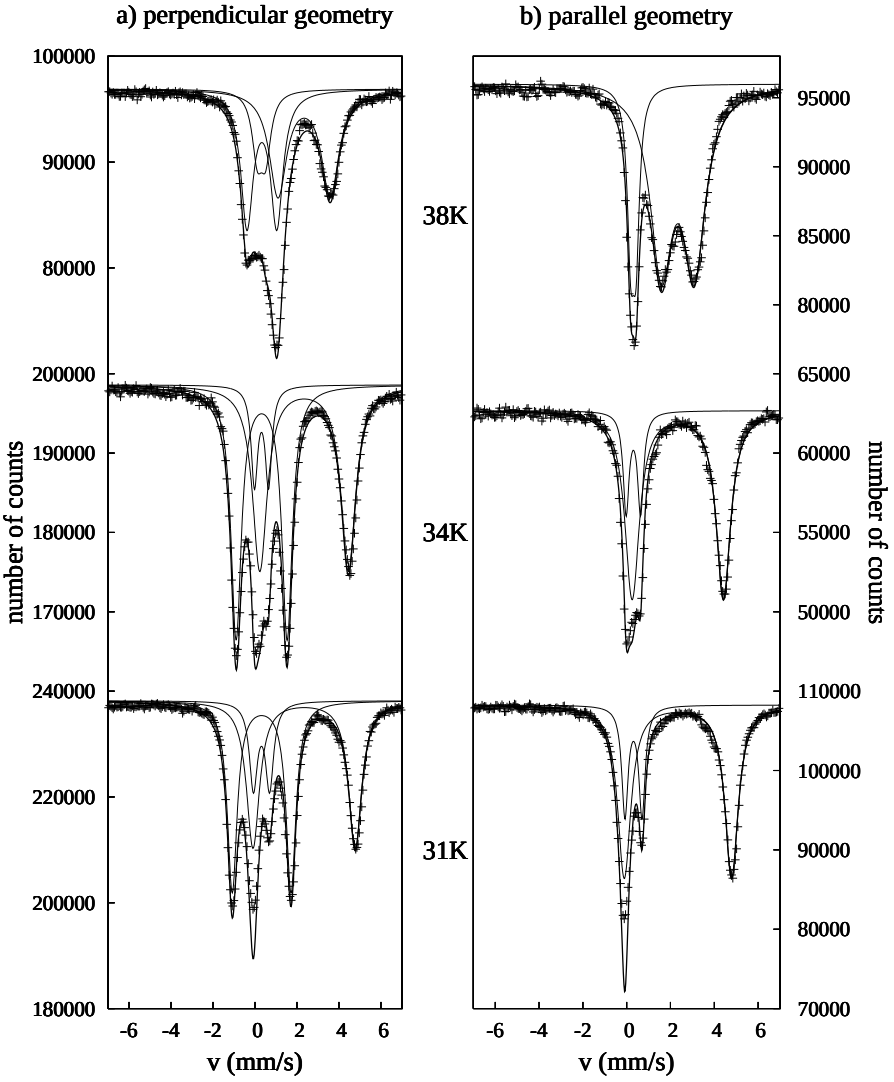

Figure 1.10: Mössbauer spectra of $FeCO_3$ (T_e=8) at different temperatures and for both perpendicular and parallel geometry. The solid line gives the best Lorentzian fit.

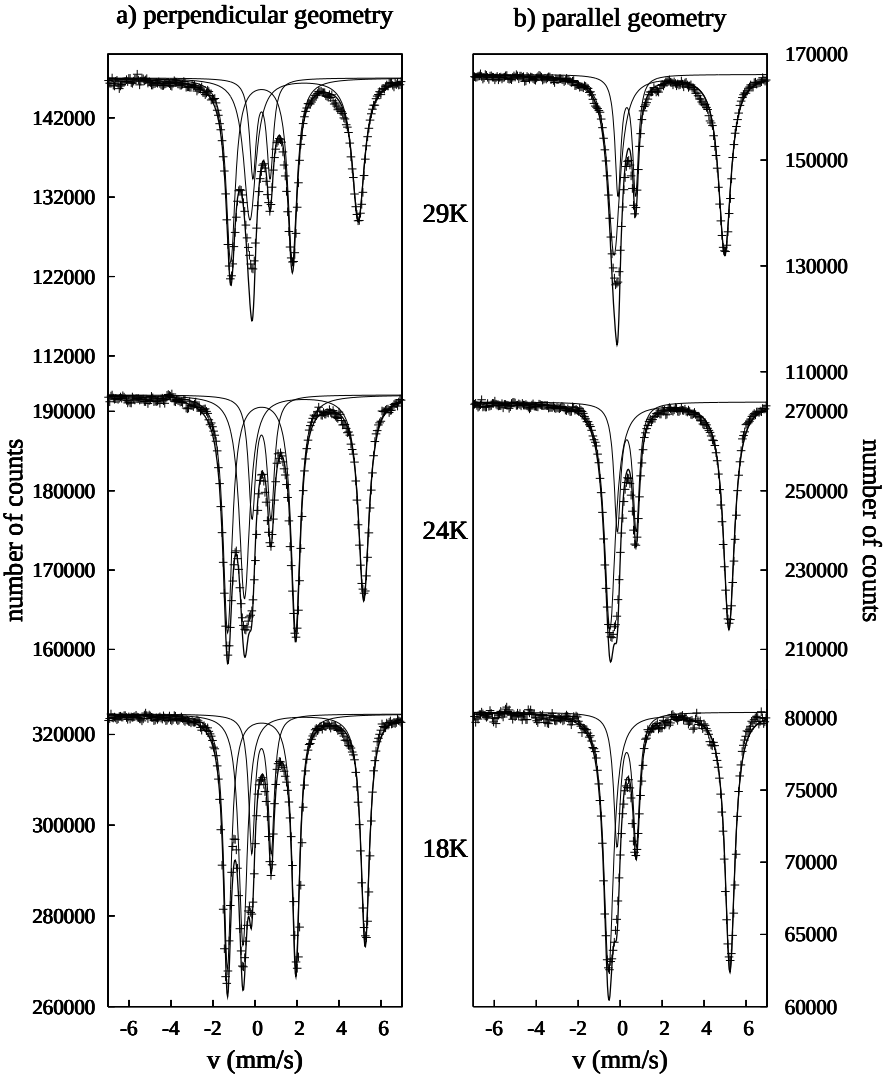

Figure 1.11: Mössbauer spectra of $FeCO_3$ (T_e=8) at different temperatures and for both perpendicular and parallel geometry. The solid line gives the best Lorentzian fit.

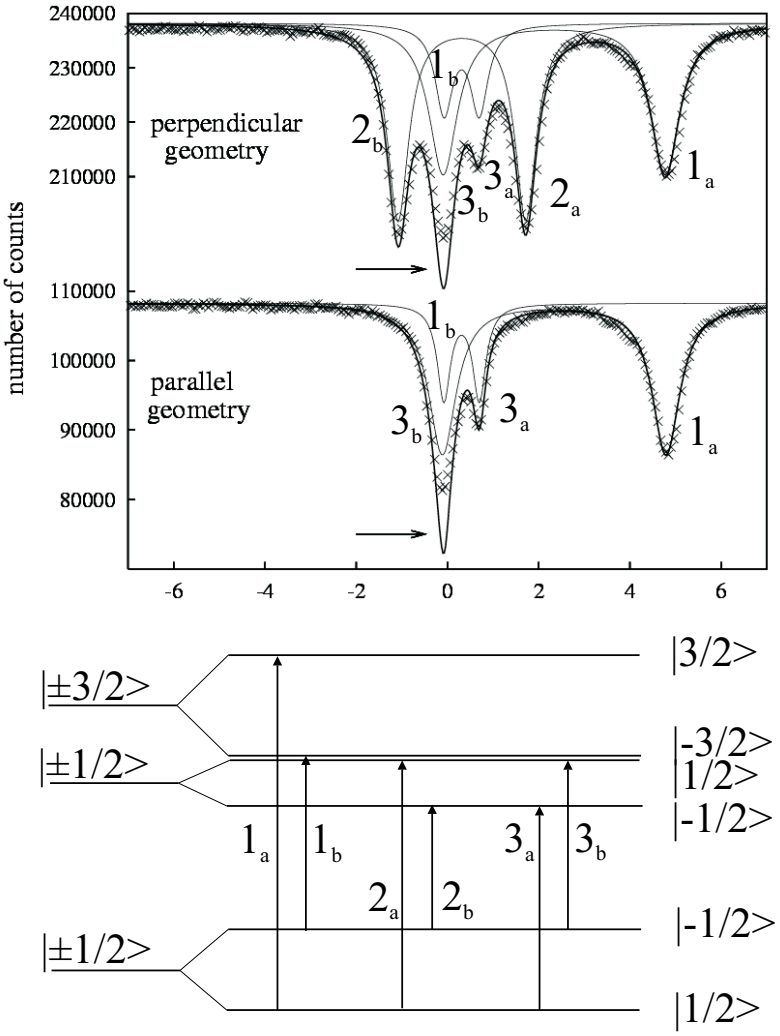

Figure 1.12: Close-up of the Mössbauer spectra of $FeCO_3$ (T_e=8) at $T = 31\,K$. Each absorption line is identified as a transition in the ^{57}Fe hyperfine structure. The transitions are grouped in three doublets (see body text).

crepancy between experiment and theory is the largest. At the level crossing ($v \approx -0.16\,\mathrm{mm/s}$) the difference between the predicted Lorentzian fit and the experimental data amounts to 25 % of the absorption line. There is less absorption observed than predicted by the fit. Therefore, we can say that the absorption line has become (partially) transparent. *This transparency is the core of this thesis and will be addressed in great detail in the following chapters.* A few other, interesting remarks can be deduced from the spectra and their first analysis:

- In Fig. 1.13 both splittings of the reference doublets Δv_2 and Δv_1, in the case of perpendicular and parallel geometry respectively, display a similar temperature dependence, which is in agreement with the temperature dependence reported in [28]. For decreasing temperatures, the magnetic hyperfine field reaches a saturation value. At 18 K, we deduce that $B^{\perp}_{18K} = 17.98(2)\,\mathrm{T}$ and $B^{\parallel}_{18K} = 17.96(2)\,\mathrm{T}$, which fall within a 2σ interval of the $B_{\approx 18K} = 18.3(3)\,\mathrm{T}$ value reported in [28].

- In Fig. 1.13 the widths of the three doublets vary widely, although they involve transitions to the same nuclear excited state, embedded in a particular chemical environment. In the parallel case, it is seen that even the temperature behavior of the doublets is quite different. An explanation of this phenomenon is given in terms of fluctuating hyperfine fields [57, 58]. As the Larmor frequency of the doublets differs, they respond in a different way to a fluctuating magnetic field (see also section 1.1.3). Doublet 1 has the highest Larmor frequency and hence is most strongly influenced by a change in the magnetic field. It 'feels' a more blurred magnetic field, which causes a larger line width than for the other doublets.

- The areas of the doublets remain more or less constant in this low-temperature interval. Because the area of a Mössbauer absorption line depends on the effective thickness T_e, the angle of incidence θ and the magnetic quantum numbers of the levels involved (see *e.g.* [26]), it is expected that this value is temperature independent.

1.3.3 T_e=8, with external magnetic field

First, a series of Mössbauer spectra with externally applied magnetic field and in the parallel geometry is recorded at RT, which is presented in Fig. 1.14. The magnetic field is applied perpendicularly to the crystal optical axis (= the $z-$axis of the efg), and thus will mix and split the m-states according to Eq. (1.24) and Eq. (1.26). The field fully mixes the $|1/2\rangle$ and $|-1/2\rangle$ degenerate levels of the ground and excited state, while the $|3/2\rangle$ and $|-3/2\rangle$ levels remain

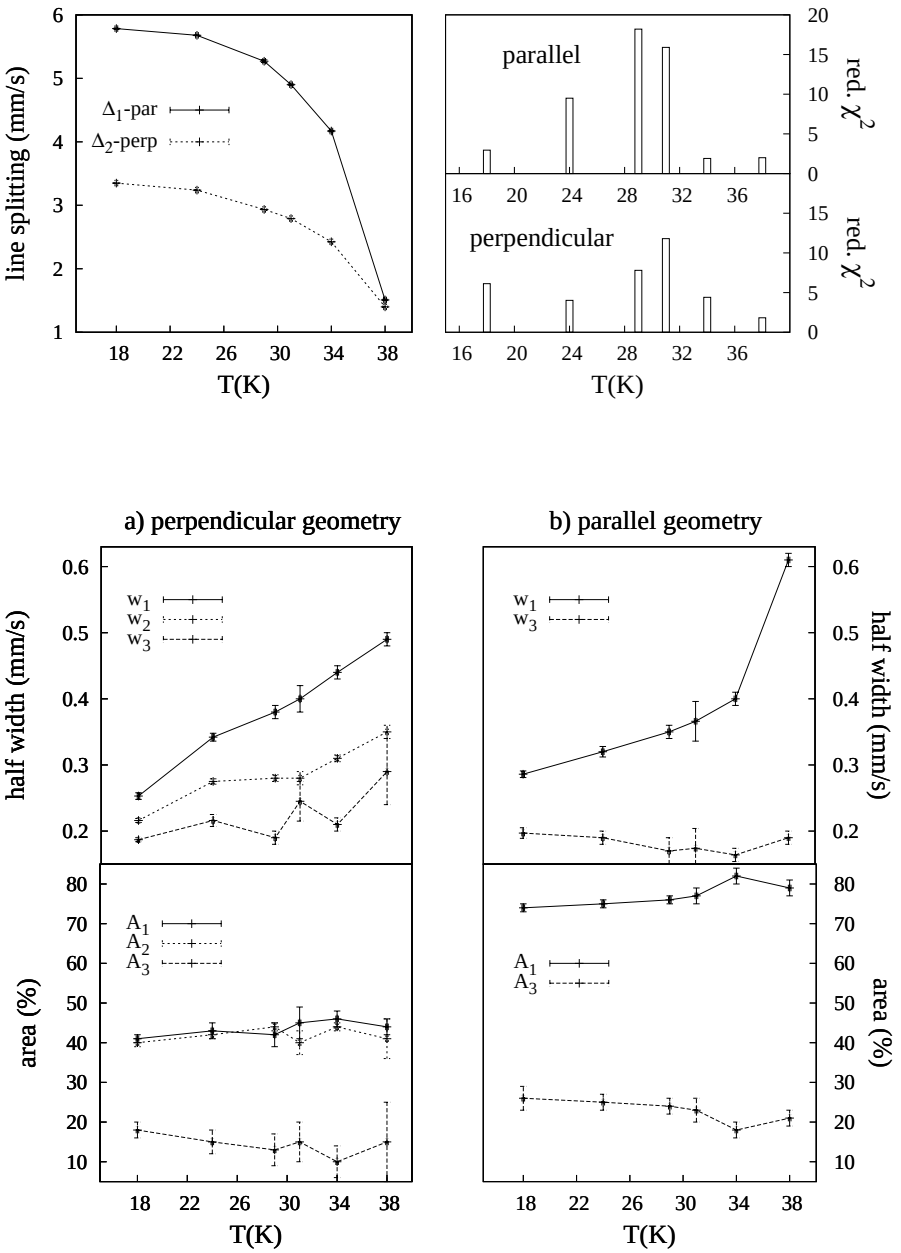

Figure 1.13: Graphical presentation of the fit results of the Mössbauer spectra of Fig. 1.10 and Fig. 1.11. The top left figure shows the temperature dependence of the splitting of the two reference doublets. The top right figure gives the values of the reduced χ^2 of each fit. The deduced line widths and areas of the Lorentzian doublets for both geometries are displayed in the bottom figures.

quasi unaffected. Therefore, we fit the π absorption line with 1 Lorentzian doublet, with a center shift equal to the case without magnetic field and with a splitting $\Delta v_1 = \Delta v_g$ where Δv_g is defined as the energy difference of the mixed ground levels. The σ absorption line is fitted with 2 Lorentzian doublets. We choose the doublets so that both have the center shift of the unperturbed σ line and splittings of $\Delta v_2 = \Delta v_g + \Delta v_e$ and $\Delta v_3 = \Delta v_g - \Delta v_e$ where Δv_e is defined as the energy difference of the mixed excited levels.
As the π line only consists of one doublet, it is expected to give the most accurate fit values. The values of the doublet splitting Δv_1 are: $\Delta v_1(1\,\mathrm{T}) = 0.13(3)\,\mathrm{mm/s}$, $\Delta v_1(2\,\mathrm{T}) = 0.21(2)\,\mathrm{mm/s}$ and $\Delta v_1(3\,\mathrm{T}) = 0.31(1)\,\mathrm{mm/s}$. From the Hamiltonian given in Eq. (1.10) we can relate the splitting of the mixed states to the magnetic field component perpendicular to the nuclear quantization axis: $B_e = \Delta v_1/0.1088$, which yields $B_e = 1.19(27)\,\mathrm{T}$, $B_e = 1.93(18)\,\mathrm{T}$ and $B_e = 2.85(9)\,\mathrm{T}$ respectively. These values are in good agreement with the values of the applied magnetic field.

In Fig. 1.15 we compare the Mössbauer spectra at $T = 31\,\mathrm{K}$ without external magnetic field and with a perpendicular external magnetic field of $B_e = 4\,\mathrm{T}$. Although the number of counts is rather low, and thus the statistical error high, we clearly see the appearance of two extra absorption lines at $v \approx -1\,\mathrm{mm/s}$ and $v \approx 2\,\mathrm{mm/s}$. From the simulation in section 3.1.2 we know that there should also be a third one at $v \approx 3\,\mathrm{mm/s}$.
The aim of this experiment is to see whether or not the absorption at the level crossing is increased or decreased upon application of the magnetic field. However, no appreciable change is observed. Only a small increase in line width is worth mentioning.

1.3.4 T_e=3

The $FeCO_3$ single crystal with T_e=3 originates from a different mother crystal than the T_e=8 crystal. Some dark spots with diameter less than 0.5 mm are visible on the crystal surface. Presumably these are oxides. Their influence on the Mössbauer spectra in Fig. 1.16 is minimal. Only at $v = -4\,\mathrm{mm/s}$ and $v = 5\,\mathrm{mm/s}$ there is a small signal of possible different lattice sites.
The results of the fits are presented in table 1.3. The area ratios of the absorption lines are also shown in Fig. 1.9. They deviate even more from the theoretical curves than the $T_e = 8$ case. The line widths of the π and σ absorption lines are similar, in contrast with the $T_e = 8$ spectra, but the lines in the perpendicular geometry have larger line widths. There has been a two year time elapse between the recording of the spectra in both geometries. A small change in the experimental setting has probably lead to additional, random vibrations and an increased line broadening.

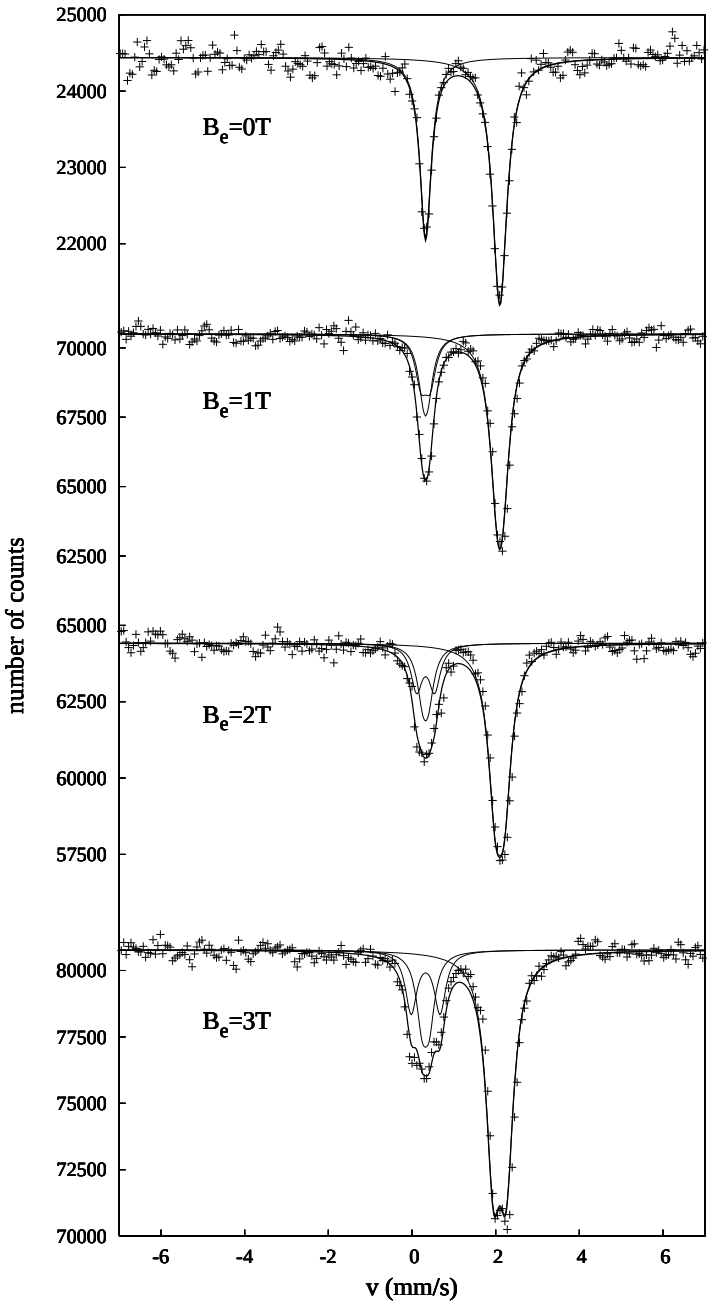

Figure 1.14: Mössbauer spectra of $FeCO_3$ (T_e=8) at RT for different values of an externally applied magnetic field B_e. The solid line gives the best Lorentzian fit.

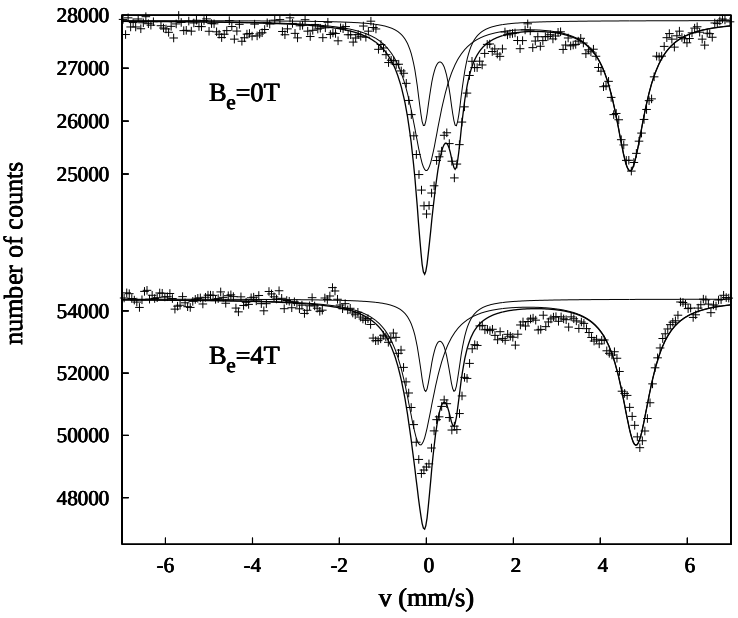

Figure 1.15: Mössbauer spectra of $FeCO_3$ at $T = 31\,\mathrm{K}$ with an externally applied magnetic field B_e. The solid line gives the best Lorentzian fit.

As in the $T_e = 8$ case, Mössbauer spectra were recorded for different temperatures below T_N. These spectra, however, do not add insight to the main study of this thesis and are, therefore, not shown. Only the spectrum at $T = 31\,\mathrm{K}$ is retained and shown in the lower half of Fig. 1.16. The misfit at the level crossing is still present but is less pronounced than for the $T_e = 8$ spectrum at $T = 31\,\mathrm{K}$. We estimate a 10 % deficit of absorption at the level crossing, with respect to the predicted Lorentzian absorption line shape. This smaller deficit can be due to different conditions inside both crystals or, if both crystals are to a high degree equivalent, to a transparency effect that is thickness dependent.

1.4 Saturation

Before embarking on our in-depth study of the measured reduction of absorption, it is necessary to refute the hypothesis of saturation as a sufficient explanation. We must, however, make a distinction between the two geometries. As

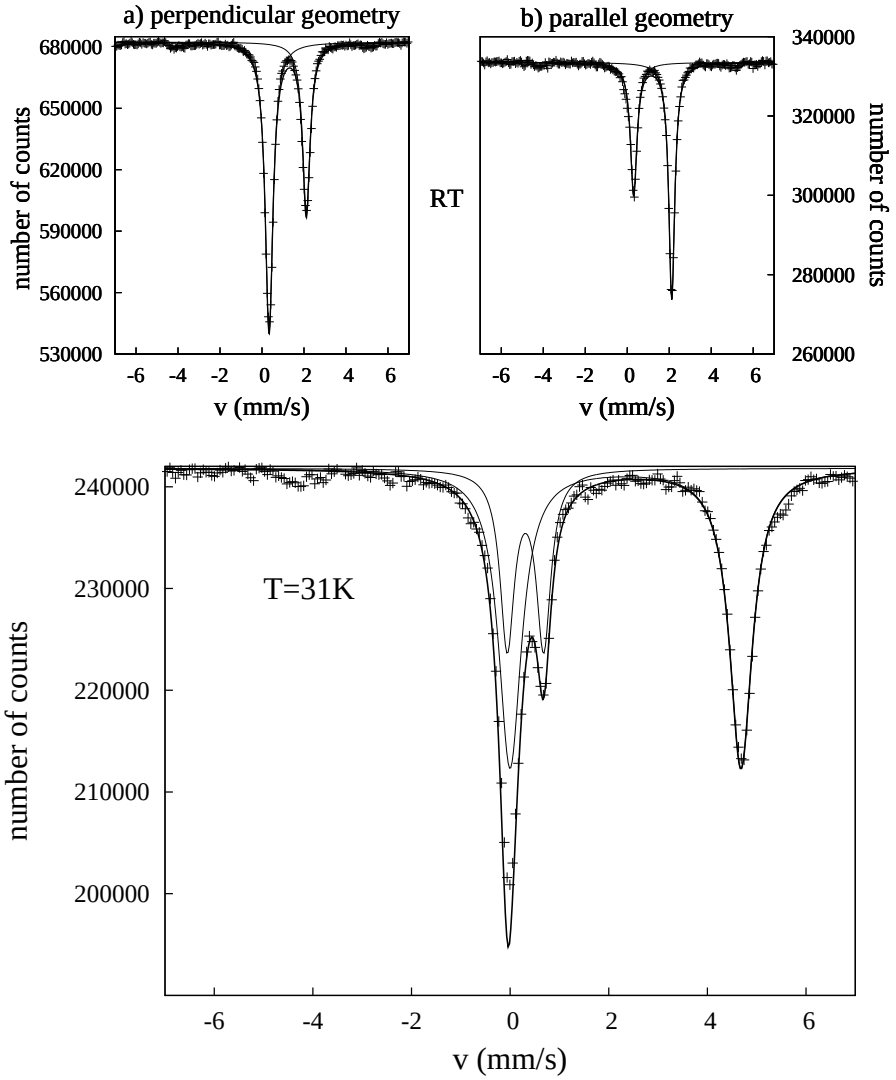

Figure 1.16: Mössbauer spectra of a $FeCO_3$ single crystal ($T_e = 3$), at RT in perpendicular and parallel geometry (top figure) and at $T = 31$ K in parallel geometry (bottom figure). The solid line gives the best Lorentzian fit.

Table 1.3: Best fit values of the $FeCO_3$ (T_e=3) Mössbauer spectra at room temperature to the fit model described in section 1.3.1.

θ	IS (mm/s)	Δ (mm/s)	Γ_π (mm/s)	Γ_σ (mm/s)	A_π/A_σ
$\pi/2$	1.225(1)	1.773(3)	0.215(3)	0.222(2)	0.57(1)
0	1.212(2)	1.813(4)	0.173(3)	0.189(3)	1.64(4)

shown in section 1.3.1, in the perpendicular geometry, each polarization state of the incident radiation can induce all three Δm transitions. Hence, at the level crossing, the interaction strength of each polarization state has doubled with respect to a noncrossing situation. This can be seen as radiative interaction with an absorber that has doubled its thickness. However, due to saturation, a doubling of the thickness does not automatically yield a doubling of the absorption. There is always less absorption, but how much less depends on the initial thickness of the absorber. In section 3.1.2 we show that for $T_e = 8$ the effect of saturation is already important. Moreover, the reduced absorption in the perpendicular geometry can even be quantitatively explained in a model that includes thickness effects.
Things are quite different in the parallel geometry. Now a polarization state that can induce one of the transitions involved in the level crossing, cannot induce the other one, even if the levels cross. It is clear that in this case no doubling of the interaction strength occurs. Therefore, the hypothesis of saturation as sole responsible for the reduced absorption is not tenable.

1.5 Conclusions

We have performed Mössbauer spectroscopy on two $FeCO_3$ single crystals in different experimental settings. The data are analyzed by applying the knowledge on the hyperfine structure of the ^{57}Fe nucleus in $FeCO_3$, which has been gathered in the first part of this chapter. The chemical analysis has revealed that we are not dealing with perfect crystals and hence, should take the influence of impurities into consideration.
The experimental data are presented along with a fit based on Lorentzian absorption profiles. The results obtained in this method of fitting are quite satisfying, except at the level crossing. For both geometries, a reduced absorption is observed, clearly at odds with our first way of analyzing, although the procedure followed is commonly applied.

From the results of that first analysis we have learned that the height of the absorption line of the crossing levels is less than the sum of the doublet partners off crossing. One is quickly led to assume this to be a saturation effect due to the crystal thickness. However, because the saturation mechanism does not give a satisfactory answer, the quest for understanding must continue. Very soon after the experimental results, it was acknowledged that the observed transparency bears close resemblance with the effect of electromagnetically induced transparency.

Chapter 2

Electromagnetically Induced Transparency

> The induced transparency may be viewed as resulting from a combination of the AC-Stark splitting *and* the interference between the two dressed states which are created by the coupling laser.
>
> in [59]

2.1 EIT in quantum optics

It is difficult to do justice to the wealth of papers that have dealt with the phenomenon of EIT since the nineties of the 20th century. We are fully aware that the following selection of cited papers merely gives a limited view on the subject. A more complete list of references can be found in the recent overview paper by Fleischhauer, Imamoglu and Marangos [60].

2.1.1 Transparency

An interesting finding along our path through EIT-related literature is that the phenomenon of EIT is known by multiple faces and names. The label of 'EIT'

has been given at the beginning of its blooming era in the early nineties [59]. An empirical definition of EIT, which is now widely accepted, goes as follows: *EIT is the effect of rendering an otherwise opaque medium, transparent for a resonant 'probe' electromagnetic field, through the coherence induced by a second, 'drive' field.*

The archetypical Λ-scheme[1] representation of the actors in this definition is given in the left part of Fig. 2.1. A probe field, labelled by its Rabi frequency[2] Ω_p, is in resonance with the $|1\rangle \rightarrow |2\rangle$ atomic transition. The drive field Ω_d couples $|2\rangle$ with $|3\rangle$. State $|3\rangle$ is sometimes called the 'coupling state'. In the text-book case, $|1\rangle$ is a ground state, $|2\rangle$ is an excited state (with decay rate γ_2) and $|3\rangle$ is a metastable state (such that $\gamma_3 << \gamma_2$).

Digging a little deeper in older papers reveals that the effect was already studied in the seventies as 'holes in spectral lines' [61] and 'nonabsorbing atomic coherences' [62, 63]. In a more subtle way, 'decay interference' [64] and 'dynamical suppression of spontaneous emission' [65] are also manifestations of the same physics. Moreover, these studies gave the impetus to the development of the 'lasing without inversion' theories [66–68]. These different names strongly suggest there is a unifying principle underlying EIT, which, however, can be approached from different directions. We briefly discuss the two most relevant points of view, which somehow can be related to the left and right part of Fig. 2.1 respectively.

Coherent population trapping

In his excellent review paper [69], Harris pinpoints the essence of EIT to the *coherent trapping of population* or the creation of a 'dark' state. It can be shown [70] that the Hamiltonian of a Λ system has an eigenstate $|d(t)\rangle$, the dark state, of the form

$$|d(t)\rangle = \cos\theta(t)|1\rangle - \sin\theta(t)|3\rangle, \tag{2.1}$$

with $\tan\theta(t) = \Omega_p(t)/\Omega_d(t)$ and Rabi frequencies that could be time-dependent, *e.g.* in the case of pulsed laser fields. Once an atom has evolved into this dark state $|d\rangle$, it can no longer be excited by the probe field to $|2\rangle$, hence, it is trapped. Because this trapping process takes time, it has been argued that the front edge of the probe pulse, together with the drive field, creates the coherence, which, subsequently, induces the transparency for the bulk of the pulse.

[1] A Λ-scheme is a particular form of a three-level system where the levels are connected by two fields according to the Greek capital Λ.

[2] The Rabi frequency is a measure of the transition strength and is proportional to the product of the transition matrix element and the EM field amplitude.

This point of view also provides an explanation why the relaxation rate γ_2 does not play a crucial role, while γ_3 does. The dark state itself does not depend on $|2\rangle$, and, therefore, not on the value of γ_2, but the time of *creation* of the dark state can be shortened[3] by a large γ_2 [71]. Decay of the coupling state $|3\rangle$, however, directly affects the dark state, which loses its stable character and leaks back into the bright state[4], leading to absorption of the probe field. In section 3.2.3, we will show that the ratio γ_3/γ_2 is a key factor in determining the induced transparency.
The principle of lasing without inversion is also easily understood within this dark state approach. If the initial state is prepared such that it coincides with the dark state, then absorption is cancelled, but the stimulated emission from the excited state $|2\rangle$ (via excitation of the coupling state $|3\rangle$) still can exhibit gain [72].

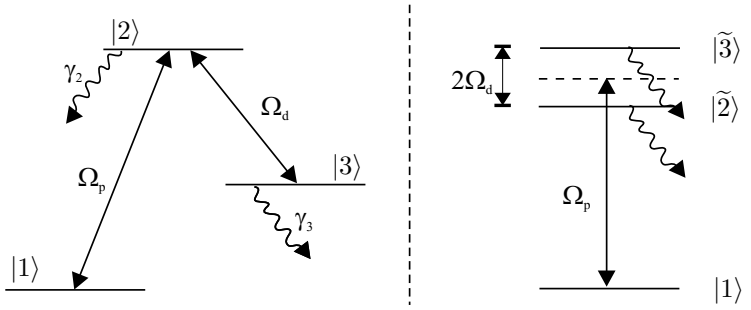

Figure 2.1: Left: a typical three-level Λ-scheme where a probe field Ω_p connects levels $|1\rangle$ and $|2\rangle$ while the driving field Ω_d connects levels $|2\rangle$ and $|3\rangle$. Right: a three-level scheme equivalent to the Λ-scheme, but with the action of the driving field implicitly present in the mixed levels $|\widetilde{2}\rangle$ and $|\widetilde{3}\rangle$.

Quantum interference and phase

The second picture is usually taken to illustrate EIT in case of a DC driving field. Then, the induced transparency can be explained as (destructive) *quantum interference*. Quantum mechanics requires that two paths that originate

[3]This is irrespective of the adiabatic condition, which is the condition on the time-dependent electromagnetic field(s) such that the state vector of the system remains nearly equal to an eigenvector of the Hamiltonian (here the dark state).

[4]The 'bright state' is given by $\sin\theta(t)|1\rangle + \cos\theta(t)|3\rangle$. This state can interact with $|2\rangle$ and, hence, lead to absorption of probe radiation.

from one particular state and result in the same end state, must interfere. In this case, the driving field mixes the states $|2\rangle$ and $|3\rangle$, giving rise to two new levels[5] that are superpositions of the unperturbed levels, as given in Eqs. (1.22) and (1.23). The energy difference between these levels is known as the Stark shift.
The (scattering) process of absorption and emission of the probe field now can occur via two intermediate quantum paths (with amplitude A_1 and A_2). The probability I for such a process to occur is, in a crude way, given by

$$I = |A_1 + A_2|^2 = |A_1|^2 + |A_2|^2 + 2\Re(A_1 A_2^*) \tag{2.2}$$

where the last term is the interference term and can, in the extreme case, result in a doubling or complete cancelling of I. In this interference picture, the question of phases arises in a natural way. Only when A_1 and A_2 have an arbitrary, but fixed, phase, the interference term does not vanish [17]. This phase could be varying in time, *e.g.* in short laser pulses, or varying in space. The latter can happen when dealing with multiple scattering in thick media. The amplitudes for each individual scattering can have a fixed phase, but the phase could vary between two scattering processes. This could be the case when inhomogeneities are the source of the driving (or mixing) interaction, inducing a random, space-dependent phase. This problem is tackled in more detail in section 3.1.7.

Susceptibility

There is a more quantitative way of describing the induced transparency. The response of a medium, *i.e.* the polarization P, to a (probe) electromagnetic field E is given by $\mathbf{P} = \chi\mathbf{E}$ and thus straightforwardly characterized by the linear susceptibility $\chi(\omega) = \chi'(\omega) + i\chi''(\omega)$. For the Λ-system of Fig. 2.1 it can be shown that [73]

$$\chi(\omega) \propto \frac{i\delta + \gamma_3/2}{(i\delta + \gamma_2/2)(i\delta + \gamma_3/2) + |\Omega_d|^2} \tag{2.3}$$

with $\delta = \omega - \omega_2$ the detuning of the probe field. The imaginary part $\chi''(\omega)$ gives the absorption, whereas the real part $\chi'(\omega)$ describes the dispersive properties of the medium. Both parts of the susceptibility are illustrated in Fig. 2.2 in the case of $\gamma_3 = \gamma_2/100$ for $\Omega_d = 0$ and $\Omega_d = \gamma_2$. It is seen that the largest reduction in absorption occurs at exact resonance, where complete transparency can be obtained when $\gamma_3 = 0$. The width of the transparency window is determined by Ω_d.

[5] These levels are eigenstates of the driving field interaction Hamiltonian.

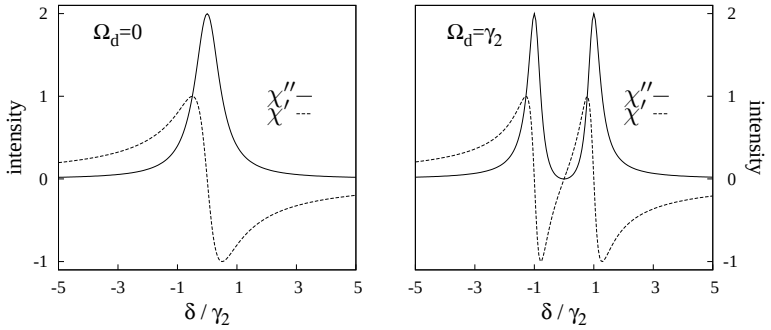

Figure 2.2: Real (χ') and imaginary (χ'') parts of the susceptibility, given in Eq. (2.3), for $\gamma_3 = \gamma_2/100$ and two values of the driving Rabi frequency Ω_d.

2.1.2 Delay

At resonance, the real part of the susceptibility, $\chi'(\omega)$, vanishes and shows a steep slope. Both of these properties are intimately connected with the interesting timing characteristics of an EIT medium. The index of refraction n is related to the susceptibility by [74]

$$n(\omega) = (1 + \chi'(\omega) + i\chi''(\omega))^{\frac{1}{2}} . \tag{2.4}$$

Therefore, at resonance, the refractive index equals unity, which means that the phase velocity v_p of the wave packet propagating through the medium equals that in vacuum. However, the transparency is accompanied by a steep variation with frequency of $\chi'(\omega)$, and hence of $n(\omega)$. This strongly influences the velocity of the envelope of a wave packet, *i.e.* the group velocity v_g, which is defined by [75]

$$v_g(\omega) \equiv \left(\frac{d\omega}{dk}\right)_{k_0} = \left(\frac{c - \omega\frac{dn}{dk}}{n(\omega) + \omega\frac{dn}{d\omega}}\right)_{k_0} , \tag{2.5}$$

see also chapter 5 for a more detailed discussion of v_g. If the medium is not strongly dispersive, v_g may be considered as the velocity at which the field energy is propagating [74]. However, in regions of anomalous dispersion, *e.g.* in a medium with a gain doublet [76, 77], v_g can exceed the velocity of light ('superluminal') or even become negative. In such cases the group velocity concept has lost its physical significance.
In an EIT medium with N atoms and an atom-field interaction constant g, the

group velocity has been calculated as [78]

$$v_g(\omega) \approx \frac{c}{1 + \frac{g^2 N}{|\Omega_d|^2}}, \tag{2.6}$$

in the case that $\gamma_3 = 0$. It is clear that v_g can be made much smaller than c by increasing the atomic density or by decreasing the power of the driving field. In their famous experiment Hau and coworkers [79] succeeded in slowing down a light pulse to $v_g = 17\,\mathrm{m/s}$. Moreover, by using a dense, ultracold gas, they could localize the pulse entirely in the medium. Recently, research groups [80–82] have established *optical storage*, where the probe field is written and stored in the atomic coherence and released (or: read out) on command.

2.2 EIT in the nuclear domain

The field of research that is dealing with the interaction of matter with gamma radiation is nowadays called nuclear quantum optics [83] or quantum nucleonics [84]. Although this research is closely connected to the vast field of quantum optics, adopting this new name is a clear statement of its distinctiveness, of having a 'mind' of its own.
But can (optical) EIT schemes be implemented in the nuclear domain? And does the reduction of absorption observed in the $FeCO_3$ Mössbauer experiment constitute a first proof of this nature? These are the main questions that we seek to answer in the remainder of this thesis. Let us first address them in this section in a semantic way.

2.2.1 Radioactive source radiation as probe field

In nuclear quantum optics, we have to face a less appealing aspect, being the very low resonant cross section for photon-matter interaction (in the order of $10^{-18}\,\mathrm{cm}^2$). This is one of the main reasons why there are still no gamma ray lasers (grasers) available today [85]. These low cross sections makes the creation of population inversion virtually impossible. There are some very nice suggestions to circumvent this problem, like there is the concept of lasing without inversion. But up till now, no physical implementation in the nuclear domain, as suggested in *e.g.* [86], has survived the harsh confrontation with reality.

Single photon source

In the meantime, we have to rely on the use of a radioactive source instead of a laser. The radiation of this radioactive source lacks the coherence of the laser field. However, there is more than meets the eye. Although the radioactive source emits its radiation in a statistical and uncorrelated manner, we show that the entire process from source emission to detection can be considered coherent, due to its *single photon* nature.

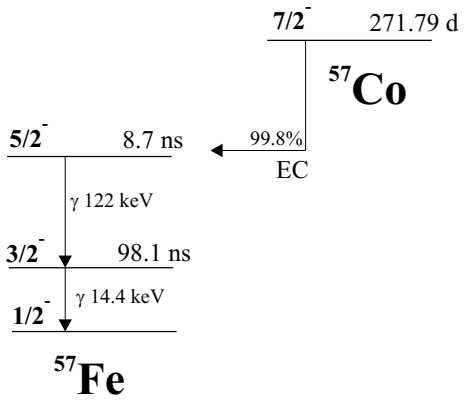

Figure 2.3: Partial decay scheme of ^{57}Co. The $I = 7/2^-$ ground state of ^{57}Co decays via electron capture (EC) to the $I = 5/2^-$ excited state of ^{57}Fe. This state decays to the $I = 1/2^-$ ground state in a two-photon cascade, where the 14.4 keV gamma is commonly used in Mössbauer spectroscopy.

The radioactive source contains radioactive nuclei, *e.g.* ^{57}Co, that decay and thereby release one or more gamma photons. The decay scheme of ^{57}Co is illustrated in Fig. 2.3. Its two-photon cascade (in ^{57}Fe) is very interesting for timing measurements, see section 5.3. This radiative decay is nothing more than spontaneous emission. That is why the photons are emitted one by one, completely uncorrelated. Furthermore, we dedicate a separate section (see below) to show that the statistical mixture of emitted photons is unpolarized.
Another obvious difference between the radiation fields of quantum optics and nuclear quantum optics is that the latter deals with short wavelength or high energy radiation (of the order of 10 keV and more). Each gamma photon carries at least 10^4 times more energy than an optical photon. This has an immediate impact on the detection mechanism. Due to their high ionizing power no special noise reducing technique, like, e.g., balanced homodyne detection [87], is needed to detect *single* gamma photons.
Because the complete process of emission by the source, scattering by an absorber and detection can be treated at the single photon level, *and* this single

photon has a coherence length far larger than the dimensions of the experimental setup[6], it is clear that this is a coherent physical process.

Unpolarized photon source

In order to predict selection rules and calculate transition amplitudes correctly, we must be sure about the polarization of the source radiation. In the used radioactive source, the ^{57}Co nuclei are embedded in a Rh matrix, without hyperfine field or electric field gradient. This means that there is no (known) preferred polarization axis to project the nuclear states onto. We are, therefore, allowed to choose any axis, which we denote as $\mathbf{z}^N$. Another way of describing this situation is stating that all nuclear magnetic sublevels $|m_I^N\rangle$ are degenerate. In Fig. 2.4 the levels are drawn for the 14.4 keV transition in ^{57}Fe, going from a $I_e = 3/2$ excited state to a $I_g = 1/2$ ground state.

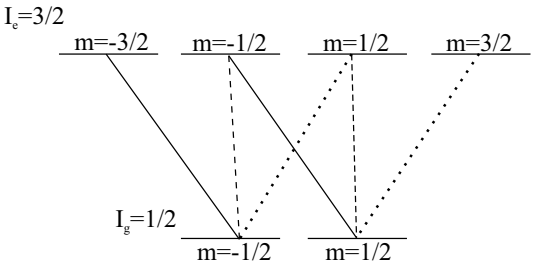

Figure 2.4: Allowed magnetic dipole transitions in ^{57}Fe, with $\Delta m = -1$ (solid line), $\Delta m = 0$ (dashed line) and $\Delta m = 1$ (dotted line).

In general, spontaneous emission to the ground state can occur obeying the selection rules for magnetic dipole transitions, so $\Delta m_I = 0, \pm 1$. Angular momentum is conserved by transfer of the angular momentum $l = 1$ to the photon. When $\Delta m_I = +1$, a photon with $m_l = -1$ is emitted to preserve the projection of angular momentum. The same rule, of course, applies to the two other cases. Because all degenerate magnetic sublevels are equally populated, the three transitions have equal probabilities.
At this moment nothing more can be said about the *spin* of the photon than that, along its propagation direction $\mathbf{k}$, only two states are possible[7], $|\sigma = \pm 1\rangle$. We say that a photon in state $|\sigma = +1\rangle$ is right circularly polarized (or short:

[6]The coherence length of a photon emitted in the decay of a nucleus can be estimated by $\Delta l \approx c\tau$, with τ the lifetime of the decaying nuclear state, hence $\Delta l \approx 42$ m.

[7]This is unlike other spin 1 particles, which have three different projections on any quan-

a σ^+ photon) and a photon in state $|\sigma = -1\rangle$ left circularly polarized (or short: a σ^- photon). This convention corresponds to the way the electric field vector is rotating in the plane perpendicular to $\mathbf{k}$, as seen by an observer travelling in the direction of the field.
The photon states $|m_l\rangle$ can be expressed either in the nuclear axis system ($|m_l^N\rangle$) or in a photon axis system ($|m_l^p\rangle$). If we define θ as the angle between the photon propagation direction $\mathbf{k}$ and the nuclear quantization axis $\mathbf{z}^N$, a transformation from the nuclear system (N) to the photon system (P) is given by [43]:

$$|m_l^p\rangle = D(0,\theta,0)|m_l^N\rangle \tag{2.7}$$

where $D(0,\theta,0)$ denotes the rotation matrix operator. We can express this in the new basis ($|\sigma = \pm 1\rangle$):

$$|m_l^p\rangle = \sum_\sigma \langle\sigma|D(0,\theta,0)|m_l^N\rangle|\sigma\rangle \tag{2.8}$$

$$= \sum_\sigma d^1_{\sigma,m_l^N}(\theta)|\sigma\rangle \tag{2.9}$$

The full expressions are:

$$|m_l^p = 1\rangle = \cos^2\frac{\theta}{2}|\sigma = +1\rangle + \sin^2\frac{\theta}{2}|\sigma = -1\rangle \tag{2.10}$$

$$|m_l^p = 0\rangle = \frac{\sin\theta}{\sqrt{2}}\left(|\sigma = +1\rangle - |\sigma = -1\rangle\right) \tag{2.11}$$

$$|m_l^p = -1\rangle = \sin^2\frac{\theta}{2}|\sigma = +1\rangle + \cos^2\frac{\theta}{2}|\sigma = -1\rangle \tag{2.12}$$

It is seen that if $\theta = 0$, the state $|m_l^p = 0\rangle$ is totally suppressed and only pure $|\sigma\rangle$ states remain. As there is no preferred direction in our source, we can always choose $\mathbf{z}^N = \mathbf{k}$. This means that, along its propagation direction, the source photon is either right or left circularly polarized (σ^+ or a σ^-). For an ensemble of photons emitted by a radioactive source each polarization has the same probability. This equal mixture of circularly polarized photons corresponds to the definition of unpolarized radiation.

Finally, the 'tuning' of the frequency of the gamma photons to match the absorber frequencies can be easily controlled. The source is Doppler shifted by mounting it on a velocity drive. Typical velocities of the order of a few mm/s are sufficient to scan the complete hyperfine energy structure.

---

tization axis. This is related to the fact that light has no mass, and cannot stand still [88].

2.2.2 Mixing interaction as driving field

In optical EIT the driving field is used to couple the excited state to a (metastable) state other than the ground state. In order for this coupling state to be a lower lying excited nuclear state or a ground state, a second gamma field is needed. As pointed out in the previous paragraphs, for now, only a radioactive source is available. However, *if* the combination of two radioactive sources is experimentally feasible, the random nature of gamma photon emission would lead to a random overlap of probe and drive field. It is clear that the concept of 'matched pulses'[8] [89] would completely lose its value.
If this coupling state is a member of the same (hyperfine) multiplet as the excited state, then one can apply a radio-frequent (rf) field, a magnetic field or take advantage of internal (hyperfine) fields. The effect of a strong rf-field on the Mössbauer absorption has been studied theoretically by Gabriel [90] and experimentally investigated by Vagizov [91] and Tittonen and coworkers [92]. These experiments have demonstrated a Stark shift of the driven nuclear levels.
The other two possible coupling fields are DC fields (with zero frequency). Hakuta and coworkers were the first to show experimentally that a DC field in atomic hydrogen can be used to create EIT [93, 94]. More recently, the application of an rf-field [95] and of an internal or external magnetic field [96, 97] has been suggested to induce transparency for gamma photons. It has also been shown [98] that the application of a DC magnetic field is equivalent to an rf-field by treating the first in a rotating frame. An overview of modification of Mössbauer spectra under the action of different kinds of electromagnetic fields is given in [99].
In this thesis, we suggest that the role of the driving field is played by a non-axially symmetrical electric field gradient[9].

2.2.3 Relaxation

If we choose the coupling state as belonging to the same multiplet as the excited state, we must acknowledge the consequence it bears for the relaxation rate. These states both originate from the same nuclear excited state, which means that they have *equal decay rates*. A hint to understand the importance of this is presented by Berman in [65]. He shows that the level scheme, which gives rise to suppression of spontaneous emission, is isomorphic to a three-level Λ-

[8] Matched pulses have the same pulse envelopes in time domain.

[9] Actually, it is sufficient to have an interaction that breaks the axial symmetry, inducing transitions between nuclear magnetic sublevels. Which sublevels are mixed depends on the specific type of interaction, as explained in section 1.1.4.

scheme, and hence can be explained in terms of coherent population trapping. However, this isomorphism only applies when the ground and coupling state are *both* metastable.
In this thesis, we show on several occasions that the interference term *vanishes* if the coupling state has the same decay rate as the excited state, greatly reducing the transparency effect.

2.2.4 Optically thick media

> To understand propagation in an optically (or refractively) thick medium, one must understand not only how the electromagnetic fields drive the atoms, but also how the atoms drive the fields.
>
> S. E. Harris in [69]

In most text-books and papers that deal with (optical) EIT the problem is restricted to the interaction of fields with ensembles of *single* atoms. The reason is that most optical experiments are performed in gases and thus multiple scattering processes can indeed be discarded. In nuclear quantum optics, however, the nuclei are closely packed in a crystal. Although the interaction cross-section is very small ($\approx 10^{-18}\,\mathrm{cm}^2$), the huge number of possible scattering centers ($\approx 10^{18}$) means that multiple scattering cannot be neglected. Therefore, we should follow the advice in Harris's quote. In chapters 3 and 4 we construct models that explicitly take into account the dependence of the transmitted radiation on the thickness of the nuclear medium. In order to compare with the results of optical EIT, we can always consider the limit of a very thin absorber.

2.2.5 Previous work on EIT with gamma photons

Prior to this work, two papers have tried to give an explanation to the observed reduction in absorption in these $FeCO_3$ crystals in terms of EIT. Both papers assume that a non-axial component of the hyperfine field lies at the origin of the mixing interation.
First, in [96] a simple model is constructed by use of the density matrix formalism. Eventually, the "absorption coefficient of gamma radiation D" is calculated as:

$$D = \Re\left(\frac{\gamma + \gamma_s + i\omega_v}{(\gamma + \gamma_s + i\omega_v)^2 + |\Omega|^2}\right), \tag{2.13}$$

with γ (γ_s) the decay rate of the excited state in the absorber (source), ω_v the Doppler shifted frequency of the incident radiation and Ω the strength of the

mixing interaction. We can prove, however, that

$$D = \frac{1}{2}\frac{\gamma+\gamma_s}{(\gamma+\gamma_s)^2+(\omega_v+\Omega)^2} + \frac{1}{2}\frac{\gamma+\gamma_s}{(\gamma+\gamma_s)^2+(\omega_v-\Omega)^2}, \tag{2.14}$$

which is no more than the sum of two Lorentzian absorption lines, shifted with $+\Omega$ and $-\Omega$ respectively. One can then wonder if this result really can be interpreted as a manifestation of EIT, as known in quantum optics, since there is clearly no interference present.

In the second paper [98] it is postulated that, in a thin absorber limit, "the absorption behavior is governed by"

$$\frac{\gamma/2}{\delta_1+i\gamma/2} + \frac{\gamma/2}{\delta_2+i\gamma/2} = \left|\frac{\gamma/2}{\delta_1+i\gamma/2}\right| e^{i\phi_1} + \left|\frac{\gamma/2}{\delta_2+i\gamma/2}\right| e^{i\phi_2} \tag{2.15}$$

with $\delta_i = \omega - \omega_i$, ω_i the frequency of an excited, mixed state (and $\omega_{1/2} = \omega_0 \pm \Omega$, see above) and $\tan\phi_i = -\gamma/(2\delta_i)$. If the frequency is tuned to the center of the split levels ($\omega = \omega_0$), then $\delta_1 = -\delta_2 = -\Omega$ and the two terms contribute with an opposite phase $\phi_1 = -\phi_2 = \arctan(\gamma/(2\Omega))$. This has been identified as the destructive interference leading to EIT[10]. However, in the next chapter we also derive the absorption in this thin absorption limit, which is proportional to the *imaginary part* of Eq. (2.15), but show that this also exactly equals a sum of two Lorentzian absorption lines. Actually, any absorption to two closely lying states yields such oppositely phased terms. This only results in a reduction of absorption due to the off-resonance condition.

2.3 Conclusions

We have first presented different views on the EIT phenomenon as it is known in the 'low frequency' domain of quantum optics. Its main features are the reduction of absorption in a resonant medium and the change of the refractive index of the medium, yielding very slow pulse group velocities. Then, we have tried to extrapolate the common Λ-scheme, which gives rise to EIT, to the realm of gamma optics. Indeed, there are strong similarities with the level crossing scheme in $FeCO_3$, *if* there is also some kind of mixing interaction present. However, the fact that the mixed nuclear states have equal decay rates seriously

[10] Furthermore, it was argued that, if $\Omega >> \gamma$, then $\phi_1 \to \pi/2$ and $\phi_1 \to -\pi/2$. This statement is not correct because for $\gamma/\Omega \to 0$, $\phi_1 \to 0 \leftarrow \phi_2$, which simply means that the incident radiation will no longer interact with these levels.

compromises the *nuclear* EIT effect. This was not explicitly recognized in the first papers on nuclear EIT, although a simple analysis of those early results reveals that no true interference is present in this nuclear case. Does this then mean that ideas about nuclear EIT are a waste of time? And how must the observed spectra be interpreted? Is the presence of interference really necessary for a consistent understanding? These questions are addressed in detail and lay out the foundations for the next chapters.

Chapter 3

Semiclassical models

Although different versions exist [100], the distinctive feature of a *semiclassical theory* is that it treats matter quantum mechanically, while the electromagnetic field is treated classically. There are two very valuable approaches to our nuclear resonant scattering problem that fall in the category of semiclassical theories. The first is based on the work of Blume and Kistner [101]. A detailed application of their model to our case is given in the next section. The second semiclassical approach is sometimes called the Maxwell-Schrödinger formalism. Density matrix equations are applied for obtaining the macroscopic polarization of the medium, which is then used to solve the Maxwell equations. A resume of this method and a sketch of its equivalence with the first is addressed in the second part of this chapter.

3.1 Approach based on Blume-Kistner model

For more details on the approach first developed by Blume and Kistner we refer to [101–103]. We just mention the results that are relevant for our case.
The propagation equation for a classical plane wave with amplitude $A(\omega)$ along the z axis is given by

$$\left(\nabla^2 + n^2 k^2\right) A(\omega, z) = 0, \tag{3.1}$$

which has the solution

$$A(\omega, z) = e^{inkz} A(\omega, 0), \tag{3.2}$$

where the magnitude k of the wave vector in vacuum, $\mathbf{k}$, is related to the frequency ω of the incident plane wave through $k = \omega/c$. The influence of the

medium on the radiation wave is completely absorbed in the refractive index n. In this case, n does not depend on $A(\omega, z)$ and, hence, this plane wave solution corresponds to a linear approximation of the full Maxwell wave equations. The linear approximation is justified by the weak interaction of the gamma radiation with the nuclei.
In general, n is a complex, non-Hermitian and frequency dependent matrix $\widetilde{n}(\omega)$. The real part describes the change of polarization and the change in phase, while the imaginary part accounts for the (polarization dependent) absorption.
The index of refraction is given by [104]:

$$\widetilde{n}(\omega) = \widetilde{1} + \frac{2\pi}{k^2}\rho\widetilde{f}(\omega) \tag{3.3}$$

where $\widetilde{1}$ is the 2×2 unit matrix, ρ the atomic volume density and $\widetilde{f}(\omega)$ the coherent forward scattering amplitude. This amplitude is, in general, a 2×2 matrix, since a scattering process can change the polarization of the incident radiation. In this treatment we choose to express $\widetilde{f}(\omega)$ in a basis of left (σ^-) and right (σ^+) circular polarization.
Forward scattering contains two contributions, scattering from electrons $\widetilde{f}_e(\omega)$ and resonant scattering from nuclei $\widetilde{f}_n(\omega)$. Scattering from electrons, however, is essentially constant over the frequency range where nuclear resonant scattering is important [105]. Therefore, $\widetilde{f}(\omega)$ can be expressed as $\widetilde{f}(\omega) = \widetilde{f}_e + \widetilde{f}_n(\omega)$. In the case of the 14.4 keV gamma ray scattering in ^{57}Fe, the influence of the electronic scattering is limited to a reduction of the overall absorption by a factor $\exp(-\mu_e d)$, with μ_e the electronic absorption factor and d the physical thickness of the medium [106]. This electronic contribution is not relevant for the remainder of the calculations and is, therefore, omitted from the following equations. We also drop the 'n' subscript from the notation of the forward scattering amplitude.
An expression for the matrix elements of $\widetilde{f}(\omega)$ in the notation of Blume and Kistner is given by:

$$\widetilde{f}^{\sigma'\sigma}(\omega) = \left(-\frac{kVf_{LM}}{2\pi c\hbar}\right)\frac{1}{2I_g+1}\sum_{m_g,m_e}\frac{\langle \mathbf{k}\sigma' m_g|\mathcal{H}|m_e\rangle\langle m_e|\mathcal{H}|\mathbf{k}\sigma m_g\rangle}{\omega - \left(\omega_{m_e} - \omega_{m_g}\right) + i\frac{\gamma}{2}}, \tag{3.4}$$

with V the volume in which the radiation is normalized and γ the total width of the excited state[1]. This is the coherent[2] resonant scattering amplitude for a plane wave with polarization σ to a plane wave with polarization σ', absorbed

[1] If τ is the lifetime of the excited state, then its width is defined by $\gamma = \tau^{-1}$.

[2] In order to have a *coherent* scattering process, the initial and final nuclear state must be the same.

by a nucleus from a ground state $|I_g m_g\rangle$ (with frequency ω_{m_g}) to an excited state $|I_e m_e\rangle$ (with frequency ω_{m_e}) and re-emitted to $|I_g m_g\rangle$. The Hamiltonian $\mathcal{H}$ describes the interaction between the electromagnetic field and the nucleus. Here, an average over the ground states $|m_g\rangle$ is made, with the assumption that they are equally populated. By including the recoil-free or Lamb-Mössbauer fraction f_{LM}, it is assumed that the energy of the incident photon is close to resonance.
The above expression also assumes that the nuclear levels can be described by a well-defined magnetic quantum number m. As we are especially interested in the case were this is no longer true (in the case of a non-axially symmetrical interaction), Eq. (3.4) should be modified. This implies a transformation of basis, *i.e.* expressing the true eigenstates $|n\rangle$ as a linear combination of magnetic substates (as prescribed in [101]):

$$|n\rangle = \sum_m \langle m|n\rangle |m\rangle. \tag{3.5}$$

The amplitude for coherent forward nuclear scattering now expands to

$$\begin{aligned} \widetilde{f}^{\sigma'\sigma}(\omega) &= \left(-\frac{kVf_{LM}}{2\pi c\hbar}\right)\frac{1}{2I_g+1}\sum_{n_g,n_e}\sum_{m_g,m_e}\sum_{m'_g,m'_e}\langle n_g|m_g\rangle\langle m'_g|n_g\rangle \\ &\quad\times\langle n_e|m_e\rangle\langle m'_e|n_e\rangle\frac{\langle \mathbf{k}\sigma' m_g|\mathcal{H}|m_e\rangle\langle m'_e|\mathcal{H}|\mathbf{k}\sigma m'_g\rangle}{\omega-\left(\omega_{n_e}-\omega_{n_g}\right)+i\frac{\gamma}{2}}. \end{aligned} \tag{3.6}$$

The matrix elements $\langle m_e|\mathcal{H}|\mathbf{k}\sigma m_g\rangle$ are given by [101]:

$$\langle m_e|\mathcal{H}|\mathbf{k}\sigma m_g\rangle = 2\pi\sqrt{\frac{\hbar c}{Vk}}\sum_{LM} i^L\sqrt{2L+1}\mathcal{D}^{(L)}_{M,\sigma_{in}}(\alpha,\beta,\gamma)\mathcal{C}(I_g L I_e; m_g M m_e)M_L \tag{3.7}$$

Here is a list with the meaning of all variables:

L, M	:	magnetic 2^L pole with M=-L,...,L
$\mathcal{C}(...)$	:	Clebsch-Gordan coefficient
$\mathcal{D}^{(L)}_{M,\sigma_{in}}(\alpha,\beta,\gamma)$	:	rotation matrix with (α,β,γ) Euler angles describing the radiation axis in the nuclear principal axis system
M_L	:	strength of the magnetic 2^L pole ($|M_L|^2 = \frac{\gamma_r}{8\pi k}$, and γ_r the radiative decay rate)

Values for the rotation matrix elements and the Clebsch-Gordan coefficients that are relevant in our case, are listed in Appendix B.
With $\widetilde{n}(\omega)$ now completely defined in terms of $f^{\sigma'\sigma}(\omega)$ and simplifying the

matrix exponential in Eq. (3.2) to a normal matrix form, the solution for the amplitude of the forward scattered plane wave is given by:

$$\begin{pmatrix} A^+(\omega,z) \\ A^-(\omega,z) \end{pmatrix} = e^{ikz}\widetilde{S}(\omega,z) \begin{pmatrix} A^+(\omega,0) \\ A^-(\omega,0) \end{pmatrix} \tag{3.8}$$

where the scattering matrix $\widetilde{S}(\omega,z)$ is calculated as

$$\begin{aligned} \widetilde{S}(\omega,z) &= \frac{e^{(a+d)/2}}{D} \\ &\times \begin{pmatrix} D\cosh\left(\frac{D}{2}\right) + (a-d)\sinh\left(\frac{D}{2}\right) & 2b\sinh\left(\frac{D}{2}\right) \\ 2c\sinh\left(\frac{D}{2}\right) & D\cosh\left(\frac{D}{2}\right) + (d-a)\sinh\left(\frac{D}{2}\right) \end{pmatrix} \end{aligned} \tag{3.9}$$

with

$$\begin{aligned} a &= i\frac{2\pi}{k}\rho z\, f^{++}(\omega) \quad , \qquad b = i\frac{2\pi}{k}\rho z\, f^{+-}(\omega), \\ c &= i\frac{2\pi}{k}\rho z\, f^{-+}(\omega) \quad , \qquad d = i\frac{2\pi}{k}\rho z\, f^{--}(\omega) \end{aligned} \tag{3.10}$$

and $D = \sqrt{(a-d)^2 + 4bc}$. Notice that expression (3.9) exactly matches the expression for the scattering matrix obtained in [107, 108].
As is discussed in section 2.2, an unpolarized radioactive source can be treated as a statistical mixture of right and left handed circular polarization. Therefore, in this basis, the vector of the incident wave has only 1 component. In the case of regular Mössbauer spectroscopy, the amplitude of this incident wave component $A^{\pm}(\omega,0)$ is Lorentzian[3]:

$$A^{\pm}(\omega,0,v) = \frac{1}{\sqrt{2}}\frac{\gamma_r/2}{\omega - \omega_v + i\frac{\gamma}{2}} \tag{3.11}$$

This frequency profile originates from the exponential lifetime decay of the excited nuclei in the source. It is centered around the Doppler shifted frequency $\omega_v = \omega_\gamma(1 + v/c)$ and has an amplitude proportional to the radiative width. The factor $(2)^{-1/2}$ stems from the equal amount of both field polarizations.
Finally, the measurable time-integrated Mössbauer intensity as a function of transducer velocity is given by $I(v) = I^+(v) + I^-(v)$ with

$$I^{\pm}(v) = \frac{1}{2\pi}\int_{-\infty}^{\infty} d\omega\, \left(|S^{\pm+}(\omega,z)A^+(\omega,0,v)|^2 + |S^{\pm-}(\omega,z)A^-(\omega,0,v)|^2\right). \tag{3.12}$$

[3]This is a valid approximation if the source is thin ($T_e << 1$) and, hence, does not experience thickness broadening.

3.1.1 Three-level system

It is straightforward to substitute all variables in the above expressions and perform basic mathematical operations in order to simulate different experimental cases. This is done in the next section. But first, we would like to focus on the special case of level crossing and deal with it in an analytical way. We limit the following treatment to the three nuclear levels involved in the level crossing/mixing transition[4], *i.e.* the $|m_g = -1/2\rangle \equiv |1\rangle$ ground state and the $|m_e = 1/2\rangle \equiv |2\rangle$ and $|m_e = -3/2\rangle \equiv |3\rangle$ excited states. In section 1.1.4 it is shown that either a magnetic field or an efg can mix the two excited states, giving rise to two fully mixed states $|\widetilde{\frac{1}{2}}\rangle \equiv |\widetilde{2}\rangle$ and $|-\widetilde{\frac{3}{2}}\rangle \equiv |\widetilde{3}\rangle$. The mixed levels have an energy difference of $2\hbar\Omega$, with Ω the strength of the mixing (expressed in frequency units) and depending on the type of mixing interaction. For example, in the case of a non-axial efg, using Eq. (1.10), we find that $\Omega = \sqrt{3}\eta\omega_Q$. In this nuclear system of mixed levels, gamma radiation with a particular circular polarization can scatter on both levels simultaneously, *if* they fall within the line width of the incident radiation.
This property of indistinguishable quantum paths makes the level mixed scheme a very promising system to investigate quantum interference effects at the nuclear level.

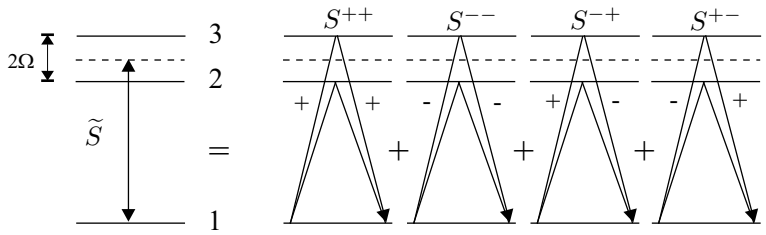

Figure 3.1: Schematical representation of scattering in a three-level system with mixed states $|\widetilde{2}\rangle$ and $|\widetilde{3}\rangle$. The four possible scattering paths are explicitly drawn.

The full picture, with all possible scattering processes, is illustrated in Fig. 3.1. The absorption and emission to and from both excited states can occur through two channels, *i.e.* with right or left circular polarization. Without mixing, however, the absorption and emission process should occur with the same polarization.
According to Eq. (3.6), the forward scattering amplitude in this three-level

[4] As long as the distance to all other transitions is larger than γ, this simplification has no ramifications for an extrapolation to the real case.

system is given by

$$f^{\sigma'\sigma}(\omega) \propto \frac{\langle\widetilde{2}|\mathcal{H}^{\sigma'}|1\rangle\langle 1|\mathcal{H}^{\sigma}|\widetilde{2}\rangle}{\omega - \left(\omega_{\widetilde{2}} - \omega_1\right) + i\frac{\gamma}{2}} + \frac{\langle\widetilde{3}|\mathcal{H}^{\sigma'}|1\rangle\langle 1|\mathcal{H}^{\sigma}|\widetilde{3}\rangle}{\omega - \left(\omega_{\widetilde{3}} - \omega_1\right) + i\frac{\gamma}{2}}. \tag{3.13}$$

If we introduce the definition of a magnetic dipole transition matrix element $\mu_{ij} = \langle i|\mathcal{H}|j\rangle$ and substitute Eq. (1.22) and (1.23) into Eq. (3.13), we find an explicit expression for the forward scattering amplitude matrix elements:

$$f^{++}(\omega) \propto \frac{|\mu_{21}|^2}{2} L_+(\omega) \qquad f^{--}(\omega) \propto \frac{|\mu_{31}|^2}{2} L_+(\omega) \tag{3.14}$$

$$f^{+-}(\omega) \propto \frac{\mu_{21}\mu_{13}}{2} L_-(\omega) \qquad f^{-+}(\omega) \propto \frac{\mu_{31}\mu_{12}}{2} L_-(\omega) \tag{3.15}$$

with

$$L_\pm = \frac{1}{\omega - \omega_0 - \Omega + i\gamma/2} \pm \frac{1}{\omega - \omega_0 + \Omega + i\gamma/2}, \tag{3.16}$$

where we have defined that $\omega_{\widetilde{2}} - \omega_1 \equiv \omega_0 - \Omega$ and $\omega_{\widetilde{3}} - \omega_1 \equiv \omega_0 + \Omega$. The scattering amplitudes clearly consist of a sum (or difference) of two Lorentzian line shapes, which are centered around the frequencies of the mixed levels and are in anti-phase in the case of the polarization changing amplitudes.
These sums at the level of amplitudes could lead to interference phenomena.

To keep things analytical and simple, we consider the thin absorber limit ($T_e << 1$). Then, only the first term in the Taylor expansion of the exponent in Eq. (3.2) is retained:

$$\begin{pmatrix} A^+(\omega,z) \\ A^-(\omega,z) \end{pmatrix} = e^{ikz}\left(\widetilde{1} + i\frac{2\pi}{k}\rho z\widetilde{f}(\omega)\right)\begin{pmatrix} A^+(\omega,0) \\ A^-(\omega,0) \end{pmatrix}. \tag{3.17}$$

Substituting Eq. (3.14) and Eq. (3.15) we find

$$\begin{aligned}\begin{pmatrix} A^+(\omega,z) \\ A^-(\omega,z) \end{pmatrix} &= e^{ikz}\left[\widetilde{1} - i\frac{3T_e}{16}\frac{\gamma}{2}\begin{pmatrix} |C_{21}|^2 L_+(\omega) & C_{21}C_{13}L_-(\omega) \\ C_{31}C_{12}L_-(\omega) & |C_{31}|^2 L_+(\omega) \end{pmatrix}\right] \\ &\quad \times \begin{pmatrix} A^+(\omega,0) \\ A^-(\omega,0) \end{pmatrix},\end{aligned} \tag{3.18}$$

with C_{ij} the product of the Clebsch-Gordan and rotation matrix coefficients of the $|j\rangle \rightarrow |i\rangle$ transition. The proportionality factor is obtained from Eq. (3.6) and (3.7). We also use the definition of the effective thickness T (Eq. (1.30)) and the definition of the maximal resonant cross-section σ_0 [37]:

$$\sigma_0 = \frac{2\pi}{k^2}\frac{2I_e+1}{2I_g+1}\frac{\gamma_r}{\gamma}. \tag{3.19}$$

Consider the case when σ^+ radiation is incident, $C_{12} = C_{13} = C_{12}^* = C_{13}^*$ and $C = 3T_e C_{12}^2/16$. For clarity, we omit the convolution with the incoming radiation. Then, the intensity of the transmitted radiation is given by

$$I(\omega) = |A^+(\omega, z)|^2 + |A^-(\omega, z)|^2 \tag{3.20}$$

$$= \underbrace{1 + 2\Im\left(C\frac{\gamma}{2}L_+(\omega)\right)}_{I_1(\omega)} + \underbrace{C^2|\frac{\gamma}{2}L_+(\omega)|^2 + C^2|\frac{\gamma}{2}L_-(\omega)|^2}_{I_2'(\omega)}. \tag{3.21}$$

In the thin absorber limit, $C << 1$ and, hence, the last two terms are negligible with respect to the first terms. The first term is the source term, which represents the case of transmission without scattering, while the second term represents the interference of the non-scattered with a single scattering event. The latter term is given by

$$2\Im\left(C\frac{\gamma}{2}L_+(\omega)\right) = -C\frac{\gamma^2}{2}\left(\frac{1}{(\omega-\omega_0-\Omega)^2+\frac{\gamma^2}{4}} + \frac{1}{(\omega-\omega_0+\Omega)^2+\frac{\gamma^2}{4}}\right), \tag{3.22}$$

which is a simple sum of two Lorentzian absorption line shapes, centered at $\omega_0 \pm \Omega$, respectively. This means that there is only a (Stark) shift of the levels, but no term that could describe additional interference effects[5]. As shown in Fig. 3.2, the absorption peaks of the first order term are subtracted from the baseline (provided by the source term) giving rise to the well-known Mössbauer absorption spectrum.
Notice that this expression is equivalent to the absorption derived in [98] (and briefly discussed in section 2.2.5), but now 'debunked' as two Lorentzian absorption lines.

But maybe we overlooked the interference term by neglecting the terms to second order in C. Closer examination of the second (or higher) order term to the transmitted radiation ($I_2'(\omega)$) can also provide more insight in the scattering process for thicker absorbers, as these terms become non-negligible. Surprisingly, after some algebraic reordering, the sum of these second order terms can be expressed as:

$$I_2'(\omega) = C^2|\frac{\gamma}{2}L_+(\omega)|^2 + C^2|\frac{\gamma}{2}L_-(\omega)|^2 = C^2\frac{\gamma^2}{2}\left(g_+(\omega) + g_-(\omega)\right), \tag{3.23}$$

with

$$g_\pm(\omega) = \frac{1}{(\omega-\omega_0\mp\Omega)^2+\frac{\gamma^2}{4}}, \tag{3.24}$$

[5]Remember the definition of EIT by Harris, given in the introduction to chapter 2, who emphasized that the EIT effect is the sum of a shift of the levels and a (destructive) interference term.

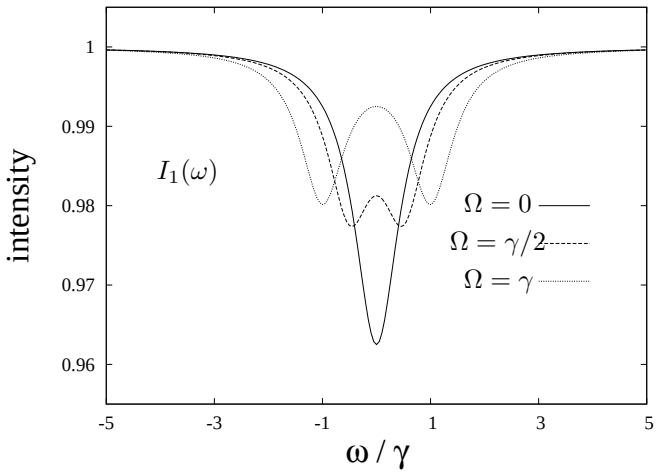

Figure 3.2: The transmitted radiation (up to first order in C) as a function of dimensionless frequency, for different values of the mixing interaction strength Ω. (thin absorber limit $\mathrm{T}_e = 0.1$)

which is exactly the same sum of Lorentzians as in the dominating term, except for the C^2 factor. It is interesting to note that only the sum of both $|L_{\pm}(\omega)|^2$ terms reduces to a sum of Lorentzians. Individually, however, they deviate from the Lorentzian shape, as shown in Fig. 3.3. The $|L_{+}(\omega)|^2$ term displays a decrease of intensity between the absorption peaks, whereas the absorption for the $|L_{-}(\omega)|^2$ term shows an equal but opposite increase.

These terms only make up a part of the full second order term. In the second order term of the Taylor expansion, there are two more terms that are quadratic in C (from the S^{++} matrix element). Their contribution to $I(\omega)$ is

$$-2\Re\left(\frac{C^2}{2}\frac{\gamma^2}{4}L_{+}^2(\omega)\right) - 2\Re\left(\frac{C^2}{2}\frac{\gamma^2}{4}L_{-}^2(\omega)\right) = \\ -C^2\frac{\gamma^2}{2}\left[g_{+}(\omega) + g_{-}(\omega) - \frac{\gamma^2}{2}\left(g_{+}^2(\omega) + g_{-}^2(\omega)\right)\right], \tag{3.25}$$

where the first two terms exactly compensate the Lorentzian terms of Eq. (3.23). The total second order contribution $I_2(\omega)$ to the transmitted radiation is now reduced to a sum of squared Lorentzians and is plotted in Fig. 3.4. This result again emphasizes the truly independent nature of the scattering process at the mixed levels. Also, the small amplitude of $I_2(\omega)$ (~ 0.001) confirms its negligibility with respect to $I_1(\omega)$.

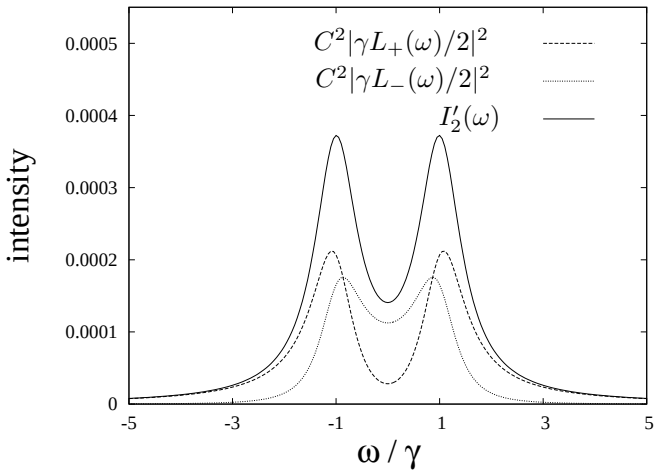

Figure 3.3: The sum of these second order contributions to the transmitted intensity exactly equals the sum of two Lorentzians (bold solid line). (thin absorber limit $\mathrm{T}_e = 0.1$)

It is clear, however, that if $C_{12} \neq C_{13}$, some terms will not cancel each other any more. However, the full expression of $I_2(\omega)$ can still be conveniently arranged:

$$I_2(\omega) = \left(\frac{3T}{16}\right)^2 \frac{\gamma^4}{4} \left[|C_{12}|^4 \left(g_+(\omega) + g_-(\omega)\right)^2 + |C_{12}|^2 |C_{31}|^2 \left(g_+(\omega) - g_-(\omega)\right)^2\right] \tag{3.26}$$

Now, $I_2(\omega)$ contains terms of the form $g_+(\omega)g_-(\omega)$, introducing 'cross talk' between the mixed levels. In Fig. 3.5 we have plotted these cross terms for both σ^+ and σ^- source radiation, taking into account the real values of $C_{12} = (3)^{-1/2}$ and $C_{13} = 1$. It is interesting to note that the cross terms always give a small, but positive contribution to $I_2(\omega)$ because $|C_{12}|^4 + |C_{13}|^4 \geq 2|C_{12}|^2|C_{13}|^2$.

In summary, we have shown that, in the thin absorber limit following the Blume-Kistner approach, the transmitted radiation is described by a sum of two Lorentzians, centered at the frequencies of the mixed levels. The sum of all terms to second order in C (or T) can be expressed as a sum of squared Lorentzians, if $|C_{12}|^2 = |C_{13}|^2$. If the transition probabilities are asymmetric, cross terms appear that give a slight increase to $I_2(\omega)$.

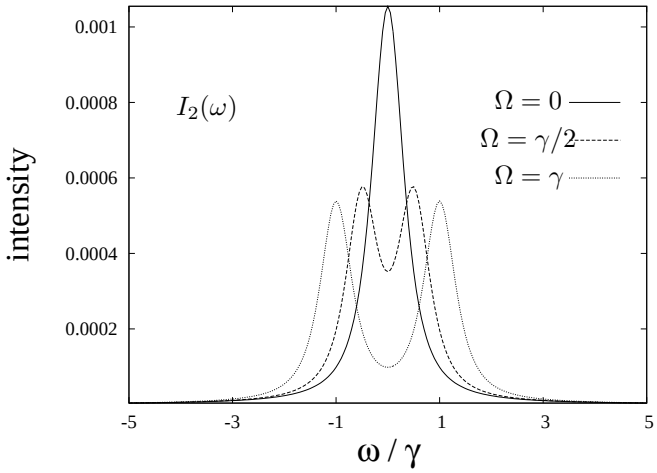

Figure 3.4: The total second order contribution $I_2(\omega)$ to the transmitted radiation for different values for the mixing interaction strength Ω as a function of dimensionless frequency. (thin absorber limit $\mathrm{T}_e = 0.1$)

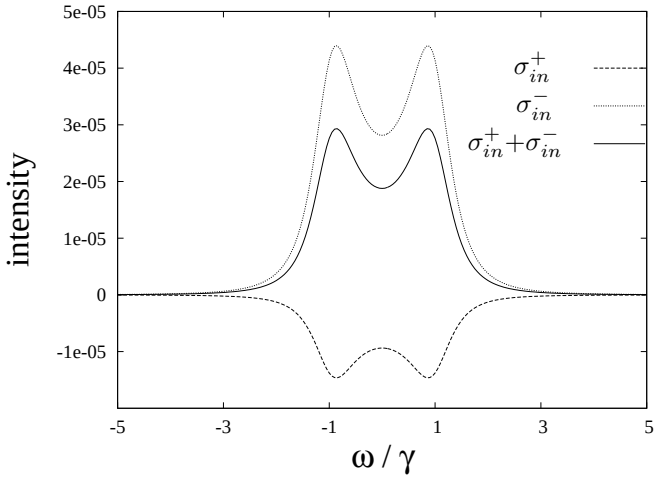

Figure 3.5: The contribution of the cross terms in Eq. (3.26) to $I_2(\omega)$ in the case of $C_{12} = (3)^{-1/2}$, $C_{13} = 1$ and $\Omega = \gamma$. Both the cases of incident σ^+ and σ^- radiation are shown. The bold solid line is the sum of both contributions. (thin absorber limit $\mathrm{T}_e = 0.1$)

3.1.2 Simulations for a multilevel system and thick absorber

In order to deal with the real case, *i.e.* the six absorption lines in the Mössbauer scheme of ^{57}Fe and an arbitrarily thick absorber, we have implemented Eq. (3.8) and (3.9) into a Fortran computer code. Also, the convolution with the incident radiation line shape (Eq. (3.12)) is included.
We continue the analysis of the transmitted radiation at the level crossing from the preceding section. In the parallel geometry, two additional transitions are observable, *i.e.* the $(3/2, 1/2)$ and $(-1/2, 1/2)$ transitions, which are the doublet partners of the transitions involved in the level crossing. In the perpendicular geometry, also the $(1/2, 1/2) - (-1/2, -1/2)$ doublet appears.
Through these simulations, we study the effect of a magnetic field B_e perpendicular to the z-axis of the (axially symmetric) efg, which can be realized by applying an external field or by a non-collinear component of the hyperfine field, and the effect of a non-axial efg, characterized by η. Both interactions have been identified as a possible mixing interaction present in the natural $FeCO_3$ crystal.

Simulations at the level crossing with perpendicular magnetic field

Fig. 3.6 shows simulations of the transmitted intensity for different values of the perpendicular magnetic field, B_e in both geometries and for a crystal with $T_e = 8$. They should be compared with the experimental spectra for $T = 31\,\mathrm{K}$ in Fig. 1.10. We have adopted the experimental values of table A.1 and, in order to simulate absorption amplitudes that are comparable with the experimental data, a resonant fraction $f_r = 0.3$ is assumed[6].
The most obvious feature of these simulations is the appearance of extra absorption lines, which have also been observed experimentally (see Fig. 1.15). They originate from the mixing of the m-states. If $B_e \neq 0$, each eigenstate of the nuclear Hamiltonian is a superposition of *all* pure m-states. Therefore, each of the 4×2 possible transitions from ground to excited state will now be allowed. Because of the level crossing/mixing, however, another pair of absorption lines lie on top of each other, *i.e.* the $(1/2, 1/2)$ and $(1/2, -3/2)$ transitions (expressed in their unperturbed m quantum number), resulting in the six resolved lines.

[6]This resonant fraction f_r usually equals f_{LM}, but is decreased by some factor f_{nr}, which expresses gamma counts that are non-resonant. Then, the altered transmitted radiation is given by $I'(v) = 1 - f_r + f_r I(v)$, with $I(v)$ from Eq. (3.12).

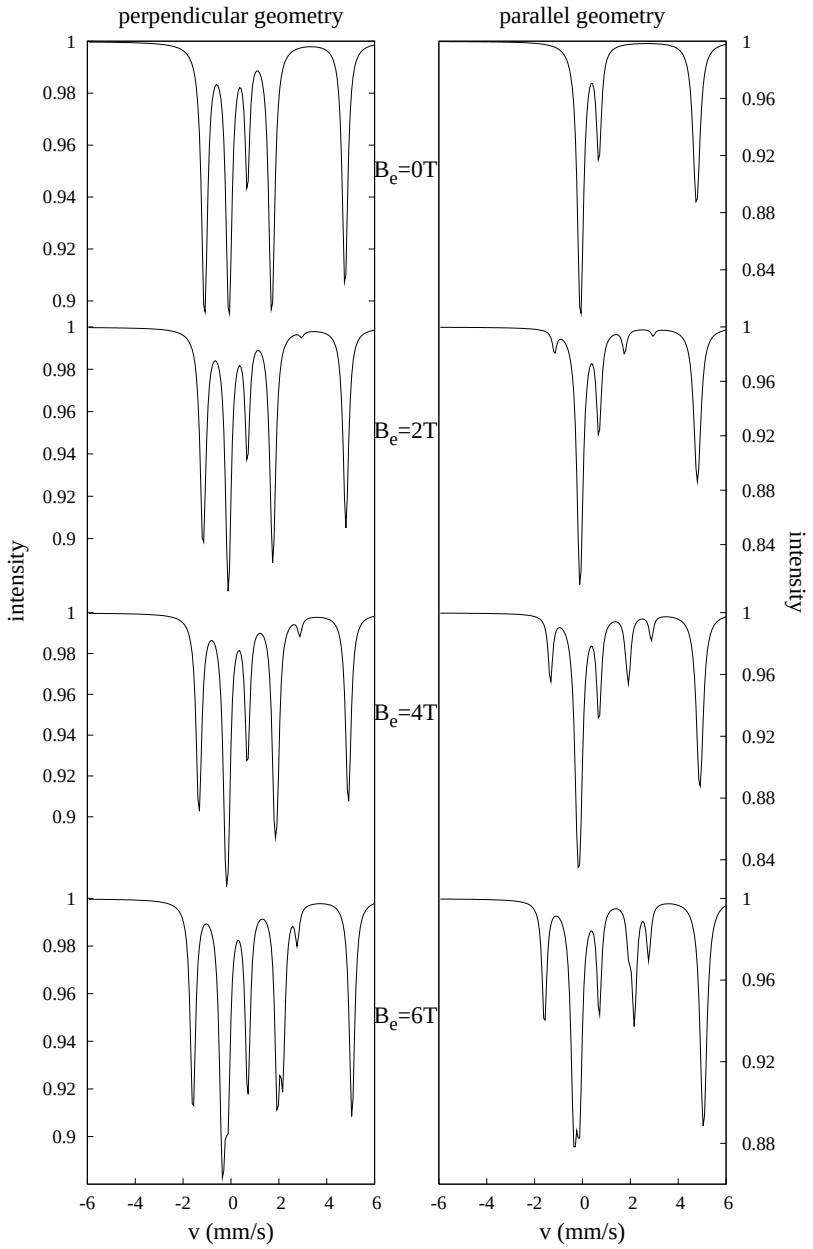

Figure 3.6: Simulation of the transmitted radiation in perpendicular and parallel geometry for different values of a magnetic field B_e perpendicular to the z-axis of the efg (see Fig. 1.5 for the geometry corresponding to this case).

The influence of B_e on the amount of absorption at the level crossing is only significant when $B_e > 4\,\mathrm{T}$. If we calculate the perpendicular component of the magnetic field necessary to resolve the mixed levels ($E_{-\frac{\tilde{3}}{2}} - E_{\frac{\tilde{1}}{2}} = 2\gamma$)[7] using Eq. (1.28), we find that $B_e \geq 11.2\,\mathrm{T}$. From diagonalizing the full Hamiltonian, however, we find that $B_e \geq 5.6\,\mathrm{T}$. The discrepancy is due to the two-level approximation of Eq. (1.28), which is no longer valid for these high values of B_e. Indeed, in Fig. 3.6 and for $B_e = 6\,\mathrm{T}$ the splitting of the mixed levels is resolved.
From these simulations, it is clear that a non-collinear component of the hyperfine field, *e.g.* due to impurities, is not consistent with the experimental data. No additional absorption lines were observed, except in the experiment where an external magnetic field was applied, which validates these simulations. Moreover, to explain the reduction in absorption quantitatively, one should assume a very large noncollinear component, which is not straightforward from the point of view of originating from impurities.

Simulations at the level crossing with a non-axial efg

As the hypothesis of a magnetic mixing interaction is refuted, we now turn to a more plausible candidate. Simulations in the parallel geometry for different values of η and for effective thicknesses of $\mathrm{T}_e = 1, 3, 8$ and 25 are shown in Fig. 3.7 and 3.8 respectively. The right part of the figure shows the transmitted radiation that has changed polarization ($I^{+-} + I^{-+}$) and the radiation that has kept its polarization ($I^{++} + I^{--}$) separately. It must be noted that, in the presentation of the simulations of $I^{+-} + I^{-+}$, we have adjusted the baseline such that they are easily combined with the presentation of $I^{++} + I^{--}$. The real baseline of the $I^{+-} + I^{-+}$ contributions is of course zero. This artificial modification is applied in the remainder of this thesis.
Because it is assumed that a non-axial efg lies at the origin of the mixing interaction, $\Omega = \gamma$ corresponds to $\eta = \gamma/(\sqrt{3}\omega_Q) = 0.149$.

From the simulations, the following observations can be made:

- The overall absorption increases with thickness and saturates at higher thicknesses. Saturation is clearly seen when comparing the spectra for $\mathrm{T}_e = 8$ and $\mathrm{T}_e = 25$. There is little increase in the heights of the absorption peaks, but instead, the absorption lines broaden.

- The presence of a mixing interaction only influences the absorption at the crossing levels, which is unlike the magnetic mixing interaction of

[7] We use 2γ because this is the minimal line width of the convoluted spectrum.

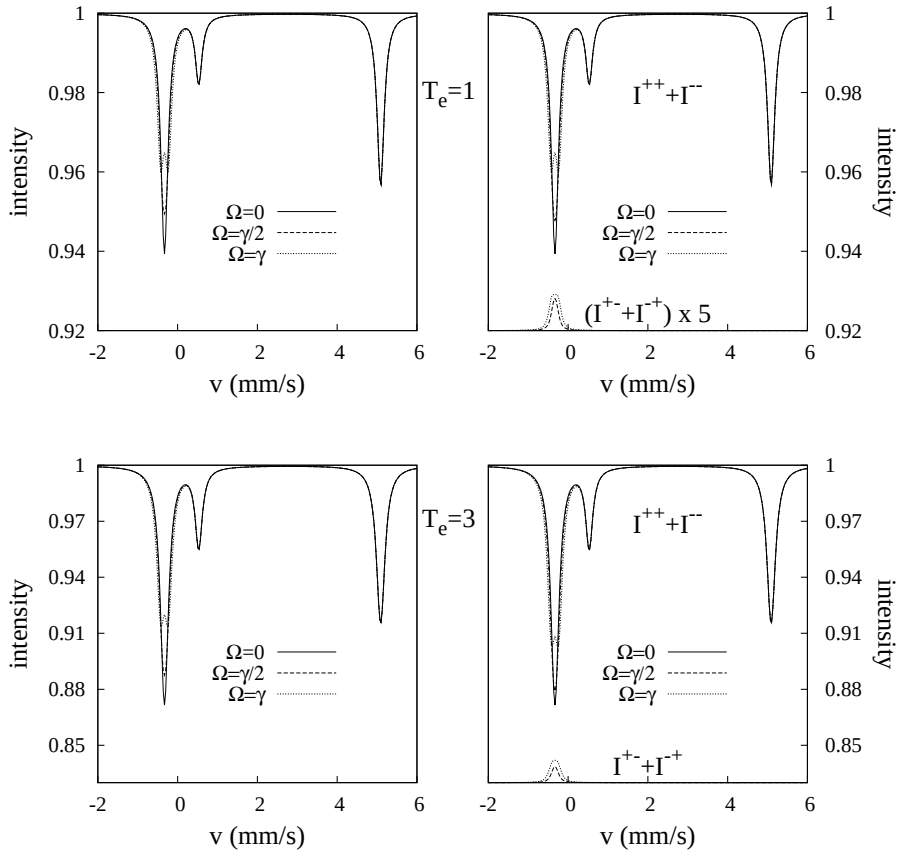

Figure 3.7: Simulated Mössbauer spectra in the parallel geometry for $T_e = 1$ (top) and $T_e = 3$ (bottom) for different values of mixing interaction strength Ω. The right figure shows the individual contributions of the transmitted radiation that has changed polarization ($I^{+-} + I^{-+}$) and the radiation that has kept its polarization ($I^{++} + I^{--}$), while the left figure shows the total transmitted radiation.

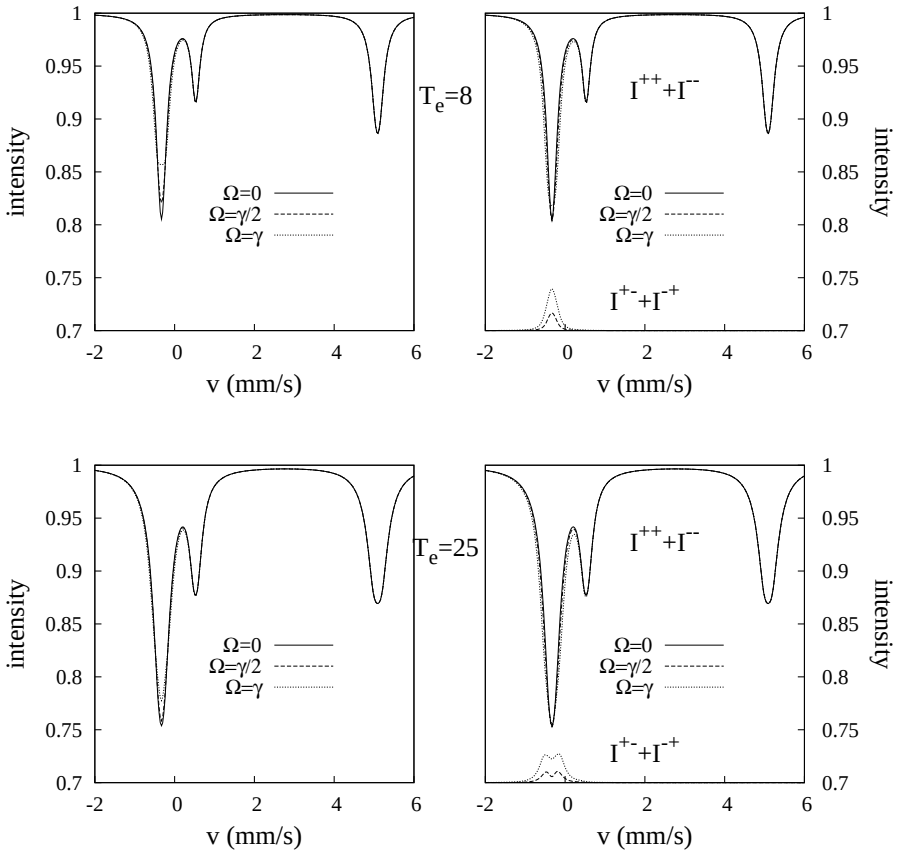

Figure 3.8: Simulated Mössbauer spectra in the parallel geometry for $T_e = 8$ (top) and $T_e = 25$ (bottom) for different values of mixing interaction strength Ω. The right figure shows the individual contributions of the transmitted radiation that has changed polarization ($I^{+-} + I^{-+}$) and the radiation that has kept its polarization ($I^{++} + I^{--}$), while the left figure shows the total transmitted radiation.

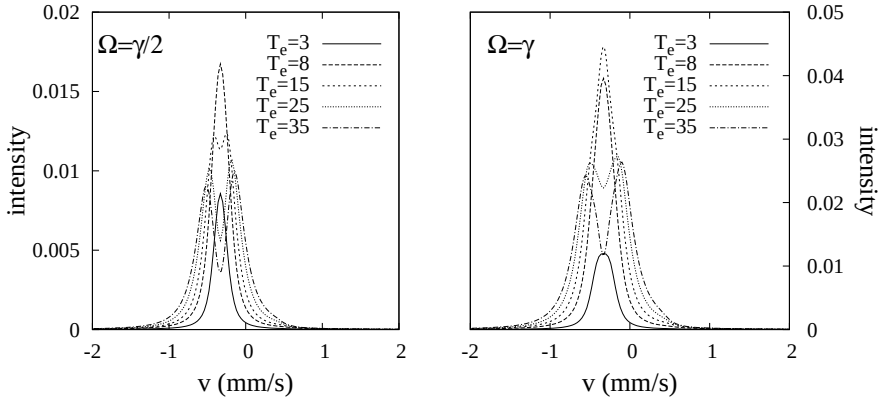

Figure 3.9: Simulation of the transmitted radiation that has changed polarization ($I^{+-} + I^{-+}$) for different absorber thicknesses T_e and for two values of the mixing interaction strength Ω.

the previous section. Here, the non-axial part of the (efg) Hamiltonian only induces transition between the $|m_e = -3/2\rangle$ and $|m_e = 1/2\rangle$ states. Because of the large energy difference, the mixing between the $|m_e = 3/2\rangle$ and $|m_e = -1/2\rangle$ states is negligible for small η.

- The turning on of the mixing interaction reduces the absorption at the crossing levels. For $T_e = 1$ and $T_e = 3$ this reduction is mainly due to the reduction of the $I^{++} + I^{--}$ contribution to the spectrum, whereas for higher thicknesses the $I^{+-} + I^{-+}$ contribution is responsible for the reduction. The latter has an upward peak orientation because, due to its changed polarization, it does not interfere any more with the incoming radiation. Therefore, an increase in $I^{+-} + I^{-+}$ results in a decrease of the total absorption.

- For $T_e = 25$ a two peak structure appears in $I^{+-} + I^{-+}$. A more detailed simulation of the $I^{+-} + I^{-+}$ transmitted radiation is presented in Fig. 3.9 for different thicknesses. For both values of Ω, the two peak structure arises when the thickness increases, although it first appears for $\Omega = \gamma/2$. More simulations for different values of Ω have made clear that the amount of peak splitting does not depend[8] on Ω, but rather on T_e. This bears a close resemblance with the double hump structure known in nuclear resonant scattering with synchrotron radiation [102, 109].

[8] Of course, Ω should be larger than zero, in order to have a change in polarization.

3.1.3 Fit procedure

We have adapted our Fortran computer code in order to be able to fit the experimental data to the theoretical line shape obtained in the Blume-Kistner model. The fit procedure is based on the maximum likelihood method, see *e.g.* [110]. We assume that the probability distribution of the data obtained is Gaussian. Then, the best fit $f(\mathbf{a}, i)$ to the data is found by minimizing the χ^2 function:

$$\chi^2 = \sum_i \frac{\left(f(\mathbf{a}, i) - c_i\right)^2}{\sigma_i^2}, \tag{3.27}$$

with $\mathbf{a} = (a_1, a_2, ..., a_n)$ the n variable fit parameters, c_i the number of counts and σ_i^2 the variance of measurement i (here: channel i). The variance can be estimated by the statistical error $\epsilon_i = \sqrt{c_i}$, such that $\sigma_i^2 = \epsilon_i^2 = c_i$.
The error analysis is performed through the reduced χ^2, χ_r^2, which is found by dividing χ^2 by the degrees of freedom. A model is a good hypothesis for a given set of data provided that $\chi_{r,min}^2 \approx 1$. The error σ_{a_j} on the value of a model parameter a_j is then calculated as a 1σ standard deviation by finding a fit $f(a_1, ..., a_j \pm \sigma_{a_j}, ..., a_n, i)$ such that

$$\chi_r^2 = \chi_{r,min}^2 + 1. \tag{3.28}$$

However, in the following fits we obtain a value for $\chi_{r,min}^2$ that is larger than unity. This can point to two problems. Either, the theoretical model does not provide a good hypothesis of the experimental data. Or, the estimated error is too small. One should of course, to some extent, trust the theoretical model, and therefore, we adjust the estimated error by multiplying σ_i^2 with $\chi_{r,min}^2$. This has as a consequence that, for the estimation of the errors, the 1 in Eq. (3.28) is replaced by $\chi_{r,min}^2$. Hence, this approach will yield higher errors on the estimated parameters.

The fit program has 9 variables: the isomer shift IS, the efg splitting Δ (defined in Eq. (1.34)), the efg asymmetry parameter η, the magnetic splitting of the excited state β_e (defined in Eq. (1.35)), the effective thickness T_e, the resonant fraction f_r and three line broadening factors q_i. The q_i factors [111] are multiplied with the line width γ in the denominator of the forward scattering amplitude $\widetilde{f}(\omega)$. q_1 belongs to the $(3/2, 1/2) - (-3/2, -1/2)$ doublet, q_2 to the $(1/2, 1/2) - (-1/2, -1/2)$ doublet and q_3 to the $(1/2, -1/2) - (-1/2, 1/2)$ doublet. Along with these variable parameters, the spherical angles (θ, ϕ), which describe the wave vector of the incident radiation in the nuclear coordinate system, and the value of an applied perpendicular magnetic field, B_e, can be modified according to the experimental settings. The baseline of the spectrum is not a fit parameter because the program automatically adjusts the scale of the theoretical spectrum to that of the experimental spectrum.

Instead of showing the fit results of all experimental spectra, we only highlight the ones most relevant to our study. In Fig. 3.10, 3.13 and 3.14 we present the fitted spectra of the $T_e = 8$ $FeCO_3$ absorber at room temperature (RT) and $T = 31\,K$, with and without mixing, respectively. The values of the parameters obtained from these fits are presented in table 3.1.

3.1.4 Fit of $T_e = 8$, at RT, no external magnetic field

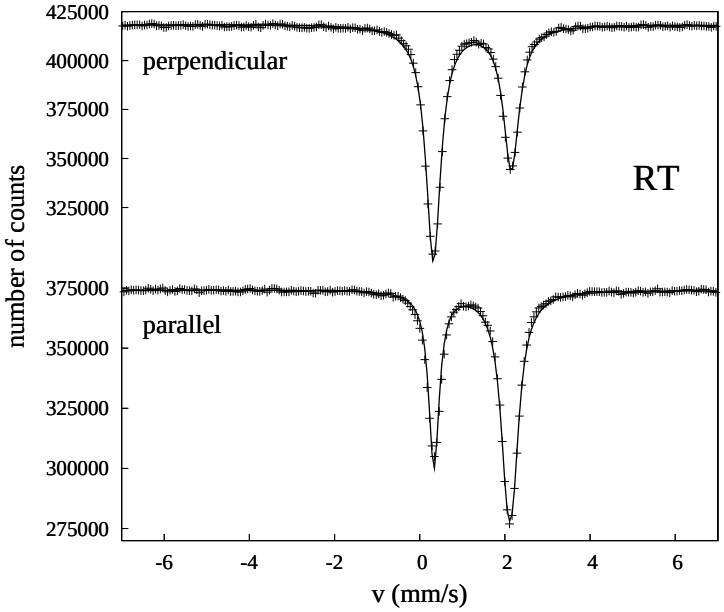

Figure 3.10: Mössbauer spectra of $FeCO_3$ at room temperature, with the solid line giving the best fit based on the Blume-Kistner semiclassical model.

For RT, Fig. 3.10 shows an excellent fit of the data. This is a little surprising in this respect that, as discussed in section 1.3.2, the deduced area ratio A_π/A_σ considerably deviates from the theoretical curve in Fig. 1.9. Moreover, by a series of simulations with the theoretical model, we have checked that our model indeed predicts the same area ratio curve as obtained in [52]. So, the most obvious reason for this discrepancy is that the area ratio obtained from the Lorentzian fit is either incorrect or should bear much larger error bars. It is clear that the Lorentzian line shape is only correct for very thin absorbers. A small deviation of the theoretical line shape from the actual line shape can

have very large effects for the calculation of the area. To illustrate this we refer to the fact that half of the area of a Lorentzian curve is found under its wings. Thus, a good fit of the 'peak part' does not necessarily mean a good fit of the entire line shape. Therefore, we are led to suggest that the area ratios of section 1.3.2 should only be considered as a crude approximation and that a good fit within our model yields a much better proof of the validity of both the theoretical area ratio curve *and* the experimental results.
The deduced values of the isomer shift and the quadrupole splitting agree with the results obtained from the Lorentzian fit. The only difference is that we now obtain much larger errors (×10), which certainly are more realistic.

Table 3.1: Values obtained from fitting the $FeCO_3$ Mössbauer spectra to the Blume-Kistner semiclassical model.

temperature	RT		31 K			
θ	0	$\pi/2$	0	$\pi/2$	0	$\pi/2$
η	-	-	-	-	0.07(1)	0.07(1)
IS (mm/s)	1.23(1)	1.24(1)	1.32(1)	1.34(1)	1.34(1)	1.36(2)
Δ (mm/s)	1.78(4)	1.79(4)	2.08(9)	2.03(8)	2.04(6)	2.07(6)
β_e (mm/s)	0	0	1.03(2)	1.02(2)	1.02(1)	1.01(2)
T_e	19(12)	18(9)	32(15)	75(24)	40(18)	20(17)
f_r	0.3(1)	0.4(1)	0.6(2)	0.2(2)	0.5(2)	0.4(2)
q_1	2.4(1)	2.1(2)	3.2(4)	2.4(3)	3.0(3)	3.2(4)
q_2	-	1.8(3)	-	2.2(5)	-	2.9(6)
q_3	2.1(2)	2.3(3)	3.1(4)	1.7(3)	2.1(3)	1.9(4)
$\chi^2_{r,min}$	3.8	3.2	11.6	5.8	7.6	8.9

Anomalous line broadening

It was also noted in section 1.3.2 that the deduced values of the line (half) widths Γ_σ and Γ_π for both geometries could not be consistently explained. The q values obtained in these new fits can not really shed some light on this issue either. However, if we make a series of simulations[9] as a function of effective absorber thickness and deduce the line widths of the absorption lines, then the experimentally observed behavior is very well reproduced. In Fig. 3.11, for small thicknesses, the line width of both absorption lines equals the minimal, and thus natural, line width[10]. With increasing thickness, all line widths also increase, which is a clear saturation effect. However, it is seen that the *slope* of the saturation curves depends on the details of the absorption resonance. This can be understood as follows. It is obvious that the amount of line broadening depends on how close the absorption line approaches the maximal absorption. Now, both this 'closeness' and the maximal absorption can be different for the different absorption lines. Let us first consider the simplest case, *i.e.* the parallel geometry. Both σ^+ and σ^- incident radiation can be absorbed by the transitions belonging to the π and the σ absorption line, which means that they have equal maximal absorption. From the different interaction strengths, $|C_\pi|^2 = 1$ and $|C_\sigma|^2 = 1/3$ respectively, we know that, for the same thickness, the π line is closer to this maximal absorption, and thus will show a larger line broadening than the σ line. Hence, they experience a 'regular' broadening pattern.

In this parallel geometry, it is also possible to derive an analytical expression for the line widths as a function of T_e. Using Eq. (3.9), with $a = d$ and $b = c = 0$, we find that

$$\Gamma_{HWHM} = \frac{\gamma}{2}\sqrt{1 + \frac{3T_e|C|^2}{4\ln\frac{2}{1+e^{-\frac{3T_e|C|^2}{4}}}}}. \tag{3.29}$$

For large T_e, Γ_{HWHM} can be approximated by

$$\Gamma_{HWHM} \approx \frac{\gamma}{2}\sqrt{1 + \frac{3T_e|C|^2}{4\ln 2}} \tag{3.30}$$

which yields the simulated $\sqrt{T_e}$-dependence as illustrated in Fig. 3.11. By differentiating this expression, we also find that the slope $d\Gamma/dT_e$ is proportional to $|C_i|^2$, as expected from the intuitive approach.

[9] In these simulations, all q values are chosen 1.

[10] Actually, due the convolution with the incident radiation spectrum the minimal $FWHM$ equals twice the natural line width. But here, the HWHM are considered.

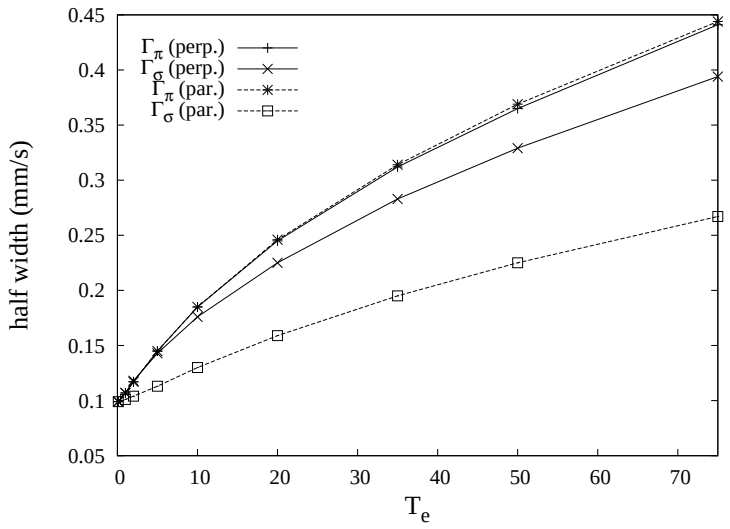

Figure 3.11: Calculated widths of the quadrupole absorption lines π and σ as a function of absorber effective thickness and for perpendicular and parallel geometry.

As seen in Fig. 3.11 for the perpendicular geometry, for small T_e, although the π and the σ absorption line have different interaction strengths, $\sum_i |C_{\pi,i}|^2 = 1/2$ and $\sum_i |C_{\sigma,i}|^2 = 5/6$ respectively, they show an equal line broadening. So, they behave as if they 'feel' a different maximal absorption. The slope $d\Gamma/dT_e$ of the σ line then gradually decreases with increasing N, with respect to the π line. This behavior is completely different from the parallel case. An answer can be found by looking at the contributions to the spectrum of the radiation that has changed polarization, $I^{+-} + I^{-+}$, and the radiation that has the same polarization as the incident radiation, $I^{++} + I^{--}$, separately. In Fig. 3.12, it is seen that the broadening of the π and σ lines of the $I^{++} + I^{--}$ contribution behaves quite similar to the parallel case. But, for the π line, $I^{+-} + I^{-+}$ pushes the total intensity upward, mainly at the line center, whereas for the σ line it shows a double hump structure with a smaller center intensity. This gives rise to a less increasing line width of the σ line with respect to the π line. As a consequence, it is seen that the π line has a maximal absorption that is about half of that of the σ line.

We admit that the above expose provides us only with a mere heuristic understanding of the anomalous behavior of the π line width. Closer examination of Eq. (3.9) for the perpendicular case reveals that the total transmitted

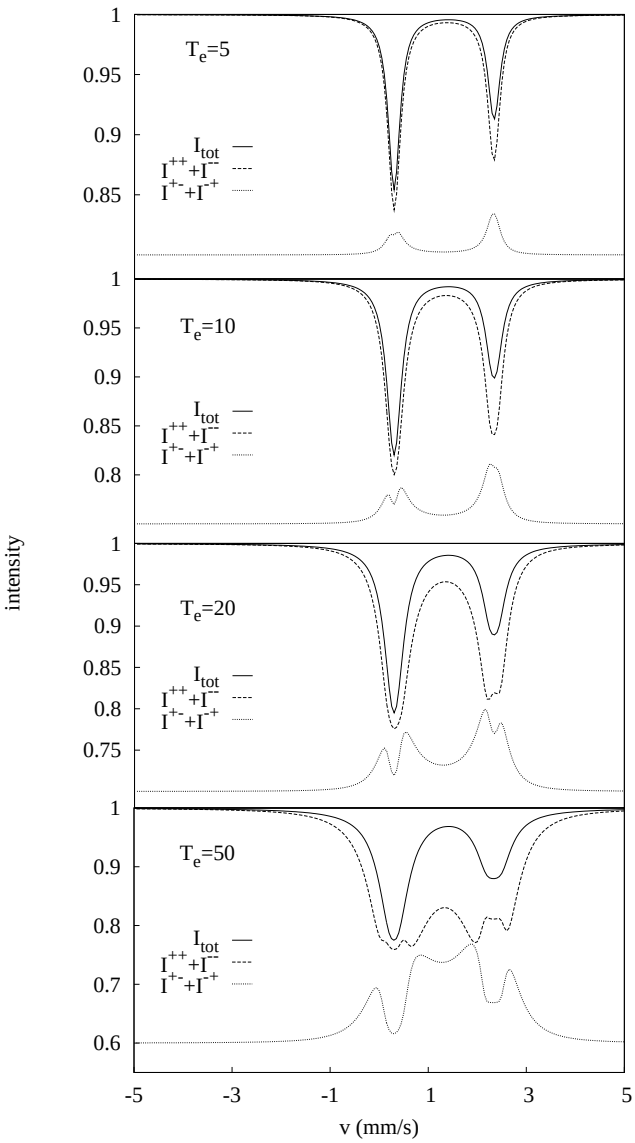

Figure 3.12: Simulations of the Mössbauer transmitted intensity for different effective thickness T_e, in the perpendicular geometry and at room temperature.

intensity at the line center can be written as

$$I_{tot,\pi}(\delta = 0) = \frac{1}{2}\left(1 + e^{-\frac{3T_e|C^{++}|^2}{8}}\right) \tag{3.31}$$

for the π line and

$$I_{tot,\sigma}(\delta = 0) = \frac{1}{2}\left(e^{-\frac{3T_e\left(|C^{++}|^2+|C^{+-}|^2\right)}{16}} + e^{-\frac{3T_e\left(|C^{++}|^2-|C^{+-}|^2\right)}{16}}\right) \tag{3.32}$$

for the σ line. This difference stems from the fact that the interaction strengths for scattering with change ($|C^{+-}|^2$) and without change ($|C^{++}|^2$) of polarization are equal for the π line, while they are not for the σ line. From the above expressions, it is clear that the maximal absorption ($T_e \to \infty$) for the π line is exactly one half of that of the σ line, leading to a stronger saturation line broadening in the former case.
Notice the importance of the inclusion of the polarization dependent terms. For a correct understanding of the line broadening behavior one not only needs a model that takes into account the absorber thickness but the polarization must also be considered.

3.1.5 Fit of $T_e = 8$, $T = 31$ K, no external magnetic field

We have analyzed the Mössbauer spectra at $T_c \approx 31$ K in two ways, with $\eta = 0$ and with a variable η, as shown in Fig. 3.13 and Fig. 3.14 respectively. The parameter values of the fit are summarized in table 3.1. In the first case ($\eta = 0$) we are able to make a reasonably good fit of the data in the perpendicular geometry ($\chi^2_{r,min}$=5.8), but the parallel case is not well reproduced[11]. This means that saturation, as explained in section 1.4, can account for the reduced absorption in the perpendicular geometry, but clearly does not provide an answer for the reduction in the parallel geometry. It must be noted, however, that the best fit for $\theta = \pi/2$ yields an effective thickness $T_e = 75(24)$, which is a factor 10 larger than expected. So, apparently more thickness saturation is needed in order to obtain a good fit, which, nevertheless, points to a shortcoming in the model used.

In the second fit analysis, we allow η to vary such that χ^2 is minimized for both geometries simultaneously. This method yields $\eta = 0.07(1)$. Both

[11] Note that the misfit is now equally distributed over all absorption lines, whereas in the Lorentzian fit we can force the fit such that most of the misfit is located on the level crossing lines.

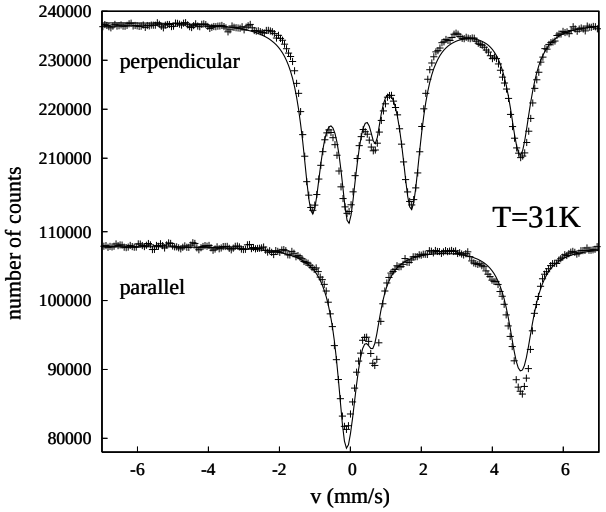

Figure 3.13: Mössbauer spectra of $FeCO_3$ at $T = 31\,\mathrm{K}$, with the solid line giving the best fit based on the Blume-Kistner semiclassical model with $\eta = 0$.

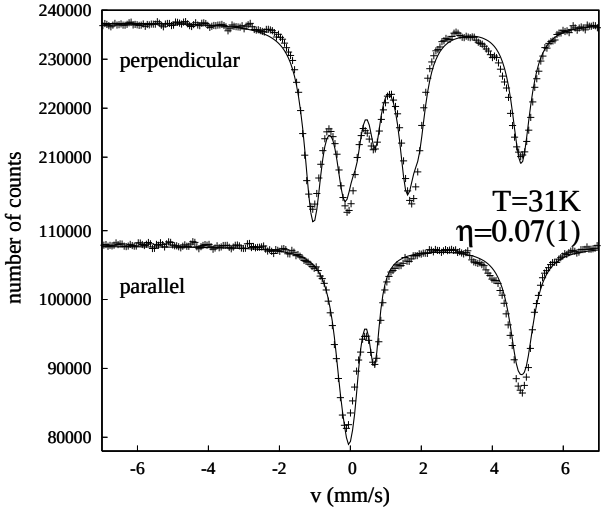

Figure 3.14: Mössbauer spectra of $FeCO_3$ at $T = 31\,\mathrm{K}$, with the solid line giving the best fit based on the Blume-Kistner semiclassical model with η as a free fit parameter.

from Fig. 3.14 and from the $\chi^2_{r,min}$ values, we see that the fit for the parallel geometry has improved at the expense of the fit for the perpendicular geometry. This is mainly due to the level mixing effect on the $(1/2, 1/2)$ transition (located at $v \approx 1.6\,\mathrm{mm/s}$). We must conclude that the model developed at this stage does not succeed in providing a consistent explanation for the data in *both* geometries.
Notice that the deduced values for T_e and f_r have quite large errors. Because both variables can alter the heights of the absorption peaks, they are correlated in the fit procedure. An increase in T_e and a decrease of f_r only yields a small change in the simulated spectrum and hence in $\chi^2_{r,min}$. This can be remedied, of course, by fixing T_e at its expected value $\mathrm{T}_e = 8$. In this case, we find slightly higher values of $\chi^2_{r,min}$ ($\approx 10\%$ higher) and values of $f_r \approx 0.6$ with almost half of the previous error.

3.1.6 Fit of $\mathrm{T}_e = 8$, with external magnetic field

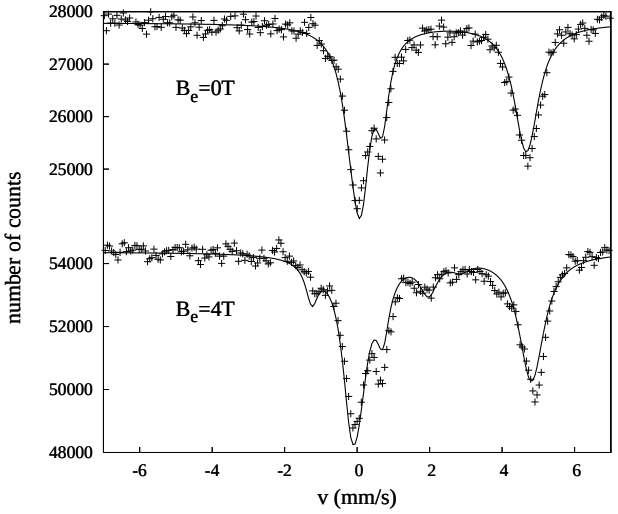

Figure 3.15: Mössbauer spectra of $FeCO_3$ in the parallel geometry at $T = 31\,\mathrm{K}$ with an externally applied magnetic field B_e. The solid line gives the best fit based on the Blume-Kistner semiclassical model.

We have first made a fit of the spectrum without external magnetic field, as shown in the top part of Fig. 3.15. Although the fit does not seem very good, we obtain $\chi^2_{r,min} = 1.5$, mainly because the low number of counts yields larger

(relative) errors. In the case of $B_e = 4\,\mathrm{T}$, except of the q-factors, all variables are fixed to the values obtained in the $B_e = 0\,\mathrm{T}$ fit. This gives $\chi^2_{r,min} = 2.1$. Considering the low statistics, the additional absorption lines at $v \approx -1\mathrm{mm/s}$ and $v \approx +2\,\mathrm{mm/s}$ are nicely reproduced. The line widths have increased by no more than 15%, which means the applied magnetic field at each ^{57}Fe is quite uniform.

3.1.7 The phase problem

As already weakly introduced in section 2.1.1, we would now like to settle the 'phase problem' in a conclusive way. The phase problem arises because the proposed mixing interaction in the $FeCO_3$ system originates from impurities in the crystal structure. It has been argued that the presence of these inhomogeneities is very likely and some evidence was presented in section 1.1. But we should, of course, answer the question whether random impurities can give rise to an observable mixing interaction.

Let us consider the case of one particular lattice site, where the efg is non-axially symmetric. In its local PAS the spherical components of the efg tensor operator are given by $\langle V^2_0\rangle = \frac{1}{2}V_{zz}$ and $\langle V^2_{\pm 2}\rangle = \frac{1}{2\sqrt{6}}\eta V_{zz}$, where the brackets mean that the operators are evaluated in electron space. Now we want to express these components in a fixed lab system (LAB). It does not matter what this LAB system is, as long as it is well-defined and fixed. If the PAS coordinate system is specified in this LAB system by the Euler angles (γ, β, α), then the transformation of any tensor from PAS to LAB is given by Eq. (1.8). As we are only interested in the quadrupole interaction terms that can mix the $|-3/2\rangle$ and $|1/2\rangle$ states, *i.e.* the terms containing $\hat{I}^2_{\pm}$, we limit this discussion to the $q = \pm 2$ terms of the Hamiltonian given in Eq. (1.7). Therefore, we calculate the $\langle V^2_{\pm 2}\rangle$ terms in the LAB system:

$$\langle V^2_{\pm 2}\rangle_{LAB} = \sum_{q'} D^n_{q'q}(-\alpha, -\beta, -\gamma)\langle V^2_{q'}\rangle_{PAS} \tag{3.33}$$

which yields

$$\begin{aligned}\langle V^2_{\pm 2}\rangle_{LAB} \;=\; & \frac{e^{\pm 2i\gamma}}{4}\Big[\sqrt{6}\sin^2\beta\langle V^2_0\rangle_{PAS} + (1 \pm \cos\beta)^2 e^{2i\alpha}\langle V^2_2\rangle_{PAS} \\ & + (1 \mp \cos\beta)^2 e^{-2i\alpha}\langle V^2_{-2}\rangle_{PAS}\Big]. \end{aligned}\tag{3.34}$$

The γ-dependence can be completely removed by applying a suitable unitary transformation. If we now *assume* that the z-axis of the PAS coincides with the z-axis of the LAB, then $\beta = 0$ and $\langle V^2_{\pm 2}\rangle_{LAB} = e^{\pm 2i\alpha}\langle V^2_{\pm 2}\rangle_{PAS}$. It can also be shown that in this case $\langle V^2_0\rangle_{LAB} = \langle V^2_0\rangle_{PAS}$ and $\langle V^2_{\pm 1}\rangle_{LAB} = 0$. This means

that, if we go from site to site, we only allow the orientation of the non-axial component in the x-y plane to change (parameterized by the angle α). In the final expression we then should average over this random α.
If we combine the above expressions with the proper nuclear quadrupole tensor components, the resulting quadrupole Hamiltonian is written as:

$$H_Q = \frac{eQV_{zz}}{4I(2I-1)\hbar^2}\left[\left(3\hat{I}_z^2 - \hat{I}^2\right) + \frac{\eta}{2}\left(\hat{I}_+^2 e^{2i\alpha} + \hat{I}_-^2 e^{-2i\alpha}\right)\right], \tag{3.35}$$

where all parameters have been defined before. The α-dependence appears in a very similar way as in the Hamiltonian of Eq. (1.10), where the magnetic field was defined by its Euler angles $(\alpha, \beta, 0)$ in the PAS of the efg. In both cases, the part of the Hamiltonian that describes the mixing interaction gains a phase factor.
At the level crossing, the eigenstates of the nuclear Hamiltonian are now given by

$$\left|-\widetilde{\frac{3}{2}}\right\rangle = \frac{1}{\sqrt{2}}\left(e^{2i\alpha}\left|-\frac{3}{2}\right\rangle + \left|\frac{1}{2}\right\rangle\right), \tag{3.36}$$

$$\left|\widetilde{\frac{1}{2}}\right\rangle = \frac{1}{\sqrt{2}}\left(e^{2i\alpha}\left|-\frac{3}{2}\right\rangle - \left|\frac{1}{2}\right\rangle\right). \tag{3.37}$$

while the energies of these eigenstates remain unchanged, and therefore $E_{-\widetilde{\frac{3}{2}}} - E_{\widetilde{\frac{1}{2}}} = 2\sqrt{3}\eta\hbar\omega_Q$ is still valid. If we substitute these α-dependent states in expression Eq. (3.13) of the forward scattering amplitude in the three-level approximation, we obtain

$$f^{++}(\omega) \propto \frac{|\mu_{21}|^2}{2} L_+(\omega) \qquad f^{--}(\omega) \propto \frac{|\mu_{31}|^2}{2} L_+(\omega) \tag{3.38}$$

$$f^{+-}(\omega) \propto \frac{\mu_{21}\mu_{13}}{2} e^{2i(\alpha-\phi)} L_-(\omega) \qquad f^{-+}(\omega) \propto \frac{\mu_{31}\mu_{12}}{2} e^{-2i(\alpha-\phi)} L_-(\omega) \tag{3.39}$$

Because the nuclear Hamiltonian in the LAB system has no axial symmetry, the transformation of the radiation coordinate system to the LAB system includes the azimuthal angle ϕ. In the above expressions the ϕ-dependence is written explicitly, such that μ_{ij} is no longer ϕ-dependent. This results in a phase factor with angle $\alpha - \phi$ for $f^{+-}(\omega)$ and $f^{-+}(\omega)$. It is important to note that the denominators of $f^{+-}(\omega)$ and $f^{-+}(\omega)$ are related by complex conjugation, as expected from their definition in Eq. (3.4) and Eq. (3.6).
In the scattering matrix $\widetilde{S}(\omega)$, $f^{+-}(\omega)$ and $f^{-+}(\omega)$ appear only once separately, *i.e.* as front factor in $S^{+-}(\omega)$ and $S^{-+}(\omega)$, respectively. Because in

this work we deal with an unpolarized source of radiation, Eq. (3.12) holds and therefore, in its unconvoluted form, the intensity of the radiation that has changed polarization is given by

$$I^{\pm\mp}(\omega) = |S^{\pm\mp}(\omega)|^2 = |f^{\pm\mp}(\omega)|^2 |S_0^{\pm\mp}(\omega)|^2 \tag{3.40}$$

with $S_0^{\pm\mp}(\omega) = S^{\pm\mp}(\omega)/f^{\pm\mp}(\omega)$ and thus not containing $f^{\pm\mp}(\omega)$ any more. In all other cases, only their product $f^{+-}(\omega)f^{-+}(\omega) = |f^{+-}(\omega)|^2$ is considered (in the expression of D). Therefore, in both cases, the phase dependence disappears.
In summary, we have shown that phase factors do appear when a mixing interaction originates from a random, non-axial component. Moreover, they completely vanish from the final expression of the (measurable) intensity. So, all previously obtained results for a non-random mixing interaction equally hold for a random interaction.

Notice that we have only considered a variation in the *orientation* of the non-axial component in the $x-y$ plane. If also the magnitude of this component varies from site to site, then the average over a certain η-distribution should be taken. As we are dealing with inhomogeneities, a Gaussian distribution is most adequate. This is taken into account in the fit program as described in section 3.2.5.

3.2 Maxwell-Schrödinger approach

This approach first implies the calculation of the macroscopic polarization $P(z,t)$, which is the medium's reaction to the electromagnetic field. The density matrix formalism is used to facilitate the statistical summations involved in obtaining $P(z,t)$ from the microscopic dipole moments.

3.2.1 Density matrix

According to a postulate of quantum mechanics, there exists a state vector $|\psi\rangle$ that contains all possible information about the system. Typically, however, we do not know if the system is described by $|\psi_i\rangle$, but we only know the probability P_{ψ_i} that the system is described by $|\psi_i\rangle$. Therefore, in order to find the expectation value of some observable O, an ensemble average must be performed: $\langle O\rangle = \mathrm{Tr}\,(\hat{\rho}O)$ with

$$\hat{\rho} = \sum_i P_{\psi_i} |\psi_i\rangle\langle\psi_i| \tag{3.41}$$

the density operator. It is convenient to express $\hat{\rho}$ in a complete set of basis states $\{|\phi_m\rangle\}$:

$$\hat{\rho} = \sum_i P_{\psi_i} \sum_{m,n} c_{mi} c_{ni}^* |\phi_m\rangle\langle\phi_n|, \tag{3.42}$$

with $\{c_{mi} = \langle\phi_m|\psi_i\rangle\}$ the expansion coefficients of $|\psi_i\rangle$ in $\{|\phi_m\rangle\}$. In this basis, the elements of the corresponding *density matrix* are defined by

$$\rho_{mn} = \langle\phi_m|\hat{\rho}|\phi_n\rangle = \sum_i P_{\psi_i} c_{mi} c_{ni}^*. \tag{3.43}$$

From the Schrödinger equation we can obtain the equation of motion for the density matrix operator:

$$\dot{\hat{\rho}} = -\frac{i}{\hbar}[H, \hat{\rho}] \tag{3.44}$$

This equation is sometimes called the Liouville or Von Neumann equation of motion.
At this point $\hat{\rho}$ still describes the total system, *i.e.* the nuclear-radiation system, and thus, also includes radiative decay of the nuclear states. However, one usually limits the density matrix states to the nuclear states (by taking the trace over the radiative ensemble) and then adds decay terms to Eq. (3.44) in a phenomenological way [112]:

$$\dot{\hat{\rho}} = -\frac{i}{\hbar}[H, \hat{\rho}] - \widehat{\Gamma}\hat{\rho}, \tag{3.45}$$

with $\widehat{\Gamma}$ a linear operator expressing all possible relaxations. In the case where only decay through spontaneous emission is important (incoherent population transfer), the explicit form of the incoherent part of the Liouville equation in terms of matrix elements is given by

$$\widehat{\Gamma}\rho_{mm} = \sum_k \gamma_{mk}\rho_{mm} + \sum_k \gamma_{km}\rho_{kk} \tag{3.46}$$

for the diagonal elements (the populations) and

$$\widehat{\Gamma}\rho_{mn} = \frac{1}{2}\sum_k (\gamma_{mk} + \gamma_{nk})\,\rho_{mn} \tag{3.47}$$

for the non-diagonal elements (the coherences), with γ_{mk} the decay rate from $|\phi_m\rangle$ to $|\phi_k\rangle$.

3.2.2 Three-level system in the parallel geometry

Let us now apply this density matrix approach to the three levels involved in the level crossing/level mixing transition, *i.e.* the $|m_g = -1/2\rangle \equiv |1\rangle$ ground state and the $|m_e = 1/2 \equiv |2\rangle$ and $|m_e = -3/2\rangle \equiv |3\rangle$ excited states. According to the selection rules for the parallel geometry, σ^+ polarized radiation (V_+) can induce a $(2,1)$ transition, whereas σ^- polarized radiation (V_-) induces a $(3,1)$ transition. We also include a mixing interaction (Ω) that allows for a $(2,3)$ transition. The basic ingredients of this three-level system are summarized in Fig. 3.16.
In [113] the same three-level system is analyzed in a slightly different way. To allow an easy comparison, we follow the same line of reasoning and notation of that paper, wherever possible.

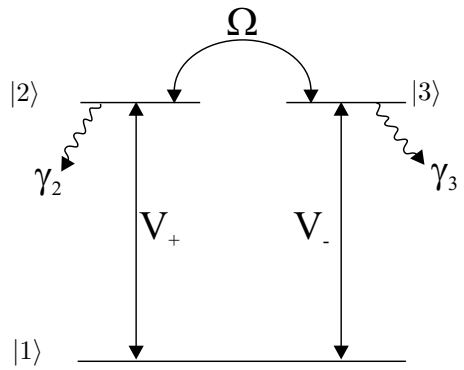

Figure 3.16: Schematical representation of the three-level system under consideration. The two excited states $|2\rangle$ and $|3\rangle$ are mixed by an interaction Ω and couple to the ground state through V_+ and V_-, respectively.

The Hamiltonian H of this system consists of an unperturbed part H_0 (which gives rise to the nuclear m states) and an interaction term:

$$H_1 = \hbar V_+ |2\rangle\langle 1| + \hbar V_- |3\rangle\langle 1| + \hbar\Omega |2\rangle\langle 3| + h.c. \tag{3.48}$$

The 14.4 keV gamma transition in ^{57}Fe is essentially an $M1$ magnetic dipole transition. Hence, the first term describes the interaction of the radiation with the nucleus in the magnetic dipole approximation, with $V_+ = \langle 2|\mathcal{H}^+|1\rangle\mathcal{E}^+(z,t)/2 \equiv \mu_c\mu_{21}\mathcal{E}^+(z,t)/2$ and $V_- = \langle 3|\mathcal{H}^-|1\rangle\mathcal{E}^-(z,t)/2 \equiv \mu_c\mu_{31}\mathcal{E}^-(z,t)/2$, with μ_c a proportionality constant. The magnetic dipole matrix elements are given by Eq. (3.7), for $L = 1$. $\mathcal{E}^+(z,t)$ ($\mathcal{E}^-(z,t)$) is the space- and time-dependent part of the σ^+ (σ^-) polarized (electro)magnetic field.

The third term is a formal expression for the mixing interaction between the crossing levels, where the mixing frequency Ω is a measure of the strength of the mixing. The explicit form of Ω depends on the nature of the interaction. Applying Eq. (3.45), the following set of density matrix equations is obtained:

$$\dot{\rho}_{11} = \gamma\rho_{22} + \gamma\rho_{33} - iV_+(\rho_{21} - \rho_{12}) - iV_-(\rho_{31} - \rho_{13}) \quad (3.49)$$

$$\dot{\rho}_{22} = -\gamma\rho_{22} - iV_+(\rho_{12} - \rho_{21}) - i\Omega(\rho_{32} - \rho_{23}) \quad (3.50)$$

$$\dot{\rho}_{33} = -\gamma\rho_{33} - iV_-(\rho_{13} - \rho_{31}) - i\Omega(\rho_{23} - \rho_{32}) \quad (3.51)$$

$$\dot{\rho}_{21} = \left(-i\omega_0 - \frac{\gamma_2}{2}\right)\rho_{21} + iV_+(\rho_{22} - \rho_{11}) - i\Omega\rho_{31} + iV_-\rho_{23} \quad (3.52)$$

$$\dot{\rho}_{31} = \left(-i\omega_0 - \frac{\gamma_3}{2}\right)\rho_{31} + iV_-(\rho_{33} - \rho_{11}) - i\Omega\rho_{21} + iV_+\rho_{32} \quad (3.53)$$

$$\dot{\rho}_{23} = -\frac{\gamma_2 + \gamma_3}{2}\rho_{23} - iV_+\rho_{13} + iV_-\rho_{21} + i\Omega(\rho_{33} - \rho_{22}) \quad (3.54)$$

with $\omega_0 = \omega_2 - \omega_1$ ($\omega_2 = \omega_3$). The decay of the populations is related to γ, which corresponds to the natural decay rate of the nuclear excited state. The coherences, however, can have different decay rates due to other relaxation phenomena such as phase relaxation by the presence of a fluctuating magnetic hyperfine field. These decay rates are therefore given a different symbol, *i.e.* γ_2 and γ_3 (such that $\gamma_2, \gamma_3 \geq \gamma$).
We are interested in the solution of the ρ_{21} and ρ_{31} coherences since the polarizations of the medium $P_+(z,t) = \mu_c\mu_{12}\rho_{21}$ and $P_-(z,t) = \mu_c\mu_{13}\rho_{31}$ [17]. The equations can be solved analytically in the linear response approximation. This means we consider the response of the medium only to first order in $V_\pm$. This is a good approximation since the interaction of the gamma radiation with the nuclei is small. In practice, it implies that we neglect the change of the populations ρ_{mm}. Instead, they are replaced with their initial values[12] $\rho^0_{11} = 1$ and $\rho^0_{22} = \rho^0_{33} = 0$. Also, since $\rho_{23} \propto V_\pm$ the $iV_-\rho_{23}$-term in the equation for ρ_{21} and the $iV_+\rho_{32}$-term in the equation for ρ_{31} are discarded.
The above set of equations is reduced to two coupled differential equations:

$$\dot{\rho}_{21} = \left(-i\omega_0 - \frac{\gamma}{2}\right)\rho_{21} - iV_+ - i\Omega\rho_{31} \quad (3.55)$$

$$\dot{\rho}_{31} = \left(-i\omega_0 - \frac{\gamma}{2}\right)\rho_{31} - iV_- - i\Omega\rho_{21} \quad (3.56)$$

where we have assumed that $\gamma_2 = \gamma_3 \equiv \gamma$, which is exact if the normal lifetime decay is the only mechanism of relaxation. These differential equations

[12] Actually, only half of the total initial population is in $|1\rangle$ since the other half occupies the $|m_g = 1/2\rangle$ state. As the three-level system is a closed system, we can renormalize the total initial population to the population in $|1\rangle$.

can be simplified to algebraic equations by applying a Fourier transformation according to the recipe:

$$F(\omega) = \int_{-\infty}^{\infty} dt\, f(t) e^{i\omega t}, \tag{3.57}$$

$$f(t) = \frac{1}{2\pi} \int_{-\infty}^{\infty} d\omega\, F(\omega) e^{-i\omega t}. \tag{3.58}$$

The solution for the coherences in frequency domain is now given by

$$\rho_{21}(\omega) = \frac{L_+(\omega)}{2} V_+(\omega) + \frac{L_-}{2}(\omega) V_-(\omega), \tag{3.59}$$

$$\rho_{31}(\omega) = \frac{L_-(\omega)}{2} V_+(\omega) + \frac{L_+}{2}(\omega) V_-(\omega) \tag{3.60}$$

with $L_\pm(\omega)$ defined in Eq. (3.16).
The appropriate wave equations for an electromagnetic field in a reactive medium is given by the Maxwell equations, see *e.g.* [74]. In most applications, however, a simplified version is used by assuming that the field functions slowly vary on the scale of the carrier wavelength λ_c. This is certainly a valid approximation in the case of gamma radiation. In the case of radiation propagating along the z-axis (and thus neglecting variations of the field intensity in the transverse directions), the wave equations are reduced to [114]

$$\left(\frac{\partial}{\partial z} + \frac{n_h}{c} \frac{\partial}{\partial t} \right) \mathcal{E}_\pm(z,t) = \frac{2\pi\omega_c \rho_r}{n_h c} i P_\pm(z,t), \tag{3.61}$$

with n_h the index of refraction of the host material, $\omega_c = c/\lambda_c$ the carrier frequency of the field and ρ_r the concentration of resonant nuclei. After Fourier transforming these wave equations to frequency domain and substituting Eq. (3.59) and (3.60), we find

$$\left(\frac{\partial}{\partial z} - i n_h k \omega \right) \begin{pmatrix} \mathcal{E}_+(z,\omega) \\ \mathcal{E}_-(z,\omega) \end{pmatrix} = i \frac{2\pi k \rho_r}{n_h} \frac{\mu_c^2}{4}$$
$$\times \begin{pmatrix} |\mu_{21}|^2 L_+(\omega) & \mu_{21}\mu_{13} L_-(\omega) \\ \mu_{31}\mu_{12} L_-(\omega) & |\mu_{31}|^2 L_+(\omega) \end{pmatrix} \begin{pmatrix} \mathcal{E}_+(z,\omega) \\ \mathcal{E}_-(z,\omega) \end{pmatrix}. \tag{3.62}$$

The solution of this equation exactly equals the exponential form of Eq. (3.2) with the two-dimensional index of refraction given by Eq. (3.3). There is a one-to-one correspondence with the solution for the amplitude of the transmitted plane wave in the Blume-Kistner model if we choose $n_h = 1$ and

$$\mu_c = \frac{1}{2\pi} \sqrt{\frac{V k T_e \gamma}{2\rho_r \hbar c \gamma_r}}. \tag{3.63}$$

This means that this Maxwell-Schrödinger approach, under the assumption of the approximations outlined above, yields exactly the same results as the treatment of the three-level system in the Blume-Kistner approach. We therefore refer to section 3.1.1 for a solution and a detailed analysis of Eq. (3.62).
In [113] it is shown that Eq. (3.62) can also be solved by finding two eigenmodes of $\mathcal{E}(z,\omega)$, which, after creation by a scattering on a first layer of resonant nuclei, propagate independently of one another through the medium. The results of this approach are exactly equal to those obtained in our analysis.

3.2.3 $\gamma_2 \neq \gamma_3$

The Maxwell-Schrödinger approach, however, has a very interesting feature that is lacking in the Blume-Kistner model. It is possible to assume that the crossing levels have different relaxation rates ($\gamma_2 \neq \gamma_3$). A physical origin of such a difference may be found in the fluctuations of the magnetic hyperfine field. The transition with the highest Larmor frequency will show a higher relaxation rate, hence $\gamma < \gamma_2 < \gamma_3$, with γ the natural line width of the 14.4 keV nuclear excited state. The experimental data in section 1.3.2 strongly support this hypothesis. Fig. 1.13 shows that $\gamma_3 \approx 2\gamma_2$.
We can solve Eq. (3.55) and Eq. (3.56) in exactly the same way as above, but now with $\gamma_2 \neq \gamma_3$:

$$\rho_{21}(\omega) = \frac{\delta_3}{\delta_+\delta_-}V_+(\omega) + \frac{\Omega}{\delta_+\delta_-}V_-(\omega) \tag{3.64}$$

$$\rho_{31}(\omega) = \frac{\Omega}{\delta_+\delta_-}V_+(\omega) + \frac{\delta_2}{\delta_+\delta_-}V_-(\omega), \tag{3.65}$$

with

$$\delta_\pm = \omega - \omega_0 + i\frac{\gamma_2+\gamma_3}{4} \mp \sqrt{\Omega^2 - \left(\frac{\gamma_2-\gamma_3}{4}\right)^2} \tag{3.66}$$

$$\delta_{2/3} = \omega - \omega_0 + i\frac{\gamma_{2/3}}{2}. \tag{3.67}$$

Again, we limit our first analysis to the thin absorber case, following the same approach as in the Blume-Kistner section. Let us first consider the case when only σ^+ is incident. Because of the square root in the definition of $\delta_\pm$ we should distinguish two cases. Then, to first order in T_e, the intensity of the

transmitted radiation is given by

$$I'(\omega) = 1 + 2\Im\left(C\gamma\frac{\delta_3}{\delta_+\delta_-}\right) \tag{3.68}$$

$$= 1 - C\gamma\left[\frac{\gamma_2}{2}\left(g'_+(\omega)+g'_-(\omega)\right)\right.$$
$$\left. + \left(\gamma_3\left(\Omega^2+\frac{\gamma_2\gamma_3}{4}\right)-\gamma_2\left(\frac{\gamma_2^2}{8}+\frac{\gamma_3^2}{8}-\Omega^2\right)\right)g'_+(\omega)g'_-(\omega)\right] \tag{3.69}$$

for $\Omega < |\gamma_2 - \gamma_3|/4$, and

$$I''(\omega) = 1 - C\gamma\left[\frac{\gamma_2}{2}\left(g''_+(\omega)+g''_-(\omega)\right)+(\gamma_3-\gamma_2)\left(\Omega^2+\frac{\gamma_2\gamma_3}{4}\right)g''_+(\omega)g''_-(\omega)\right] \tag{3.70}$$

for $\Omega \geq |\gamma_2 - \gamma_3|/4$, where we have introduced the notation

$$g'_\pm(\omega) = \frac{1}{(\omega-\omega_0)^2+\left(\frac{\gamma_2+\gamma_3}{4}\mp\sqrt{\Omega^2-\left(\frac{\gamma_2-\gamma_3}{4}\right)^2}\right)^2} \tag{3.71}$$

$$g''_\pm(\omega) = \frac{1}{\left(\omega-\omega_0\mp\sqrt{\Omega^2-\left(\frac{\gamma_2-\gamma_3}{4}\right)^2}\right)^2+\left(\frac{\gamma_2+\gamma_3}{4}\right)^2} \tag{3.72}$$

in analogy with the definition of $g_\pm(\omega)$ in Eq. (3.24). C is defined in section 3.1.1. It is seen that, as well as a Lorentzian contribution, there is the appearance of an interference term proportional to $g_+(\omega)g_-(\omega)$. When $\gamma_2 = \gamma_3$, the interference term vanishes and the transmitted radiation ($I''(\omega)$) reduces to the sum of Lorentzians, as obtained previously.
When $\gamma_3 << \gamma_2$, *e.g.* if $|3\rangle$ is a metastable state, the conditions of optical EIT are met[13] . Simulations of the intensity of the transmitted radiation for $\gamma_3 = \gamma_2/100$ are shown in the left part of Fig. 3.17. The effect of the interference term is quite dramatic. A *transparency window* is created where most absorption is cancelled. At the center of the absorption line $I''(\omega = \omega_0) - 1 \propto \gamma_3/(\Omega^2 + \gamma_2\gamma_3/4)$, hence the absorption is completely suppressed only if $\gamma_3 = 0$. Also, in order to have a large reduction of the absorption, the condition that $\Omega^2 >> \gamma_2\gamma_3/4$ should be fulfilled. These conclusions are in

[13]There are two other reasons why this special case corresponds to a 'common' optical EIT scheme. First, the restriction to the incidence of σ^+ radiation is equivalent with one probe field. Second, in the thin absorber limit, the possible transition $|3\rangle \rightarrow |1\rangle$, with emission of σ^- radiation, which is not present in a common EIT scheme, is neglected (see also section 2.1).

perfect agreement with the generic results of optical EIT, see *e.g.* [115]. A further explanation of this induced transparency in terms of dark and bright states is given in section 2.1.

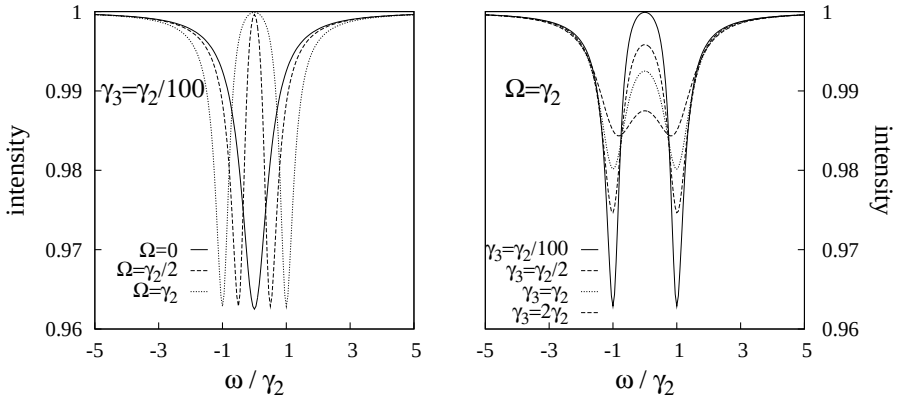

Figure 3.17: Simulation of the transmitted radiation in the case of: (left figure) the optical EIT regime ($\gamma_3 = \gamma_2/100$) for different values of Ω and (right figure) different values of γ_3 with a fixed mixing strength $\Omega = \gamma_2$ (thin absorber limit $T_e = 0.1$).

The importance of the value of γ_3 with respect to γ_2 is reflected in the spectra in the right part of Fig. 3.17. It is clearly seen that, even in the presence of a mixing interaction (here $\Omega = \gamma_2$), there is no reduction but an *increase* in absorpion at the line center if $\gamma_3 \geq \gamma_2$. This is also obvious from Eq. (3.70), where the sign of the interference term is determined by $(\gamma_3 - \gamma_2)$. Let us now add the incidence of σ^- radiation. We only consider the most recurrent case of $\Omega \geq |\gamma_2 - \gamma_3|/4$. Using the result in Eq. (3.70), the total transmitted radiation intensity is calculated as

$$I''(\omega) = 1 + 2\frac{3T_e}{16}\gamma\left[\Im\left(|C_{12}|^2\frac{\delta_3}{\delta_+\delta_-}\right) + \Im\left(|C_{13}|^2\frac{\delta_2}{\delta_+\delta_-}\right)\right] \quad (3.73)$$

$$= 1 - \frac{3T_e}{16}\gamma\left[\left(\frac{\gamma_2}{2}|C_{12}|^2 + \frac{\gamma_3}{2}|C_{13}|^2\right)\left(g''_+(\omega) + g''_-(\omega)\right)\right.$$

$$+ \left.\left(|C_{12}|^2 - |C_{13}|^2\right)(\gamma_3 - \gamma_2)\left(\Omega^2 + \frac{\gamma_2\gamma_3}{4}\right)g''_+(\omega)g''_-(\omega)\right], \quad (3.74)$$

with C_{ij} the product of the Clebsch-Gordan and rotation matrix coefficients of the $|j\rangle \rightarrow |i\rangle$ transition. The addition of the σ^- contribution is of crucial importance for the interference term. Now, the sign of this term, which defines

whether there is destructive (-) or constructive (+) interference, depends on the strength of one transition with respect to the other. For example, if $|C_{12}|^2 = |C_{13}|^2$, there is no observable interference, even if there is a mixing interaction *and* $\gamma_3 << \gamma_2$. This is of course due to the perfect symmetry of such a case, where the destructive and constructive terms exactly cancel each other. In our nuclear level mixing case, we have $|C_{12}|^2 = 1/3$, $|C_{13}|^2 = 1$ and $\gamma_3 \approx 2\gamma_2 \approx 2\gamma$, which yield‘ a *net destructive interference* contribution. This is a promising result in regard with the explanation of the experimentally observed reduction of absorption. However, the simulated spectra in Fig. 3.18 do not show a large effect. On the contrary, a comparison with Fig. 3.2 reveals that, at the line center there is even more absorption than is the case for $\gamma_2 = \gamma_3 = \gamma$. The reason is that the increased line width reduces the influence of the mixing interaction. Indeed, at the line center, we have

$$I''(\omega = \omega_0) - 1 \propto \frac{\gamma_2|C_{13}|^2 + \gamma_3|C_{12}|^2}{\Omega^2 + \frac{\gamma_2\gamma_3}{4}}, \tag{3.75}$$

which means that, for a particular value of Ω, the absorption increases with increasing relaxation rates.
Nevertheless, a small but destructive interference term is present in the intensity of the transmitted gamma radiation at the level crossing transition. This is due to the combination of asymmetrical transition strengths and different relaxation rates, such that the strongest transition involves the level with the highest relaxation rate.

Remark: It is interesting to note that the integrated absorption over the full frequency range is *independent* of Ω. Although it seems that there is less absorption, which is of course true at the line center, this reduction is exactly compensated by an increase of absorption spread over the wings of the resonance. It would therefore be more correct to designate this effect as a *redistribution* instead of a reduction of absorption.

3.2.4 Three-level system in the perpendicular geometry

In the perpendicular geometry, we must distinguish two different three-level systems. First, there is the $\Delta m = 0$ transition from $|m_g = 1/2\rangle$ to the ($|m_e = 1/2\rangle$ component of the) mixed levels. The intensity of this absorption line is correctly described by Eq. (3.74) (or an extension of Eq. (3.69)) with $|C_{13}|^2 \approx 0$ because the $|-3/2\rangle \rightarrow |1/2\rangle$ is negligible with respect an $M1$ transition. Then, it is clear that, for $\gamma_3 > \gamma_2$, the interference is always *constructive*, which gives rise to an enhanced absorption at the line center. Therefore, although there is

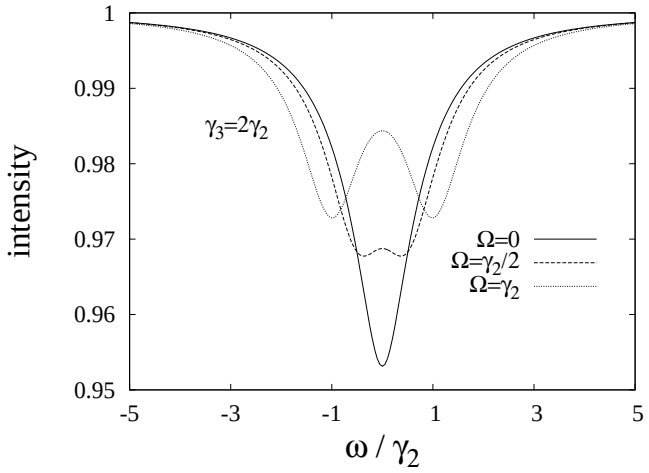

Figure 3.18: Simulation of the transmitted intensity in the case of incident both σ^+ and σ^- radiation, with realistic values $|C_{12}|^2 = 1/3$, $|C_{13}|^2 = 1$ and $\gamma_3 = 2\gamma_2$. (thin absorber limit $\mathrm{T}_e = 0.1$)

a reduction of absorption due to splitting of the mixed levels, this reduction is partially counteracted by the interference term. This result certainly helps to understand why there is no important reduction observed at this absorption line (with respect to its partner line), while it is present in the parallel geometry.
The second three-level system involves the same states as in the parallel geometry. The difference now is that both polarization states of the incident radiation can induce both transitions $(2,1)$ and $(3,1)$ simultaneously. Taking into account the different relaxation rates, Eq. (3.64) and Eq. (3.65) are modified as

$$\rho_{21}(\omega) = \frac{\delta_3}{\delta_+\delta_-}\left(V_2^-(\omega)+V_2^-(\omega)\right)+\frac{\Omega}{\delta_+\delta_-}\left(V_3^+(\omega)+V_3^-(\omega)\right), \quad (3.76)$$

$$\rho_{31}(\omega) = \frac{\delta_2}{\delta_+\delta_-}\left(V_3^+(\omega)+V_3^-(\omega)\right)+\frac{\Omega}{\delta_+\delta_-}\left(V_2^+(\omega)+V_2^-(\omega)\right), \quad (3.77)$$

with $V_i^{\pm}(\omega) = \langle i|\mathcal{H}^{\pm}|1\rangle\mathcal{E}^{\pm}(z,\omega)/2 \equiv \mu_c\mu_{i1}^{\pm}\mathcal{E}^{\pm}(z,\omega)/2$. The polarizations of the medium are also changed accordingly: $P_{\pm}(z,t) = \mu_c\mu_{12}^{\pm}\rho_{21} + \mu_c\mu_{13}^{\pm}\rho_{31}$.

3.2.5 New fit of T_e=8

These generalized expressions for the polarizations are substituted in the Fourier transformed propagation equation of (3.61) and implemented in a simulation and fit computer program. Also, the way that the mixing interaction is taken into account has changed with respect to the code of section 3.1. Now, we assume that the magnitude of the non-axial component of the efg (η) is distributed in a Gaussian way around the mean value of $\overline{\eta}$. This should be in much closer correspondence with the real conditions in the crystals, than the assumption of a uniform, non-zero value of η. In practice, we make a convolution of the initial spectrum $I(v,\eta)$ with the Gaussian distribution $G(\eta)$:

$$I(v,\overline{\eta}) = \int_0^\infty d\eta\, I(v,\eta) G(\overline{\eta}-\eta), \tag{3.78}$$

with

$$G(\overline{\eta}-\eta) = \frac{1}{\Gamma_\eta\sqrt{2\pi}} e^{\frac{1}{2}\left(\frac{\overline{\eta}-\eta}{\Gamma_\eta}\right)^2} \tag{3.79}$$

and Γ_η the width of the distribution. In the fit, we choose $\overline{\eta}=0$, corresponding to the most prevalent situation in our $FeCO_3$ crystal (see section 1.1.2), and vary Γ_η. This means that there is no additional degree of freedom with respect to the previous fit program. The errors on the free parameters are estimated in the same way as outlined in section 3.1.3.
Notice that, because η is defined to be positive, the convolution of Eq. (3.78) is limited to an integral over the positive values of η.

The fit results of the spectra of the T_e=8 crystal at three different temperatures below T_N are summarized in table 3.2 and visualized in Fig. 3.19 and Fig. 3.20. First, we fit the spectrum in the parallel geometry at $T = 31\,\mathrm{K}$, yielding the reasonable value of $\Gamma_\eta = 0.14(2)$. This value is kept fixed during the fit of all other spectra (no estimated error). Also, to simplify the fit procedure, the values of two hyperfine parameters are fixed to their mean value of previous fits: $IS = 1.33\,\mathrm{m/s}$ and $\Delta = 2.04\,\mathrm{mm/s}$.
Not only does the fitted curves agree very well with the experimental data, quantified in the reasonably small values of $\chi^2_{r,min}$, also the derived values for the different parameters are mutually consistent. The transition-dependent broadening of the absorption lines, which is parameterized by the q-values (see section 3.1.3), is also in correspondence with the broadening deduced in the first, Lorentzian analysis. Furthermore, the values obtained for T_e and f_r are in much better agreement with their theoretical values of T_e=8 and $f_r = f_{LM} \approx 0.7$.

Table 3.2: Best fit values to the Maxwell-Schrödinger model of the $FeCO_3$ ($T_e = 8$) Mössbauer spectra for three different temperatures.

T	34 K		31 K		18 K	
θ	0	$\pi/2$	0	$\pi/2$	0	$\pi/2$
Γ_η	0.14	0.14	0.14(2)	0.14	0.14	0.14
β_e	0.88(1)	0.87(1)	1.02(2)	1.02(2)	1.21(1)	1.21(1)
T_e	10(3)	9(1)	9(2)	10(3)	9(2)	9(4)
f_r	0.52(2)	0.55(5)	0.52(2)	0.57(4)	0.52(2)	0.54(6)
q_1	2.8(1)	3.2(1)	2.8(1)	3.0(1)	2.0(1)	1.9(2)
q_2	-	2.6(1)	-	2.5(1)	-	2.0(2)
q_3	1.6(1)	1.6(1)	1.5(1)	1.7(1)	2.0(1)	1.3(2)
$\chi^2_{r,min}$	2.4	6.2	4.3	4.6	2.7	8.1

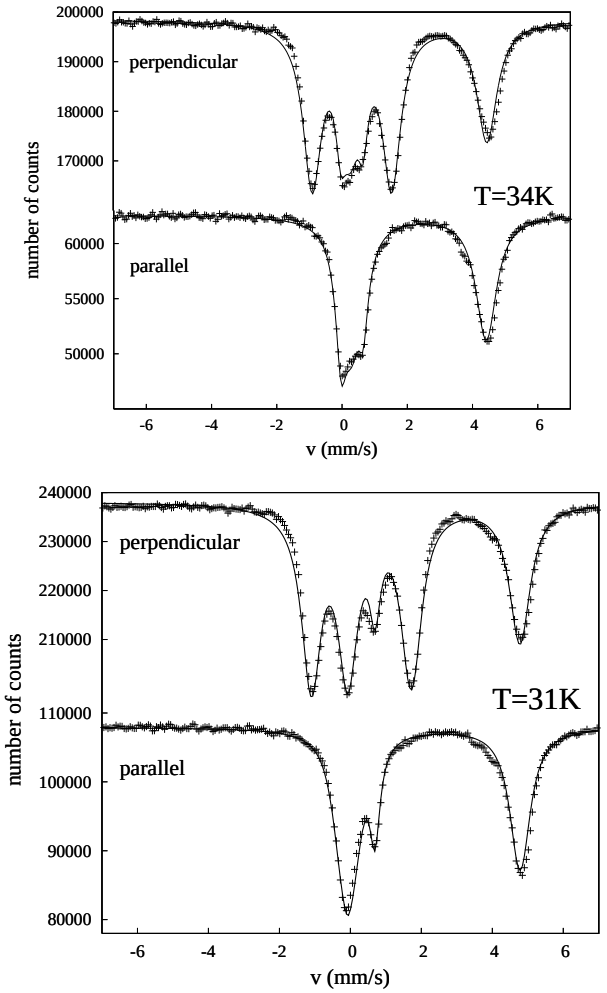

Figure 3.19: Mössbauer spectra of T_e=8 at $T = 34\,\mathrm{K}$ and $T = 31\,\mathrm{K}$, with the solid line giving the best fit based on the Maxwell-Schrödinger model, taking into account different relaxation rates and a Gaussian distributed η.

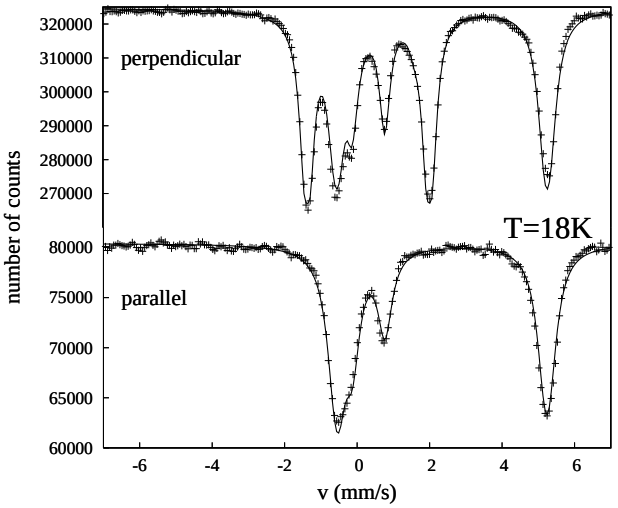

Figure 3.20: Mössbauer spectra of T_e=8 at $T = 18\,\mathrm{K}$, with the solid line giving the best fit based on the Maxwell-Schrödinger model, taking into account different relaxation rates and a Gaussian distributed η.

3.2.6 Four-level system

There is one particular case in the Mössbauer spectra studied where the regular two-level and the three-level system discussed above are not applicable. In section 1.3.3 the spectra are presented for the $FeCO_3$ T_e=8 crystal with an *externally applied magnetic field* and in the parallel geometry.
At room temperature, this perpendicular magnetic field mixes the degenerate $|m = \pm 1/2\rangle$ states, in the ground state as well as in the excited state. The interaction of these four levels with radiation can be schematized as the four-level scheme of Fig. 3.21. The four levels are relabelled as $|m_g = -1/2\rangle \equiv |1\rangle$, $|m_g = 1/2\rangle \equiv |4\rangle$, $|m_e = 1/2\rangle \equiv |2\rangle$, and $|m_g = -1/2\rangle \equiv |3\rangle$, where σ^+ radiation induces a $(2,1)$ transition and σ^- radiation induces a $(3,4)$ transition. The magnetic field provides both a mixing interaction between the ground levels (Ω_g) and between the excited levels (Ω_e), with

$$\left|\frac{\Omega_g}{\mu_g}\right| = \left|\frac{\Omega_e}{\mu_e}\right|. \tag{3.80}$$

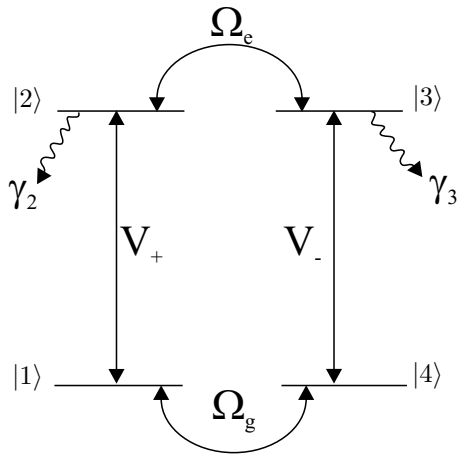

Figure 3.21: Schematical representation of the four-level system under consideration. With respect to the three-level system in Fig.3.16, an extra mixing field (Ω_g) and a nuclear state ($|4\rangle$) is added.

The density matrix equations for the (relevant) coherences of this four-level system are given by

$$\dot{\rho}_{21} = \left(-i\omega_0 - \frac{\gamma_2}{2}\right)\rho_{21} + iV_+\left(\rho_{22} - \rho_{11}\right) - i\Omega_e\rho_{31} + i\Omega_g\rho_{24} \quad (3.81)$$

$$\dot{\rho}_{24} = \left(-i\omega_0 - \frac{\gamma_2}{2}\right)\rho_{24} + +iV_-\rho_{23} - iV_+\rho_{14} - i\Omega_e\rho_{34} + i\Omega_g\rho_{21} \quad (3.82)$$

$$\dot{\rho}_{31} = \left(-i\omega_0 - \frac{\gamma_3}{2}\right)\rho_{31} + iV_+\rho_{32} - iV_-\rho_{41} - i\Omega_e\rho_{21} + i\Omega_g\rho_{34} \quad (3.83)$$

$$\dot{\rho}_{34} = \left(-i\omega_0 - \frac{\gamma_3}{2}\right)\rho_{34} + iV_-\left(\rho_{33} - \rho_{44}\right) - i\Omega_e\rho_{24} + i\Omega_g\rho_{31} \quad (3.84)$$

with the same definitions of section 3.2.2. The equations are again solved analytically in the linear response approximation. The populations are replaced with their initial values $\rho_{11}^0 = \rho_{44}^0 = 1/2$ and $\rho_{22}^0 = \rho_{33}^0 = 0$. Also, since the terms with $\rho_{23}\,(\rho_{32})$ and $\rho_{14}\,(\rho_{41})$ are proportional to $V_\pm$, they are discarded. A Fourier transformation turns the differential equations into four coupled algebraic equations that can be solved in a straightforward way. In the case that the decay rates of both excited states are equal ($\gamma_2 = \gamma_3 = \gamma$), which is certainly true for the experimental conditions under consideration, we find that

$$\rho_{21}(\omega) = \frac{1}{2}\frac{\delta + i\gamma/2}{\delta_+^2\delta_-^2 - 4\Omega_e^2\Omega_g^2}\left(\delta_+\delta_- V_+(\omega) - 2\Omega_e\Omega_g V_-(\omega)\right), \quad (3.85)$$

$$\rho_{31}(\omega) = \frac{1}{2}\frac{\delta + i\gamma/2}{\delta_+^2\delta_-^2 - 4\Omega_e^2\Omega_g^2}\left(\delta_+\delta_- V_-(\omega) - 2\Omega_e\Omega_g V_+(\omega)\right), \quad (3.86)$$

with $\delta_\pm = \omega - \omega_0 + i\gamma/2 \pm \sqrt{\Omega_e^2 + \Omega_g^2}$.
These results show that Ω_e and Ω_g are treated on the same footing, and, hence, are completely interchangeable. This is a little surprising because the two cases have a different coupling state. If $\Omega_g = 0$, then the coupling state is the decaying excited state $|3\rangle$, while, if $\Omega_e = 0$ the coupling state is a stable ground state. The latter case corresponds to a so-called $V-$scheme. Our solution then coincides with the generic solution for V-schemes [116], with $\rho_{11}^0 = \rho_{44}^0$. It is argued that, in this system, EIT can be achieved if $\Omega >> \gamma_2$. However, as only one decay rate is involved, it can be shown that the result for $\rho_{21}(\omega)$ now corresponds to the first term of Eq. (3.64) with $\gamma_3 = \gamma_2$. In the previous sections, we have illustrated that the reduction of absorption in such a case is solely due to the Stark shift of the levels and not related to an interference term. Hence, this (possible) implementation of a V-scheme does not provide the desired interference either.
In their general form, the denominators of $\rho_{21}(\omega)$ and $\rho_{31}(\omega)$ can be written as

$$\prod_{\pm\mp} (\delta \pm \Omega_g \mp \Omega_e + i\gamma/2)^{-1}\,, \tag{3.87}$$

where all four combinations of + and − must be taken. This means that the combination of the two mixing interactions gives rise to four new eigenstates with the above frequencies, which has been correctly assumed in the discussion in section 1.3.3 (where two Lorentzian doublets are used to fit the σ absorption line).

3.3 Conclusions

This chapter has focussed on the detailed analysis of the $FeCO_3$ Mössbauer spectra. The two semiclassical models both correctly take into account thickness and polarization effects, which has proven to be crucial for a good understanding of not only the spectra at the level crossing, but also for a correct interpretation of the anomalous line widths at RT. The Blume-Kistner approach has been valuable in the identification of the nuclear absorption as the sum of two Lorentzians and in the deduction that the phase induced by a random mixing interaction has no consequences for the final spectrum. However, fitting the experimental data of *both* geometries to this model has not been successful in providing a consistent interpretation.
The Maxwell-Schrödinger approach is then seen as the necessary generalization of the former semiclassical model. This approach allows a more detailed modelling of the (single) forward scattering response, now including a difference in the relaxation rates of the mixed levels. This is shown to be crucial

for the understanding of the difference between the three-level system in the parallel geometry and the '$\Delta m = 0$' three-level system in the perpendicular geometry. By modifying the fit program according to these new insights, we have finally succeeded in explaining the reduction of absorption in both geometries as *the combined effect of polarization, saturation and level mixing induced transparency in* Λ*-schemes with different decay rates.*
It should certainly be mentioned that, in the latter fit program, the random nature of the mixing interaction is accounted for by the convolution with a Gaussian distribution in η, centered around $\eta = 0$. Since the efg mixing interaction mainly influences the crossing levels, this Gaussian distribution leads to a broadening of the absorption line involving the crossing levels, with respect to the other lines. This certainly has helped to reduce the absorption at the line center.

With the puzzle of the experimental observations solved, we can now focus our attention to a completely different model in the hope that it can supply us with some deeper insight into the nuclear resonant (multiple) scattering process.

Chapter 4

Coherent path model

The coherent path model is a fully quantum mechanical model of the interaction of (gamma) photons with nuclei. It is based on the work of Heitler [4] and Harris [117] and recently updated by Hoy [118]. The model bears this particular name because it describes the gamma-nuclei interaction as a coherent sum of many, discrete, 'quantum paths' or amplitudes. It gives the user a privileged view on the quantum mechanical creation of an observable quantity (here: transmitted radiation intensity) by allowing one to (theoretically) distinguish every possible quantum path. It is, therefore, a very natural choice of description since we are dealing with single photons in interaction with an ensemble of nuclei. Furthermore, this coherent path model has been very successful in describing a resonant Mössbauer detector [119] and has provided a novel interpretation of the gamma echo [120]. It can also be used for time-differential Mössbauer analysis, where it has added some new insight in the phenomena of speed-up and dynamical beats present in nuclear resonant forward scattering of synchrotron radiation [121].

4.1 Model outline

First, a brief, but general description of the model is given. We start from the time-dependent Schrödinger equation. The Hamiltonian of the system can be written as the sum of two parts: H_0 describes the unperturbed nuclei ánd the free radiation field (if present), while V is the interaction Hamiltonian that describes the transitions between the nuclear levels. The actual state of the

system is given by

$$|\Psi(t)\rangle = \sum_n c_n(t) e^{-iE_n t/\hbar} |\phi_n\rangle \tag{4.1}$$

with $|\phi_n\rangle$ an eigenstate of H_0 and $E_n = \hbar\omega_n$ its corresponding energy. The coefficients $c_n(t)$ have to satisfy the Schrödinger equation, which leads to a set of coupled differential equations

$$i\hbar \frac{dc_n(t)}{dt} = \sum_m c_m(t) e^{i(\omega_n - \omega_m)t} \langle \phi_n | V | \phi_m \rangle + i\hbar \delta_{1n} \delta(t) \tag{4.2}$$

where δ_{1n} is the Kronecker delta and $\delta(t)$ the Dirac delta function. The inhomogeneous term is added for the following reasons [4]. First, the solution has to satisfy the initial condition that the system is in a well-defined state, *e.g.*, $c_n(0) = \delta_{1n}$. Second, although we choose a solution that only involves positive times, it will be extended to the negative time axis for analytical reasons. All amplitudes $c_n(t)$ are chosen such that $c_n(t < 0) = 0$. Following Heitler the discontinuity in $c_1(t)$ arising at $t = 0$ is correctly dealt with by addition of the inhomogeneous term.
It is more interesting, however, to use the Fourier transform of Eq. (4.2). If we apply

$$c_n(t) = -\frac{1}{2\pi i} \int_{-\infty}^{\infty} d\omega \, C_n(\omega) e^{i(\omega_n - \omega)t}, \tag{4.3}$$

then Eq. (4.2) can be rewritten as

$$(\omega - \omega_n + i\epsilon) C_n(\omega) = \sum_m C_m(\omega) \frac{V_{nm}}{\hbar} + \delta_{n1} \tag{4.4}$$

with $V_{nm} \equiv \langle \phi_n | V | \phi_m \rangle$ a time-independent matrix element describing a transition from the mth to the nth eigenstate of H_0. The introduction of $+i\epsilon$ ($\epsilon > 0$) ensures the proper causality relations [4]. This term eventually disappears from any physical result by considering the limit $\epsilon \to 0^+$.
The eigenstates of H_0 are given by the direct product of an ensemble of unperturbed nuclear states and the states of the free radiation field: $|\phi_n\rangle = |\text{nuclei}\rangle \otimes |\text{field}\rangle$. In the case of a Mössbauer scheme (see section 1.2) the nuclear ensemble is divided into one source nucleus (S) and N absorber nuclei (A) while the radiation field can be expressed as a photon number state (P): $|\phi_n\rangle = |S\rangle |A_1\rangle |A_2\rangle \ldots |A_N\rangle |P\rangle$. The number of $|\phi_n\rangle$ states is limited by a proper choice of the initial state as will be clear later on.

4.2 Three-level system

As in the semiclassical treatments, we consider the case of the interaction of a gamma photon with the three levels involved in the level crossing/mixing, *i.e.* the $|m_g = -1/2\rangle \equiv |1\rangle$ ground state and the $|m_e = 1/2\rangle \equiv |2\rangle$ and $|m_e = -3/2\rangle \equiv |3\rangle$ excited states. The energies of the excited states with respect to the ground state are $\hbar\omega_2$ and $\hbar\omega_3$ respectively. The interaction Hamiltonian is similar to that given by (3.48), where the pure nuclear states states or now replaced with the corresponding product of nuclear and photon states (see the next section for the exact expression of these product states). In the parallel geometry, a σ^+ photon can induce a $(1/2, -1/2)$ transition, designated with V_+, whereas a σ^- photon can induce a $(-3/2, -1/2)$ transition, designated with V_-. It is assumed that a mixing interaction Ω between the excited states is present. This three-level system is summarized by Fig. 3.16, but now allowing for $\omega_2 \neq \omega_3$.
We restrict the model to σ^+ source photons and keep in mind that the treatment of σ^- source photons can be done analogously. Due to the breaking of the axial symmetry by the level mixing, however, a σ^+ source photon can be absorbed while a σ^- photon is re-emitted. Therefore, as soon as the first scattering takes place, we have to take into account the two photon fields. Because these two fields have mutual orthogonal polarizations, the total radiation intensity will be just the sum of both field intensities.
The absorber is treated as a collection of N identical nuclei, which effectively scatter the gamma photon. The number of scattering centers N is shown to be proportional to the more common effective thickness T_e [118]:

$$N = \frac{T_e \gamma}{2 f_{LM} \gamma_r} \tag{4.5}$$

with γ the total decay rate of the nuclear excited state, γ_r the radiative decay rate and f_{LM} the recoilless fraction. In the case of the $FeCO_3$ experiment, the crystals used have an effective thickness of $T_e = 8$ and $T_e = 3$. to Eq. (4.5), this corresponds to $N \approx 52$ and and $N \approx 20$ respectively. In a multilevel nucleus, however, the effective thickness is reduced according to [122]

$$T_e \to \frac{1}{2I_g + 1} \frac{2L + 1}{2I_e + 1} T_e \tag{4.6}$$

with L the multipolarity of the radiation (here $L = 1$), which leads to $N \approx 19$ and $N \approx 7$ respectively.

A schematical overview of the physical system under consideration is given in Fig. 4.1. A single-line source nucleus decays and emits a σ^+ (or σ^-) photon. This photon is scattered by N absorber nuclei. In this process the photon can

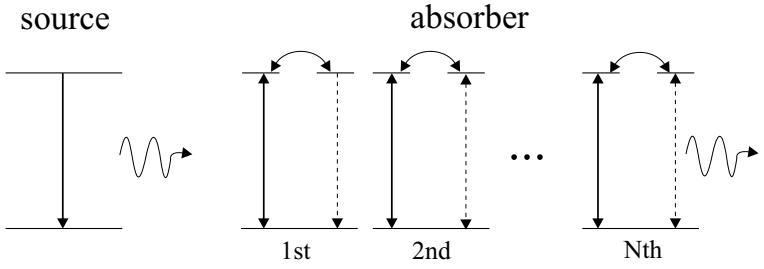

Figure 4.1: Physical model of the nuclear resonant scattering under consideration. The photon emitted from a single line source can interact with N three-level absorber nuclei. The horizontal lines represent the unperturbed nuclear eigenstates and the arrows indicate the interactions.

retain its initial polarization (solid line) or it can change its polarization through the mixing interaction (dashed line).

4.2.1 General equations

If we apply the above mathematical formalism to the system of a source nucleus and N resonant absorber nuclei, located between the source and the detector, then five structurally distinct[1] eigenstates of H_0 and their corresponding amplitudes can be identified:

i) $|\phi_1\rangle \equiv |S\rangle = |S^e, \{A^1_{m=1,N}\}, \{0_{\mathbf{k},\sigma^+}\}, \{0_{\mathbf{k}',\sigma^-}\}\rangle$ with $\mathrm{S}(\omega)$ the amplitude corresponding to the source nucleus in the excited state ($\hbar\omega_s$), the absorber nuclei in the ground state and no photons present. This state $|S\rangle$ is *chosen* as the initial state in the model considered.

ii) $|\phi_2\rangle \equiv |P^+_{\mathbf{k}}\rangle = |S^g, \{A^1_{m=1,N}\}, 1_{\mathbf{k},\sigma^+}, \{0_{\mathbf{k}',\sigma^-}\}\rangle$ with $\mathrm{P}^+_{\mathbf{k}}(\omega)$ the amplitude corresponding to the source nucleus in the ground state, the absorber nuclei in the ground state and one photon with wave number $\mathbf{k}$, σ^+ polarization and energy $\hbar\omega_k$.

iii) $|\phi_3\rangle \equiv |P^-_{\mathbf{k}'}\rangle = |S^g, \{A^1_{m=1,N}\}, \{0_{\mathbf{k},\sigma^+}\}, 1_{\mathbf{k}',\sigma^-}\rangle$ with $\mathrm{P}^-_{\mathbf{k}'}(\omega)$ the amplitude corresponding to the source nucleus in the ground state, the absorber nuclei in the ground state and one photon with wave number $\mathbf{k}'$, σ^- polarization and energy $\hbar\omega_{k'}$.

[1]There are more than 5 eigenstates, actually, $1 + 2m + 2 \times \infty$, but all $|A_m\rangle$ and $|B_m\rangle$ states, for $m = 1, N$, and all $|1_k\rangle$ and $|1_{k'}\rangle$ photon states, for $-\infty \leq k \leq \infty$, are considered to be structurally equal.

iv) $|\phi_4\rangle \equiv |A_m\rangle = |S^g, A^2_m, \{A^1_{i\neq m, i=1,N}\}, \{0_{\mathbf{k},\sigma^+}\}, \{0_{\mathbf{k}',\sigma^-}\}\rangle$ with $\mathrm{A}_m(\omega)$ the amplitude corresponding to the absorber nucleus m at position $\mathbf{x_m}$ in the excited state $|2\rangle$ ($\hbar\omega_2$), all other nuclei in the ground state and no photons present.

v) $|\phi_5\rangle \equiv |B_m\rangle = |S^g, A^3_m, \{A^1_{i\neq m, i=1,N}\}, \{0_{\mathbf{k},\sigma^+}\}, \{0_{\mathbf{k}',\sigma^-}\}\rangle$ with $\mathrm{B}_m(\omega)$ the amplitude corresponding to the absorber nucleus m at position $\mathbf{x_m}$ in the excited state $|3\rangle$ ($\hbar\omega_3$), all other nuclei in the ground state and no photons present.

It must be noted that this model considers one particular value of $\mathbf{k}$ (and $\mathbf{k}'$), which can be seen as a plane wave approximation. However, at the end of the derivation, a realistic wave packet is reconstructed as the (infinite) sum of these plane wave solutions.
Here, decay processes due to electron conversion are not explicitly taken into account. It can be easily shown, however, that their contribution is limited to an additional term γ_c in the total decay rate $\gamma = \gamma_r + \gamma_c$ [118].
If we assume that at $t = 0$ only the source nucleus, at the origin, is excited, or $|\Psi(t=0)\rangle = |S\rangle$, the following set of coupled linear equations from Eq. (4.4) is obtained:

$$(\omega - \omega_s + i\epsilon)\, S(\omega) = 1 + \sum_{\mathbf{k}} P^+_{\mathbf{k}}(\omega) \frac{V_{SP_{\mathbf{k}}}}{\hbar} \tag{4.7}$$

$$(\omega - \omega_k + i\epsilon)\, P^+_{\mathbf{k}}(\omega) = S(\omega) \frac{V_{P_{\mathbf{k}}S}}{\hbar} + \sum_m A_m(\omega) \frac{V_{P_{\mathbf{k}}A}}{\hbar} e^{-i\mathbf{k}.\mathbf{x_m}} \tag{4.8}$$

$$(\omega - \omega_{k'} + i\epsilon)\, P^-_{\mathbf{k}'}(\omega) = \sum_m B_m(\omega) \frac{V_{P_{\mathbf{k}'}B}}{\hbar} e^{-i\mathbf{k}'.\mathbf{x_m}} \tag{4.9}$$

$$(\omega - \omega_2 + i\epsilon)\, A_m(\omega) = \sum_{\mathbf{k}} P^+_{\mathbf{k}}(\omega) \frac{V_{AP_{\mathbf{k}}}}{\hbar} e^{i\mathbf{k}.\mathbf{x_m}} + B_m(\omega)\Omega \tag{4.10}$$

$$(\omega - \omega_3 + i\epsilon)\, B_m(\omega) = \sum_{\mathbf{k}'} P^-_{\mathbf{k}'}(\omega) \frac{V_{BP_{\mathbf{k}'}}}{\hbar} e^{i\mathbf{k}'.\mathbf{x_m}} + A_m(\omega)\Omega^* \tag{4.11}$$

where the factors $e^{\pm i\mathbf{k}.\mathbf{x_m}}, m = 1$ to N, take into account the phase according to the position where the photon absorption (+) or emission (-) takes place.
The interpretation of the above equations is straightforward. For example, Eq. (4.8) describes the production of a photon having wave number $\mathbf{k}$ and σ^+ polarization. The first term at the right-hand side states that this can occur through the emission of such a photon by the source. The second term says that this can also occur by the emission by any of the absorber nuclei, at positions $\mathbf{x}_m$, that were in the excited state $|2\rangle$. Eq. (4.11) describes how nucleus m can reach the excited state $|3\rangle$. This is possible by the absorption of a σ^- photon, described by $P^-_{\mathbf{k}}(\omega)$, or by a transition from the excited state $|2\rangle$ in

the same nucleus, described by $A_m(\omega)$. The other equations can be interpreted in a similar way.

4.2.2 Solving the equations

Let us first try to find a solution for $S(\omega)$. After substitution of Eq. (4.8) into Eq. (4.7), we have

$$\begin{aligned}(\omega - \omega_s + i\epsilon)\, S(\omega) &= 1 + S(\omega) \sum_{\mathbf{k}} \frac{|V_{SP_\mathbf{k}}|^2}{\hbar^2} \frac{1}{\omega - \omega_k + i\epsilon} \\ &\quad + \sum_m A_m(\omega) \sum_{\mathbf{k}} \frac{V_{P_\mathbf{k}A} V_{SP_\mathbf{k}}}{\hbar^2} \frac{e^{-i\mathbf{k}.\mathbf{x_m}}}{\omega - \omega_k + i\epsilon} \quad (4.12)\end{aligned}$$

The summation over $\mathbf{k}$ is transformed into an integral through the prescription

$$\sum_{\mathbf{k}} \rightarrow \frac{V}{(2\pi)^3} \int d^3\mathbf{k}. \quad (4.13)$$

The sums over $\mathbf{k}$ of Eq. (4.12), which are now converted to integrals, can be evaluated using the relation [4]

$$\lim_{\epsilon \rightarrow 0^+} \frac{1}{x - a \pm i\epsilon} = P\left(\frac{1}{x-a}\right) \mp i\pi\delta(x-a) \quad (4.14)$$

where P indicates the principal part of a function. The principal part value gives rise to an energy shift, which can be incorporated into ω_s. For the second term on the right-hand side of Eq. (4.12) the δ-function results in an imaginary term that is identified as a (partial radiative) line width of the source excited state:

$$\gamma_s^r = \frac{V}{(2\pi\hbar)^2} \int d^3\mathbf{k} |V_{SP_k}|^2 \delta(\omega - \omega_k). \quad (4.15)$$

It is straightforward to verify that all other (incoherent) decay channels of the source excited state, *e.g.*, electron conversion, contribute in a similar way. Eventually, the total decay rate γ_s should correspond to the inverse of the lifetime of the source excited state.

The third term on the right-hand side of Eq. (4.12) describes a higher-order contribution with rapidly oscillating factors that will be neglected. This term describes the probability of re-excitation of the source nucleus by a photon coming back from the absorber, expressed by the sum over $A_m(\omega)$. Such a process is negligible due to geometry considerations [2]. In fact, this is the

[2] In our experimental setup the solid angle subtended by the source with respect to the absorber is very small.

same as assuming that the source nucleus will decay in the same manner as it would if the absorber were absent [117]. The source term can, therefore, be approximated by

$$S(\omega) \approx \frac{1}{\omega - \omega_s + i\frac{\gamma_s}{2}}. \tag{4.16}$$

where the limit $\epsilon \to 0^+$ is taken. Solving Eq. (4.8) for $P_k^+(\omega)$ and substituting into Eq. (4.10) and solving Eq. (4.9) for $P_{k'}^-(\omega)$ and substituting into Eq. (4.11) gives the following set of coupled linear equations

$$\begin{aligned}
(\omega - \omega_2 + i\epsilon)\, A_m(\omega) &= \Omega B_m(\omega) + \sum_{\mathbf{k}} \frac{V_{AP_\mathbf{k}} V_{P_\mathbf{k}S}\; e^{i\mathbf{k}.\mathbf{x_m}}}{\hbar^2 \left(\omega - \omega_k + i\epsilon\right)\left(\omega - \omega_s + i\frac{\gamma_s}{2}\right)} \\
&\quad + \sum_{m'} A_{m'}(\omega) \sum_{\mathbf{k}} \frac{|V_{AP_\mathbf{k}}|^2}{\hbar^2} \frac{e^{-i\mathbf{k}.(\mathbf{x_{m'}} - \mathbf{x_m})}}{\omega - \omega_k + i\epsilon} \qquad (4.17) \\
(\omega - \omega_3 + i\epsilon)\, B_m(\omega) &= \Omega^* A_m(\omega) \\
&\quad + \sum_{m'} B_{m'}(\omega) \sum_{\mathbf{k'}} \frac{|V_{BP_{\mathbf{k'}}}|^2}{\hbar^2} \frac{e^{-i\mathbf{k'}.(\mathbf{x_{m'}} - \mathbf{x_m})}}{(\omega - \omega_{k'} + i\epsilon)}. \qquad (4.18)
\end{aligned}$$

The sum over $\mathbf{k}$ and $\mathbf{k}'$ is evaluated in the same way as described above. Although the general model is formulated in 3-dimensional space, we now restrict the calculations to the forward direction only. It can be argued that photons that reach the detector from a non-forward direction have experienced different optical paths and thus have different optical path lengths. Therefore, since we must sum over all coherent paths, destructive interference between the non-forward paths makes their contribution negligible. If only forward scattering is considered, all paths have the same optical path length and give a non-zero contribution to the radiation detected.
In this one dimension, the sum over m can be limited by assuming that an absorber nucleus can only be excited by radiation coming from other nuclei that are located 'upstream' ($x_{m'} < x_m$) and not by radiation scattered from nuclei downstream. In the first case all possible optical path lengths are the same and will add constructively, while in the latter they are not (see also [119] for a more quantitative treatment of this approximation). The terms with $m = m'$ yield the radiative decay $\gamma_{2/3}^r$ of the excited states and again, all other decay channels can be added to this decay leading to the full decay $\gamma_{2/3}$. The set of

equations can then be rewritten as

$$\left(\omega-\omega_2+i\frac{\gamma_2}{2}\right)A_m(\omega) = \Omega B_m(\omega)-\frac{i\sqrt{\gamma_2^r}}{2}\left(\frac{V_{P_kS}}{\hbar}\right)\frac{e^{i\frac{\omega}{c}x_m}}{\left(\omega-\omega_s+i\frac{\gamma_s}{2}\right)} -\frac{i\gamma_2^r}{2}\sum_{m'=1}^{m-1}A_{m'}(\omega)\,e^{i\frac{\omega}{c}(x_m-x_{m'})}, \tag{4.19}$$

$$\left(\omega-\omega_3+i\frac{\gamma_3}{2}\right)B_m(\omega) = \Omega^* A_m(\omega) -\frac{i\gamma_3^r}{2}\sum_{m'=1}^{m-1}B_{m'}(\omega)\,e^{i\frac{\omega}{c}(x_m-x_{m'})}, \tag{4.20}$$

with γ_i^r the partial radiative decay rate from $|i\rangle$ to $|1\rangle$. This decay rate can be related to the total radiative decay rate by $\gamma_i^r=|C_{1i}|^2\gamma_r$, with C_{ij} defined in the previous sections as the product of Clebsch-Gordan and rotation matrix coefficients. Furthermore, we have defined

$$\sqrt{\gamma_2^r}\equiv\left(\frac{V_{P_kA}}{\hbar}\right)^{-1}\frac{V}{(2\pi\hbar)^2}\int d^3\mathbf{k}|V_{AP_k}|^2\delta(\omega-\omega_k), \tag{4.21}$$

where it is assumed that V_{P_kA} varies little around $\omega=\omega_k$.

Solution of $A_m(\omega)$ and $B_m(\omega)$

We first cast Eq. (4.19) and (4.20) in a more symmetrical form by solving them for $A_m(\omega)$ and $B_m(\omega)$, but still as a function of $A_{m'}(\omega)$ and $B_{m'}(\omega)$:

$$A_m(\omega) = e^{i\frac{\omega}{c}x_m}\left[S^+(\omega)+\sum_{m'=1}^{m-1}\left(\frac{-i\gamma_2^r}{2}\right)\frac{\delta_3}{\delta_+\delta_-}A_{m'}(\omega)e^{-i\frac{\omega}{c}x_{m'}} +\sum_{m'=1}^{m-1}\left(\frac{\Omega}{\delta_2}\right)\left(\frac{-i\gamma_3^r}{2}\right)\frac{\delta_2}{\delta_+\delta_-}B_{m'}(\omega)e^{-i\frac{\omega}{c}x_{m'}}\right] \tag{4.22}$$

$$B_m(\omega) = e^{i\frac{\omega}{c}x_m}\left[\left(\frac{\Omega^*}{\delta_3}\right)S^+(\omega)+\sum_{m'=1}^{m-1}\left(\frac{-i\gamma_3^r}{2}\right)\frac{\delta_2}{\delta_+\delta_-}B_{m'}(\omega)e^{-i\frac{\omega}{c}x_{m'}} +\sum_{m'=1}^{m-1}\left(\frac{\Omega^*}{\delta_3}\right)\left(\frac{-i\gamma_2^r}{2}\right)\frac{\delta_3}{\delta_+\delta_-}A_{m'}(\omega)e^{-i\frac{\omega}{c}x_{m'}}\right], \tag{4.23}$$

with $S^+(\omega)$ defined in Eq. (4.25). We have adopted the short-hand notation $\delta_{s/2/3}=\omega-\omega_{s/2/3}+i\frac{\gamma_{s/2/3}}{2}$ and $\delta_\pm=\omega-\omega_\pm$. We introduce the two new

frequencies $\omega_\pm$ according to

$$\omega_\pm = \frac{\left(\omega_2 - i\frac{\gamma_2}{2}\right) + \left(\omega_3 - i\frac{\gamma_3}{2}\right)}{2} \pm \sqrt{\left(\frac{\left(\omega_2 - i\frac{\gamma_2}{2}\right) - \left(\omega_3 - i\frac{\gamma_3}{2}\right)}{2}\right)^2 + |\Omega|^2}. \tag{4.24}$$

Note that these new *eigen*frequencies exactly correspond to the new frequencies appearing in the semiclassical models, see *e.g.* Eq. (3.66). Now, however, they are defined in their most general form ($\omega_2 \neq \omega_3$ and $\gamma_2 \neq \gamma_3$).
For the moment, let us neglect the phase factors in Eq. (4.22) and Eq. (4.23). They only give rise to an overall phase factor of the solution of A_m (and B_m) proportional to x_m.
According to this set of equations, there are five ways to reach state $|2\rangle$ or state $|3\rangle$ in nucleus m, corresponding respectively with $A_m(\omega)$ and $B_m(\omega)$. These five paths can be divided into one source path $S^+(\omega)$, two intranuclear paths (transitions in nucleus m) and two extranuclear paths (transitions in different nuclei). It is obvious that every scattering process should include (and start with) the source path, which is given by the expression:

$$S^+(\omega) \equiv \left(\frac{V_{P_k S}}{\hbar}\right)\left(\frac{-i\sqrt{\gamma_2^r}}{2}\right)\frac{\delta_3}{\delta_s\delta_+\delta_-} \tag{4.25}$$

As we consider the incidence of a σ^+ photon, the source path always yield an excitation to state $|2\rangle$ (in any nucleus m).
The two intranuclear paths arise due to the mixing interaction and are schematically depicted in Fig. 4.2. The two extranuclear paths are shown in Fig.4.3

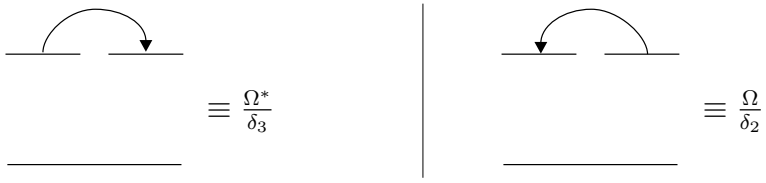

Figure 4.2: Pictographical representation of the two intranuclear paths along with their mathematical expression.

and represent the process of σ^+ (σ^-) emission in nucleus m' and absorption of this σ^+ (σ^-) photon by nucleus m, with $m' < m$.
Now, to find a solution for $A_m(\omega)$ and $B_m(\omega)$, for arbitrary m, it is a question of counting. First, to reach state $|2\rangle$ or $|3\rangle$ in nucleus m, not all preceding nuclei have to participate in the scattering process. If n nuclei are involved,

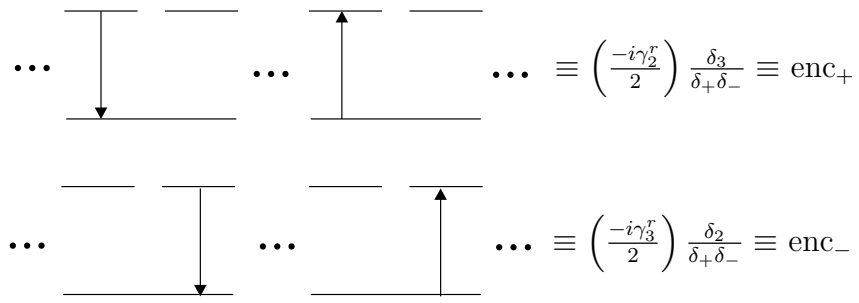

Figure 4.3: Pictographical representation of the two extranuclear paths (or extranuclear combinations (enc)) along with their mathematical expression.

then

$$A_m(\omega) = \sum_{n=0}^{m-1} \left(\begin{array}{c} m-1 \\ n \end{array} \right) A_m^n(\omega), \tag{4.26}$$

where the binomial coefficient gives the number of ways n nuclei can be picked out of a set of $m-1$ nuclei. $A_m^n(\omega)$ describes the amplitude of state $|2\rangle$ in nucleus m, for the case where the photon has first been scattered by n preceding nuclei.
Each nucleus can interact in 4 possible ways, depending on the polarization state of the absorbed and emitted photon: $++$, $--$, $+-$ and $-+$. However, there are certain restrictions. If a nucleus has emitted a σ^+ photon, then the next nucleus must absorb this σ^+ photon, and, hence, it has only two possible ways of interacting ($++$ and $+-$). Therefore, it is better not to consider all possible nuclear configurations, as they are not truly independent, but to consider the combination of emission in one nucleus and absorption in a following one. In Fig. 4.4 it is shown that these extranuclear combinations (or: enc) can assume values of $+$ and $-$, independent of the preceding enc. They also coincide with the extranuclear paths identified in Fig. 4.3.

If there are $n+1$ absorber nuclei (n preceding $+$ the last one) and if we apply the initial condition of a σ^+ incident photon and the final condition of arriving in state $|2\rangle$ (or $|3\rangle$), there are n enc. Thus, there are 2^n possible paths contributing to $A_m^n(\omega)$.
If there are p enc_+, then there should be $n-p$ enc_- processes. The number of *intranuclear* paths depends on how the p enc_+ are arranged between the $n-p$ enc_-. For example, for $n=5$ and $p=3$, the $+++--$ enc series yield a different number of intranuclear paths than the $+-+-+$ enc series. It can be shown that, if k denotes the number of enc_+ enclosed by at least one enc_-

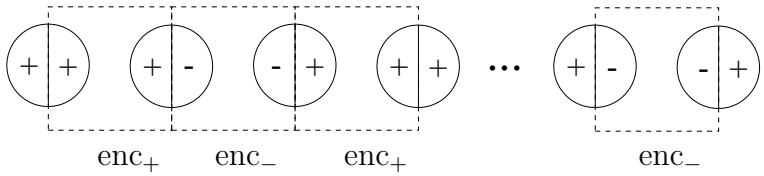

Figure 4.4: Schematical representation of scattering of a σ^+ incident photon leading to the excitation of state $|2\rangle$ in nucleus m. Each nucleus that takes part in the process is depicted by a circle where the left half represents the absorption and the right half the emission process. The dashed squares represent the independent extranuclear combinations (see text).

(preceding and succeeding), then

$$\sum_{k=0}^{p} \begin{pmatrix} n-p-1 \\ k \end{pmatrix} \left(\frac{|\Omega|^2}{\delta_2\delta_3}\right)^{k+1} \sum_{l=0}^{(p-k-1)} \begin{pmatrix} p-k-1 \\ l \end{pmatrix} \begin{pmatrix} k+2 \\ l+1 \end{pmatrix} \tag{4.27}$$

for $A_m^n(\omega)$, and

$$\frac{\Omega^*}{\delta_3} \sum_{k=0}^{p} \begin{pmatrix} n-p \\ k \end{pmatrix} \left(\frac{|\Omega|^2}{\delta_2\delta_3}\right)^{k} \sum_{l=0}^{(p-k-1)} \begin{pmatrix} p-k-1 \\ l \end{pmatrix} \begin{pmatrix} k+1 \\ l+1 \end{pmatrix} \tag{4.28}$$

for $B_m^n(\omega)$ are the amplitudes of intranuclear paths belonging to each (n,p) pair. The sum over l accounts for the possible ways to arrange $(p-k)$ other enc_+ on $(k+2)$ (or $(k+1)$) places.
Finally, taking into account the above prescription, we can reconstruct the solutions:

$$\begin{aligned} A_m(\omega) = {} & \frac{-i\sqrt{\gamma_2^r}}{2} \left(\frac{V_{P_k S}}{\hbar}\right) \frac{\delta_3 \; e^{i\frac{\omega}{c}x_m}}{\delta_s\delta_+\delta_-} \left[1 + \sum_{n=1}^{m-1} \begin{pmatrix} m-1 \\ n \end{pmatrix} \frac{1}{(\delta_+\delta_-)^n} \right. \\ & \times \left\{ \left(\frac{-i\gamma_2^r\delta_3}{2}\right)^n + \sum_{p=0}^{n-1} \left(\frac{-i\gamma_3^r\delta_2}{2}\right)^{n-p} \left(\frac{-i\gamma_2^r\delta_3}{2}\right)^p \right. \\ & \times \left[\begin{pmatrix} n-p-1 \\ p \end{pmatrix} \left(\frac{|\Omega|^2}{\delta_2\delta_3}\right)^{p+1} \right. \\ & \left. \left. \left. + \sum_{k=0}^{p-1} \begin{pmatrix} n-p-1 \\ k \end{pmatrix} \left(\frac{|\Omega|^2}{\delta_2\delta_3}\right)^{k+1} \sum_{l=0}^{(p-k-1)} \begin{pmatrix} p-k-1 \\ l \end{pmatrix} \begin{pmatrix} k+2 \\ l+1 \end{pmatrix} \right] \right\} \right] \end{aligned} \tag{4.29}$$

and

$$
\begin{aligned}
B_m(\omega) \;=\; & \frac{-i\sqrt{\gamma_2^r}}{2}\left(\frac{V_{P_kS}}{\hbar}\right)\frac{\Omega^*\; e^{i\frac{\omega}{c}x_m}}{\delta_s\delta_+\delta_-}\left\{1+\sum_{n=1}^{m-1}\left(\begin{array}{c} m-1 \\ n \end{array}\right)\frac{1}{(\delta_+\delta_-)^n}\right. \\
& \times\sum_{p=0}^{n}\left(\frac{-i\gamma_3^r\delta_2}{2}\right)^{n-p}\left(\frac{-i\gamma_2^r\delta_3}{2}\right)^{p}\left[\left(\begin{array}{c} n-p \\ p \end{array}\right)\left(\frac{|\Omega|^2}{\delta_2\delta_3}\right)^{p}\right. \\
& \left.\left.+\sum_{k=0}^{p-1}\left(\begin{array}{c} n-p \\ k \end{array}\right)\left(\frac{|\Omega|^2}{\delta_2\delta_3}\right)^{k}\sum_{l=0}^{(p-k-1)}\left(\begin{array}{c} p-k-1 \\ l \end{array}\right)\left(\begin{array}{c} k+1 \\ l+1 \end{array}\right)\right]\right\}.
\end{aligned}
\tag{4.30}
$$

The binomials in the above expressions of course vanish whenever the lower term exceeds the upper term. We have also checked the result manually up to $m = 5$.

Solution of the photon wave function

Let us first consider the σ^+ photon field. Substituting the expression for $S(\omega)$ and $A_m(\omega)$ into Eq. (4.8), we find an expression for $P_k^+(\omega)$

$$
P_k^+(\omega) = \left(\frac{V_{P_kS}}{\hbar}\right)\frac{1}{\delta_s\left(\omega-\omega_k+i\epsilon\right)}\left(1-\frac{i\gamma_2^r}{2}\sum_{m=1}^{N}P_{k,m}^+(\omega)\right) \tag{4.31}
$$

with

$$
\begin{aligned}
P_{k,m}^+(\omega) = {} & e^{i\frac{x_m}{c}(\omega-\omega_k)}\frac{\delta_3}{\delta_+\delta_-}\left[1+\sum_{n=1}^{m-1}\left(\begin{array}{c} m-1 \\ n \end{array}\right)\frac{1}{(\delta_+\delta_-)^n}\left\{\left(\frac{-i\gamma_2^r\delta_3}{2}\right)^{n}\right.\right. \\
& +\sum_{p=0}^{n-1}\left(\frac{-i\gamma_3^r\delta_2}{2}\right)^{n-p}\left(\frac{-i\gamma_2^r\delta_3}{2}\right)^{p}\left[\left(\begin{array}{c} n-p-1 \\ p \end{array}\right)\left(\frac{|\Omega|^2}{\delta_2\delta_3}\right)^{p+1}\right. \\
& \left.\left.\left.+\sum_{k=0}^{p-1}\left(\begin{array}{c} n-p-1 \\ k \end{array}\right)\left(\frac{|\Omega|^2}{\delta_2\delta_3}\right)^{k+1}\sum_{l=0}^{p-k-1}\left(\begin{array}{c} p-k-1 \\ l \end{array}\right)\left(\begin{array}{c} k+2 \\ l+1 \end{array}\right)\right]\right\}\right].
\end{aligned}
\tag{4.32}
$$

The interpretation of $P_k^+(\omega)$ is straightforward. The first term is the amplitude of a photon k that is not scattered (the original σ^+ source photon), while the subsequent terms describe the amplitudes for scattering at position x_1, x_2, ...x_m. The factor δ_s^{-1} will eventually lead to a convolution of the (frequency) spectrum of the photon field with the spectrum of the incident field, centered at ω_s. Hence, this term is equivalent to the $A^{\pm}(\omega, 0, v)$ term in Eq.

(3.12).

According to [117–121], one can represent the (one-dimensional) radiation wave function $\psi(x,t)$ as an infinite sum of plane waves

$$\psi(x,t) = \sum_k \frac{e^{i(kx-\omega_k t)}}{\sqrt{L}} p_k(t) = \frac{\sqrt{L}}{2\pi c} \int_{-\infty}^{\infty} d\omega_k \, e^{-i\omega_k (t-\frac{x}{c})} p_k(t) \tag{4.33}$$

with $p_k(t)$ the time-dependent (classical) amplitude of a plane wave with wave number k. We admit that this transition from the quantum to the classical domain is rather sudden and should be more thoroughly derived. In the next section we will try to justify this suggestion for the photon wave function, by extending our discussion of the introductory section. For now, we take Eq. (4.33) for granted and continue the derivation of the wave function.
It is also possible to express $\psi(x,t)$ in frequency domain by a Fourier transformation of Eq. (4.33):

$$\psi(x,\omega) = \int_{-\infty}^{\infty} dt \, \psi(x,t) e^{i\omega t} \tag{4.34}$$

$$= \frac{\sqrt{L}}{2\pi c} \int_{-\infty}^{\infty} d\omega_k \, e^{i\omega_k \frac{x}{c}} \underbrace{\int_{-\infty}^{\infty} dt p_k(t) e^{i(\omega-\omega_k)t}}_{=iP_k(\omega)} \tag{4.35}$$

If we consider the ω_k-dependent terms of $P_k^+(\omega)$ in Eq. (4.31), then we distinguish the m-th absorber term ($P_{k,m}^+(\omega)$), which has a phase factor proportional to x_m, and a source term ($P_s(x,\omega)$), without phase factor[3]. The calculation of the integral over ω_k is reduced to the integration of these ω_k-dependent terms (see appendix C on the theorem of residues):

$$\psi_s(x,\omega) \propto \int_{-\infty}^{\infty} d\omega_k \, \frac{e^{i\omega_k \frac{x}{c}}}{\omega - \omega_k + i\epsilon} \tag{4.36}$$

$$\propto 2\pi i e^{i\omega \frac{x}{c}} \theta(x) \qquad \text{for } \epsilon \to 0^+ \tag{4.37}$$

and

$$\psi_{k,m}^+(x,\omega) \propto e^{i\omega \frac{x_m}{c}} \int_{-\infty}^{\infty} d\omega_k \, \frac{e^{i\omega_k \left(\frac{x}{c} - \frac{x_m}{c}\right)}}{\omega - \omega_k + i\epsilon} \tag{4.38}$$

$$\propto 2\pi i e^{i\omega \frac{x}{c}} \theta(x - x_m) \qquad \text{for } \epsilon \to 0^+ \tag{4.39}$$

The appearance of the $\theta(x)$ Heaviside step function ensures a physical meaningful result. For the source term this means the detector position x should be

[3] This is because we have chosen $x_0 = 0$.

downstream of the source (nucleus), located at $x = 0$, whereas the m-th absorber term only is relevant when this m-th nucleus is in front of the detector. The σ^+ photon field is now calculated as

$$\psi^+(x,\omega) = e^{i\omega\frac{x}{c}}\psi_s(\omega)\left(1+\sum_{n=0}^{N-1}\left(\begin{array}{c} N \\ n+1 \end{array}\right)\psi_n^+(\omega)\right) \tag{4.40}$$

with the source term

$$\psi_s(\omega) = -\left(\frac{V_{P_kS}\sqrt{L}}{\hbar c}\right)\frac{1}{\delta_s} \tag{4.41}$$

and the absorber terms

$$\begin{aligned}\psi_n^+(\omega) &= \frac{1}{(\delta_+\delta_-)^{n+1}}\left(\left(\frac{-i\gamma_2^r\delta_3}{2}\right)^{n+1}+\sum_{p=0}^{n-1}\left(\frac{-i\gamma_3^r\delta_2}{2}\right)^{n-p}\left(\frac{-i\gamma_2^r\delta_3}{2}\right)^{p+1}\right. \\ &\times\left[\left(\begin{array}{c} n-p-1 \\ p \end{array}\right)\left(\frac{|\Omega^2|}{\delta_2\delta_3}\right)^{p+1}+\sum_{k=0}^{p-1}\left(\begin{array}{c} n-p-1 \\ k \end{array}\right)\left(\frac{|\Omega^2|}{\delta_2\delta_3}\right)^{k+1}\right. \\ &\left.\left.\times\sum_{l=0}^{p-k-1}\left(\begin{array}{c} p-k-1 \\ l \end{array}\right)\left(\begin{array}{c} k+2 \\ l+1 \end{array}\right)\right]\right).\end{aligned} \tag{4.42}$$

It is seen that, due to the reconstruction of the total wave packet, the dependence on the positions of the individual scattering centers disappears. Instead, the field amplitude gains a uniform phase factor, which only depends on the total path length x between its creation in the source and its destruction at the detector. Moreover, this phase factor is identical to the phase factor obtained in the semiclassical models, see *e.g.* Eq. (3.8).
The derivation of the σ^- photon wave function is completely analogous. Eventually, we obtain the σ^- wave function

$$\psi^-(x,\omega) = e^{i\omega\frac{x}{c}}\psi_s(\omega)\sum_{n=0}^{N-1}\left(\begin{array}{c} N \\ n+1 \end{array}\right)\psi_n^-(\omega) \tag{4.43}$$

with $\psi_s(\omega)$ defined in Eq. (4.41) and

$$\begin{aligned}\psi_n^-(\omega) &= \left(\frac{-i\sqrt{\gamma_2^r\gamma_3^r}}{2}\right)\frac{\Omega^*}{(\delta_+\delta_-)^{n+1}}\left(\sum_{p=0}^{n}\left(\frac{-i\gamma_3^r\delta_2}{2}\right)^{n-p}\left(\frac{-i\gamma_2^r\delta_3}{2}\right)^{p}\right. \\ &\times\left[\left(\begin{array}{c} n-p \\ p \end{array}\right)\left(\frac{|\Omega^2|}{\delta_2\delta_3}\right)^{p}+\sum_{k=0}^{p-1}\left(\begin{array}{c} n-p \\ k \end{array}\right)\left(\frac{|\Omega^2|}{\delta_2\delta_3}\right)^{k}\right. \\ &\left.\left.\times\sum_{l=0}^{p-k-1}\left(\begin{array}{c} p-k-1 \\ l \end{array}\right)\left(\begin{array}{c} k+1 \\ l+1 \end{array}\right)\right]\right).\end{aligned} \tag{4.44}$$

Except for the source term, the expression of the σ^- wave function bears a very close resemblance with the σ^+ wave function. So, once the photon has undergone one scattering, both fields develop in more or less the same way.
In the case without mixing interaction ($\Omega = 0$), the photon fields reduce to

$$\psi^+(x,\omega) = e^{i\omega\frac{x}{c}}\psi_s(\omega)\left[1+\sum_{n=1}^{N}\begin{pmatrix} N \\ n \end{pmatrix}\left(-\frac{i\gamma_2^r}{2}\frac{1}{\delta_2}\right)^n\right], \tag{4.45}$$

$$\psi^-(x,\omega) = 0, \tag{4.46}$$

which is exactly the Fourier transform of the time-dependent photon wave function calculated by Hoy in the case of scattering in a single-resonance nuclear medium (see Eq.(A24) in [118]).

The measurable transmitted intensity in the case of a σ^+ source photon as a function of ω_s is given by

$$I(\omega_s) = \frac{1}{2\pi}\int_{-\infty}^{\infty} d\omega\ \left(|\psi^+(x,\omega)|^2 + |\psi^-(x,\omega)|^2\right), \tag{4.47}$$

which is the observable that should be compared with the experimental spectra.

4.2.3 The photon wave function in more detail

The aim of this section is to justify the use of Eq. (4.33) as the photon wave function. In the introduction we already discussed the 'fuzzy' nature of this concept, but argued that, following Scully and Zubairy [17], it is possible to assign a photon wave function status to the probability that a single photon will lead to the ejection of a photo-electron in a detector at point $\mathbf{r}$. As shown in the introductory section, the photon wave function $\psi(\mathbf{r},t)$ is then given by [17]

$$\psi(\mathbf{r},t) = \langle 0|\mathbf{E}^{(+)}(\mathbf{r},t)|\psi_\gamma\rangle \tag{4.48}$$

with $|\psi_\gamma\rangle$ the single photon field state and $\mathbf{E}^{(+)}(\mathbf{r},t)$ the positive frequency part of the electric field operator, defined in Eq. (3). In the following, we assume that the electric field is polarized and thus discard the sum over λ.
Let us now try to find an expression for this $|\psi_\gamma\rangle$ in the coherent path model. For simplicity, we only consider a source nucleus, and deal with the radiation it emits. Substituting the expression of the 'source' amplitude $S(\omega)$ of Eq. (4.16) in Eq. (4.8) we find that

$$P_{\mathbf{k}}(\omega) = \left(\frac{V_{P_{\mathbf{k}}}S}{\hbar}\right)\frac{e^{-i\mathbf{k}.\mathbf{r_0}}}{(\omega-\omega_k+i\epsilon)\left(\omega-\omega_s+i\frac{\gamma_s}{2}\right)} \tag{4.49}$$

where we discarded the polarization dependence. Note that this equation is expressed in its three-dimensional form with $\mathbf{r_0}$ the position of the source nucleus. Applying the Fourier transform (Eq. 4.3) back to time domain, we have

$$s(t) = e^{-\gamma_s t/2} \tag{4.50}$$

and

$$p_{\mathbf{k}}(t) = \left(\frac{V_{P_{\mathbf{k}}S}}{\hbar}\right) e^{-i\mathbf{k}.\mathbf{r_0}} \frac{1 - e^{it(\omega_k - \omega_s + i\gamma_s/2)}}{\omega_k - \omega_s + i\frac{\gamma_s}{2}} \tag{4.51}$$

According to Eq. (4.1), the state vector of this system can now be reconstructed as

$$\begin{aligned} |\Psi(t)\rangle &= e^{-i\omega_s t} e^{-\gamma_s t/2} |S^e, \{0_{\mathbf{k}}\}\rangle \\ &+ \sum_{\mathbf{k}} \left(\frac{V_{P_{\mathbf{k}}S}}{\hbar}\right) e^{-i\omega_k t} e^{-i\mathbf{k}.\mathbf{r_0}} \frac{1 - e^{it(\omega_k - \omega_s + i\gamma_s/2)}}{\omega_k - \omega_s + i\frac{\gamma_s}{2}} |S^g, 1_{\mathbf{k}}\rangle. \end{aligned} \tag{4.52}$$

However, to stay consistent with the derivation of the photon wave function, resulting in the definition in Eq. (4.48), we should express this state vector in an interaction representation. In this transition only the exponential factors corresponding to the eigenfrequencies of the states are omitted. The resulting expression now exactly equals Eq. (6.3.17) of [17], where the state vector of a decaying two-level atom is derived in a fully quantum mechanical way. Now, we can define the single-photon field state by taking the trace over the nuclear subsystem:

$$|\psi_\gamma(t)\rangle = \sum_{\mathbf{k}} p_{\mathbf{k}}(t) |1_{\mathbf{k}}\rangle \tag{4.53}$$

$$= \sum_{\mathbf{k}} \left(\frac{V_{P_{\mathbf{k}}S}}{\hbar}\right) e^{-i\mathbf{k}.\mathbf{r_0}} \frac{1 - e^{it(\omega_k - \omega_s + i\gamma_s/2)}}{\omega_k - \omega_s + i\frac{\gamma_s}{2}} |1_{\mathbf{k}}\rangle \tag{4.54}$$

which actually is a linear superposition of single-photon states with different wave vectors. Substituting this result and Eq.(3) into Eq. (4.48), we find

$$\psi(\mathbf{r}, t) = \sum_{\mathbf{k},\mathbf{k}'} \mathcal{E}_{\mathbf{k}'} \left(\frac{V_{P_{\mathbf{k}}S}}{\hbar}\right) e^{-i\omega_{k'} t} e^{i(\mathbf{k}'.\mathbf{r} - \mathbf{k}.\mathbf{r_0})} \frac{1 - e^{it(\omega_k - \omega_s + i\gamma_s/2)}}{\omega_k - \omega_s + i\frac{\gamma_s}{2}} \langle 0|a_{\mathbf{k}}|\psi_\gamma\rangle \tag{4.55}$$

$$= \sum_{\mathbf{k}} \mathcal{E}_{\mathbf{k}} \left(\frac{V_{P_{\mathbf{k}}S}}{\hbar}\right) e^{-i\omega_k t} e^{i\mathbf{k}.(\mathbf{r} - \mathbf{r_0})} \frac{1 - e^{it(\omega_k - \omega_s + i\gamma_s/2)}}{\omega_k - \omega_s + i\frac{\gamma_s}{2}} \tag{4.56}$$

$$= \sum_{\mathbf{k}} \mathcal{E}_{\mathbf{k}} e^{i\mathbf{k}.\mathbf{r} - i\omega_k t} p_{\mathbf{k}}(t) \tag{4.57}$$

This last expression for the photon wave function equals the suggested expression in Eq. (4.33), except for the $\mathcal{E}_{\mathbf{k}}$ factor. Evaluating the sum over $\mathbf{k}$ in the Weisskopf-Wigner approximation[4], this term only yields an overall multiplication factor and can be neglected if one is only interested in relative magnitudes.
Therefore, we can state that, although the introduction of the photon wave function in Eq. (4.33) was not well founded, its use for our purposes is now rigorously proven.

4.3 Thin absorber limit

We start the discussion of Eq. (4.40) and Eq. (4.43) with the most simple case, *i.e.* a thin absorber. This corresponds to a system where multiple scattering effects are negligible. Also in the most common experiments where optical EIT is observed, *i.e.* in vapors, dynamical effects are not taken into account. This limiting case, therefore, presents an ideal opportunity to make a thorough comparison between optical EIT and the nuclear level mixing induced transparency.
We could simply consider the case where there is only one absorber nucleus or $N = 1$. However, it is more interesting to retain the first term ($n = 0$) of the photon field for N absorber nuclei. From Eq. (4.40) and Eq. (4.43) we obtain:

$$\psi_1^+(x,\omega) = e^{i\omega\frac{x}{c}}\psi_s(\omega)\left[1 + N\left(\frac{-i\gamma_2^r}{2}\right)\frac{\delta_3}{\delta_+\delta_-}\right] \tag{4.58}$$

$$\psi_1^-(x,\omega) = e^{i\omega\frac{x}{c}}\psi_s(\omega)N\left(\frac{-i\sqrt{\gamma_2^r\gamma_3^r}}{2}\frac{\Omega^*}{\delta_+\delta_-}\right), \tag{4.59}$$

where all parameters have been defined in the previous section. If we disregard the convolution with the source spectrum, then the transmitted intensity is given, to first order in γ_2^r, by

$$I_1(\omega) = 1 + 2\Im\left(N\frac{\gamma_2^r}{2}\frac{\delta_3}{\delta_+\delta_+}\right). \tag{4.60}$$

This expression equals the semiclassical results, given by Eq. (3.21) and Eq. (3.68). A one-to-one correspondence between the models is found when

$$N = \frac{3}{8}\frac{T_e\gamma}{\gamma_r}, \tag{4.61}$$

[4]We deal with the explicit evaluation of Eq. (4.57) in section 5.2.

where the 3/8 factor is already correctly dealt with by Eq. (4.6) and originates from the multilevel system. We further investigate this expression and the relation with the semiclassical models in more detail in section 4.4.1.
For a discussion of the expression obtained in Eq. (4.60), we refer to the semiclassical models. Here, we briefly consider the case where $\omega_2 \neq \omega_3$, because this was not included in the analysis of the previous chapter. In Fig. 4.5 the transmitted intensity is simulated for different values of $\omega_2 - \omega_3 \equiv \Delta$. The influence of the mixing interaction decreases for increasing Δ, as is also clear from Eq. (4.24). It is shown in section 1.1.4 that the excited states are only fully mixed when $\Delta = 0$. Here, the reduction of the admixture of the coupling state $|3\rangle$, is seen as the decreasing amplitude of the left absorption peak. The creation of the orthogonal polarization state (I^{+-}) is also affected and is reducing with increasing Δ, as expected.
The analogue of Δ in optical EIT is the detuning of the driving field with respect to the $|2\rangle \rightarrow |3\rangle$ transition, see *e.g.* [65].

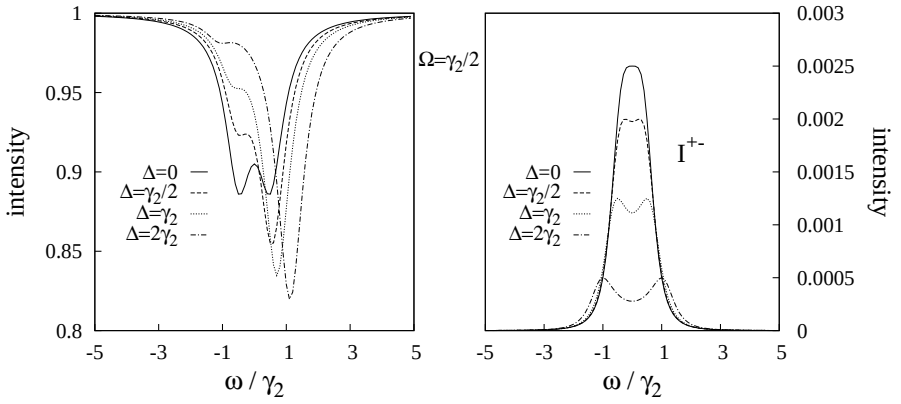

Figure 4.5: Simulated spectra of the transmitted intensity for $N = 1$, $\Omega = \gamma_2/2$, $\gamma_3 = \gamma_2$ for different values of Δ. The right figure shows the intensity of the radiation that has changed polarization (I^{+-}), while the left figure shows the total transmitted radiation.

4.4 Thick absorber: multiple scattering

Now we extend the model to include the case of a σ^- incident photon[5]. The radiative decay rates γ_2^r and γ_3^r are substituted with their real experimental values: $\gamma_2^r = |C_{12}|^2\gamma_r = \gamma_r/3$ and $\gamma_3^r = |C_{13}|^2\gamma_r = \gamma_r$. The treatment of thick absorbers in this section still differs somewhat from that of section 3.1.2. Here, the model is still limited to the three-level system. Also, the convolution with the spectrum of the source photon is discarded. These limitations hardly pose a threat to the generality of the simulations, but greatly reduce the computer power needed for the simulations. For example, the effect of the convolution with the Lorentzian source profile is to smooth out small[6] changes in the initial spectrum, as illustrated in Fig. 4.6.

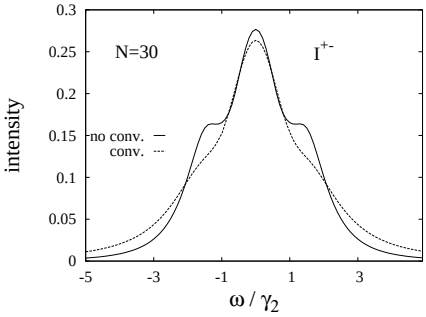

Figure 4.6: Illustration of the convolution of the spectrum of I^{+-}, for $N = 30$ and $\Omega = \gamma_2$, with the solid line representing the initial spectrum and the dashed line the convoluted spectrum.

But before discussing some simulations, we first try to make a detailed comparison with the semiclassical results.

4.4.1 Semiclassical vs. coherent path result

In the thin absorber limit, we could chose N in order to have a one-to-one correspondence between the semiclassical and coherent path results. But can this correspondence be extended for arbitrary thicknesses?
Absorbing the 3/8 factor of Eq. (4.61) into T_e, then $N\gamma_r = T_e\gamma$. It appears

[5]This is no more than interchanging the label '2' with label '3' in the equations for a σ^+ incident source photon.

[6]Small with respect to the line width γ_s of the source profile.

that it doesn't matter whether one uses N absorber nuclei with a decay rate (or: interaction constant) γ_r *or* T_e absorber nuclei with a an interaction constant γ. In the semiclassical models these two possibilities are perfectly interchangeable, because they are treated on an equal footing (as a factor in the exponential function). However, in the coherent path model, interchanging both sets results in quite different spectra. This is most pronounced in the extreme case of setting $N = 1$, which combines with a large scattering amplitude $\gamma_r = T_e\gamma$. The coherent path intensity for this single nucleus absorber will never show multiple scattering effects, for any value of γ_r. The semiclassical result, however, only depends on the product $N\gamma_r$ and will show multiple scattering effects, if the product is large enough, of course.
We can treat the problem in a more general way by introducing the dimensionless variable x:

$$N\gamma_r = (Nx)\frac{\gamma_r}{x} = N'\gamma_r', \tag{4.62}$$

with $N' = Nx$ and $\gamma_r' = \gamma_r/x$. In [118] Hoy also introduced such kind of variable, assuming that $x = f_{LM}^{-1}$. In this way, he increased the number of scattering nuclei (see his definition of N in Eq. (4.5)), but he decreased the amplitude with which they interact. One can certainly question this 'recoil free' modification. Does it follow naturally from the model or is it rather manually added? And how should this be interpreted?

In the semiclassical model, the exponential form of the spectrum function arises due to the assumption that the absorber is seen as the sum of infinitesimal slices dz. Each preceding slice acts as a source term for the next slice, which, in its simplest form, results in the differential equation

$$dE \propto Edz \tag{4.63}$$

for a radiative field E. The assumption of infinitesimal slices is justified when counting the (real) number of individual nuclei along the path of the incident radiation. Making use of the definition of T_e in Eq. (1.30), we can write

$$T_e\gamma = \underbrace{\left(f_{LM}\chi\rho\frac{d}{\sin(\beta+\theta)}A\right)}_{N'}\underbrace{\left(\frac{\sigma_0\gamma}{A}\right)}_{\gamma_r'}, \tag{4.64}$$

with A the area of the absorber surface. It is clear that the dimensionless variable $(A/\sigma_0) \equiv (\sigma_0')^{-1}$ plays the role of x in Eq. (4.62). If, for simplicity, we take a crystal of $A = 1\,\mathrm{cm}^2$ and assume that the incident radiation interacts with the whole crystal, then $N' = T_e(\sigma_0')^{-1} \approx 3.10^{18}$ ^{57}Fe nuclei (interacting without recoil). Although this (always) is a discrete number of nuclei, its approximation as a continuum of possible scattering centers is certainly not far-fetched.

Nevertheless, let us now assume that this continuum approximation should be replaced by the 'real' discrete scattering process. Thus, we use these values of a very large N' and a very small γ'_r in the coherent path model. For simplicity, we consider the single-resonance case as given by Eq. (4.45). The σ^+ photon field function can be expanded as

$$\begin{aligned}\psi^+(\omega) \quad \propto \quad & 1 + N'\left(\frac{-i\gamma'_r}{2\delta}\right) + \frac{N'(N'-1)}{2!}\left(\frac{-i\gamma'_r}{2\delta}\right)^2 \\ & + \frac{N'(N'-1)(N'-2)}{3!}\left(\frac{-i\gamma'_r}{2\delta}\right)^3 + ... \end{aligned} \tag{4.65}$$

Rearranging the terms and substituting $\gamma'_r = \sigma'_0\gamma$ and $N' = T_e(\sigma'_0)^{-1}$ yields

$$\begin{aligned}\psi^+(\omega) \quad \propto \quad & 1 + \left(\frac{-iT_e\gamma}{2\delta}\right) + \frac{1}{2!}\left(\frac{-iT_e\gamma}{2\delta}\right)^2 + \frac{1}{3!}\left(\frac{-iT_e\gamma}{2\delta}\right)^3 + ... \\ & + \sigma'_0\left[-\frac{1}{2!}\left(\frac{-iT_e\gamma}{2\delta}\right)^2 + \frac{2\sigma'_0 - 3}{3!}\left(\frac{-iT_e\gamma}{2\delta}\right)^3 + ...\right] \end{aligned} \tag{4.66}$$

Because $\sigma'_0 \approx 10^{-18}$, which in this case should be compared with processes of the order of 1, it is justified taking the limit $\sigma'_0 \to 0$:

$$\lim_{\sigma'_0 \to 0} \psi^+(\omega) \propto e^{-iT_e\frac{\gamma}{2\delta}}. \tag{4.67}$$

From the semiclassical point of view, one can state that this result, obtained in a fully quantum mechanical model (with discrete scattering events), validates the semiclassical exponential form of the scattering amplitude.
From the coherent path point of view, one can argue that only by taking the grid[7] and the interaction constant infinitesimally small the exponential form is recovered. However, due to the very low cross-section, only a limited number of nuclei ($N << T_e/\sigma'_0$) effectively participate in the scattering process, with this number given by Eq. (4.61). Furthermore, *when* a nucleus interacts with the radiation, it does so with an interaction strength γ_r, and not with γ_r/σ'_0. The derivation of γ_r in this model (see Eq. (4.15)) is very clear about this. Also, in a response to the multiplication of γ_r with f_{LM} suggested in [118], there is nothing in its definition that dictates us that γ_r should be multiplied with the recoil free fraction. γ_r is no more than the radiative interaction strength of a particular nuclear level, whether this nucleus recoils after emission or not. It is our opinion that the fact that only a fraction of the nuclei does not experience recoil, should, and can easily, be taken into account in N.
One can also imagine these effective nuclei as N 'super nuclei' or groups of

[7] We imagine the physical system as a grid, with each node representing a scattering center.

nuclei such that the probability of interaction with gamma radiation equals 1. Remember that this was also one of the premises early in the development of the model, *i.e.* we assumed that these nuclei *were* interacting.

Remark 1: We have consulted the exhaustive work of Hannon and Trammell on the dynamical theory of coherent gamma ray optics [123, 124] in the hope to shed some light on the issue of multiple scattering. They also treat the total scattering amplitude as a superposition of a finite sum of plane contributions. They explain that: "The amplitude that a wave $A_\mu(\mathbf{k}_{(s+)})$ is incident on the mth plane is equal to the amplitude that such a wave is incident on the $(m-1)$ plane, plus the forward scattering (...) of this wave by the $(m-1)$ plane (...)". This clearly agrees with the picture of scattering in the coherent path model. They also state that: "We assume that some set of infinite crystalline planes is parallel to the surface, which we take as the xy plane, and that the crystal is of finite thickness l in the z direction, $l = Md$, where M is the number of planes, and d is the interplanar distance. The thickness of the layers is rather arbitrary, but they must be sufficiently thin so that the Born approximation is good within the layer. We generally assume a unit cell thickness (chemical or magnetic, whichever is larger)." The Born approximation involves the neglect of planar self-action. It is shown that planar self-action leads to a change of the frequency and the width of the resonance [105] (the terms in the denominator of the forward scattering amplitude $\widetilde{f}(\omega)$). However, except for special cases like grazing incidence experiments, the Born approximation is very accurate.
According to this theory, in the case of a crystal with physical thickness $l \approx 10^{-4}$ m and unit cell thickness $d \approx 5$ Å, there are about 10^5 scattering planes. This is of course a much higher number than the $N = 20$ effective nuclei in the coherent path model, but it is certainly not an infinite number either. Although the authors claim that they solve the *finite difference* equations to obtain the final transmitted intensity, their result exactly matches the Blume-Kistner result, which, however, was obtained through a differential equation of the type of Eq. (4.63). We have not succeeded in unravelling the finite difference derivation of [124], but we believe that the same type of infinitesimal approximation of the plane thickness must have been used in order to obtain the same result as in the Blume-Kistner approach. In that respect it is even harder to understand why the plane thickness could be "rather arbitrary".
We can summarize that the work of Hannon and Trammell agrees with the fundamental picture of the coherent path model that the scattering process of radiation in a crystal has a discrete nature. However, this discreteness is *not* reflected in their final solution.

Remark 2: One could be led to believe that by seeking a one-to-one correspondence with the semiclassical models through Eq. (4.61), we grant these

models a higher level of confidence. This is only true in regard with their 'experience' of being used for multiple decennia. However, it is certainly possible to assign a value to N *independently* from the semiclassical result. In the coherent path model N is defined as the number of nuclei that effectively scatter the gamma photon. Hence, we have to count the number of ^{57}Fe nuclei along the photon path and multiply this with the interaction cross-section: $N = f_{LM}\sigma_0\chi\rho d/\sin(\beta+\theta)$. The recoil free fraction is added because only that fraction corresponds to 'resonant' nuclei, which actively participate in the scattering process. In the model also conversion electron decay is taken into account, though not explicitly (only by adding γ_c to the decay rate). However, σ_0 has been defined in Eq. (3.19) as the *radiative* cross-section. Hence, we should replace it by the total absorption cross-section

$$\sigma_T = \sigma_0 \frac{\gamma}{\gamma_r}. \tag{4.68}$$

The final expression for N now exactly equals Eq. (4.61), apart from the multilevel factor, with T_e given by Eq. (1.30).

Remark 3: We have compared higher order terms in the Taylor expansion of the semiclassical exponent, given in Eq. (3.2) and Eq. (3.18), with multiple scattering terms of Eq. (4.40) and Eq. (4.43). It is seen that, at least up to the fourth order, both results yield the same frequency dependent terms. If we apply $N = T_e\gamma/\gamma_r$ from the thin absorber limit, then each nth order term of the coherent path result $\psi_n(\omega)$ only differs from the semiclassical terms $A_n(\omega)$ by a numerical factor:

$$\psi_n(\omega) = A_n(\omega) \prod_{i=1}^{n-1} \frac{(N-i)}{N^{n-1}}. \tag{4.69}$$

4.4.2 Simulations for different N

Simulations for $N = 5$, 10, 20, 30, 50 and 80 are shown in Fig. 4.7, 4.8, and 4.9, respectively. Each right figure shows the individual contributions of the transmitted radiation that has changed polarization ($I^{+-} + I^{-+}$) and the radiation that has retained its polarization ($I^{++} + I^{--}$), while the left figure shows the total spectrum. We have also assumed a resonant fraction of $f_r = 0.3$, in correspondence with the assumptions made in section 3.1.2. This limits the maximal resonant absorption to 30% (or: compresses the spectrum by 30%). It is seen that this maximum absorption is almost reached for $N = 50$ and saturation clearly broadens the spectrum for $N = 80$.

Similar observations can be drawn from these simulations as from the simulations in the Blume-Kistner approach. Here, the Rabi splitting of the lines,

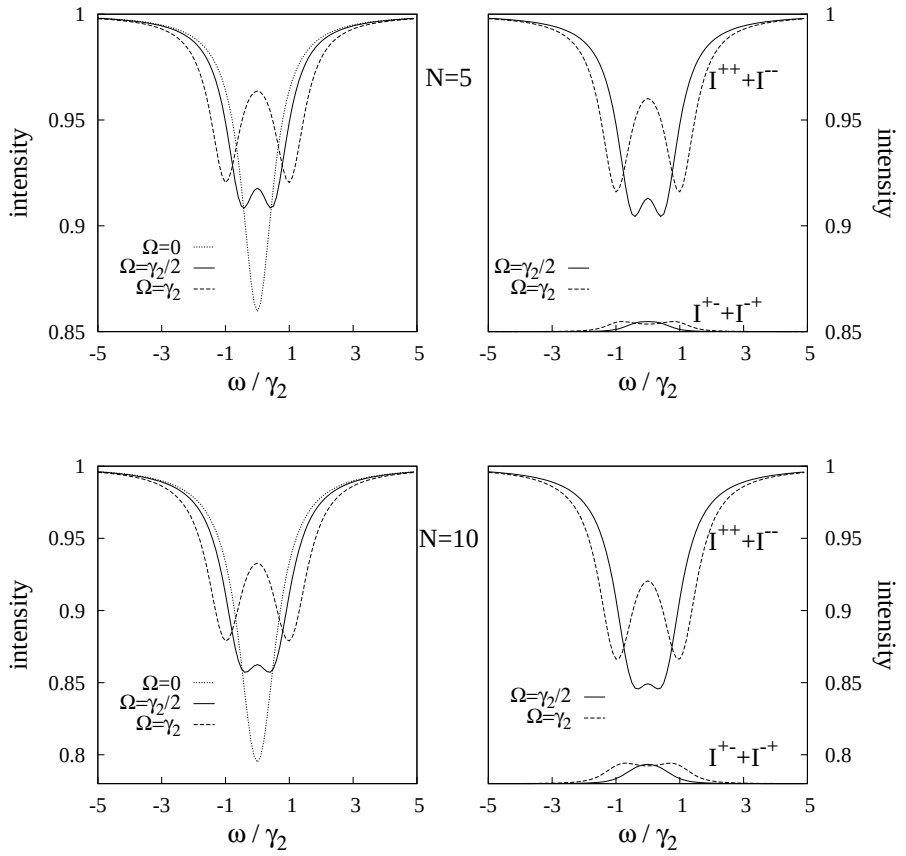

Figure 4.7: Simulated spectrum for $N = 5$ (top) and $N = 10$ (bottom) for different values of mixing interaction strength Ω. The right figure shows the individual contributions of the transmitted radiation that has changed polarization (I^{+-}) and the radiation that has kept its polarization (I^{++}), while the left figure shows the total transmitted radiation.

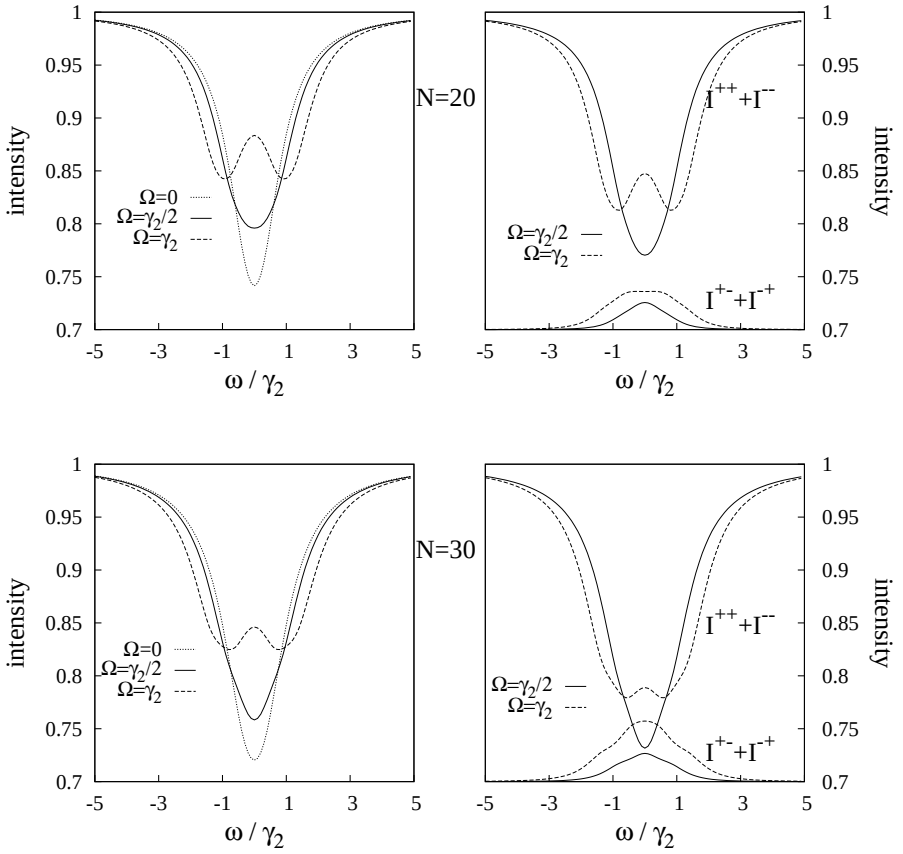

Figure 4.8: Simulated spectrum for $N = 20$ (top) and $N = 30$ (bottom) for different values of mixing interaction strength Ω. The right figure shows the individual contributions of the transmitted radiation that has changed polarization (I^{+-}) and the radiation that has kept its polarization (I^{++}), while the left figure shows the total transmitted radiation.

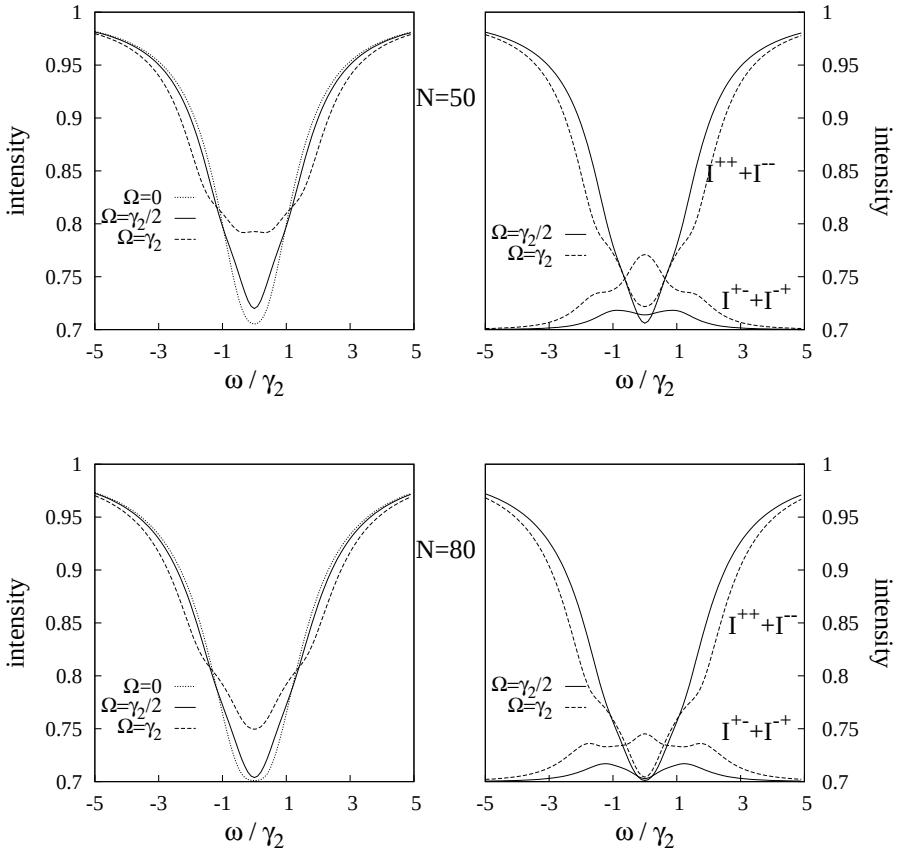

Figure 4.9: Simulated spectrum for $N = 50$ (top) and $N = 80$ (bottom)for different values of mixing interaction strength Ω. The right figure shows the individual contributions of the transmitted radiation that has changed polarization (I^{+-}) and the radiation that has kept its polarization (I^{++}), while the left figure shows the total transmitted radiation.

due to the mixing interaction, is more pronounced, which must be attributed to the neglect of the convolution with the incident photon spectrum. Also, there is less reduction in absorption with increasing thickness. For example, for $N = 5$, a mixing interaction of $\Omega = \gamma_2/2$ almost reduces the absorption at the line center with 50%, whereas the same mixing field has no observable effect any more for $N = 80$.
We can also see a shift in the mechanism of the transparency. First, for small N, the main reason for the transparency is the Rabi splitting of the excited states, which is best seen in the $I^{++} + I^{--}$ spectrum for $N = 5$. For increasing N, however, the contribution of the $I^{+-} + I^{-+}$ part becomes more important, see also Fig. 4.10. It first reaches a maximum, at line center, depending on Ω, and then shows a two- or three-peak structure. This two-peak structure (for $\Omega = \gamma_2/2$) was also found in the Blume-Kistner model (see Fig. 3.9). But the three-peak structure has no semiclassical analogue. More simulations have shown that the center peak eventually disappears for large N, leaving behind a two-peak structure.

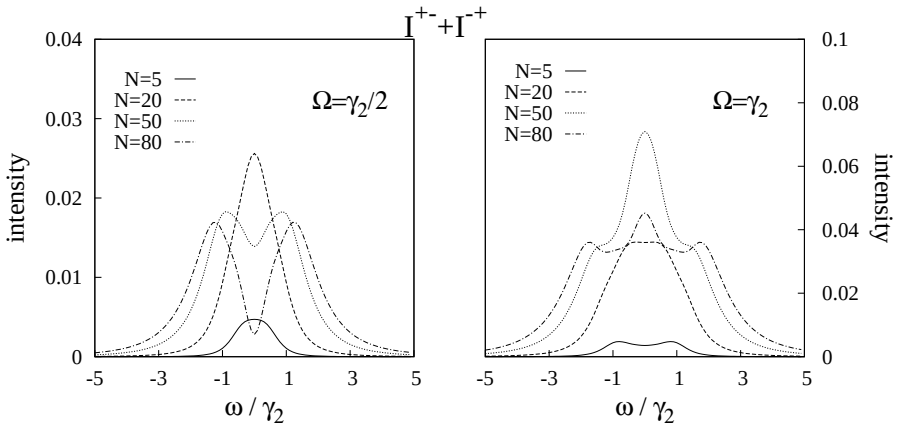

Figure 4.10: Simulated spectrum of the transmitted radiation that has changed polarization (I^{+-}) for different N and for $\Omega = \gamma_2/2$ (left) and $\Omega = \gamma_2$ (right).

More insight in the multiple scattering 'construction' of the final wave function is gained by simulating the different $\psi_n(\omega)$ terms of Eq. (4.42) (or Eq. (4.44)), *including the preceding binomial coefficient*. In [118] these $\psi_n(\omega)$ terms are referred to as the n-'hop' amplitudes[8], because n is the number of nuclei

[8]We must remark that, due the specific form of our result, a $\psi_n^+(\omega)$ term corresponds to

with which the photon interacts, while 'hopping' from one to the other. Simulations of the five first n-hop amplitudes for N=20 are shown in Fig. 4.11. The left part of the figure gives the hop amplitudes for $\Omega = 0$, expressed in Eq. (4.45), whereas the right part shows the $\psi_n^+(\omega)$ terms for $\Omega = \gamma_2/2$. It is clearly seen that the dominant first term yields a negative contribution, giving rise to the 'downward' absorption peak in the Mössbauer transmission spectrum. This is the result of the π-phase shift [118] for single scattering at resonance. The second term (double scattering) yields a positive contribution, the third term again negative, and so on. For increasing n, however, this simple picture is seen to blur out, leading to an oscillating and rapidly decreasing net contribution.

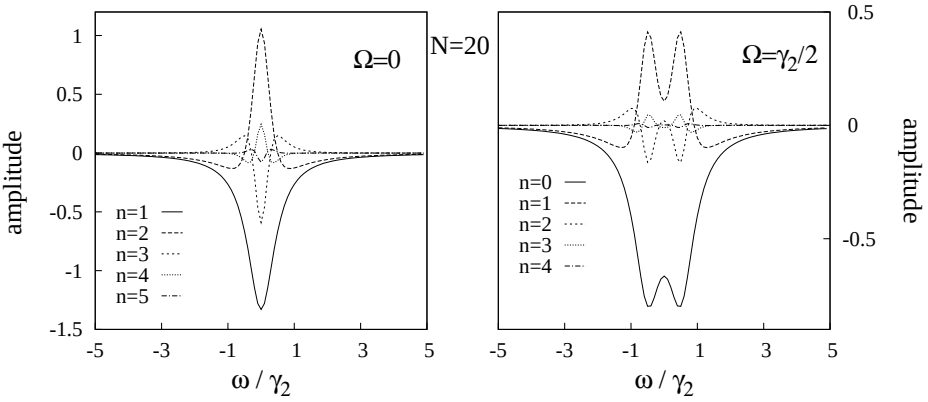

Figure 4.11: Simulation of the first n-hop amplitudes for N=20 with $\Omega = 0$ (left figure) and $\Omega = \gamma_2/2$ (right figure).

The $\psi_n^+(\omega)$ terms in Fig. 4.11 show a highly decreasing peak amplitude for increasing n. It is worthwhile to go into more detail on this. For simplicity, let us take $\gamma_2^r = \gamma_3^r \equiv \gamma_r$. Then the strength (or peak amplitude at resonance) of each n is seen to be proportional to

$$\psi_n^+(\omega = \omega_0) \propto \left(\begin{array}{c} N \\ n+1 \end{array} \right) \left(\frac{\gamma_r}{\gamma} \right)^{n+1} . \tag{4.70}$$

Because the condition that $\gamma_r < \gamma$ is always fulfilled, the second factor decreases exponentially for increasing n. The binomial coefficient, however, has a maximum for $n \approx N/2$. Hence, the significance of the contribution of an

an $n+1$-hop (only in the right figure).

n-hop amplitude depends on the interplay between both terms. For example, the $(n = 1)$-hop amplitude can gain a higher probability than the $(n = 0)$-hop amplitude if the condition $N > 1 + (2\gamma_r/\gamma)$ is satisfied (*e.g.* if $\gamma_r/\gamma = 0.1$ then $N > 21$). Nevertheless, it is clear from Eq. (4.70) that terms with $n > N/2$ will always yield a very small contribution. Thus, at least half of the n-hop amplitudes can be neglected in the calculations. In Fig. 4.12 we illustrate this convergence of n-hop amplitudes by simulating the $I^{+-} + I^{-+}$ spectrum for $N = 80$, including an increasing number of $\psi_n(\omega)$ terms. The solid line represents the full solution. It is seen that, already for $n = 0$ to 12, the spectrum matches the full solution within the resolving power of the eye.
This information about the rapid convergence of the ψ_n series can drastically cut into the quite extensive computer time needed for simulations in the coherent path model.

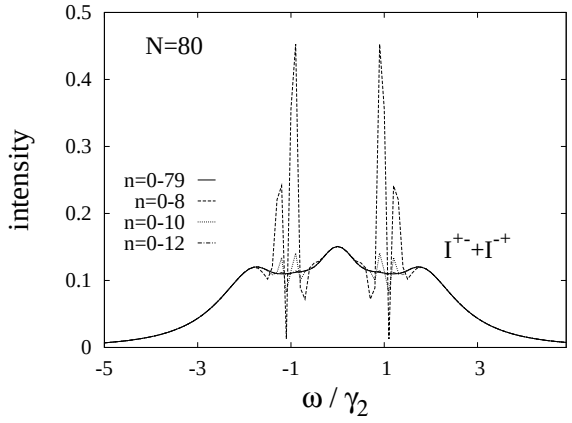

Figure 4.12: Simulation of the $I^{+-} + I^{-+}$ spectrum for $N = 80$, including an increasing number of $\psi_n(\omega)$ terms. The solid line represents the full solution.

This coherent path model also allows us to study the combined effect of different relaxation rates and multiple scattering in thick absorbers. Remember that in section 3.2.3 the Maxwell-Schrödinger approach also gives us the opportunity to investigate the case when $\gamma_3 \neq \gamma_2$. However, we only did so in the thin absorber limit. Now, let us consider the cases of $N = 5$ and $N = 20$. In Fig. 4.13 the total transmitted radiation is shown for $\Omega = \gamma_2/2$ and different values of γ_3, in the case of a σ^+ incident source photon. Comparing the spectra for N=5 with those of Fig. 3.17, we see that they are qualitatively equal. For $N = 20$, however, the spectra are considerably different. It is seen that the multiple scattering process destroys the transparency window. This can be

understood as follows: even in a perfect 'EIT nucleus' ($\gamma_3 << \gamma_2$) an incident photon will always show a little absorption from its wings. In the scattering process with the next perfect EIT nucleus there is again a little absorption. Eventually, the absorption profile will show a considerable absorption even in the frequency region where there is only negligible absorption in the single scattering event. In fact, this kind of explanation also holds for the effect of 'saturation broadening'. Hence, the effect of a decreasing reduction of absorption with increasing thickness is understood as a plain saturation effect.

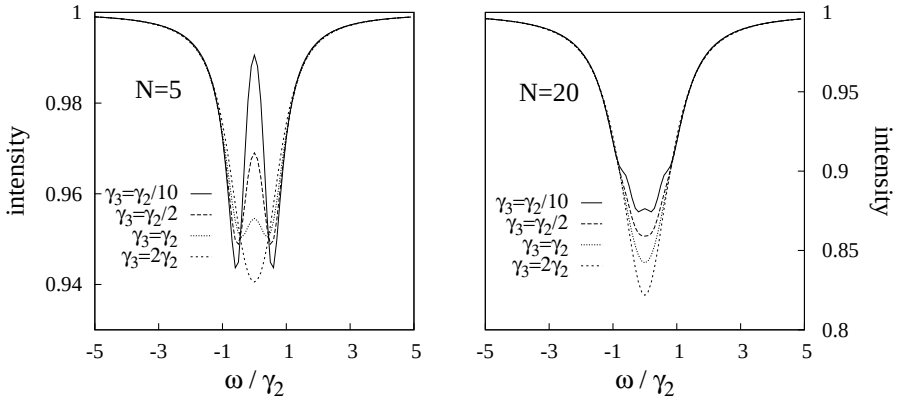

Figure 4.13: Simulation of the transmitted radiation in the case of $\Omega = \gamma_2/2$ for different values of γ_3, for $N = 5$ (left figure) and for $N = 20$ (right figure).

4.5 Conclusions

A fully quantum mechanical model for resonant scattering of gamma photons in a medium with an arbitrary number of nuclei, exhibiting a Λ-type of level structure, is developed. At the conceptual level, it is shown that the photon wave function obtained in this model corresponds to the probability amplitude that the photon gives rise to the detection of a photo-electron in a detector at position x.

Also, a detailed comparison with the semiclassical models reveals that the results of both models only coincide when $N \to \infty$ and $\gamma_r \to 0$, such that $N\gamma_r = T_e\gamma$. The question whether multiple scattering is best described by a

discrete scattering on N effective nuclei or by scattering on an infinite number of infinitesimal slices, however, remains unanswered. An experiment can be imagined that could shed some light on the true nature of the scattering process. Simulations show that for $N \approx 50$ a three-peak structure arises that is certainly due to the discrete scattering process in the coherent path model since it is not reproduced in the semiclassical models. In order to experimentally observe this I^{+-} $(+I^{-+})$ spectrum, a polarized source and a polarization dependent detection mechanism are required.
Otherwise, simulations of the Mössbauer spectra for different N are in close agreement with those obtained in the semiclassical models. In addition, it is seen that multiple scattering destroys the transparency window, simply because the absorption is saturated.

Chapter 5

Time-differential Mössbauer spectroscopy

No corporeal substance can be so subtle and swift as this.
William of Conches, 12th century

By identifying the observed reduced absorption as a (weak) form of EIT, a logical step is now to investigate the time properties of the scattered radiation. In section 2.1.2 it is mentioned that EIT is accompanied by a delay of the probe pulse, expressed as a reduction of the group velocity. Is it possible to delay gamma radiation in a similar way as optical radiation?
First, we approach this question from a theoretical point of view, in the semi-classical as well as in the coherent path model. Then, we extrapolate the results to an experimental setting and simulate a possible measurement of a time-differential Mössbauer spectrum.

5.1 Group velocity in the Maxwell-Schrödinger model

5.1.1 Concept

The concept of group velocity naturally arises when dealing with *wave packets*. Each wave (packet) may be regarded as a superposition of monochromatic wave of different frequencies (Fourier's theorem). To illustrate some of their properties, let us consider a wave $E(z,t)$ formed by the superposition of two monochromatic (plane) waves with the same amplitude $E_i(z,t) = E_0(z,t)\cos(k_i z - \omega_i t)$:

$$E(z,t) = E_1(z,t) + E_2(z,t) \tag{5.1}$$

$$= 2E_0 \cos(\Delta k\, z - \Delta\omega\, t)\cos(k_0 z - \omega_0 t), \tag{5.2}$$

with $\Delta k = (k_1 - k_2)/2$, $\Delta\omega = (\omega_1 - \omega_2)/2$, $k_0 = (k_1 + k_2)/2$ and $\omega_0 = (\omega_1 + \omega_2)/2$. As also illustrated in Fig. 5.1, the resulting wave packet has a 'carrier' wave with wave number k_0 and frequency ω_0, while its amplitude is modulated in time and space by $\cos(\Delta k\, z - \Delta\omega\, t)$. The carrier wave (or: the planes of constant phase) is propagating with the *phase velocity* $v_p = \omega_0/k_0$, while the envelope of the wave packet (or: the planes of constant amplitude) propagates with the *group velocity* $v_g = \Delta\omega/\Delta k$.

Because each wave packet obeys the wave equation, ω and k are related by the dispersion equation $kc = \omega n(\omega)$, with $n(\omega)$ the refractive index of the medium. In general, the group velocity is defined by

$$v_g = \left(\frac{d\omega}{dk}\right)_{k_0} \tag{5.3}$$

$$= \left(\frac{c}{n(\omega) + \omega\frac{dn(\omega)}{d\omega}}\right)_{k_0} \tag{5.4}$$

where $(..)_{k_0}$ signifies that v_g is evaluated at the wave vector of the carrier wave. The right-hand side of the second line in the above definition also assumes that there is no appreciable spatial dispersion, *i.e.* $\partial n/\partial k \approx 0$, which is valid in our case. In order to circumvent some interpretational problems, we only consider the case where the imaginary part of v_g is small and can be neglected.

5.1.2 Group velocity in the Λ-scheme

According to the definition of the group velocity in Eq. (5.4), if the index of refraction of the medium is known, then v_g can be deduced. For the case of

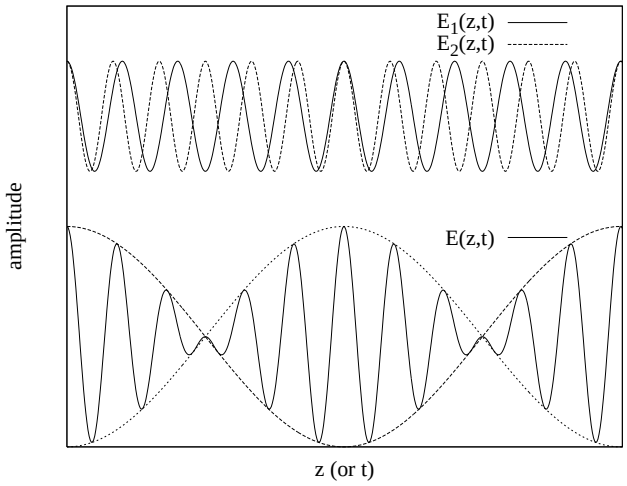

Figure 5.1: The wave packet $E(z,t)$ as a superposition of two monochromatic waves $E_1(z,t)$ and $E_2(z,t)$.

the nuclear Λ-scheme, see *e.g.* Fig. 3.16, we can use the results obtained in chapter 3. As shown before, the $\rho_{21}(\omega)$ coherence in Eq. (3.64) for $\gamma_2 \neq \gamma_3$ is proportional to the forward scattering amplitude $f^{+\pm}(\omega)$. Taking into account the correct proportionality factors, the index of refraction defined in Eq. (3.3) for this three-level system is given by

$$n^{++}(\omega) = 1 - \frac{3T_e}{16d}\frac{\gamma}{2k}|C_{21}|^2\frac{\delta_3}{\delta_+\delta_-} \tag{5.5}$$

$$n^{+-}(\omega) = 1 - \frac{3T_e}{16d}\frac{\gamma}{2k}C_{21}C_{13}\frac{\Omega}{\delta_+\delta_-} \tag{5.6}$$

where a distinction is made for radiation that has changed its polarization. All parameters have been defined before. Substituting $n(\omega)$ and its derivative in Eq. (5.4) we find that

$$\frac{v_g}{c} = \left[1 - \frac{\rho_l c}{\omega_0}\frac{\delta_3}{\delta_+\delta_-} + \frac{\rho_l c}{\gamma_2}\left(\frac{\delta_3(\delta_+ + \delta_-) - \delta_+\delta_-}{\delta_+^2\delta_-^2}\right)\right]^{-1} \tag{5.7}$$

for radiation that has retained its initial polarization, with $\rho_l = 3T_e|C_{21}|^2/(32d)$ a 'linear density' (or: the number of effective scattering nuclei per meter) and ω_0 the carrier frequency of the gamma radiation. In this expression, all δ_i are frequency differences divided by γ_2 and thus are dimensionless. Typical values

for the remaining parameters are: $\rho_l \approx T_e \times 10^5$ nuclei/m, $\omega_0 \approx 2.10^{19}$ Hz and $\gamma_2 \approx 7.10^6$ Hz. The second term is about 10^{12} times smaller than the third term and can therefore be neglected.
For radiation that has changed its polarization, however, the imaginary part of v_g is much larger than its real part. Therefore, we omit this case in the following discussion.

Let us first consider the ideal EIT case, *i.e.* when $\gamma_3 = 0$. If the radiation is tuned to the center of the (split) absorption line ($\omega = \omega_0$), the group velocity reduces to

$$v_g = \frac{c}{1 + \frac{\rho_l c}{\gamma_2}\frac{1}{\Omega^2}}, \tag{5.8}$$

which indeed matches the expression obtained in [78] (see Eq. (2.6)).
In Fig. 5.2 we calculate the group velocity as a function of ρ_l and Ω in the case of a 'nuclear' EIT scheme ($\gamma_3 = \gamma_2$) and for an optical EIT scheme ($\gamma_3 = \gamma_2/100$), for the case of radiation that has not changed its polarization (I^{++}). The group velocity clearly reduces with increasing linear density, reaching values of $v_g \approx 10^{-7}c$ for $\mathrm{T}_e = 8$, with v_g in the optical EIT case two times lower than the nuclear case (for I^{++}).
These values must be compared with v_g in the case without mixing interaction. For example, let us consider a two-level medium with the incident radiation detuned from resonance[1], *i.e.* $\delta = \omega - \omega_0 \neq 0$. As seen in Fig. 2.2, for $\delta > \gamma/2$ the slope $dn/d\omega$ is positive and also gives rise to a slow group velocity [125]. Values for v_g in this two-level medium are plotted in Fig. 5.3 for different values of δ. For large values of δ the influence of the medium of course decreases, resulting in a less altered v_g. If $\delta \approx \gamma_2$, however, the reduction of v_g is comparable with the reduction in the Λ-scheme. In fact, v_g is even slightly more reduced than in the optical EIT case! This comparison puts the results of the Λ-scheme in the right perspective.
However, if we take a look at v_g as a function of Ω (right graph in Fig. 5.2), it is seen that the choice of $\Omega = \gamma_2$ is close to the value of Ω with the lowest v_g in the nuclear case, but it certainly does not yield the lowest v_g in the optical case. Actually, the mixing strength Ω_m that yields the lowest group velocity is calculated as

$$\Omega_m = \sqrt{\frac{\gamma_3^2}{2} + \frac{\gamma_2\gamma_3}{4}}. \tag{5.9}$$

Now, for $\Omega = \Omega_m$ the reduction of v_g in the optical EIT case can be several orders of magnitude higher than the nuclear case or the two-level system. However, papers dealing with EIT mainly consider systems with $\Omega^2 >> \gamma_2\gamma_3/4$ in

[1] On resonance, the imaginary part of $n(\omega)$ (absorption) is non-negligible. Also, the slope $dn/d\omega$ becomes negative and the group velocity loses its simple kinematic meaning.

order to create a large transparency window. This condition can clearly not be reconciled with Eq. (5.9). Hence, there is always a trade off between creating a transparent medium and maximally reducing the group velocity of the pulse. Notice that $v_g(\Omega)$ is only plotted for $\Omega \geq \gamma_3/2$. When $\Omega < \gamma_3/2$, v_g becomes negative. This condition marks the transition from an 'absorptive' medium, where the concept of group velocity is not straightforward, to a 'dispersive' medium.

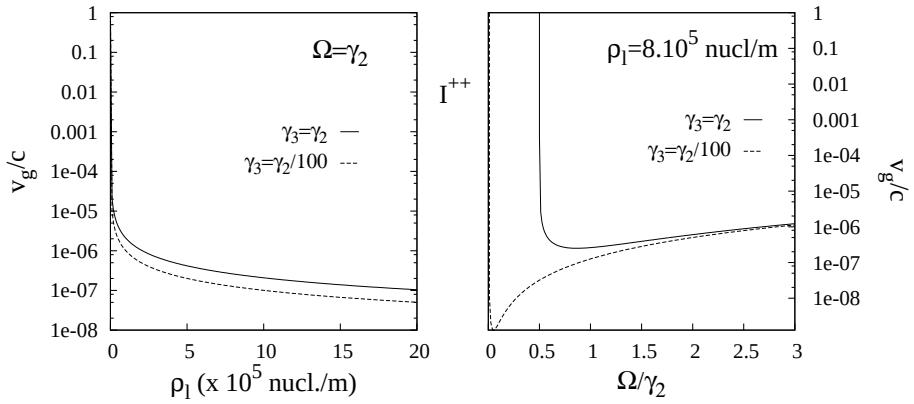

Figure 5.2: Calculated group velocity v_g in a Λ-system as a function of linear density ρ_l (left figure) and as a function of mixing interaction strength Ω (right figure). The nuclear case ($\gamma_3 = \gamma_2$) and a possible optical case ($\gamma_3 = \gamma_2/100$) are compared.

5.2 Time-dependent photon wave function in the coherent path model

In chapter 4 an expression for the time-dependent photon wave function $\psi(x,t)$ is presented (Eq. (4.33)). It is instructive to first consider the case when there is only a (decaying) source nucleus, as in section 4.2.3. The expression for $p_k(t)$ is then given by Eq. (4.51). Substituting its one-dimensional form in Eq. (4.33) yields

$$\psi(x,t) = \frac{\sqrt{L}}{2\pi c}\left(\frac{V_{P_{\mathbf{k}}S}}{\hbar}\right)\int_{-\infty}^{\infty} d\omega_k\, e^{-i\omega_k(t-\frac{x}{c}+\frac{x_0}{c})}\frac{1-e^{it(\omega_k-\omega_0+i\gamma_s/2)}}{\omega_k-\omega_s+i\frac{\gamma_s}{2}}. \quad (5.10)$$

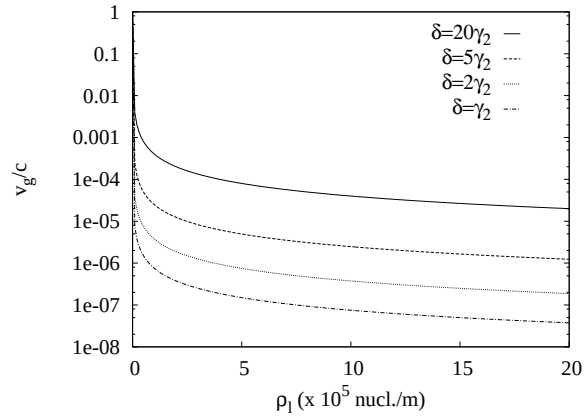

Figure 5.3: Calculated group velocity v_g in a two-level system as a function of linear density ρ_l for different values of detuning from resonance ($\delta = \omega - \omega_0$).

The integral can be solved by conversion to complex coordinates and applying the theory of residues for complex closed loop integrals. The integral of the second term is non-zero for $(\frac{x}{c} - \frac{x_0}{c}) < 0$, *i.e.* for radiation from the source emitted in the opposite direction of the detector. Only the first term gives a physical contribution:

$$\psi(x,t) = -\frac{i\sqrt{L}}{c}\left(\frac{V_{P_{\mathbf{k}}S}}{\hbar}\right) e^{-i(t-(\frac{x}{c}-\frac{x_0}{c}))(\omega_s - i\gamma_s/2)}\theta\left(t-\left(\frac{x}{c}-\frac{x_0}{c}\right)\right). \quad (5.11)$$

The appearance of the Heaviside step function ensures that the signal emitted by the source nucleus does not travel faster than the speed of light in vacuum. Eq. (5.11) is very similar to the photon wave function obtained in [17], except for a $|\mathbf{r}-\mathbf{r}_0|^{-1}$ dependence. The intensity of radiation emitted from a point source into 4π should indeed decrease according to $|\mathbf{r}-\mathbf{r}_0|^{-2}$. The reason why we do not obtain this factor is simply because our approach is one-dimensional. In one dimension the energy of the field is not distributed over an ever increasing spherical surface, but instead, propagates undiminished in the one-dimensional space. In our case, all photons emitted by the point source have travelled more or less the same distance before detection. Hence, the $|\mathbf{r}-\mathbf{r}_0|^{-1}$ factor yields no more than an overall reduction of intensity.

Let us now turn to the case with an absorber consisting of N effective nuclei. To find an expression for $p_k(t)$, we make a Fourier transformation to time domain of $P_k(\omega)$ (Eq. (4.31)). We only deal with poles with negative imaginary part, which means that only for $t \geq 0$ the integral is non-zero. The physical

meaning is obvious.
The calculations are simplified as it turns out that only the pole $\omega = \omega_k - i\epsilon$ will contribute to the final expression of ψ. When integrated over ω_k all other poles only give a contribution if $x \leq x_m$, *i.e.* a non-physical situation in which the detector (at position x) would be positioned in front of the absorber nuclei instead of behind.
The integral over ω_k is calculated in appendix D. Eventually, one finds the expression for the σ^+ photon wave field at position $x\,(\geq x_N)$ and time t, parameterized by $t' = t - x/c$ with the condition that $t' \geq 0$, for N effective scattering nuclei:

$$\psi_N^+(t') = \psi_s(t')\left[1 + \sum_{n=0}^{N-1}\sum_{p=0}^{n}\sum_{k=0}^{p}\sum_{l=0}^{p-k-1}\binom{N}{n+1}\binom{n-p-1}{k}\right.$$
$$\left.\binom{p-k-1}{l}\binom{k+2}{l+1}\left(\frac{-i\gamma_3^r}{2}\right)^{n-p}\left(\frac{-i\gamma_2^r}{2}\right)^{p+1}\left(|\Omega|^2\right)^{k+1}\psi_{npk}^+(t')\right] \tag{5.12}$$

with

$$\psi_s(t') = \left(\frac{-i\sqrt{L}}{\hbar c}\frac{V_{P_kS}}{\hbar}\right)e^{-it'(\omega_v - i\frac{\gamma_s}{2})}, \tag{5.13}$$

and

$$\begin{aligned}\psi_{npk}^+(t') &= \frac{\delta_{s3}^{p-k}\delta_{s2}^{n-p-k-1}}{\delta_{s+}^{n+1}\delta_{s-}^{n+1}} + \sum_{i=0}^{n}\sum_{q=0}^{i}\sum_{r=0}^{q}\binom{n-p-k-1}{q-r}\binom{i-q+n}{i-q}\\ &\times \binom{p-k}{r}(-1)^{n-q}\left(\frac{\delta_{+3}^{p-k-r}\delta_{+2}^{n-p-k-1-q+r}}{\delta_{+s}^{n-i+1}\delta_{+-}^{n+i-q+1}}e^{-it'\delta_{+s}}\sum_{j=0}^{n-i}\frac{(it'\delta_{+s})^j}{j!}\right.\\ &+ \left.\frac{\delta_{-3}^{p-k-r}\delta_{-2}^{n-p-k-1-q+r}}{\delta_{-s}^{n-i+1}\delta_{-+}^{n+i-q+1}}e^{-it'\delta_{-s}}\sum_{j=0}^{n-i}\frac{(it'\delta_{-s})^j}{j!}\right),\end{aligned} \tag{5.14}$$

with $\delta_{ij} = \omega_i' - \omega_j'$ and $\omega_i' = \omega_i - i\gamma_i/2$. All parameters have been defined in the previous chapter. In a similar way, one can calculate the σ^- photon wave field using the expression for $B_m(\omega)$ and Eq. (4.9). The general expression for

the σ^- photon field is

$$\begin{aligned}\psi_N^-(t') &= \psi_s(t')\frac{-i\sqrt{\gamma_2^r\gamma_3^r}}{2}\Omega^* \sum_{n=0}^{N-1}\sum_{p=0}^{n}\sum_{k=0}^{p}\sum_{l=0}^{p-k-1}\begin{pmatrix} N \\ n+1 \end{pmatrix}\begin{pmatrix} n-p \\ k \end{pmatrix} \\ &\times \begin{pmatrix} p-k-1 \\ l \end{pmatrix}\begin{pmatrix} k+1 \\ l+1 \end{pmatrix}\left(\frac{-i\gamma_3^r}{2}\right)^{n-p}\left(\frac{-i\gamma_2^r}{2}\right)^{p}\left(|\Omega|^2\right)^k \psi_{npk}^-(t') \end{aligned} \tag{5.15}$$

with

$$\begin{aligned}\psi_{npk}^-(t') &= \frac{\delta_{s3}^{p-k}\delta_{s2}^{n-p-k}}{\delta_{s+}^{n+1}\delta_{s-}^{n+1}} + \sum_{i=0}^{n}\sum_{q=0}^{i}\sum_{r=0}^{q}\begin{pmatrix} n-p-k \\ q-r \end{pmatrix}\begin{pmatrix} i-q+n \\ i-q \end{pmatrix} \\ &\times \begin{pmatrix} p-k \\ r \end{pmatrix}(-1)^{n-q}\left(\frac{\delta_{+3}^{p-k-r}\delta_{+2}^{n-p-k-q+r}}{\delta_{+s}^{n-i+1}\delta_{+-}^{n+i-q+1}}e^{-it'\delta_{+s}}\sum_{j=0}^{n-i}\frac{(it'\delta_{+s})^j}{j!}\right. \\ &+ \left.\frac{\delta_{-3}^{p-k-r}\delta_{-2}^{n-p-k-q+r}}{\delta_{-s}^{n-i+1}\delta_{-+}^{n+i-q+1}}e^{-it'\delta_{-s}}\sum_{j=0}^{n-i}\frac{(it'\delta_{-s})^j}{j!}\right). \end{aligned} \tag{5.16}$$

As these amplitudes have mutually orthogonal polarizations, the total photon intensity that impinges on a detector at time t is given by

$$I(t) = |\psi^+(t)|^2 + |\psi^-(t)|^2, \tag{5.17}$$

$$\equiv I^{++} + I^{+-}, \tag{5.18}$$

for a σ^+ source photon.

Simulations

We believe that the easiest way to address these photon wave functions is through numerical simulations. It must be noted that the following simulations are only valid for the 'ideal' case, *i.e.* there is no line broadening (except due to the finite lifetime), there are no neighboring absorption lines and all interaction is resonant ($f_r = 1$). Deviations from the ideal case are discussed in detail in the next section.

In order to allow for a correct interpretation of the time-differential spectra in a three-level nuclear medium, we first consider the two-level system ($\Omega = 0$) as a reference case. In Fig. 5.4 the total transmitted intensity for $N = 50$ is plotted for different values of detuning $\delta = \omega - \omega_0$. The other parameters involved are chosen as: $\gamma_s = \gamma$ and $\gamma_r = \gamma/10$. In comparison with the bold

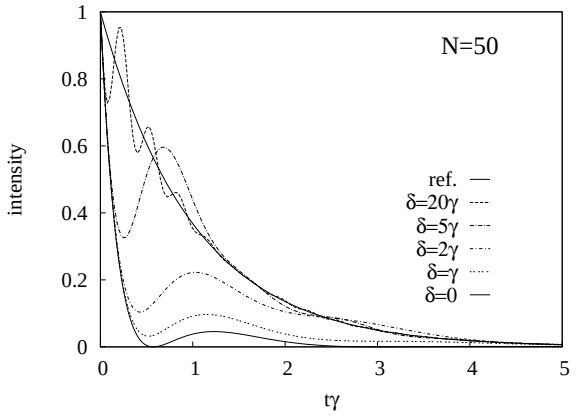

Figure 5.4: Simulated time-differential spectra in a two-level system ($\Omega = 0$) for different values of $\delta = \omega - \omega_0$.

solid line, which represents the normal lifetime curve (without absorber), there is a considerable 'speed-up' effect at small times, *i.e.* the exponential has a steeper slope. It is followed by a 'dynamical beat'. Both features are pure multiple scattering effects and have been discussed in detail in many papers, see *e.g.* [102, 103, 118, 125, 126].
If the incident radiation is detuned from resonance, the beating pattern shifts towards smaller times, while its amplitude increases. When $\delta \gtrsim 2\gamma$, it is seen that, for certain times, even more radiation is detected than without absorber[2]. Eventually, for large detuning, the spectrum approaches the normal lifetime curve, as is expected.

Fig. 5.5 shows the simulations of the time-differential spectra in a three-level Λ nuclear medium ($\Omega \neq 0$) for incidence of a σ^+ photon. Two absorbers ($N = 5$ and $N = 20$) and four different values of mixing interaction Ω are compared. We have chosen $\gamma_s = \gamma_3 = \gamma_2 =$ and $\gamma_2^r = \gamma_3^r = \gamma_2/10$ and the incident radiation is tuned at the center of the (mixed) absorption lines: $\omega = \omega_0$. The bold solid line again represents the normal lifetime curve.
The speed-up and dynamical beat signatures are now less pronounced because the absorbers are chosen to be less thick. A novel feature for $\Omega \neq 0$ is the appearance of radiation with the orthogonal polarization state (I^{+-}). This

[2]This is seen at times when the intensity curve crosses the normal lifetime curve. The overall, time-integrated intensity, however, is always smaller than in the case without absorber.

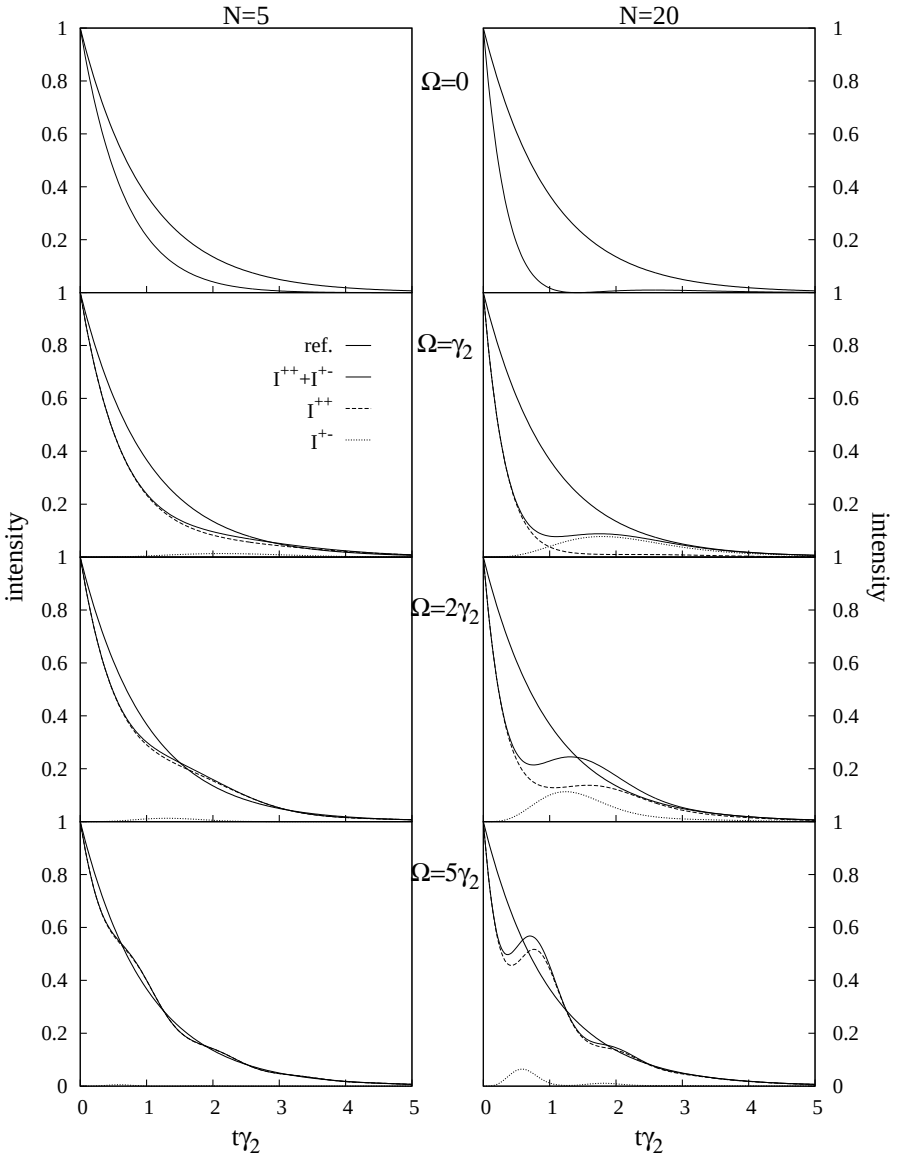

Figure 5.5: Simulated time-differential spectra in a three-level nuclear Λ system ($\gamma_3 = \gamma_2$) for different values of the mixing interaction Ω.

radiation does not interfere with the incoming radiation and, hence, does not display the initial exponential decay curve (which originates from the decay of the source nucleus). It contributes to the total spectrum mainly at times several lifetimes later than $t = 0$. This delay decreases, however, with increasing Ω, along with the amplitude of its contribution. For large Ω, the spectra tend to coincide with the normal lifetime curve, which could be compared with the case of a large detuning in the two-level system. For $N = 5$ the effects are similar but less pronounced.
Simulations in the case of $\gamma_3 = \gamma_2/100$ are presented in Fig. 5.6. The spectra are very similar to the case with equal decay rates, except that the peak amplitude of the I^{+-} contribution is a little higher. Its shape and position have not changed.

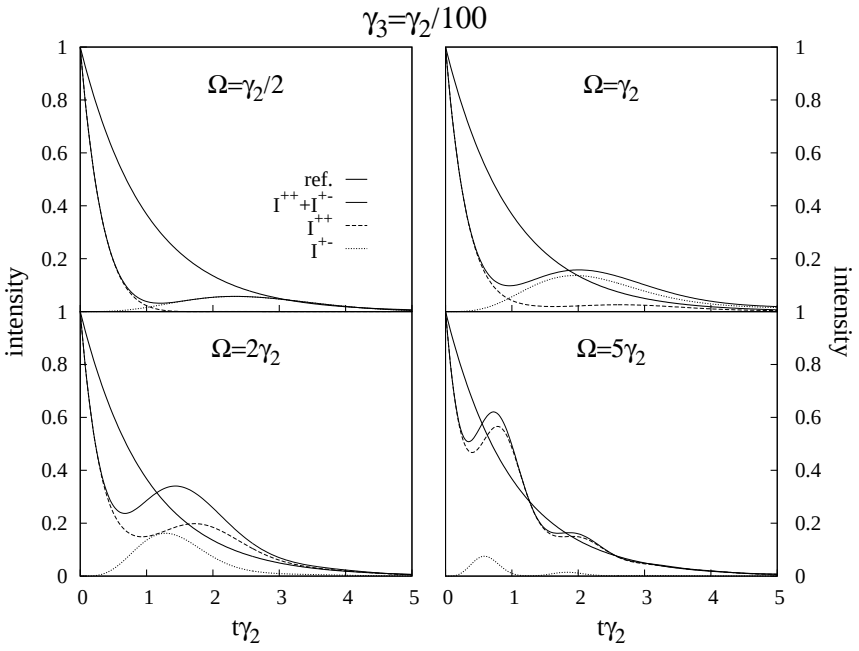

Figure 5.6: Simulated time-differential spectra in a three-level Λ system with $\gamma_3 = \gamma_2/100$ and $N = 20$, for different values of the mixing interaction Ω.

From the solutions of the photon wave functions in the coherent path model we know that they are superpositions of $n-$hop amplitudes, with n (or $n+1$) the number of real scattering events. It is instructive to also visualize these

$n-$hop amplitudes in their time-differential form. The first $n-$hop amplitudes for $N = 20$ are shown in Fig. 5.7. As in the time-integrated picture, the first hop yields a negative contribution with respect to the (positive) exponential contribution of the noninteracting part of the radiation. This first hop amplitude decreases the transmitted intensity for small times, giving rise to the apparent speed-up effect. The contributions of the next $n-$hop amplitudes not only decrease, but also shifts towards later times. It can be shown that, for $\Omega = 0$, they reach their maximum strength exactly at $t_n = n(\gamma_2/2)^{-1}$. Hence, each $n-$hop amplitude is seen to be *delayed* with respect to the noninteracting radiation, which has its maximum transmission at $t = 0$. The specific form of t_n supports the interpretation that the delay is simply due to the interaction of the radiation with the nuclear medium, where each interaction (scattering) adds $(\gamma_2/2)^{-1}$ to the delay. This also coincides with the intuitive picture that, upon absorption of the radiation, the nucleus decays with a lifetime of γ_2^{-1} and therefore 'slows down' the radiation by the same factor.
For $\Omega = \gamma_2$, although the concept of a peak amplitude is less applicable, the contribution of an $n-$hop amplitude is also seen to shift towards later times with increasing n. Their oscillatory behavior, however, makes a straightforward interpretation more cumbersome. At least, we observe that the $n-$hop amplitudes for I^{+-} experience more delay than their I^{++} counterparts. The creation of the amplitudes belonging to I^{+-} involves at least one interaction with the mixing field. This interaction time is the reason for the additional delay.

Can these time-differential spectra somehow be related with the concept of group velocity, discussed in the previous section? First, we know that the intensity measured at $t = 0$ corresponds to radiation that has travelled the distance from source to detector with $v_g = c$ (remember that $t \to t' = t - x/c$). In fact, without an interacting medium, the entire source pulse should propagate with c. The reason that, in this case, radiation is detected at times later than $t = 0$ is of course due to the delayed emission by the source itself, resulting in the exponential 'lifetime' curve.
The $n-$hop amplitudes show that radiation that *interacts* with the nuclear medium, experiences a delay $\Delta t = t_n - t_0$ (for $\Omega = 0$). The corresponding group velocity of an $n-$hop amplitude can then be calculated as

$$v_g = \frac{d}{\Delta t} = c\left(\frac{t_c\gamma_2}{2n}\right) \tag{5.19}$$

with d the physical thickness of the absorber and $t_c = d/c$ the time it takes to travel through the absorber at the speed of light in vacuum. If we consider an absorber with $d \approx 10^{-4}\,\mathrm{m}$ and $\gamma_2/(2\pi) \approx 1\,\mathrm{MHz}$, then $v_g/c \approx 10^{-7}$ for $n = 1$. This is of the same order of magnitude as the group velocities obtained in the

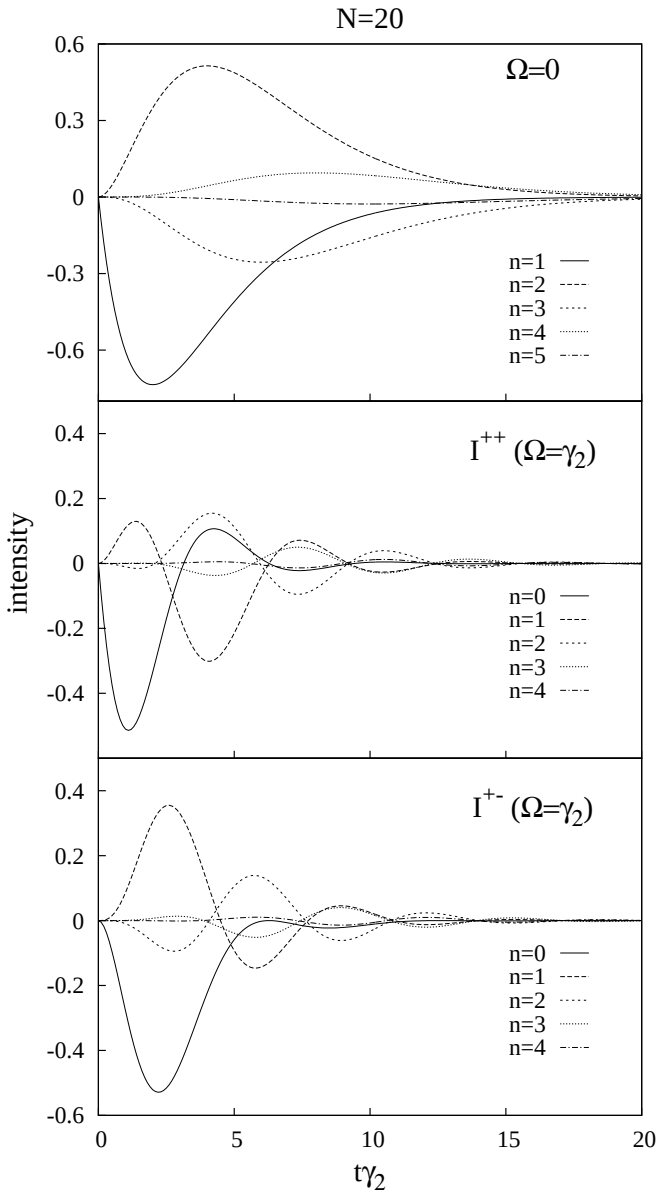

Figure 5.7: Simulations of the time-differential $n-$hop amplitudes in a two-level system (top figure) and in a three-level Λ nuclear system (middle and bottom figure) with $\gamma_3 = \gamma_2$

semiclassical analysis.
It must be noted that v_g as defined in Eq. (5.4) does not take into account multiple scattering. The use of the index of refraction only accounts for a single scattering event (multiplied by a factor proportional to the linear density). Therefore, we can limit the comparison to the 1-hop case.
In the same figure, the effect of the strength of the mixing interaction upon the delay of I^{+-} is clearly seen. The peak shifts to smaller times with increasing Ω. This is in qualitative agreement with the Ω-dependence calculated in Fig. 5.2.

5.3 Time-differential Mössbauer spectroscopy

It was already recognized almost half a century ago [125] that ^{57}Fe is not only an ideal candidate to perform time-integrated Mössbauer spectroscopy, but it lends itself perfectly for Mössbauer experiments *as a function of time*, *i.e.* time-differential Mössbauer spectroscopy (TDMS). In the decay of ^{57}Co, as shown in Fig.2.3, the emission of the 122 keV gamma photon announces the formation of the 14.4 keV state. Hence, the detection of the 122 keV gamma photon can act as a start of the clock, while the detection of the 14.4 keV photon stops it. To maximize the chance that both photons belong to the decay of the same nucleus, two measures can be taken. First, the 122 keV and 14.4 keV are detected in coincidence, *i.e.* their detection should occur within a certain time interval, typically taken to be a few times the lifetime of the 14.4 keV state. Second, the strength of the radioactive source should be low enough to assure that in this time interval only few ^{57}Co nuclei decay. However, there is a trade-off with the time necessary to obtain a reasonable spectrum, which of course increases for decreasing source strength.
The experimental difficulties, combined with the complex analysis of the spectra, quickly cooled down the initial interest of the Mössbauer community. Only a limited number of researchers have published on TDMS, mainly in the sixties of the 20th century, see *e.g.* [127–129]. It was not before the advent of the synchrotron that the interest in time-differential measurements was revived [130]. The use of synchrotron radiation has solved most of the experimental problems and has opened up the range of candidate nuclei. The further increase of the complexity of the measured spectra and the lack of a table-top synchrotron, however, can be considered serious drawbacks.

5.3.1 Experimental setup

The setup described in section 1.2 is extended with a second detector. Both detectors are now NaI scintillation detectors, which have a good time resolution *and* a sufficient energy resolution to resolve the 6 keV X-ray[3] and the 14.4 keV gamma-ray. The driving signal of the transducer is modified in order to run in a 'constant velocity' mode. This is achieved by electronically levelling of the triangular driving function at the desired velocity. This method, however, reduces the number of accepted counts by a factor of 4.
A good choice of the signal processing electronics is of crucial importance in this kind of experiments. In theory, the best timing resolution is achieved in a fast/slow coincidence setup, where the timing signal is separately processed from the energy signal. However, former research [131] has learned that, in the case of ^{57}Fe, a combined energy and time configuration results in a good timing resolution as well. A typical example of such a setup is shown in Fig. 5.8. The upper network is set to analyze the 14.4 keV signal (by means of the single-channel analyzer (SCA)) and the lower part processes the 122 keV signal. The signal from SCA2 will start the time-to-amplitude converter (TAC), while SCA1 provides the stop signal. The height of the output pulse from the TAC is now proportional to the time difference between the start and stop pulses. The height (or time) information is stored as a count in one particular channel of the multichannel analyzer, finally yielding the time-differential spectrum.

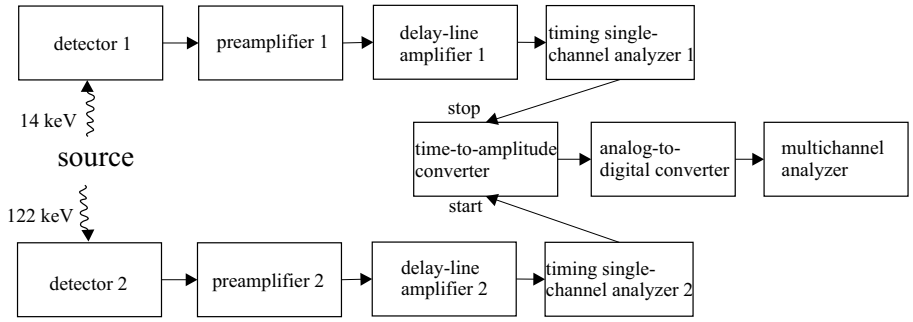

Figure 5.8: Schematic overview of a delayed-coincidence timing data system for a TDMS measurement.

[3]This 6 keV X-ray originates from the deexcitation of ^{57}Fe by electron conversion. When this electron vacancy is filled by an electron from a higher orbital, the reduction of the energy is balanced by the emission of this X-ray.

5.3.2 Simulations of a realistic experiment

Without actually performing a series of TDMS experiments, it is possible to simulate the outcome of such an experiment through the models developed in the previous chapters. We start from the ideal case that is discussed in section 5.2, and then change some parameters to their realistic values. We do this step by step in order to study the influence of these parameters.
We consider the ideal case to correspond to the conditions that all interaction is resonant, *i.e.* $f_r = 1$, with no line broadening, *i.e.* $q_i = 1$, and no other absorption lines except for those involved in the Λ-scheme. The simulations are obtained in the Blume-Kistner model for an absorber with $T_e = 8$ in the parallel geometry.

Ideal case and mixing interaction The top figure in Fig. 5.9 shows the TDMS spectrum in the ideal case and without mixing interaction. The contribution of the σ^- incident radiation ($I^{--} + I^{-+}$) displays a dynamical beat and more speed-up than the $I^{++} + I^{+-}$ contribution. The higher value of the Clebsch-Gordan coefficient in the σ^- case results in an apparent higher thickness, giving rise to the more pronounced multiple scattering features. As in all following figures, the normal lifetime curve is shown as a reference case.
The lower figure in Fig. 5.9 shows the change in the spectra when a mixing interaction is present. The mixing is assumed to originate from a non-axial efg, which is parameterized by η. From $\eta \approx 0.1$ on, which corresponds to $\Omega \approx 0.7\gamma_2$, the spectrum is changed considerably, with the appearance of a delayed fraction of the transmitted radiation.

Resonant fraction and line broadening The top figure in Fig. 5.10 shows the strong influence of the resonant fraction. The best achievable value for this experiment is $f_r = f_{LM} \approx 0.7$. The non-resonant counts due to scattering with recoil also exhibit an exponential decay curve. If we assume that the multiple scattering effects before recoiling are negligible, then this non-resonant fraction yields a normal lifetime curve. Its contribution partially masks the interesting features of the resonant fraction.
In a TDMS experiment, the background events originating from scattering with recoil must be distinguished from another source of 'noise'. Background counts in the gamma detection, which originate from events other than the 14.4 keV photon, and false coincidence counts between the 14.4 keV and 122 keV photons give rise to a uniform background baseline.
The simulations in the lower figure in Fig. 5.10 illustrate the dependence on the widths of the absorption lines. Up till now, we assumed that the width of the excited levels equals the natural width ($\gamma = \tau^{-1}$). But these widths could

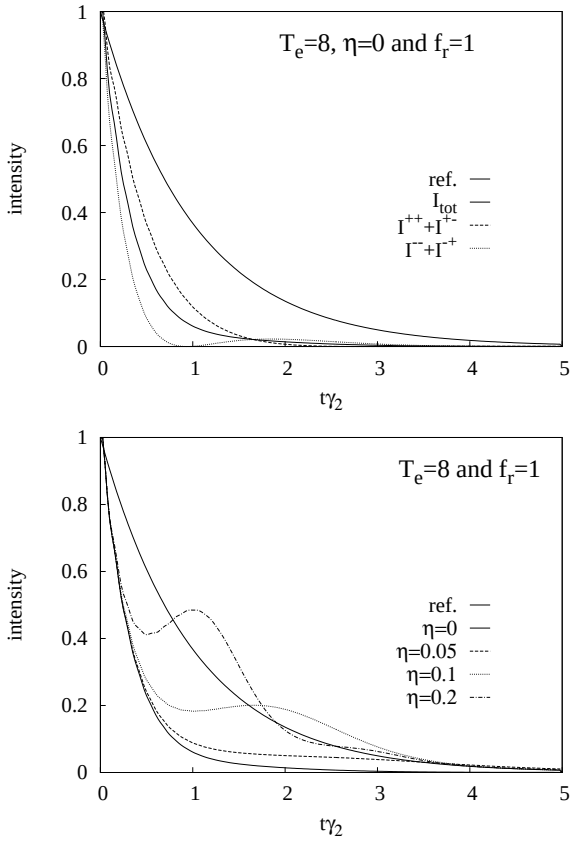

Figure 5.9: Simulations of the experimental time-differential spectrum in the ideal case, without mixing interaction ($\eta = 0$) in the top figure, and with a mixing interaction due to a non-axial efg in the bottom figure. The total intensity in the top figure is the weighted sum of the four polarization dependent contributions: $I_{tot} = \frac{1}{2}\left(I^{++} + I^{+-}\right) + \frac{1}{2}\left(I^{--} + I^{-+}\right)$

.

be increased through different line broadening mechanisms, *e.g.* distributions in hyperfine fields and/or a fluctuating magnetic field. Also external effects, like small vibrations in the setup, can result in an increase in line widths. It is seen that the effect of the mixing interaction is being 'blurred out' upon increasing line width.

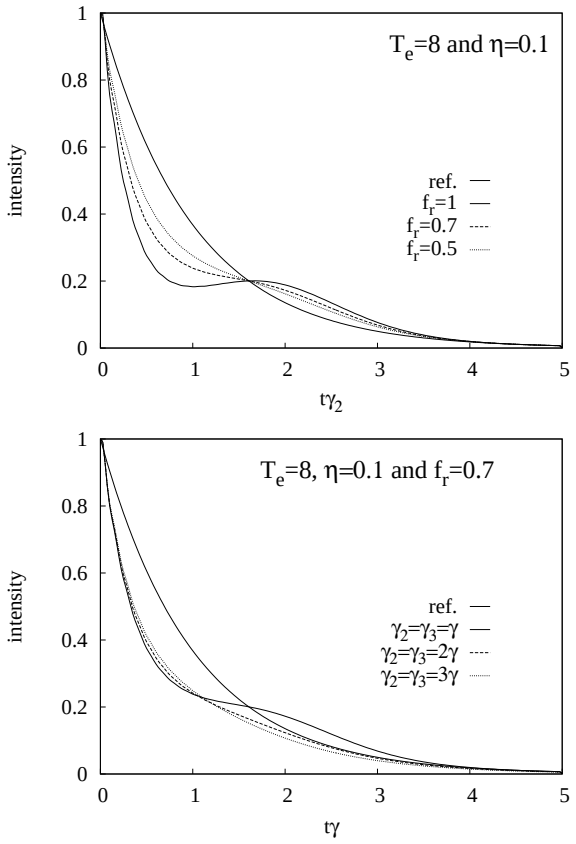

Figure 5.10: Simulations of the experimental time-differential spectrum for the case with a non-resonant fraction ($f_r < 1$) (top figure) and for the case with line broadening (bottom figure).

Multilevel scheme Finally, in Fig. 5.11 the presence of other absorption lines is simulated. Although the energy difference with the incident photon

can be large, due to its Lorentzian frequency spectrum, there is always a small part in the wings that will interact with these distant transitions. The effect is limited to the appearance of wiggles on the original time spectrum.
In the same figure a comparison is made with the case without mixing interaction, but also including all of the above considerations. There is still an important difference between both spectra. In our opinion, however, it does not present strong evidence for an induced *delay* of the transmitted radiation, since the spectrum still falls within the borders of the normal lifetime curve.
The spectrum for $\eta = 0.05$ (not shown) almost coincides with the spectrum without the mixing interaction, leaving a possible interpretation in terms of delay very hard to prove.

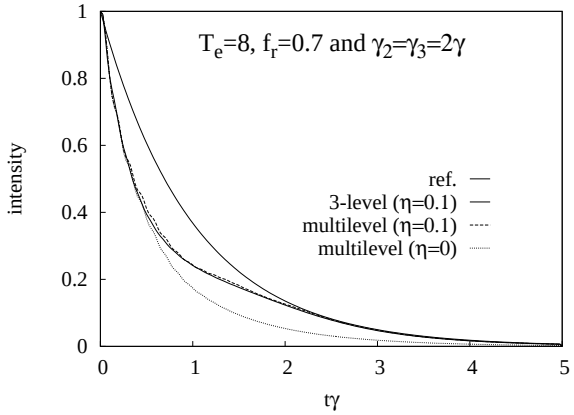

Figure 5.11: Simulations of the experimental time-differential spectrum for the case of a multilevel system with $\eta = 0.1$, in comparison with a three-level system (with same mixing interaction) and a multilevel system without mixing.

5.4 Conclusions

Although the concept of group velocity is not always applicable and must be handled with care, we have followed the mainstream trend and estimated v_g in a nuclear medium. By comparison with the reduction of the group velocity in a two-level system we hope to have put the results in the right perspective. It is shown that the case of the lowest group velocity does not correspond with the conditions for a large transparency window. In the latter case, the influence

of the decay rate of the coupling state (γ_3) becomes negligible. Not only does this mean that the decrease of v_g is mainly due to the off-resonance situation, but also that the nuclear case should not be considered inferior to the optical case with respect to slow group velocities.
Simulations of the time-differential photon amplitudes in the coherent path model suggest that a delay in the peak amplitude with respect to the initial time of emission can be related to the (classical) concept of group velocity. From the total transmitted intensity, however, it is almost impossible to derive v_g for the pulse. There is not only the effect of speed-up, but also the interference with the incident radiation, which has an exponential curve. If we could realize an experimental setup that is polarization sensitive, then a delay could unequivocally be observed in the detection of the I^{+-} contribution.
Although the calculations are convincing and very hopeful, simulations that take into account the real experimental conditions leave little room for spectacular observations. Even in the case of a perfect data system, it is shown that the measurable time-differential Mössbauer spectrum will be quite featureless, yielding only very weak evidence for a delay of gamma photons.

Conclusions and outlook

This thesis has mainly been concerned with understanding the reduced absorption, which was observed in the Mössbauer spectra of $FeCO_3$ at the level crossing temperature. The spectra recorded in the parallel, as well as in the perpendicular geometry, display a partial transparency at the absorption line that involves the crossing levels. Whereas the latter spectrum can be explained as a saturation effect, the first certainly can not.
If there is an interaction present that induces transitions between these crossing levels, then this nuclear system is analogous to a quantum optical Λ-scheme in which electromagnetically induced transparency can be observed. The best candidate for an interaction, whose influence is limited to the mixing of the crossing levels, has been identified as a non-axial component of the electric field gradient. This assumption is also supported by the chemical analysis. A 6.4 % Mn content on substitutional lattice sites can indeed disturb the, initially symmetrical, electric field gradient. As these impurities have, most probably, a random distribution, also the resulting mixing interaction must have a random nature. However, we have shown that the (random) *phase* of the mixing interaction does not play a role in the final solution of the transmitted intensity. A random *magnitude* of the mixing interaction is, eventually, modelled by a Gaussian distribution centered around its zero value. Then the only, but important, difference between the optical and nuclear scheme is due to the decay rates of the mixing levels, which are (close to) equal in the nuclear case. It is shown that, if the decay rates are exactly equal, the interference term vanishes, resulting in a spectrum consisting of two Lorentzian absorption lines. The experimental data, however, suggest slightly different decay rates for each absorption doublet, which is explained by the presence of a fluctuating magnetic field. The differences are such that the absorption at the level crossing from the $|m_g = -1/2\rangle$ yields a net destructive interference, leading to less absorption at the line center, whereas the absorption from the $|m_g = 1/2\rangle$ (perpendicular geometry only) yields a net constructive interference. These results qualitatively explain the reduced absorption in the parallel geometry and the difference with

the perpendicular geometry in a consistent way.
Another distinctive feature of the nuclear Λ-scheme is the creation of radiation with a polarization that is complementary to the polarization of the incident radiation. This radiation does not interfere with the incident radiation and, therefore, contributes positively to the transmitted radiation, thereby further reducing the absorption at the level mixing. It also shows a particular thickness dependence, having its maximum intensity at the line center around $T_e = 10$ and, for higher T_e, displaying a double hump structure with a splitting increasing with increasing thickness.

Some collateral, though interesting, aspects have been studied in more detail. The experimentally deduced line width of the π absorption line in the perpendicular geometry displays an anomalous broadening behavior. This is now understood as a polarization effect.
The results obtained in the quantum mechanical coherent path model, in general, qualitatively agree with the semiclassical results. There are some discrepancies, however, that are due to the discrete nature of the coherent path solution. We have shown that the two-level result ($\Omega = 0$) coincides with the first N terms of the classical exponential function of the transmitted intensity as long as the classical approximation of a continuous scattering process is taken. Otherwise, the quantum mechanical result yields the same frequency dependent terms, but with different amplitudes (this is also true in the case of a three-level system).
We have shown that the photon wave function as used in the coherent path model corresponds to the probability amplitude of the detection of an ejected photo-electron. It is also here, at the time and place of the measurement, that the quantum picture of light in terms of single gamma photons meets its classical counterpart, where the radiation intensity is given as a first order correlation function of the electric field.
Some time-dependent aspects of the transmitted gamma radiation in a three-level nuclear Λ-scheme have been studied and compared to a reference two-level system. The group velocity deduced in both systems shows a reduction of the order of $v_g/c \approx 10^{-7}$ and is comparable to an optical Λ-system. Extrapolation of the results of the ideal case to the experimental conditions, however, predicts only a small observable signature of the delay of the gamma radiation.

The work as presented in this thesis could certainly be improved by collecting more unambiguous experimental evidence. If one could use a pure, artificially grown $FeCO_3$ single crystal and then apply a known mixing interaction, the resulting transparency should be controllable. As we have shown, however, a strong magnetic field, of the order of 5 T, is necessary to yield an observable effect. The transparency effect will nevertheless always be limited

due to the (almost) equal decay rates of the crossing levels. We do not know how to overcome this limitation.
This work also suggests some interesting polarization dependent experiments. In the case of level mixing, the transmitted radiation can change its polarization with respect to the incident radiation. This property could be applied to observe a double hump structure in an 'ordinary' Mössbauer setup or to study time-dependent properties of the scattered radiation, like delay, without the disturbing effect of the non-scattered radiation. Such experiments, of course, presume an emission and detection process that is polarization sensitive.
An appealing feature of these experiments with gamma radiation and nuclei, and this research in general, is their single photon nature. Therefore, such experiments can help to understand fundamental processes like, *e.g.*, the interaction of a single photon with one or with a large number of atoms or nuclei.

Nevertheless, we must be honest with ourselves and the reader, and note that this quantum nucleonic research is still strongly confined to the conceptual level, making it less attractive for investments of time and money. The contradictory situation, that no investments lead to no progress and hence no investments, is the fate of fundamental research and is difficult to dispute as long as science is dictated by short-term economic vision. But maybe we should not complain as *we* were given the opportunity to study with the aim to increase the collective knowledge of mankind.
We hope that this work has somehow fulfilled that goal, at least by shedding some light onto light from a different perspective. We only regret that this is more than the end of this thesis, it is also the virtual end of the Gamma Optics Group of Leuven.

Have you ever wondered how it must be to travel at the speed of light?
Rejoicing the eternal present? And how would the universe appear to you?
Has it not become a photon itself? A truly enlightening experience!

Appendix A

^{57}Fe and $FeCO_3$ general parameters

The two tables below give a summary of the most relevant parameters of the ^{57}Fe isotope and the siderite mineral respectively.

Table A.1: Some relevant properties of ^{57}Fe.

parameter	symbol	value
spin of ground state	I_g	1/2
spin of first excited state	I_e	3/2
magnetic moment of ground state	μ_g	$+0.09044(7)\,\mu_B$ [132]
magnetic moment of excited state	μ_e	$-0.1549(2)\,\mu_B$ [132]
isotopic abundance	χ	2.2%
maximum resonant cross section	σ_0	$2.57 \times 10^{-18}\,\mathrm{cm}^2$
energy of lowest γ-transition	E_γ	14.41300(15) keV
frequency of 14.4 keV gamma	$\omega_0 = E_\gamma/\hbar$	2.19×10^{19} Hz
half life of 14.4 keV level	$t_{1/2}$	98.1(3) ns
lifetime of 14.4 keV level	τ	141.5(4) ns
total line width of 14.4 keV level		
(in frequency units)	γ	7.067 MHz
(in velocity units)	γ	0.097 mm/s

Table A.2: Some relevant properties of $FeCO_3$, see also [22].

parameter	symbol	value
density	ρ	3.96 g/cm^3
molar weight	m	115.86 g

Appendix B

Clebsch-Gordan coefficients and d functions

In table B.1 and table B.2 we have listed the Clebsch-Gordan coefficients and d functions most relevant to this work, *i.e.* belonging to the six allowed $M1$ transitions in ^{57}Fe. The sign convention is that of Rose [133] and Brink and Satchler [43].

Table B.1: Clebsch-Gordan coefficients $\mathcal{C}(I_g L I_e; m_g M m_e)$ for $I_g = 1/2$, $I_e = 3/2$ and $L = 1$

m_g	M	m_e	$\mathcal{C}(\frac{1}{2}\,1\,\frac{3}{2}; m_g M m_e)$
$1/2$	1	$3/2$	1
$1/2$	0	$1/2$	$\sqrt{2/3}$
$-1/2$	1	$1/2$	$\sqrt{1/3}$
$1/2$	-1	$-1/2$	$\sqrt{1/3}$
$-1/2$	0	$-1/2$	$\sqrt{2/3}$
$-1/2$	-1	$-3/2$	1

Table B.2: Selection of d functions $d^L_{m',m}(\beta)$, with $d^L_{m,m'} = (-1)^{m'-m} d^L_{m',m} = d^L_{-m',-m}$.

$d^1_{0,0} = \cos\beta$	$d^1_{1,1} = \frac{1+\cos\beta}{2}$	$d^1_{1,0} = -\frac{\sin\beta}{\sqrt{2}}$	$d^1_{1,-1} = \frac{1-\cos\beta}{2}$
$d^2_{0,0} = \frac{3\cos^2\beta - 1}{2}$	$d^2_{2,2} = \left(\frac{1+\cos\beta}{2}\right)^2$	$d^2_{2,0} = \frac{\sqrt{6}}{4}\sin^2\beta$	$d^2_{2,-2} = \left(\frac{1-\cos\beta}{2}\right)^2$

Appendix C

Contour integration and the theorem of residues

If $f(\omega)$ is an analytic function of the form:

$$f(\omega) = \frac{e^{-i\omega t}}{(\omega - \omega_i)^n}, \tag{C.1}$$

then its integration over ω can be seen as the real part of a complex closed loop integral:

$$\oint dz\, f(z) = \int_{-\infty}^{\infty} dz\, f(z) + \underbrace{\lim_{R\to\infty} \int_0^{\pm\pi} d\theta\, iRf(Re^{i\theta})}_{I_R} \tag{C.2}$$

where we changed ω into z and $z = Re^{i\theta}$. The first integral on the right hand side is the integration along the real axis. The second integral closes the loop in the imaginary plane along a semi-circular path. Functions of the form of $f(\omega)$ belong to the group of functions for which Jordan's lemma applies. This lemma shows that the value of I_R is exactly zero in the case for integration over the upper semi-circle, when $t < 0$, and for integration over the lower semi-circle, when $t > 0$. For example, if we close our loop in the negative half of the complex plane, $I_R = 0$ for $t > 0$ and we have to consider the poles with negative imaginary part (see fig.C.1).
The solution of the complex closed loop integral is given by the theorem of

residues

$$\oint dz\, f(z) = \pm 2\pi i \sum_i Res\left(f(a_i)\right), \tag{C.3}$$

with $Res\left(f(a_i)\right)$ the residue of pole $z = a_i$ and with the $+/-$ sign for anti-clockwise/clockwise integration over the loop. In this work, we only encounter 'normal' poles of n-th order, which can be calculated as:

$$Res\left(f(a_i)\right) = \frac{1}{(n-1)!} \lim_{z \to a_i} \frac{\partial^{n-1}}{\partial z^{n-1}} \left((z - a_i)^n f(z)\right). \tag{C.4}$$

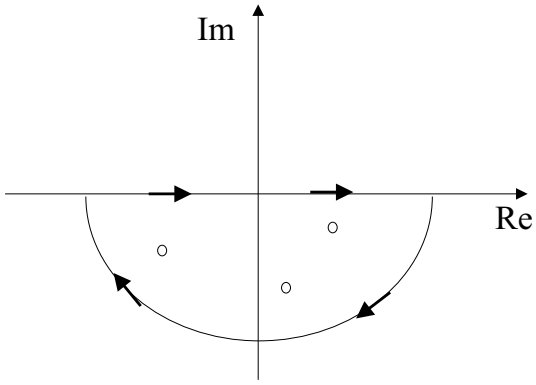

Figure C.1: Closed integration loop in the complex plane (here with three poles).

Appendix D

Derivation of the time dependent photon wave function

In this appendix we derive the expression for the time dependent photon wave field $\psi(x,t')$, as discussed in section 5.2. In the Fourier transformation to time domain of $P_k(\omega)$ (Eq.(4.31)) only the pole of $\omega = \omega_k - i\epsilon$ should be considered (see section 5.2). This means that the expression for $p_k(t)$ equals that of $P_k(\omega)$, except that the factor $(\omega - \omega_k + i\epsilon)^{-1}$ has disappeared and that ω is replaced by ω_k. For the integration over ω_k we only retain these ω_k dependent terms:

$$p^+_{npk}(t') \propto \frac{\delta_{k3}^{p-k}\delta_{k2}^{n-p-k-1}}{\delta_{ks}\delta_{k+}^{n+1}\delta_{k-}^{n+1}}, \tag{D.1}$$

with $\delta_{ks/2/3} = \omega_k - \omega_{s/2/3} + i\gamma_{s/2/3}/2$ and $\delta_{k\pm} = \omega_k - \omega_\pm$. Substituting this expression into Eq.(4.33), the (npk)-term of the photon wave field is given by

$$\psi^+_{npk}(t') \propto \int_{-\infty}^{\infty} \omega_k \frac{\delta_{k3}^{p-k}\delta_{k2}^{n-p-k-1}}{\delta_{ks}\delta_{k+}^{n+1}\delta_{k-}^{n+1}} e^{-i\omega_k t'}. \tag{D.2}$$

This integral can be solved by using the theorem of residues, which is explained in appendix C. Here, the integrand has three poles in the negative imaginary

plane: $\omega_k = \omega_s - i\gamma_s/2$ and $\omega_k = \omega_\pm$. The powers of the terms in the numerator are always positive, hence they should not be considered as poles. The solution of the integral is the sum of the three residues of these poles.

Pole $\omega_k = \omega_s - i\gamma_s/2$: The residue is found by straightforwardly substituting ω_k with $\omega_s - i\gamma_s/2$:

$$Res(\omega_k = \omega_s - i\gamma_s/2) = \frac{\delta_{s3}^{p-k}\delta_{s2}^{n-p-k-1}}{\delta_{s+}^{n+1}\delta_{s-}^{n+1}} e^{-i(\omega_s - i\gamma_s/2)t'}. \tag{D.3}$$

Pole $\omega_k = \omega_\pm$: Each of these poles can be treated in the same way. We consider the pole $\omega_k = \omega_+$. Because they are of the (n+1)-th order, the residue should be calculated by

$$Res(\omega_k = \omega_\pm) = \frac{1}{n!}\lim_{\omega_k \to \omega_\pm} \frac{\partial^n}{\partial \omega_k^n} \underbrace{\left(\frac{\delta_{k3}^a \delta_{k2}^b e^{-i\omega_k t'}}{\delta_{ks}\delta_{k-}^c} \right)}_{=I_1}, \tag{D.4}$$

with $a = p - k$, $b = n - p - k - 1$ and $c = n + 1$. The n-th derivative of a product of functions is given by Leibniz identity:

$$\{I_1\}^n = \sum_{i=0}^{n} \binom{n}{i} \underbrace{\left\{ \frac{e^{-i\omega_k t'}}{\delta_{ks}} \right\}^{n-i}}_{=I_2} \underbrace{\left\{ \frac{\delta_{k3}^a \delta_{k2}^b}{\delta_{k-}^c} \right\}^{i}}_{=I_3}, \tag{D.5}$$

with $\{\}^n$ the n-th derivative of the functions between brackets. The solution of the I_2 derivative is given by:

$$I_2 = (-1)^{n-i} \frac{(n-i)! e^{-i\omega_k t'}}{\delta_{ks}^{n-i+1}} \sum_{j=0}^{n-i} \frac{(it'\delta_{ks})^j}{j!}. \tag{D.6}$$

The I_3 derivative is further divided into smaller derivatives:

$$I_3 = \sum_{q=0}^{i} \binom{i}{q} \underbrace{\left\{ \frac{1}{\delta_{k-}^c} \right\}^{i-q}}_{=I_4} \underbrace{\left\{ \delta_{k3}^a \delta_{k2}^b \right\}^{q}}_{=I_5}, \tag{D.7}$$

with

$$I_4 = (-1)^{i-q} \frac{(c+i-q+1)!}{(c-1)!\delta_-^{c+i-q}}. \tag{D.8}$$

Again, I_5 is divided into two parts:

$$I_5 = \sum_{r=0}^{q} \left(\begin{array}{c} q \\ r \end{array} \right) \underbrace{\{\delta_{k3}^{a}\}^{q-r}}_{=I_6} \underbrace{\{\delta_{k2}^{b}\}^{r}}_{=I_7}, \tag{D.9}$$

with

$$I_6 = \frac{a!\delta_{k3}^{a-q+r}}{(a-q+r)!} \tag{D.10}$$

and

$$I_7 = \frac{b!\delta_{k2}^{b-r}}{(b-r)!}. \tag{D.11}$$

Combining the results of all derivatives and rearranging the binomial coefficients, we find that

$$\begin{aligned} Res(\omega_k = \omega_+) &= e^{-i\omega_+ t'} \sum_{j=0}^{n-i} \frac{(it'\delta_{+s})^j}{j!} \sum_{i=0}^{n} \sum_{q=0}^{i} \sum_{r=0}^{q} \left(\begin{array}{c} n-p-k-1 \\ q-r \end{array} \right) \\ &\times \left(\begin{array}{c} i-q+n \\ i-q \end{array} \right) \left(\begin{array}{c} p-k \\ r \end{array} \right) (-1)^{n-q} \frac{\delta_{+3}^{p-k-r} \delta_{+2}^{n-p-k-1-q+r}}{\delta_{+s}^{n-i+1} \delta_{+-}^{n+i-q+1}}. \end{aligned} \tag{D.12}$$

The sum of all three residues results in the expression for the time-dependent photon wave field presented in Eq.(5.12) and Eq.(5.15).

Nederlandstalige samenvatting

Deze samenvatting volgt dezelfde indeling als de vijf hoofdstukken uit de volledige tekst.

Inleiding

Dit proefschrift bevat het relaas van ons onderzoek naar elektromagnetisch geïnduceerde transparantie (afgekort als EIT) voor gammastraling. EIT is een intensief onderzocht fenomeen in de kwantumoptica en kan kort omschreven worden als het transparent maken van een medium voor een resonant elektromagnetisch veld, door middel van een tweede elektromagnetisch veld. In het tweede deel van deze samenvatting wordt dit meer uitvoerig beschreven.
In de kwantumoptica wordt EIT meestal gerealizeerd met behulp van lasers in een atomair drie-niveau Λ-schema. Het doel van dit werk is om na te gaan of er een equivalent *nucleair* systeem bestaat. In deel 1 geven we de resultaten van verschillende Mössbauer metingen op een één-kristal van het mineraal sideriet, $FeCO_3$.
Om deze experimentale spectra te verklaren, worden in deel 3 twee modellen ontwikkeld, gebaseerd op de semiklassieke benadering van voorwaartse nucleaire verstrooiing. Deze modellen worden ook wel aangeduid als de Blume-Kistner en de Maxwell-Schrödinger benadering.
Omdat we in deze thesis ook de nadruk willen leggen op het één-foton karakter van het verstrooiingsproces, wijden we deel 4 aan een volledig kwantummechanische beschrijving van de verstrooiing van gamma fotonen in een nucleair Λ-schema.
Tenslotte wordt er in deel 5 dieper ingegaan op de tijdsafhankelijke eigenschap-

pen van de gammastraling.

1. $FeCO_3$ Mössbauer experimenten

We hebben de hyperfijnstructuur van twee $FeCO_3$ één-kristallen van verschillende effectieve dikte ($T_e = 3$ en $T_e = 8$) bestudeerd met behulp van Mössbauer spectroscopie. De opgemeten spectra zijn onderworpen aan een eerste analyse. Hierin zijn de absorptielijnen gefit als (verbrede) Lorentzlijnen, waarbij we voor de bepaling van hun onderlinge posities gebruik gemaakt hebben van de kennis van de hyperfijninteracties in $FeCO_3$ uit de literatuur. De fits uit deze eerste analyse zijn vrij goed, behalve wanneer de $|m_e = -3/2\rangle$ en $|m_e = 1/2\rangle$ toestanden kruisen. Zowel in de loodrechte als in de parallelle geometrie is in deze eerste analyse minder absorptie waargenomen dan verwacht. De absorptie op de toestandskruising is duidelijk minder dan de som van de doublet partners[1] die niet betrokken zijn bij de kruising. Men is snel geneigd om dit toe te schrijven aan saturatie. Maar simpele argumenten gebaseerd op de selectieregels in de parallelle geometrie weerleggen deze stelling.
Als snel viel het ons op dat deze verminderde absorptie gelijkenissen vertoont met de transparantie die gekend is als EIT in de kwantumoptica.

2. Elektromagnetisch geïnduceerde transparantie

Een vrij empirische definitie van elektromagnetisch geïnduceerde transparantie (EIT) gaat als volgt: "EIT is het effect van het transparant maken van een anders opaak medium voor een resonant elektromagnetisch (EM) veld, d.m.v. een tweede EM veld."Meer technisch wordt het geformuleerd als de geïnduceerde transparantie, waarbij de transparantie het resultaat is van de combinatie van een Stark opsplitsing en de interferentie tussen de twee aangeklede toestanden, die gecreëerd zijn door het tweede EM veld. Het archetypisch optisch schema waarin EIT waargenomen kan worden is een zogenaamd drie-niveau Λ-schema (zie Fig. 2.1). Een EM 'probe- of signaalveld' is resonant met de $|1\rangle \rightarrow |2\rangle$ atomaire overgang, terwijl de $|3\rangle \rightarrow |2\rangle$ overgang aangedreven wordt door een EM 'koppelveld'. Een dergelijk systeem vertoont niet alleen een verminderde absorptie maar ook een verandering van de brekingsindex. Dit leidt o.a. tot een vermindering van de groepssnelheid van de EM puls in het medium.
We hebben aangetoond dat het nucleair schema bij toestandskruising analoog is aan het optisch Λ-schema op voorwaarde dat er een bijkomende interactie

[1] De zes mogelijke absorptielijnen in een Fe Mössbauer spectrum kunnen gegroepeerd worden in drie doubletten, waarbij de partnerlijnen omwille van pariteitsinvariantie gelijke eigenschappen hebben.

aanwezig is die in staat is om de kruisende niveaus op te mengen. Deze mengende interactie fungeert dan als het EM koppelveld, terwijl de gammastraling gezien wordt als EM signaalveld. Er is echter een belangrijk verschil tussen het optisch en nucleair schema wat betreft de vervalconstantes van de betrokken toestanden. In het optisch geval is toestand $|3\rangle$ een stabiele of metastabiele toestand, maar in ons nucleair schema vervalt deze toestand even snel als de andere geëxciteerde toestand ($|2\rangle$). Het belang van dit verschil bij de totstandkoming van de transparantie werd zeker niet onderkend in de eerste artikels over nucleaire EIT. Het is eenvoudig aan te tonen dat wanneer de vervalconstantes van de mengende niveaus gelijk zijn ($\gamma_2 = \gamma_3$) de interferentie helemaal verdwijnt, wat een verminderde transparantie tot gevolg heeft.

3. Semiklassieke modellen

Een model voor de interactie tussen straling en materie wordt semiklassiek genoemd wanneer de straling op een klassieke manier wordt beschreven (volgens de vergelijkingen van Maxwell) en de materie kwantummechanisch. In een eerste dergelijk model volgen we de benadering van Blume en Kistner. Hierin wordt de voortplanting van straling in een medium gegeven door de oplossing van de golfvergelijking in functie van de frekwentie van de straling en de dikte van het medium. Alle eigenschappen van het medium zitten vervat in de 2×2 complexe matrix van de brekingsindex. Deze brekingsindex is evenredig met de voorwaartse verstrooiingsamplitude, die op zijn beurt afhangt van de overgangsmatrixelementen. We hebben dit model toegepast op het nucleair drieniveau systeem, waarbij de twee geëxciteerde niveaus opgemengd zijn. In het geval van een heel dunne absorber kan de intensiteit van de doorgelaten straling inderdaad teruggebracht worden tot een som van 2 Lorentz absorptielijnen, opgesplitst door de mengende interactie maar zonder interferentie. Voor een kristal van willekeurige dikte hebben simulaties aangetoond dat de mengende interactie niet afkomstig kan zijn van een magnetisch veld maar wel van een (kleine) niet-axiale component van de elektrische veldgradiënt. Deze laatste zal enkel de $|m_e = -3/2\rangle$ en $|m_e = 1/2\rangle$ toestanden opmengen op toestandskruising. De verminderde absorptie treedt dus enkel op bij de toestandskruising en kan gezien worden als een combinatie van de Stark opsplitsing en de creatie van straling met een polarisatie die complementair is met de polarisatie van de invallende straling. Deze zal daardoor niet meer interfereren met de doorgaande (niet-verstrooide) straling en een niet-verwaarloosbare, versterkende bijdrage leveren tot het transparantie-effect (transmissiepieken die naar boven gericht zijn).
We hebben ook bewezen dat, zelfs wanneer de niet-axiale component afkomstig is van onzuiverheden in het kristal, en dus een willekeurige fase (en grootte) heeft, deze toch aanleiding kan geven tot een effectieve opmenging.

Desondanks zijn we niet geslaagd om binnen de lijnen van dit model een kwantitatieve fit te maken van de experimentele data, die ook nog eens consistent is voor beide geometrieën.
Daarom hebben we onze toevlucht gezocht in de meer algemene Maxwell-Schrödinger benadering, waarbij we ook rekening kunnen houden met kleine verschillen in de vervalconstantes van de coherenties van beide geëxciteerde toestanden. Dit heeft ons geleerd dat het al dan niet optreden van interferentie in het nucleaire geval afhankelijk is van zowel de vervalconstantes als van de overgangswaarschijnlijkheden. Wanneer de sterkste overgang gepaard gaat met de grootste vervalconstante, dan is er destructieve interferentie (minder absorptie). In het andere geval is er constructieve interferentie (meer absorptie). Dit resultaat is in perfecte overeenstemming met het verschil tussen de spectra in beide geometrieën. In de parallelle geometrie wordt de verminderde absorptie (vanaf de $|m_g = -1/2\rangle$ grondtoestand), afkomstig van de Stark opsplitsing, versterkt door de destructieve interferentie. In de loodrechte geometrie daarentegen, alhoewel er een zelfde Stark opsplitsing moet zijn, wordt de verminderde absorptie (vanaf de $|m_g = 1/2\rangle$ grondtoestand) tegengewerkt door de constructieve interferentie. Samen leiden ze tot een kwantitatief goede fit en een consistente verklaring van de opgemeten spectra.

4. Coherent pad model

Om dieper in te gaan op het één-foton karakter van de nucleaire verstrooiing en om na te gaan of de semiklassieke benadering in dit geval wel toegepast kon worden, hebben we het volledig kwantummechanisch 'coherent pad' model toegepast op het nucleair Λ-schema. Door verstrooiing aan een willekeurig aantal kernen (N) te beschouwen houdt dit model ook rekening met de dikte van het medium. De simulaties van de Mössbauer spectra in dit model zijn in goeie overeenstemming met deze verkregen in de semiklassieke benadering. Enkel door het discreet karakter van de meervoudige verstrooiing zijn er kleine verschillen tussen beide modellen. Dit is bijvoorbeeld zichtbaar in de intensiteit van de straling die haar polarisatie veranderd heeft, die voor $N \approx 50$ een drie-piek structuur vertoont in dit model, maar een twee-piek structuur in de semiklassieke benadering.
We hebben aangetoond dat de uitdrukking voor de doorgelaten intensiteit, in het geval zonder mengende interactie (een twee-niveau systeem), exact overeenkomt met het semiklassieke resultaat, op voorwaarde dat $N \to \infty$ en de radiatieve vervalconstante $\gamma_r \to 0$.
Op conceptueel niveau hebben we een eenduidig verband gevonden tussen de gesuggereerde foton golffunctie en de waarschijnlijkheidsamplitude dat dit foton een elektron losmaakt in de detector. Hierdoor is het mogelijk om een golffunctie, die gelokaliseerd is in tijd en ruimte, te associëren aan het foton-

concept.

5. Tijdsdifferentiële Mössbauer spectroscopie

Door de waargenomen verminderde absorptie te identificeren als een vorm van EIT, is het een logische stap om ook de tijdseigenschappen van de doorgelaten straling te beschouwen, en dan in het bijzonder haar groepssnelheid v_g. Doordat v_g rechtstreeks in verband staat met de brekingsindex hebben we meteen de resultaten uit de semiklassieke benadering kunnen gebruiken. De groepssnelheid neemt zowel in het optische ($\gamma_3 << \gamma_2$) als in het nucleaire geval ($\gamma_3 \approx \gamma_2$) sterk af, met een vermindering in de grootte-orde van $v_g/c \approx 10^{-7}$. Deze vermindering neemt af bij toenemende sterkte van de mengende interactie (vooral zichtbaar in het optische geval), hoewel de geassocieerde transparantie juist toeneemt. Om deze resultaten in het juiste perspectief te plaatsen, hebben we ook het twee-niveau systeem bestudeerd, waarbij nu de invallende straling niet meer exact in resonantie is met de overgang, maar daar in meer of mindere mate van afwijkt. Een dergelijke situatie leidt immers ook tot een verminderde groepssnelheid. Onze berekeningen hebben bevestigd dat dit van de zelfde grootte-orde is als in het drie-niveau systeem.
Simulaties van de tijdsafhankelijke intensiteit in het coherent pad model tonen, naast de gekende effecten van meervoudige verstrooiing als 'speed-up' en 'dynamical beats', duidelijk het ontstaan van de straling met een polarisatie die complementair is aan de polarisatie van de invallende straling. Deze straling vertoont een grote vertraging bij een kleine waarde voor de mengende interactie en een maximale doorgelaten intensiteit voor $\Omega \approx 2\gamma_2$. Uit een analyse van de individuele amplitudes die bijdragen tot de foton golffunctie hebben we een uitdrukking gevonden voor de geassocieerde groepssnelheid. Hieruit blijkt dat de vermindering van de groepssnelheid, of de vertraging van het stralingspakket, volledig te wijten is aan het proces van absorptie en emissie door de kernen.
Tenslotte hebben we nagegaan of dit vertragingseffect waarneembaar zou zijn in een tijdsafhankelijke Mössbauer meting. In het ideale geval, d.i. er is geen lijnverbreding (met uitzondering van de natuurlijke lijnbreedte), alle interactie resonant en er is geen invloed van andere absorptielijnen, is de vertraging zichtbaar als een toename van de intensiteit van de doorgelaten straling op latere tijden, wanneer dit vergeleken wordt met het geval zonder mengende interactie. Maar wanneer we rekening houden met een niet-ideale experimentele configuratie, dan wordt deze vertraging heel moeilijk waarneembaar. Een dergelijk tijdsafhankelijk spectrum zou geen harde bewijzen kunnen leveren voor de waarneming van vertraagde gamma fotonen.

Bibliography

[1] M. V. D. Bergh, *Quantum Optische Beschouwingen voor Gammastralen*, PhD thesis, Instituut voor Kern- en Stralingsfysica, K.U.Leuven, Belgium, 1994.

[2] A. Einstein, *Albert Einstein, Correspondence avec Michele Besso* 1903 – 1955, chapter 2. Letter to Besso, Hermann, Paris, 1972.

[3] A. Zajonc, *Catching the Light*, Oxford University Press, 1993.

[4] W. Heitler, *The Quantum Theory of Radiation*, Oxford University Press, 3rd edition, 1954.

[5] R. Loudon, *The quantum theory of light*, Clarendon Press, Oxford, 2nd edition, 1986.

[6] E. T. Jaynes, *Complexity, Entropy and the Physics of Information*, chapter 2, Addison-Wesley, Reading, 1972.

[7] L. de la Peña and A. M. Cetto, *The Quantum Dice, An Introduction to Stochastic Electrodynamics*, Kluwer Academic Publishers, 1996.

[8] L. de la Peña and A. M. Cetto, preprint: arXiv:quant-ph/0501011 (2005).

[9] S. Scheel, K. Nemoto, W. J. Munro, and P. L. Knight, Phys. Rev. A **68**, 032310 (2003).

[10] S. A. Babichev, B. Brezger, and A. I. Lvovsky, Phys. Rev. Lett. **92**, 047903 (2003).

[11] E. Knill, R. Laflamme, and G. J. Milburn, Nature **409**, 46 (2001).

[12] C. H. Bennett, G. Brassard, and A. Ekert, Sci. Am. **267**, 50 (1992).

[13] B. Sanders, J. Vuckovic, and P. Grangier, Europhys. News **267**, 56 (2005).

[14] B. Sanders, J. Vuckovic, and P. Grangier, editors, *Single Photons on Demand*, volume 6 of *New J. Phys.*, 2004.

[15] I. Bialynicki-Birula, *Progress in Optics Vol. XXXVI*, Elsevier, Amsterdam, 1996.

[16] R. J. Glauber, *Quantum Optics and Electronics*, Les Houches, Gordan and Breach, New York, 1965.

[17] M. O. Scully and S. Zubairy, *Quantum Optics*, Cambridge University Press, 1999.

[18] M. E. Peskin and D. V. Schroeder, *An introduction to quantum field theory*, Addison-Wesley, Reading, 3rd edition, 1996.

[19] I. Bialynicki-Birula, Acta Phys. Polonica **96**, 97 (1994).

[20] G. A. Prinz, D. W. Forester, and J. L. Lewis, Phys. Rev. B **8**, 2155 (1973).

[21] C. Klein and C. Hurlbut, *Manual of Mineralogy*, John Wiley and Sons, 20th edition, 1985.

[22] R. V. Gaines, H. C. W. Skinner, E. E. Foord, B. Mason, and A. Rosenzweig, *Dana's New Mineralogy*, John Wiley and Sons, 8th edition, 1997.

[23] R. A. Alikhanov, Soviet. Phys. - JETP **36 (9)**, 1204 (1959).

[24] I. S. Jacobs, J. Appl. Phys. **34**, 1106 (1963).

[25] K. Ono and A. Ito, J. Phys. Soc. Jpn. **19**, 899 (1964).

[26] R. M. Housley, U. Gonser, and R. W. Grant, Phys. Rev. Lett. **20**, 1279 (1968).

[27] D. W. Forester and N. C. Koon, J. Appl. Phys. **40**, 1316 (1969).

[28] H. N. Ok, Phys. Rev. **185**, 472 (1969).

[29] P. Boolchand, W. Bresser, G. Anaple, Y. Wu, R. N. Enzweiler, R. Coussement, and J. Grover, Phys. Rev. B **50**, 6833 (1994).

[30] T. P. Scoffin, *An introduction to carbonate sediments and rocks*, Blackie and Son, first edition, 1987.

[31] B. Dewever, private communication (2005).

[32] H. Bethe, Ann. Physik **3**, 133 (1929).

[33] C. J. Ballhausen, *Introduction to Ligand Field Theory*, McGraw-Hill, New York, 1962.

[34] A. Okiji and J. Kanamori, J. Phys. Soc. Jpn. **19**, 908 (1964).

[35] Z. Yi-Yang and Y. Chun-Hao, Phys. Rev. B **47**, 5451 (1993).

[36] J. W. Lynn, H. A. Mook, and W. J. L. Buyers, Phys. Rev. B **12**, 238 (1975).

[37] A. Vértes, L. Korecz, and K. Burger, *Mössbauer Spectroscopy*, Elsevier Scientific Publishing Company, 1979.

[38] A. J. Freeman and R. E. Watson, Phys. Rev. **131**, 2566 (1963).

[39] M. Abramowitz and I. A. Stegun, *Handbook of Mathematical Functions*, Dover Publications, 1964.

[40] P. Dufek, P. Blaha, and K. Schwarz, Phys. Rev. Lett. **75**, 3545 (1995).

[41] S. Cottenier, private communication (2005).

[42] A. Abragam and B. Bleaney, *Electron Paramagnetic Resonance of Transition Ions*, Clarendon Press, Oxford, 1970.

[43] D. M. Brink and G. R. Satchler, *Angular momentum*, Clarendon Press, Oxford, 1968.

[44] B. L. van der Waerden, *A History of Algebra: From Al-Khwarizmi to Emmy Noether*, Springer-Verlag New York, 1985.

[45] L. I. Schiff, *Quantum Mechanics*, McGraw-Hill, New York, third edition edition, 1968.

[46] R. Mössbauer, Z. Physik **151**, 124 (1958).

[47] I. Waller, Ann. Physik **79**, 261 (1926).

[48] W. E. Lamb, Phys. Rev. **55**, 190 (1939).

[49] R. Giovanelli and A. Orefice, Hyp. Int. **131**, 51 (2000).

[50] R. Giovanelli and A. Orefice, Physica B **293**, 155 (2000).

[51] V. I. Goldanskii, E. F. Makarov, I. P. Suzdalev, and I. A. Vinogradov, Phys. Rev. Lett. **20**, 137 (1968).

[52] R. M. Housley, R. W. Grant, and U. Gonser, Phys. Rev. **178**, 514 (1969).

[53] K. Lagarec, *Recoil - Mössbauer Spectral Analysis Software for Windows*, Mössbauer group, University of Ottawa, 2002.

[54] R. V. Pound and G. A. Rebka, Phys. Rev. Lett. **4**, 274 (1960).

[55] B. J. Josephson, Phys. Rev. Lett. **4**, 341 (1960).

[56] E. N. Kaufmann and R. J. Vianden, Rev. Mod. Phys. **51**, 161 (1979).

[57] M. Blume and J. A. Tjon, Phys. Rev. **165**, 446 (1968).

[58] F. van der Woude and A. J. Dekker, Solid State Commun. **3**, 319 (1965).

[59] S. E. Harris, J. E. Field, and A. Imamoglu, Phys. Rev. Lett. **64**, 1107 (1990).

[60] M. Fleischhauer, A. Imamoglu, and J. P. Marangos, Rev. Mod. Phys. **77**, 633 (2005).

[61] P. R. Fontana and R. P. Srivastava, Phys. Rev. A **7**, 1866 (1973).

[62] E. Arimondo and B. Orriols, Lett. al Nuovo Cimento **17**, 333 (1976).

[63] G. Alzetta, A. Gozzini, L. Moi, and B. Orriols, Nuovo Cimento B **36**, 5 (1976).

[64] E. Paspalakis, N. J. Kylstra, and P. L. Knight, Phys. Rev. Lett. **82**, 2079 (1999).

[65] P. R. Berman, Phys. Rev. A **58**, 4886 (1998).

[66] S. E. Harris, Phys. Rev. Lett. **62**, 1033 (1989).

[67] M. O. Scully, S. Y. Zhu, and A. Gavrielides, Phys. Rev. Lett. **62**, 2813 (1989).

[68] O. Kocharovskaya and P. Mandel, Phys. Rev. A **42**, 523 (1990).

[69] S. E. Harris, Physics Today **50**, 36 (1997).

[70] J. R. Kuklinski, U. Gaubatz, F. T. Hioe, and K. Bergmann, Phys. Rev. A **40**, 6741 (1989).

[71] S. Alam, *Lasers without Inversion and Electromagnetically Induced Transparency*, SPIE Optical Engineering Press, 1999.

[72] A. Imamoglu and S. E. Harris, Opt. Lett. **14**, 1344 (1989).

[73] M. D. Lukin, Rev. Mod. Phys. **75**, 457 (2003).

[74] M. Born and E. Wolf, *Principles of Optics*, Cambridge University Press, seventh (expanded) edition, 1999.

[75] J. Jackson, *Classical Electrodynamics*, 3rd Ed., John Wiley and Sons, 1998.

[76] A. M. Steinberg and R. Y. Chiao, Phys. Rev. A **49**, 2071 (1994).

[77] L. J. Wang, A. Kuzmich, and A. Dogariu, Nature **406**, 277 (2000).

[78] S. E. Harris, J. E. Field, and A. Kasapi, Phys. Rev. A **46**, 29 (1992).

[79] L. V. Hau, S. E. Harris, Z. Dutton, and C. H. Behroozi, Nature **397**, 594 (1999).

[80] C. Liu, Z. Dutton, C. H. Behroozi, and L. V. Hau, Nature **409**, 490 (2001).

[81] D. Philips, A. Fleischhauer, A. Mair, R. Walsworth, and M. D. Lukin, Phys. Rev. Lett. **86**, 783 (2001).

[82] A. V. Turukhin, V. S. Sudarhanam, M. S. Shahriar, J. A. Musser, B. S. Ham, and P. R. Hemmer, Phys. Rev. Lett. **88**, 023602 (2002).

[83] J. Odeurs, editor, *Nuclear Quantum Optics*, volume 135 of *Hyp. Int.*, Kluwer Academic Publishers, 2001.

[84] L. A. Rivlin, Laser Phys. **9**, 12 (1998).

[85] G. C. Baldwin and J. C. Solem, Rev. Mod. Phys. **69**, 1085 (1997).

[86] R. Coussement, M. V. den Bergh, G. S'heeren, G. Neyens, and R. Nouwen, Phys. Rev. Lett. **71**, 1824 (1993).

[87] U. Leonhardt, *Measuring the Quantum State of Light*, Cambridge Studies in Modern Optics, Cambridge University Press, 1997.

[88] R. P. Feynman, R. B. Leighton, and M. Sands, *The Feynman Lectures on Physics Vol.3*, Addison-Wesley, Reading, 1966.

[89] S. E. Harris, Phys. Rev. Lett. **70**, 552 (1993).

[90] H. Gabriel, Phys. Rev. **184**, 359 (1969).

[91] F. G. Vagizov, Hyp. Int. **61**, 1359 (1990).

[92] I. Tittonen, M. Lippmaa, E. Ikonen, J. Lindén, and T. Katila, Phys. Rev. Lett. **69**, 2815 (1992).

[93] K. Hakuta, L. Marmet, and B. P. Stoicheff, Phys. Rev. Lett. **66**, 596 (1991).

[94] K. Hakuta, L. Marmet, and B. P. Stoicheff, Phys. Rev. A **45**, 5152 (1992).

[95] R. N. Shakhmuratov and J. Odeurs, Hyp. Int. **135**, 215 (2001).

[96] R. Coussement, Y. Rostovtsev, J. Odeurs, G. Neyens, H. Muramatsu, S. Gheysen, R. Callens, K. Vyvey, G. Kozyreff, R. N. Shakhmuratov, O. Kocharovskaya, and P. Mandel, Phys. Rev. Lett. **89**, 107601 (2002).

[97] J. Odeurs, R. Coussement, K. Vyvey, H. Muramatsu, S. Gheysen, R. Callens, G. Neyens, I. Serdons, R. N. Shakhmuratov, Y. Rostovtsev, and O. Kocharovskaya, Hyp. Int. **143**, 97 (2002).

[98] R. Coussement, S. Gheysen, I. Serdons, R. Callens, K. Vyvey, , R. N. Shakhmuratov, J. Odeurs, P. Mandel, Y. Rostovtsev, and O. Kocharovskaya, Hyp. Int. **151**, 93 (2003).

[99] Y. Rostovtsev and O. Kocharovskaya, Hyp. Int. **135**, 233 (2001).

[100] P. W. Milonni, Phys. Rep. **25**, 1 (1976).

[101] M. Blume and O. C. Kistner, Phys. Rev. **171**, 417 (1968).

[102] G. V. Smirnov, Hyp. Int. **123/124**, 31 (1999).

[103] U. van Bürck, Hyp. Int. **123/124**, 483 (1999).

[104] M. Lax, Rev. Mod. Phys. **23**, 287 (1951).

[105] J. P. Hannon and G. T. Trammell, Hyp. Int. **123/124**, 127 (1999).

[106] D. P. Siddons, U. Bergmann, and J. B. Hastings, Hyp. Int. **123/124**, 681 (1999).

[107] R. Coussement, S. Cottenier, and C. Labbé, Phys. Rev. B **54**, 16003 (1996).

[108] R. Coussement, J. Odeurs, C. L'abb'e, and G. Neyens, Hyp. Int. **125**, 113 (2000).

[109] R. Callens, *Stroboscopic Detection of Nuclear Forward Scattered Synchrotron Radiation*, PhD thesis, Instituut voor Kern- en Stralingsfysica, K.U.Leuven, Belgium, 2003.

[110] S. Eidelman and *et al.* (Particle Data Group), Phys. Lett. B **592**, 1 (2004).

[111] G. V. Smirnov, Hyp. Int. **97/98**, 551 (1996).

[112] B. W. Shore, *The Theory of Coherent Atomic Excitation*, volume 2, John Wiley and Sons, New York, 1991.

[113] R. N. Shakhmuratov, J. Odeurs, S. Gheysen, Y. Rostovtsev, O. Kocharovskaya, and P. Mandel, Appl. Phys. B **81**, 883 (2005).

[114] N. Bloembergen, *Quantum Optics*, chapter Review of Nonlinear Optical Phenomena in Condensed Matter, pages 355–394, Academic Press, 1970.

[115] P. Mandel, Hyp. Int. **135**, 223 (2001).

[116] H. Lee and M. O. Scully, Found. Phys. **28**, 585 (1998).

[117] S. Harris, Phys. Rev. **124**, 1178 (1961).

[118] G. R. Hoy, J. Phys.: Condens. Matter **9**, 8749 (1997).

[119] J. Odeurs, G. R. Hoy, C. L'abbé, R. N. Shakhmuratov, and R. Coussement, Phys. Rev. B **62**, 6148 (2000).

[120] G. R. Hoy and J. Odeurs, Phys. Rev. B **63**, 064301 (2001).

[121] G. R. Hoy, J. Odeurs, and R. Coussement, Phys. Rev. B **63**, 184435 (2001).

[122] I. I. Sobel'man, *Introduction to the theory of atomic spectra*, Pergamon Oxford, 1972.

[123] J. Hannon and G. Trammell, Phys. Rev. **169**, 315 (1968).

[124] J. Hannon and G. Trammell, Phys. Rev. **186**, 306 (1969).

[125] F. J. Lynch, R. E. Holland, and M. Hamermesh, Phys. Rev. **120**, 513 (1960).

[126] G. R. Hoy, Hyp. Int. **107**, 381 (1997).

[127] C. S. Wu, Y. K. Lee, N. Benczer-Koller, and P. Simms, Phys. Rev. Lett. **5**, 432 (1960).

[128] W. Triftshäuser and P. P. Craig, Phys. Rev. Lett. **16**, 1161 (1966).

[129] D. W. Hamill and G. R. Hoy, Phys. Rev. Lett. **21**, 724 (1968).

[130] E. Gerdau and H. D. Waard, editors, *Nuclear resonant scattering of synchrotron radiation*, volume 123-124 of *Hyp. Int.*, Springer Netherlands, 1999.

[131] W. C. McDermott and G. R. Hoy, Hyp. Int. **107**, 81 (1997).

[132] R. B. Firestone, *Table of Isotopes*, John Wiley and Sons, 8th edition, 1996.

[133] M. E. Rose, *Elementary theory of angular momentum*, John Wiley and Sons, New York, 1957.